UNIVERSITY OF CAPE TOWN
IYUNIVESITHI YASEKAPA • UNIVERSITEIT VAN KAAPSTAD

The response of aluminium and glass fibre FMLs subjected to blast loading

MSc Dissertation

Gideon Volschenk

Supervisors:
Prof Genevieve Langdon
A/Prof Chris von Klemperer

Blast Impact and Survivability Research Centre
Department of Mechanical Engineering
University of Cape Town

May 12, 2015

Plagiarism Declaration

I know that plagiarism is wrong. Plagiarism is to use another's work (even if it is summarized, translated or rephrased) and pretend that it is one's own. This assignment is my own work. Each contribution to and quotation in this assignment from the work(s) of other people has been explicitly attributed, and has been cited and referenced. In addition to being explicitly attributed, all quotations are enclosed in inverted commas, and long quotations are additionally in indented paragraphs. I have not allowed, and will not allow, anyone to use my work with the intention of passing it off as his/her own work. I know that students involved in plagiarism will be reported to the Registrar and/or the Central Disciplinary Committee.

_____

Gideon Volschenk

_____

Signed at

_____

Date

This page has been intentionally left blank.

Acknowledgements

I would like to acknowledge the following people for all their help and support throughout the course of this project:

First and foremost I would like to thank my MSc supervisors, Prof G. Langdon and A/Prof C. von Klemperer, for their invaluable guidance and patience.

A special thanks to Dr R. Govender for his help and guidance during critical stages of the project.

A great many thanks to Ms P. Park-Ross and Dr S. George for all their help in testing and treatment at CME. Also thanks to Mr G. Newins and all the workshop staff for their help in manufacturing the various specimens.

Thanks to Mr R. Curry for all his help and guidance around the lab and to my fellow post-graduate colleagues, Mr V. Shekhar, Mr I. Gallaher and Mr L. Zacharias for their help and friendship and to all the other BISRU students and staff members for their support.

Finally, a special thanks Ms T. Hammond for her consistent support and motivation and unwavering faith in me, throughout the course of this project. Without you, none of this would have been possible.

This page has been intentionally left blank.

Abstract

Fibre-Metal Laminates (FMLs) have long been of interest to the aeronautics industry due to their exceptional strength to weight ratio, fatigue and impact resistance. Due to the increasing global risk of subversive activity in this industry, the focus of research in recent years has shifted to the blast resistance of these materials. A particularly interesting material being GLARE, a commercially available Aluminium-GFRP FML. This dissertation presents the results of an experimental study into the effects of glass fibre configuration and epoxy type on the response of glass fibre reinforced, epoxy-based FMLs, subjected to localised and uniform blast loading conditions.

Standard tensile specimens and Single-Leg Bend (SLB) specimens were manufactured and tested to determine the properties constitutive materials and interfacial bond strength. Bond strength between the composite and metal interfaces was improved by employing a combination of surface treatments, consisting of both mechanical and chemical as well as the use of a film adhesive. FMLs were manufactured from Al 2024-T3 and e-glass fibre reinforced epoxy composite. Both woven and unidirectional fibre configurations were used as part of either a prepreg or wet layup to construct the composite layers.

Tensile and SLB specimens were used to characterise the constitutive materials and interfacial bond strength. SLB tests were used to determine the effect of cure cycle and composite layup technique on interfacial bond strength. These tests and revealed a variety of interfacial failure modes for different cure cycles and epoxy configurations, each resulting in different levels of strength. The modes, in increasing order of strength, included debonding of the film adhesive from either the metal or composite interface or both, and in some cases also included delamination in the composite layer. Tests showed that a single stage layup and cure cycle resulted in the strongest bonds between interfaces, compared to a multi-stage manufacturing processes. It was also shown that the use of prepreg resulted in stronger inter-facial bonds than a wet-layup process.

The properties of the constitutive materials were used to construct a numerical model to aid in experimental design. The model was used to determine a suitable range of charge masses for testing.

Localised and uniform blast loading tests were performed on three sets of FMLs. None of the test series performed well under highly localised blast loading (20 mm SOD) however. These conditions generally resulted in tearing of the FML surface layers, petalling and hole punching. Detonator shrapnel also resulted in variations in consistency of panel surface damage. Increasing the stand-off distance to 40 mm resulted in in more consistent damage and deformation, but results were still distorted by some detonator shrapnel damage. Consistent debonding was observed in both of the wet-layup FML series (WLW and WLUD) under localised loading conditions. The woven PPW series showed no debonding, transitioning directly from inelastic deformations to tearing and petal formation. The FMLs exhibited an aluminium dominated response resulting in the absence of the characteristic diamond-shaped back face damage in FMLs subjected to localised loading.

Debonding was also observed in both of the wet-layup FML series (WLW and WLUD) subjected to uniform loading, starting at charge masses as low as 10 g and showing minor increase with increasing impulse. At higher impulses, superimposed bulges of inelastic deformation was observed in the debonded regions of the WLUD series. The prepreg FML (PPW) series exhibited no sign of debonding, similar to GLARE 3, even when subjected to charge masses as high as 30 g. The PPW series showed deformation behaviour and failure modes similar to that of monolithic metal, transitioning directly from large inelastic deformations to tearing at the clamped boundary. The FML response to uniform loading was also dominated by the aluminium laminates, showing large inelastic deformation and yield line formation. Similar dimensionless responses were also seen from all three test series. Pulling-in at the clamped boundary was observed at all charge masses above 25 g, with the exception of the WLW series which started showing this behaviour from 20 g. The degree of pulling-in also increased with increasing charge mass. Analysis of the FMLs revealed that pulling-in may have absorbed enough energy in some cases to stop the occurrence of certain failure modes.

The FMLs showed a slight reduction the experienced d/t ratios, when compared to the dimensionless response of GFPP and GFPA based FMLs available in literature, indicating a more favourable response. When compared to GLARE 3, all the tested FMLs showed a lower tolerance to blast damage. The FMLs were tested at a lower dimensionless impulse range and resulted in higher dimensionless displacements. Due to the dependence of dimensionless impulse on thickness (1/t3), a decrease in constituent material thickness could produce an FML with properties comparable to that of GLARE 3, should the bond strength be retained.

Table of Contents

This page has been intentionally left blank.

List of Tables

List of Figures

This page has been intentionally left blank.

Nomenclature

List of Abbreviations

Al Aluminium

ALE Arbitrary-Lagrangian-Eulerian

ARALL Aramid Reinforced Aluminium Laminate

ARALL Aramid Reinforced Aluminium Laminates

BF Back face of the FML

BISRU Blast Impact and Survivability Research Unit

CME Centre for Materials Engineering

ENF End-Notch Flexure

EOS Equation of State

FF Front face of the FML

FML Fibre-Metal Laminates

GFRP Glass-Fibre Reinforced Polymer

GLARE Glass Laminate Aluminium Reinforced Epoxy

LV Low Viscosity

MSM Multi-Stage Manufacturing

PCJ Chapman-Jouget pressure

PE4 Plastic Explosive No. 4

PPW FMLs manufactured using 295 $\mathrm{g\,m^{-1}}$ woven SE 84LV prepreg for the GFRP layer

Prepreg Indicating the fibres has been pre-impregnated with resin

Prime 20LV An epoxy resin

Redux 609 A film adhesive

SERR Strain Energy Release Rate

SE 84LV A hot-melt epoxy prepreg

SLB Single-Leg Bend

SOD Standoff Distance

SSM Single-Stage Manufacturing

TEM Transmission Electron Microscopy

TPB Three-Point Bend

UCT University of Cape Town

UD Uni-Directional

VARTM Vacuum Assisted Resin Transfer Molding

VCCT Virtual Crack Closure Technique

WLUD FMLs manufactured using 2 $\times$ 220 $\mathrm{g\,m^{-1}}$ 0°/90° UD E-glass and Prime 20LV epoxy for the GFRP layer

WLW FMLs manufactured using 400 $\mathrm{g\,m^{-1}}$ woven E-glass and Prime 20LV epoxy for the GFRP layer

List of Symbols

δ Displacement

$\epsilon_{1/2}^{c,f,m}$ Strain in the longitudinal/transverse directions of the composite, fibre or matrix

ϵ_{ENG} Engineering Strain

ϵ_T True Strain

$\gamma_{12}^{c,f,m}$ Shear strain between the longitudinal/transverse directions of the composite, fibre or matrix

μ Poisson's ratio

ϕ_{ql} Localised dimensionless impulse

ϕ_q Uniform dimensionless impulse

$\rho_{c,f,m}$ Density of the composite, fibre or matrix

$\sigma_{1/2}^{c,f,m}$ Stress in the longitudinal/transverse directions of the composite, fibre or matrix

σ_{ENG} Engineering Stress

σ_T True Stress

A Area

$a_{c,f,m}$ Area of the composite, fibre or matrix

d/t Displacement or Deflection/thickness ratio

$E_{1/2}^{c,f,m}$ Young's modulus in the longitudinal/transverse directions of the composite, fibre or matrix

F Force

G Shear stress

$G_{I/II}$ Mixed mode I/II energy release rate

G_{II} Mode II energy release rate

G_I Mode I energy release rate

I Impulse

l Length

m mass

$M_{c,f,m}$ Mass of of the composite, fibre or matrix

$m_{f,m}$ Mass fraction of the fibre or matrix

T Temperature

$V_{c,f,m}$ Volume of of the composite, fibre or matrix

$v_{f,m}$ Volume fraction of the fibre or matrix

This page has been intentionally left blank.

Chapter 1

Introduction

1.1 Background

Fibre-Metal Laminates (FMLs) are hybrid laminated structures consisting of thin layers of metal alloy and fibre-reinforced composite. With their superior strength and stiffness properties compared to product mass, as well as exceptional fatigue strength, these materials are increasingly being used in the design and manufacture of primary structures in the aeronautics industry [1]. Due to the increasing global risk of subversive activity in this industry, the focus of research in recent years has been on the blast resistance of these structures. The Lockerbie air disaster in 1982 [2] is evidence of the catastrophic effects of blast loading on-board an aircraft. The terrorist attack claimed the lives of 270 people when an explosive device in the cargo hold tore through the fuselage bringing Pan Am flight 103 crashing down in the town of Lockerbie, Scotland [3].

Great strides have since been made in the field of fibre-reinforced laminates in an attempt to replace monolithic aluminium alloys with a more damage resistant material. The most popular commercially available FML is GLARE®, an aluminium and Glass-Fibre Reinforced Polymer (GFRP) laminate. Fleischer [4] investigated the blast response of GLARE® and claimed that a cargo-hold container manufactured from this material could withstand an explosive blast of similar magnitude to the blast that brought down Pan Am flight 103. Langdon et al. [5] further researched this claim and found the blast properties of GLARE® comparable to that of steel when normalised by mass. The GLARE® panels showed very little evidence of debonding with the main energy absorption mechanism that of bending and membrane deformation, similar to behaviour described by Hoo Fatt et al. [6]. Research has suggested that debonding plays a minimal role in the energy

absorption of FMLs subjected to blast and impact loading [7, 8]. Research into the effects of using different fibre configurations in the GFRP layer suggested that woven thermoplastic FMLs had both better impact [9, 10] and blast [11] resistance than their uni-directional counterparts. This revealed the opportunity to develop a woven variant of GLARE® with equally good bond strength that could potentially have better blast resistance than the commercially available material.

GLARE® is a proprietary product manufactured exclusively for Airbus. Previous attempts at manufacturing thermoset FMLs using similar constituents to GLARE® have proven unsuccessful largely due to inadequate bond strength resulting in large scale debonding of the laminate. van Tonder [12] investigated the effects of surface treatments of the aluminium alloy on the bond strength of the Al/GFRP interface. She found promising results using a combination of different chemical and mechanical surface treatments with surface treated specimens showing greater interfacial fracture toughness and more resistance to debonding during impact. This study therefore investigated the blast response of FMLs manufactured using the recommended surface treatments.

1.2 Research Objectives

The purpose of this study was to manufacture thermoset FMLs for testing in blast loading, using different composite layup techniques and fibre configurations (woven and uni-directional), in order to determine the effects of these components on the blast response of the FML. The FMLs had to be compared to their commercial equivalent, GLARE®, as well as other researched FMLs to determine the quality of the product relative to current technologies. The FMLs was to be manufactured using the surface treatments recommended by van Tonder [12]. The bond strength and various constituents of the FMLs had to be characterised through tests to obtain material models for use in numerical modelling. The study focussed on analysing the blast response of the FMLs resulting from their constituent materials and inter-laminar bond strength, by identifying the various failure modes and mechanisms at work.

1.3 Outline

Chapter 2 contains a summary of the relevant literature published. The various constituent materials, composite layup techniques and surface treatments were investigated. The chapter contains a short history of FMLs and GLARE® and the

response of these materials to various loading conditions. An investigation is also made into blast loading and the effects thereof on FMLs and GLARE®.

Chapter 3 describes the manufacturing process followed and the techniques used to construct the various test specimens. Specimens were also investigated to determine the effect of surface treatments on their morphology.

Chapter 4 reports the methods used to perform material tests on the various specimens. Quasi-static tensile tests were conducted to determine the tensile response of the aluminium alloy and perform material characterisation. A numerical model of the tensile tests were created to aid in the characterisation of a material model for use in experimental design. Single-leg bend tests were performed to determine the Al/GFRP interfacial fracture toughness for the various manufacturing methods and layup techniques.

Chapter 5 describes the construction of a numerical model to aid in the design of the blast loading experiments. Models were constructed for both the localised and uniform loading conditions. The model is constructed using the LS-DYNA finite element package.

Chapter 6 details the experimental set-up and test procedure for subjecting the FMLs to both localised and uniform blast loading. This chapter contains a description of the test equipment used as well as method of analysis of the test results.

Chapter 7 reports the experimental results and observations. This chapter contains images of the test results and digitizations of the tested panels. The calculated impulses and midpoint deflections for the tested panels are also shown.

Chapter 8 contains an in depth analysis of the results with dimensionless analysis of the panels, cross-sectional views showing inter-laminar damage and determination of failure modes and mechanisms.

Chapter 9 summarises the findings of this report and contains various recommendations for future studies.

This page has been intentionally left blank.

Chapter 2

Literature Review

2.1 Composites

The term composite usually refers to a single material consisting of two or more materials, each having significantly different physical or chemical properties. Unlike alloys, each material retains its original chemical, physical and mechanical properties [13]. The two main constituents of a composite are its reinforcing phase and the matrix in which this phase is embedded. The matrix is a continuous material providing structure to the composite whereas the reinforcing phase can consist of either fibres, particles or flakes and provides the composite with its strength and stiffness [14, 15].

This project concerns the use of fibre reinforced composites as structural materials. A fibre is defined as having a large length-to-diameter ratio (l/d), also known as aspect ratio [13]. Fibre-reinforcement is used to generate a composite material with a high specific strength and high specific modulus [16]. This reinforcement can take different forms, such as Uni-Directional (UD), woven, filament wound, chopped and mat. Examples of these are shown in Figure 2.1, and are further subdivided into continuous and discontinuous fibre reinforcement. The fibres in a composite can either be oriented randomly or arranged in a preferred direction where the highest stresses are expected. This type of material is generally referred to as being anisotropic as it has different material properties in different directions. Having control of anisotropy is important when trying to optimise a material for a specific application [15]. This is one of the biggest advantages of composites as it allows application-specific manufacturing. Fibres can be manufactured from a variety of materials, with typical ones including glass, aramid and carbon. The properties of some common fibres are shown in Table 2.1.

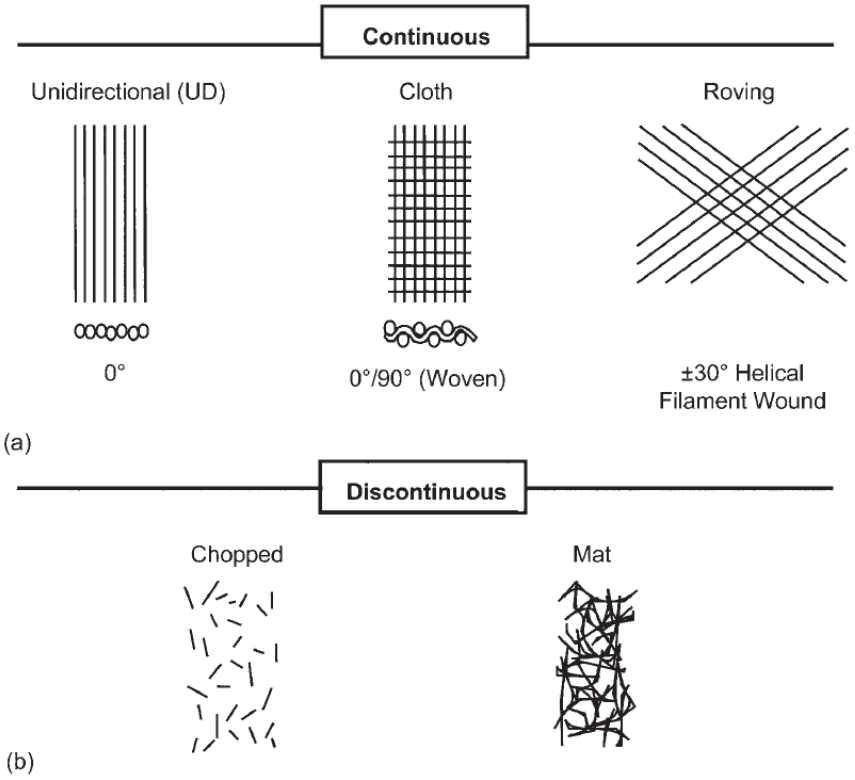

Figure 2.1: Fibre reinforcement types [13].

Table 2.1: Typical properties of different fibre materials [15].

Material	E GPa	σ_b GPa	ε_b %	ρ Mg/m^3	E/ρ MJ/kg	σ/ρ MJ/kg	cost $/kg
E-glass	72.4	2.4	2.6	2.54	28.5	0.95	1.1
S-glass	85.5	4.5	2.0	2.49	34.3	1.8	22 - 33
aramid	124	3.6	2.3	1.45	86	2.5	22 - 33
boron	400	3.5	1.0	2.45	163	1.43	330 - 440
HS graphite	253	4.5	1.1	1.80	140	2.5	66 - 110
HM graphite	520	2.4	0.6	1.85	281	1.3	220 - 660

The superior properties of fibre-reinforced composites are achieved by having the applied loads transmitted to the fibres through the matrix material [16]. The matrix phase of the composite can consist of either a polymer, metal or ceramic. The matrix phase provides the structure of the composite which, in the case of fibre reinforced composites, means maintaining the fibres in the proper orientation and spacing. The matrix phase also protects the fibres from abrasion and environmental conditions [13, 15].

2.1.1 Analytical Approach to Composites

In order to analyse the structural response of a composite material, certain material properties are required. These properties of the composite depend not only on the type of fibres used but also their orientation and distribution in the matrix. The study of the fibre properties and their interaction with a matrix is known as micromechanics [16]. To relate the properties of both constituents to the macromechanical properties of the composite, the concepts of volume fractions, v, and mass fractions, m, need to be introduced. In Equations (2.1) and (2.2) the subscripts f, m and c correspond to the fibre, matrix and composite respectively while V and M denotes both the volume and mass.

$$v_f = \frac{V_f}{V_c}, \qquad v_m = \frac{V_m}{V_c} \tag{2.1}$$

$$m_f = \frac{M_f}{M_c}, \qquad m_m = \frac{M_m}{M_c} \tag{2.2}$$

Since the total volume and mass of the composite can be calculated by $V_c = V_f + V_m$ and $M_c = M_f + M_m$, we have Equation (2.3).

$$v_f + v_m = 1, \qquad m_f + m_m = 1 \tag{2.3}$$

The volume and mass fractions can be related to one another by Equation (2.4), where ρ_c, ρ_f, ρ_m are the respective densities of the composite, fibres and matrix. During analysis, the volume fractions are preferable as they can be used directly to calculate the stiffness coefficients of a ply. The mass fractions can be directly measured during experimentation and fabrication but require some manipulation before being used in analysis [17].

$$v_f = \frac{\rho_c}{\rho_f} m_f, \qquad v_m = \frac{\rho_c}{\rho_m} m_m \tag{2.4}$$

The simplest method of analysing the structural response of a composite is by using a first order method. This method allows the structural properties of a single ply to be calculated using only one parameter, namely the fibre volume fraction v_f. As this method does not take into account the fibre distribution, each ply can be represented as a combination of fibre and matrix strips, seen in Figure 2.2 [17].

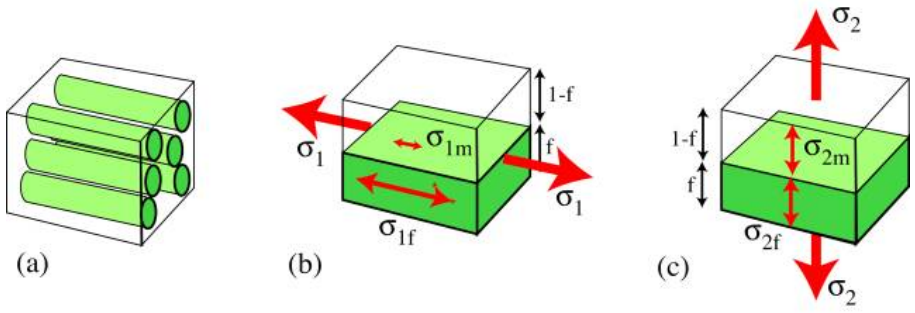

Figure 2.2: (a) A representation of the matrix and fibres in a composite (b), (c) First order model expressing the principal stresses as a combination of the stresses on fibre and matrix volume fractions [17].

From this assumption, the respective volume fractions can be calculated as a fraction of the unit area as seen in Equation (2.5).

$$\frac{a_f}{a_c} = v_f, \qquad \frac{a_m}{a_c} = v_m, \qquad v_f + v_m = 1 \tag{2.5}$$

The next assumption that can be made is that the longitudinal strains in all these strips are the same, illustrated in Equation (2.6). Furthermore, the total force acting on the ply can be taken as the sum of the forces acting on each component of the ply, seen in Equation (2.7). In both these equations, the subscript or superscript f and m denotes either fibre or matrix while a numerical subscript denotes the direction.

$$\varepsilon_1^f = \varepsilon_1^m = \varepsilon_1^c \tag{2.6}$$

$$F_1^c = \sigma_1^c a = \sigma_1^f a_f + \sigma_1^m a_m \tag{2.7}$$

It can also be seen from Figure 2.2, that the transverse tensional stress in both the fibres and the matrix must be the same, illustrated numerically in Equation (2.8). The total elongation in the transverse direction will then be equal to the sum of both the fibre and the matrix elongation, introducing the transverse strains as seen in Equation (2.11) [14, 17].

$$\sigma_2^c = \sigma_2^f = \sigma_2^m \tag{2.8}$$

$$\Delta a = \Delta a_f + \Delta a_m \tag{2.9}$$

$$\varepsilon_2^c = \frac{\Delta a}{a}, \qquad \varepsilon_2^f = \frac{\Delta a_f}{a}, \qquad \varepsilon_2^m = \frac{\Delta a_m}{a} \tag{2.10}$$

$$\varepsilon_2^c a = \varepsilon_2^f a_f + \varepsilon_2^m a_m \tag{2.11}$$

The same approximations can be made for the shear stresses and strains as Equations (2.12) and (2.13) illustrate. [17]

$$\tau_{12} = \tau_{12}^f = \tau_{12}^m \tag{2.12}$$

$$\gamma_1^c 2a = \gamma_{12}^f a_f + \gamma_{12}^m a_m \tag{2.13}$$

The constitutive equations for isotropic fibre and matrix strips can be written as seen in Equation (2.16) [17]. These equations can then be reduced to yield the material properties of the composite material, seen in Equation (2.17).

$$\varepsilon_1^{f,m} = \frac{1}{E_{f,m}} \left(\sigma_1^{f,m} - v_{f,m} \sigma_2^{f,m} \right) \tag{2.14}$$

$$\varepsilon_2^{f,m} = \frac{1}{E_{f,m}} \left(\sigma_2^{f,m} - v_{f,m} \sigma_1^{f,m} \right) \tag{2.15}$$

$$\gamma_{12}^{f,m} = \frac{1}{G_{f,m}} \tau_{12}^{f,m} \tag{2.16}$$

$$E_1^c = E_f v_f, \qquad E_2 = \frac{E_m}{v_m \left(1 - v_m^2\right)}, \qquad G_{12} = \frac{G_m}{v_m} \tag{2.17}$$

2.2 Fibre-metal Laminates and GLARE®

Although composites have many benefits as structures, they lack the high combination of strength and fracture toughness gained from metals [14]. In an attempt to gain these benefits a new material was designed, namely Fibre-Metal Laminates (FMLs). FMLs comprise of thin metal layers alternating with composite plies as shown in Figure 2.3.

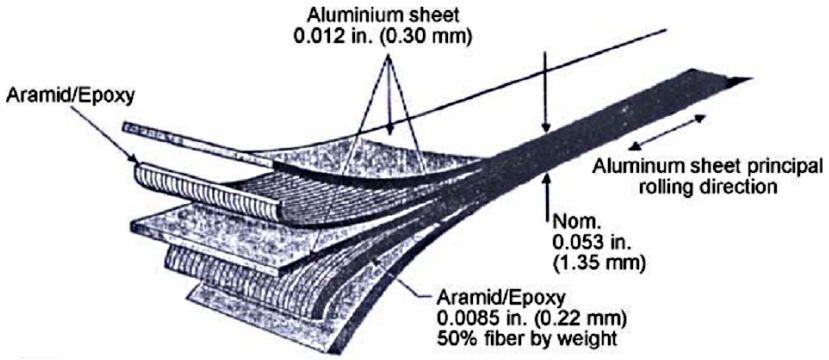

Figure 2.3: Illustration of ARALL 3 fibre-metal laminate layup [18].

The surfaces of the metal layers need to be specially treated in order to bond to the composite layers, which can be made up of uni-directional, cross-ply or woven fabrics impregnated with resin [17, 19]. The bonding of these materials will be discussed in more detail in Section 2.3.

2.2.1 Origin and History of FMLs

In 1945, five years after the destruction of their Dutch facilities in the war, Fokker Aircraft Engineers started to rebuild, experimenting with new materials and techniques [20–22]. In the process they perfected the pretreatment of aluminium surfaces and production processes of bonded structures [20, 22].

Schijve [20–22] found that the layered aluminium sheets displayed exceptional fatigue properties, noting that cracks grew only within a single layer. Although widely studied, composites were expensive, leading to researchers in the US and Britain combining it with metal to try and obtain a strong cost effective material. In the 1970's, Fokker engineers performed the first tests with the introduction of fibres in the adhesive between the laminated metal layers [20–22]. Initial results did not look promising and the project was eventually stopped by Fokker. Delft Universty, however, continued investigating and optimizing the fibre-reinforced metal laminates and in the 1980's, with industry partners (ALCOA, AKZO and 3M), released the first semi-finished sheet, known as ARALL® (Aramid Reinforced Aluminium Laminates). This first generation fibre-metal laminate consisted of 0.3 mm thick Al2024-T3 with uni-directional aramid fibres reinforcing the adhesive layer between plates, shown in Figure 2.5 [20–22]. Figure 2.4 shows an image from the patent filed by AKZO for the process of creating the laminate structures.

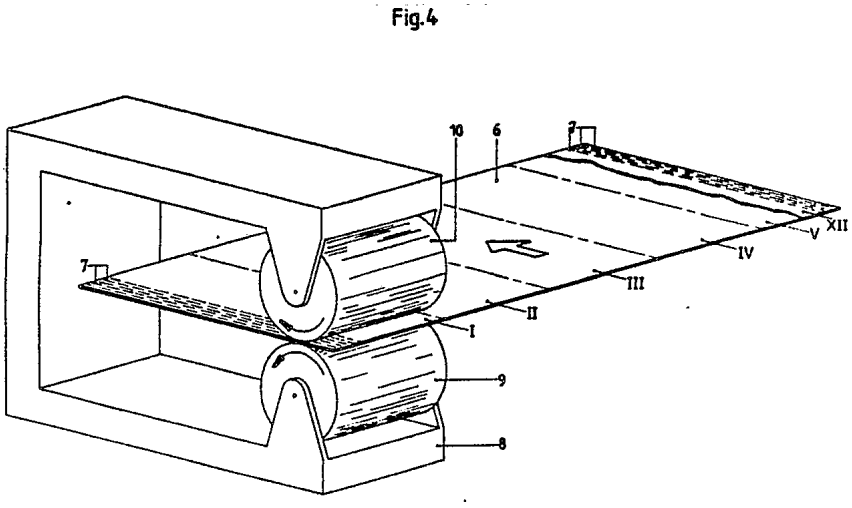

Figure 2.4: Illustration of the patent filed for creating laminated metal structures [23].

Figure 2.5: Photograph showing the first generation FML layup [20].

2.2.2 Development of FMLs and GLARE®

Schijve and Vogelesang [20–22] reported results from flight simulation tests on carbon and aramid reinforced laminates. Under fatigue loading conditions, the loads were being transmitted from the metal layers, via the adhesive to the fibres, slowing down crack growth. This behaviour, illustrated in Figure 2.6, is named fibre bridging and caused the fibre-metal laminate to withstand fatigue loads for much longer periods than their monolithic counterparts.

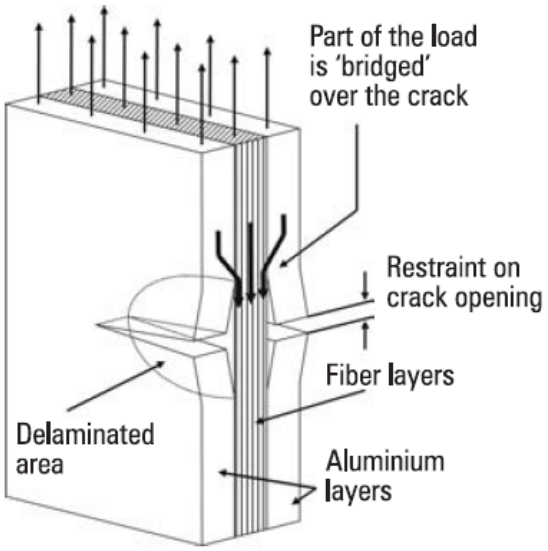

Figure 2.6: Schematic showing fibre bridging [21].

In addition, delamination of the adhesive layer from the metal was observed [20–22]. Without delamination, fibres would be overstretched when the crack starts to grow, however too much delamination would cause excessively high crack growth rates. A delicate balance between delamination and crack growth was found to exist.

ARALL® finally achieved commercial success between 1984 and 1987 when it showed promising characteristics in full scale tests as a wing panel for the Fokker 50, providing a weight saving of 20% while maintaining structural integrity. ARALL® was also used in the cargo door of the C17, but proved inadequate as fuselage material [20]. Tests showed failure occurred in ARALL® under realistic fuselage skin loading conditions due to the poor compression properties of aramid fibres [21, 22]. Roebroeks [20, 24] reported that the fibres in ARALL had inadequate bonding with the adhesive layer.

In 1987 a patent was filed for GLARE®, the second generation of FMLs. Specifically designed for fuselage applications, GLARE® used glass fibres instead of aramid and was developed in both unidirectional (GLARE® I and II) and biaxial (GLARE® 3 and 4) variants. GLARE® soon proved to be the superior material for use in fuselage skins, demonstrated through extensive testing of the A330 and A340 fuselages [21, 22].

2.2.3 Properties and Structural Applications of GLARE®

GLARE® was first introduced to the skies as a bonded patch repair on a C5-A Galaxy aircraft by USAF in 1995. The first civil applications were as the bulk cargo floor in the B777 from Boeing and the bulkhead from the Bombardier Learjet 125 [20–22].

GLARE® not only had exceptional fatigue properties, but several other benefits, such as increased impact, residual and blunt notch strength as well as improved flame and corrosion resistance when compared with monolithic aluminium [20–22]. With an estimated 20% of aircraft operating cost going toward maintenance, these properties play an integral part in material selection. Studies performed on the repairs done on 71 Boeing 747's, with an average of 29,000 flying hours, found that 57.6% of repairs are done on fatigue cracks, 29.4% on corrosion damage and 13% of repairs on impact damage [22]. A material that offers improvements on these properties, such as GLARE®, could not only translate into major economic savings over the operational lifetime of the of the aircraft, but even extend the operational life.

Fatigue

The spectacular failure of Aloha Airlines Boeing 737 in 1988, Figure 2.7, reinforced the view that damage tolerance should be considered for the entire lifespan of an aircraft. Investigations into the crash yielded evidence that after 90 000 flights, small cracks in the lap joint rivet row joined up forming a single large crack that caused the loss of a 4 m to 6 m section of the upper fuselage [20–22]. This disaster proved that more advanced materials were required to deal with the loads experienced by modern pressurized fuselages.

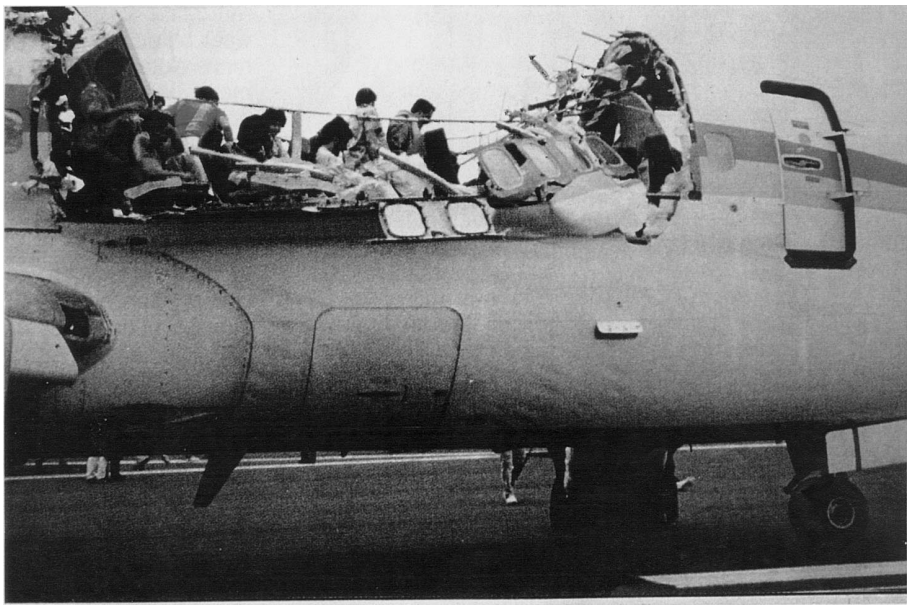

Figure 2.7: Main fuselage failure of Aloha Airlines Boeing 737 [22].

The crack growth behaviour of two variants of GLARE®, ARALL® II and monolithic AL2024-T3 under fuselage loading conditions are shown in Figure 2.8 [21, 25]. It was

found that crack growth rates in all the laminates were anything from 10 (ARALL®) to 100 (GLARE® II and III) times slower than in the monolithic aluminium. This would mean that a structural inspection for fatigue would be almost unnecessary for the entire operational life of the aircraft. GLARE® offered huge potential benefits [25].

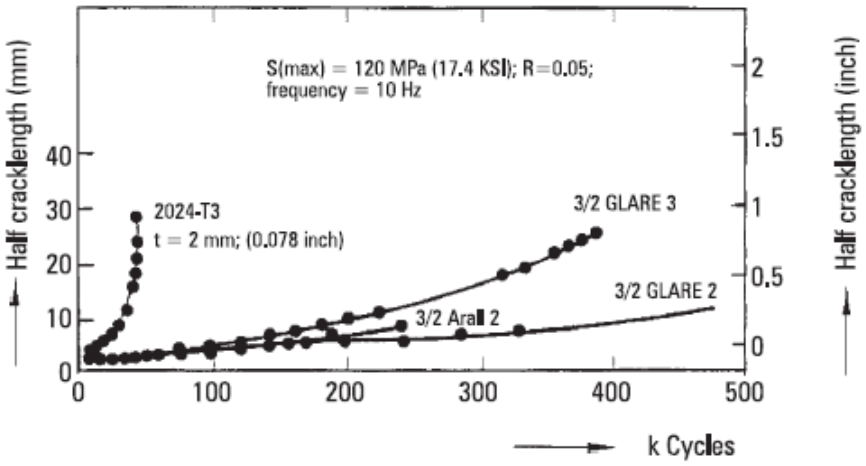

Figure 2.8: Crack growth behaviour for GLARE® 2 and 3, ARALL® II and AL2024-T3 for fuselage loading [25].

In reality, the longitudinal and circumferential joints are the places where fatigue damage would most likely take place. Roebroeks [24] reports results from fatigue tests on GLARE® and 2024-T3 aluminium alloy. Figure 2.9 shows a comparison of the residual strength of these joints after some fatigue cycles. Joints manufactured from GLARE® showed increased residual strength, far superior to that of the monolithic aluminium [21, 22].

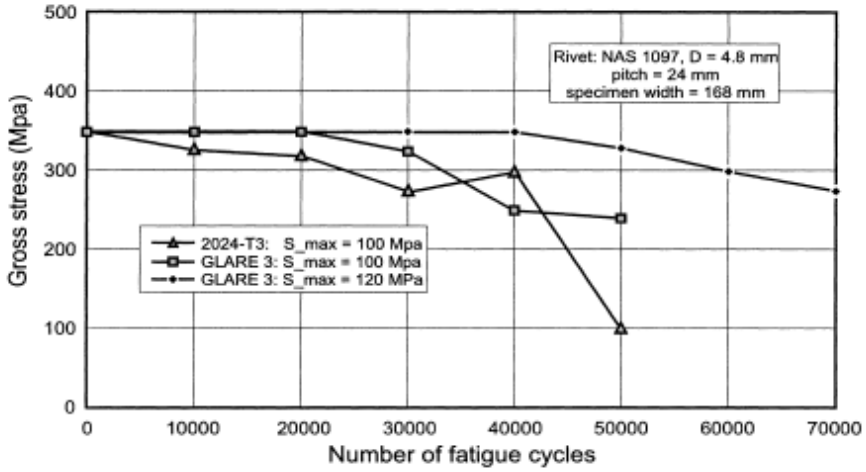

Figure 2.9: Residual strength in Al2024-T3 and GLARE® 3 riveted lap joints after fatigue loading [26].

Impact

Glass fibre based composites have proven to be more resilient to impact damage and easier to maintain than their brittle carbon fibre counterparts [27]. In aerospace engineering impact damage is a very relevant design consideration. Vlot et al. [28] investigated the impact resistance of GLARE® compared to other aerospace materials. Figure 2.10 shows a comparison of the minimum energies required to produce failure for the different materials. The impact properties of GLARE® proved to be at least as good as those of monolithic aluminium and even better than those of carbon. For large deflections in GLARE®, only minor internal damage was found. The good impact performance of the GLARE® and other glass fibre reinforced metal laminates is attributed to the phenomena of high strain rate strengthening occurring in the glass fibres [21, 29].

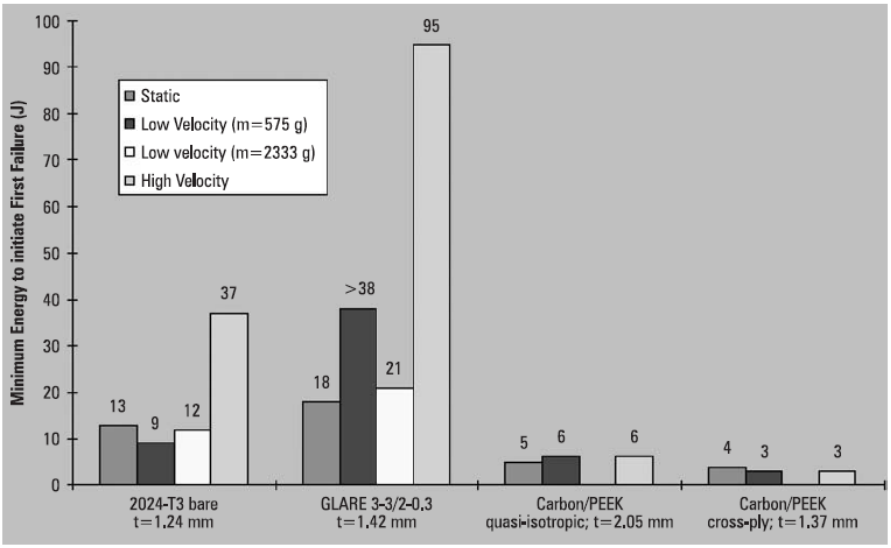

Figure 2.10: Impact properties of fibre-metal laminates [28].

Flame Resistance

Using burn test data, Vogelsang and Vlot [22] showed that GLARE® was more flame resistant than monolithic aluminium alloys. Aluminium alloys was found to melt away within 20 to 30 seconds in a kerosene fire while GLARE® lasted over 10 minutes with no flame penetration [22]. The key mechanism at work was found to be the delamination of the glass fibre layer. Although the outer aluminium layers melt away in seconds, the glass fibre layers delaminate and the epoxy surrounding them burns away forming a carbon layer insulating the centre layer of aluminium [22].

Blast Resistance

GLARE® also proved to have exceptional blast resistance in tests done on an ECOS^{3}® cargo hold container [21]. The blast resistant container, manufactured from GLARE®, was reportedly able to withstand a confined blast load of greater magnitude than the blast that brought down Pan Am flight 103 [2] over Lockerbie, Scotland. This container was developed by Galaxy Scientific Corporation and tested by the FAA in 1995 in an attempt to prevent future incidents like the Lockerbie bombing [20]. Figure 2.11 shows the results of the test. Further research into the blast resistance of FMLs and GLARE® is discussed in Section 2.4.

Figure 2.11: ECOS[3®] cargo hold subjected to blast loading [20].

2.3 Structural Adhesive Bonding Techniques

As discussed in Section 2.2.1, the adhesion between the aluminium and the composite material is a complicated process. van Tonder [12] studied the influence of different surface treatments on the bond strength of various glass-fibre composites bonded to aluminium. These treatments included mechanical and chemical surface treatments and the addition of a film adhesive. These bonding methods were applied to two different glass-fibre composites, each with a different epoxy variant as a matrix material. The different matrix materials used during manufacturing were Prime 20LV, a low viscosity epoxy infusion resin, and SE84LV, a hot-melt epoxy prepreg.

2.3.1 Surface Treatments of Constituent Materials

Various techniques are used to increase the bond strength between metal and composite surfaces. Mechanical surface treatments are one of the most basic methods and are performed to alter the surface morphology of materials and gain macro-roughness. This can usually be achieved by either sanding or bead blasting [30]. Mechanical surface treatments directly influence the contact angles of the metal substrate and its wettability [31]. Increasing surface roughness also increases surface area and the amount of chemical surface interactions with the adhesive. van Tonder [12] employed bead blasting to obtain the required surface roughness on the surface of the aluminium plates. Figure 2.12 shows the results of an SEM[1] scan performed on the treated metal plates at $\times$ 750 magnification.

[1]Scanning Electron Microscope

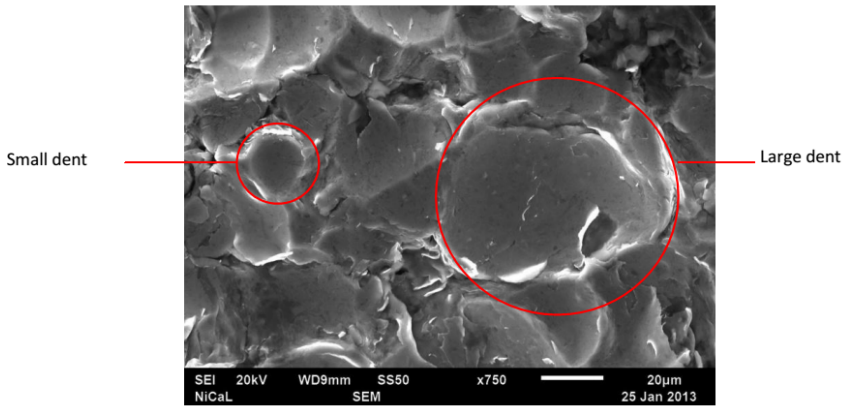

Figure 2.12: Metal surface morphology after bead blasting [12].

Another common technique is acid etching, sometimes considered an intermediate step between degreasing and electrochemical treatments [12, 32]. Acid etching involves immersing the metal substrate in an aqueous acid solution. This process serves to remove grease, contaminants, unstable aluminium hydroxides and oxides from the surface.

Anodizing is one of the most popular techniques employed in the aerospace industry due to its ability to improve corrosion and hydration resistance. It also promotes bonding to organic polymer adhesives [33]. Anodising of aluminium is an electrochemical surface treatment where the aluminium is placed in an acid electrolyte bath as the anode of the electrolytic cell, illustrated in Figure 2.13a. The applied current causes oxidation at the anode resulting in a thick, highly absorptive, aluminium oxide layer, Figure 2.13b, that promotes bonding [34, 35].

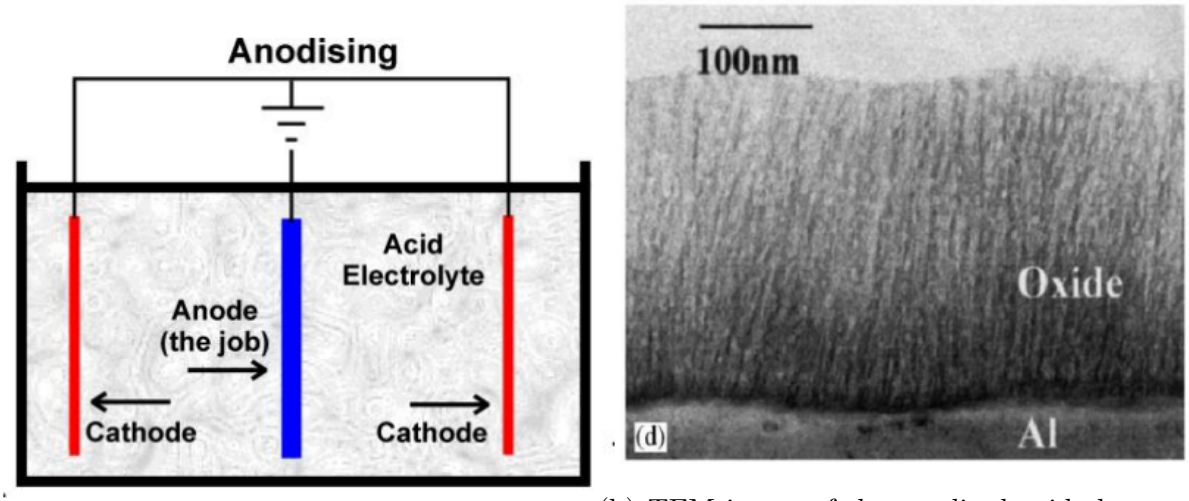

(a) Electrolytic cell set-up for anodising [12].

(b) TEM image of the anodised oxide layer on the aluminium [12].

Figure 2.13: Illustration and TEM image of anodising process [12].

Silane coupling agents are compounds whose molecules contain functional groups that bond with both organic and inorganic materials, Figure 2.14. This allows it to act as an intermediary between organic and inorganic materials [36]. Silane conversion coatings have been introduced in many industries as an environmentally friendly replacement to chromate coatings used in anodising [37, 38]. Improved durability and shorter pre-treatment times gives silane coupling agents added advantages.

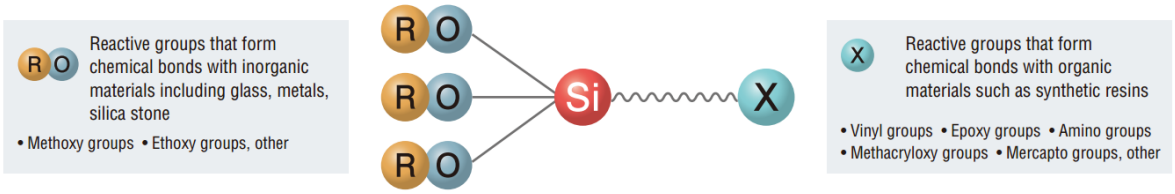

Figure 2.14: Silane coupling mechanism [36].

Film adhesives are thermoset or thermoplastic adhesives cast in a precise areal density and width. They have been used extensively by the British Aerospace industry and Fokker aircrafts to bond structural components. The first film adhesive to be used commercially in aircraft structural bonding was Redux 775 [39]. Developed by Norman de Bruyne at the Cambridge Aeroplane Company [40], Redux (Research at Duxford) film adhesives had the added benefit of being in a more handleable form than its powder predecessor [40].

2.3.2 Material Testing Results

van Tonder [12] reported results from single leg bend tests on aluminium and glass fibre samples. The results were used to determine the influence of surface treatment on bond strength. Specimens were manufactured with pre-existing cracks and subjected to quasi-static flexural loading as shown in Figure 2.15. The crack growth and energy release rates were determined for a given surface treatment by photographing the crack tip progression at set intervals.

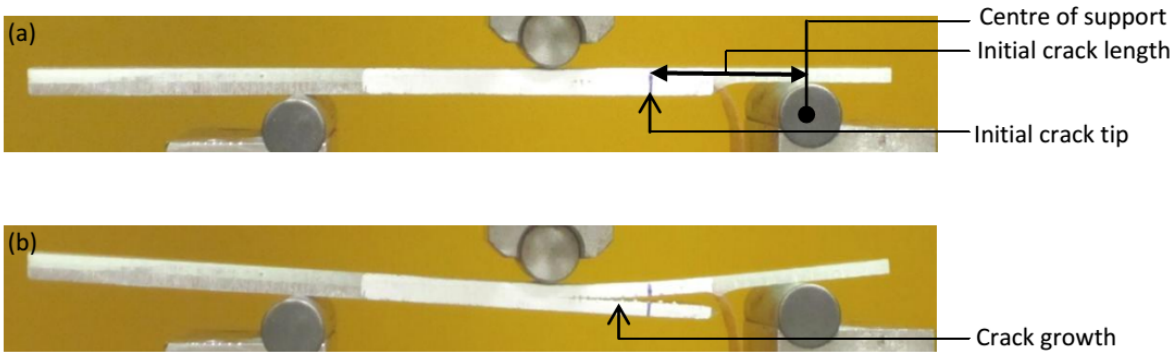

Figure 2.15: The SLB test specimen set-up, indicating (a) the initial crack length and (b) the crack growth [12].

The specimens and surface treatment combinations tested by van Tonder [12] are shown in Table 2.2 with the calculated mixed mode energy release rates ($G_{I/II}$). Stable crack growth at relatively constant forces was reported for most of the specimens. Combining macro and micro surface roughening resulted in better adhesion and the combination of bead blasting and silane treatment produced the best results of all the surface treatments. The SE84 prepreg outperformed the Prime 20LV resin as a matrix material. It was also found that the inclusion of Redux 609 as a film adhesive improved the adhesion in all cases. van Tonder [12] recommended a combination of grit blasting for macro roughness, a silane chemical treatment to promote adhesion of inorganic to organic material and a film adhesive to further increase the bond strength.

Table 2.2: SLB tests performed by van Tonder [12].

Specimen:	Resin	Surface Treatment	Glass Fibre
PG	Prime 20LV	Bead-blasted (GB)	Plain weave $400g/m^2$
PGE	Prime 20LV	GB, etched	Plain weave $400g/m^2$
PGEN	Prime 20LV	GB, etched, anodised	Plain weave $400g/m^2$
PGES	Prime 20LV	GB, etched, silane	Plain weave $400g/m^2$
PGS	Prime 20LV	GB, silane	Plain weave $400g/m^2$
PEN	Prime 20LV	Etched, anodised	Plain weave $400g/m^2$
PL	Prime 20LV	Alodined	Plain weave $400g/m^2$
PGR	Prime 20LV	GB, Redux 609	Plain weave $400g/m^2$
PLR	Prime 20LV	Alodined, Redux 609	Plain weave $400g/m^2$
SL	SE 84LV (prepreg)	Alodined	Plain weave Prepreg
SGR	SE 84LV (prepreg)	GB, Redux 609	Plain weave Prepreg
SLR	SE 84LV (prepreg)	Alodined, Redux 609	Plain weave Prepreg

2.4 Explosions and Blast Waves

Baker [41] defined an explosion as a large amount of energy rapidly released in the form of light, heat and sound. This release leads to a pressure wave forming, known as a blast or shock wave. Glasston and Dolan [42] define it as the expansion of intensely hot gasses at extreme pressures which cause a shock wave travelling at high velocities.

Explosions are divided into two main groups, either confined or unconfined. These groups are further divided into categories shown and described in Table 2.3 and illustrated by Figures 2.16a and 2.16b. The focus of this study was on free air and fully vented explosions.

Table 2.3: Types of explosions as depicted by Draganić and Sigmund [43]

Charge Confinement	Categories	Description
Confined	Full ventilation	Containing object in one direction of the blast
	Partially Confined	Explosion is confined in a few directions
	Fully Confined	Explosion is fully confined
Unconfined	Free air explosion	The blast wave propagates away from the centre of explosion impacting the structure directly
	Explosion with stand-off distance	The blast wave is located a distance away from the structure resulting in ground reflections occurring first
	Surface Blasts	The blast wave is amplified at the point of detonation due to ground reflections

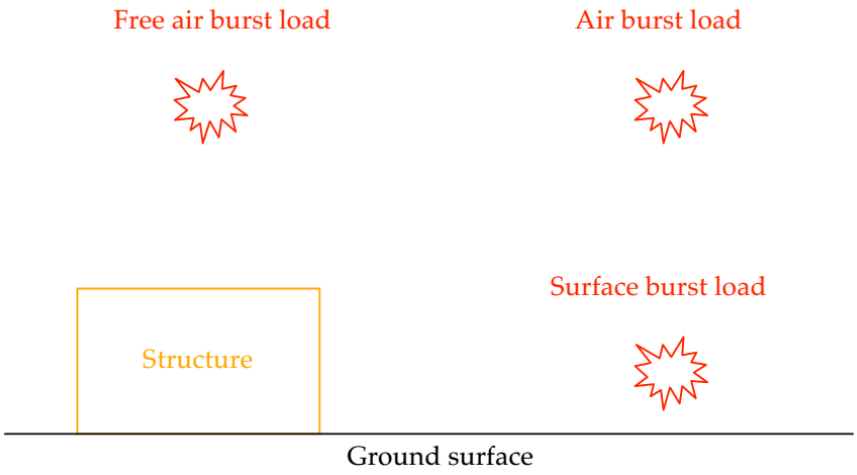

(a) Unconfined blast loads [43].

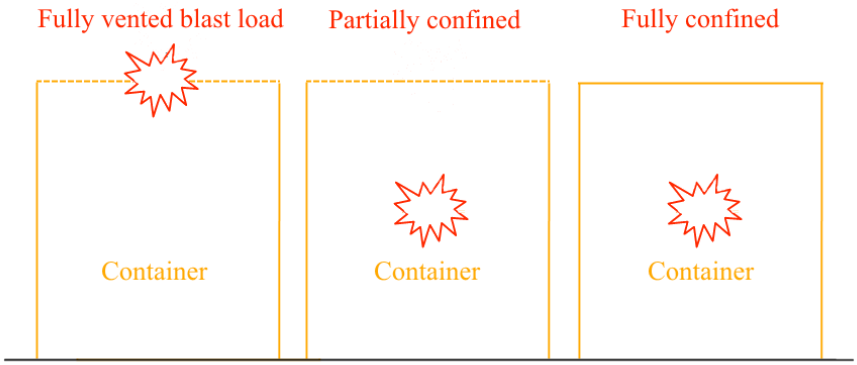

(b) Blast loads subject to various degrees of confinement.

Figure 2.16: General classification of explosions.

Explosives are also divided into both primary[2] and secondary[3] explosives. Due to their stability, secondary explosives are generally used in experimentation. They require a detonator and booster charge (generally made of primary explosives) to generate an explosion. The detonator and booster produce a shock wave of sufficient energy which results in a sustained chemical reaction in the explosive material [44, 45]. The compression and heat caused by the shock wave results in ignition of the explosive. Detonation entails a supersonic, exothermic front propagating through a medium driving a shock front [44]. A rapid pressure rise during detonation (Von Neuman spike - Figure 2.17) results in the reaction. The Chapman-Jouget (C-J) pressure referred to in Figure 2.17 refers to the state of detonation products at the end of the reaction [46].

[2]Explosives that can be initiated by small amounts of heat or pressure
[3]Less sensitive explosives that require more substantially more energy to be initiated

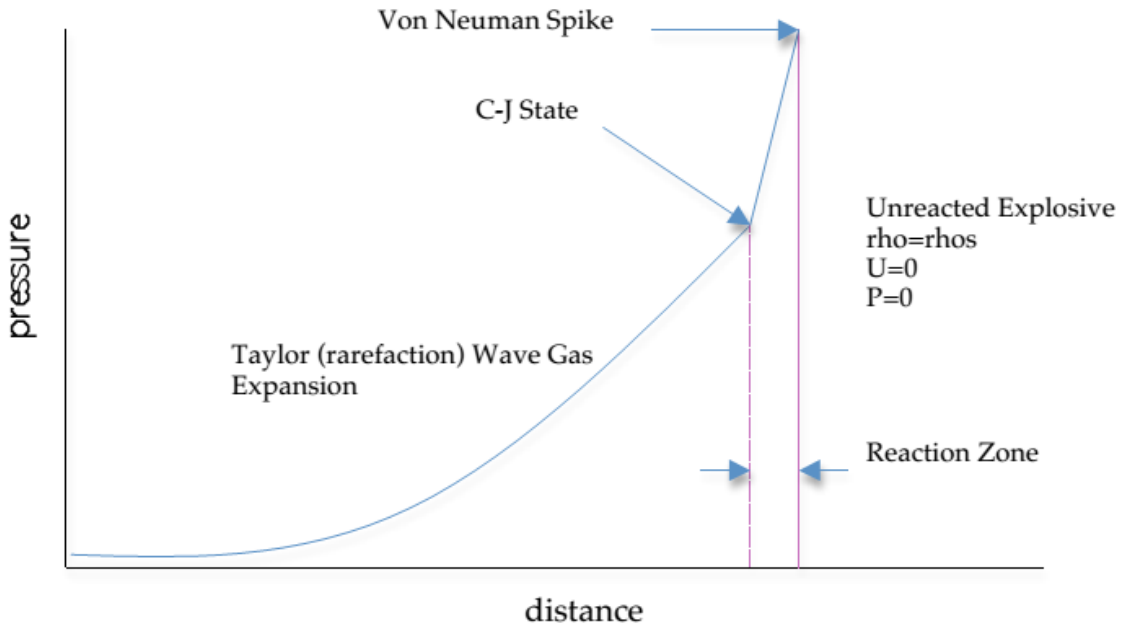

Figure 2.17: Pressure vs distance diagram of a detonation wave [46].

2.4.1 Blast Waves and Pressure-Time History

After detonation, the propagating shock front compresses the air ahead of it, generating a blast wave. The propagation of the blast wave is generally considered as a steady-state process. Working under this assumption, Zukas and Walters [47] made the following conclusions with regards to the blast wave characteristics.

- The wave propagation velocity is greater than the speed of sound of the material it travels into.
- The wave velocity of any given explosive material is constant
- Wave velocity is proportional to the density of the explosive material.
- Wave velocity decreases with charge diameter and propagation becomes impossible below a certain level.

Figure 2.18 shows the pressure-time history for a typical blast wave [48], with three distinct zones of the impulse loading. The first, t_0 to t_A, depicts the initial time it takes for the blast wave to reach the structure, illustrated with the constant atmospheric pressure P_0. This is followed by an instantaneous jump to a higher pressure, P_{S0}, referred to as the peak overpressure at t_A. After the blast wave, this value decays

rapidly and reaches P_0 again at time $t_A + t_d$. The pressure then continues to decay further to a value of P_{S0}^-, less than P_0, resulting in a negative pressure or partial vacuum. Responding to this vacuum, the pressure gradually rises again until it reaches equilibrium at t_d^-.

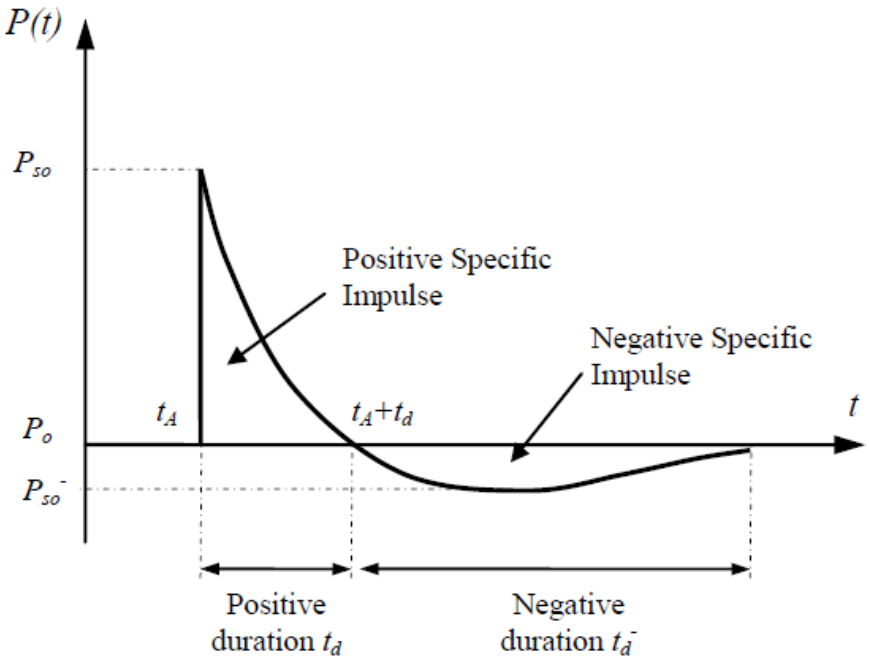

Figure 2.18: Typical blast impulse waveform for far field explosions [48].

The zone where the initial pressure spikes above P_0 for the time period t_d is referred to as the positive specific impulse whereas the other is called the negative specific impulse. The pressure of the blast wave can be described mathematically by Friendlander's Equation (2.18) where α is the waveform or decay parameter.

$$P(t) = P_{S0}\left[1 - \frac{t}{t_d}\right] e^{-\alpha t/t_d} \tag{2.18}$$

Mays and Smith [49] defines the explosion wave-front speed, U_S, and the maximum dynamic pressure, q_S, as seen in Equations (2.19) and (2.20).

$$U_S = a_0\sqrt{\frac{6P_{S0} + 7P_0}{7P_0}} \tag{2.19}$$

$$q_S = \frac{5P_{S0}^2}{2(P_{S0} + 7P_0)} \tag{2.20}$$

2.4.2 Impulse Calculation

During blast loading, it is convenient to calculate the specific impulse due to the peak overpressure P_{S0}, defined in Figure 2.18. The pressure-time curve can be used to calculated the specific impulse (i_s) Equation (2.21):

$$i_s = \int_{t_A}^{t_A+t_d} P(t)\, dt \tag{2.21}$$

This negative pressure phase generated during the blast wave, P_{S0}^{-}, is usually much smaller than that of overpressure, P_{S0}, in unconfined blasts. Due to this, its impulse contribution is usually neglected [50].

2.4.3 Structural Response of Metals to Blast Loading

Menkes and Opat [51] investigated the response of fully clamped aluminium beams subjected to an increasing uniform impulse. They identified three distinct failure modes in the monolithic structures shown in Table 2.4 and illustrated in Figure 2.19, where (a) illustrates the default loading condition.

Table 2.4: Failure modes of monolithic materials under blast loading [11]

In Mode I failure category	
Mode I	Large inelastic deformation (b)
In Mode II failure category	
Mode II	large inelastic deformation with tensile tearing at the supports (c)
In Mode III failure category	
Mode III	transverse shear failure at the supports (d)

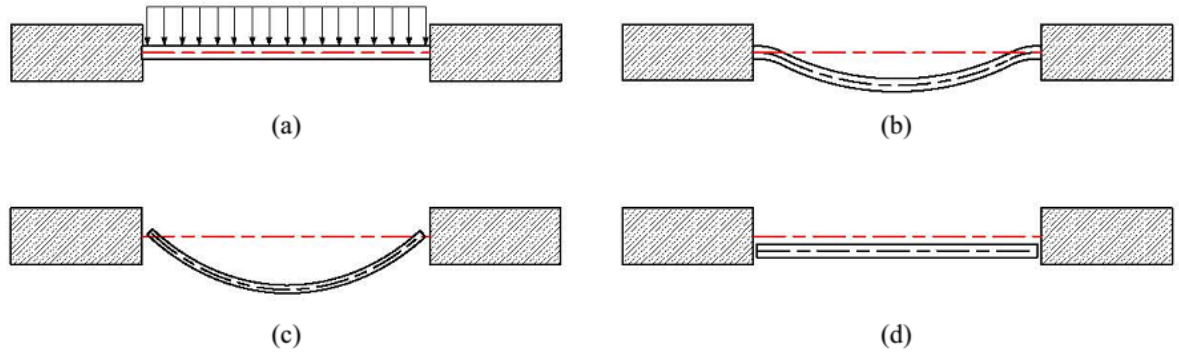

Figure 2.19: Illustration of the failure modes of fully clamped aluminium beams subjected to uniform impulsive loads [51].

Nurick and et al. [2, 52–54] investigated the response of square and circular fully clamped plates and found similar failure modes. Nurick et al. [55] reported further categories within Mode I failure:

- Mode I: large inelastic deformation: no necking.
- Mode Ia: large inelastic deformation: necking at places on the boundary.
- Mode Ib: large inelastic deformation: necking around the entire boundary.

Nurick and Shave [53] also discovered three additional variations of Mode II failure:

- Mode II* where the plate exhibits only partial tearing and the midpoint deformation continues to increase with increasing impulse.
- Mode IIa where the plate is completely failed and the mid-point deformation continues to increase with increasing impulse.
- Mode IIb where the plate is totally torn but the mid-point deflection decreases with increasing impulse.

They discovered that mode IIa applied only to square plates. Nurick and Radford [56] also investigated the response of circular, fully clamped plates subjected to localised blast loading and discovered additional categories in Mode I and II failure.

- Mode Itc: large inelastic response with thinning in the central area.
- Mode II*c: partial tearing in the central area.
- Mode IIc: complete tearing in the central area "capping failure".

2.5 Blast Response of FMLs and GLARE®

2.5.1 Localised Blast Loading of FMLs

Localised blast loading is obtained by detonating the explosive in close proximity to the target. This method of loading is used to determine the material response under highly irregular and dynamic loading conditions as well as onset of various failure modes.

Cantwell et al. [57] investigated the behaviour of FMLs comprising layers of aluminium and glass fibre polyamide (GFPA) under localised blast loading. Loading conditions were achieved on a ballistic pendulum using PE4 as the explosive material. This is the same method reported on by multiple references [11, 58, 59]. They detonated a cylindrical shaped charge with a diameter of 20 mm. This was separated from the FML by a polystyrene pad equal to a total stand-off of 13 mm. Jacob [60] showed that the effect of the polystyrene on impulse transfer was negligible. Various configurations of the GFPA panels were tested at charge masses ranging from 3 to 8g.

They found the main structural damage occurred at the front[4] and back[5] faces of the panels. On the front face, damage occurred in the form of pitting and/or permanent deformation while back face damage was defined as the area that debonded from the fibre reinforced polyamide. Back face damage was observed to be localised, centred and either diamond or circular in shape. Furthermore it was found that a small nipple or bulge formed in the centre of the back face superimposed on the circular or diamond-shaped damaged area. When the impulse increased past a certain threshold, it was found that the nipple/bulge tore, forming a cap (referred to as Mode II* failure).

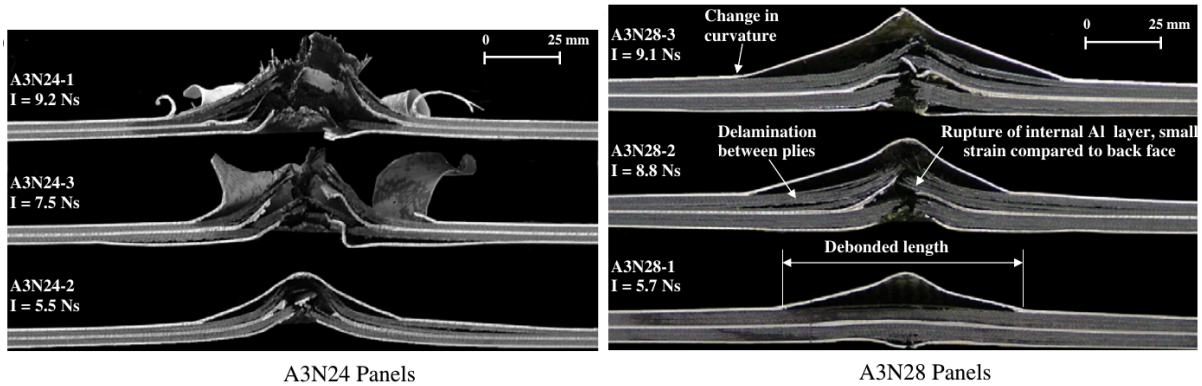

(a) Damage of 4 layer composite (b) Damage of 8 layer composite

Figure 2.20: Photographs of cross-sections of blast loaded FMLs, showing variation in panel damage for different thickness composite layers by Cantwell et al. [57].

[4]face closest to the blast
[5]face furthest from the blast

Higher impulses were required to rupture the back face of the thicker FMLs. Debonding of the back face from the composite material was seen in all panels. This is illustrated clearly in Figures 2.20a and 2.20b. Increased damage in the composite layers was found to occur mostly further from the front face, except in cases where the localised response of the aluminium layer caused damage to adjacent plies.

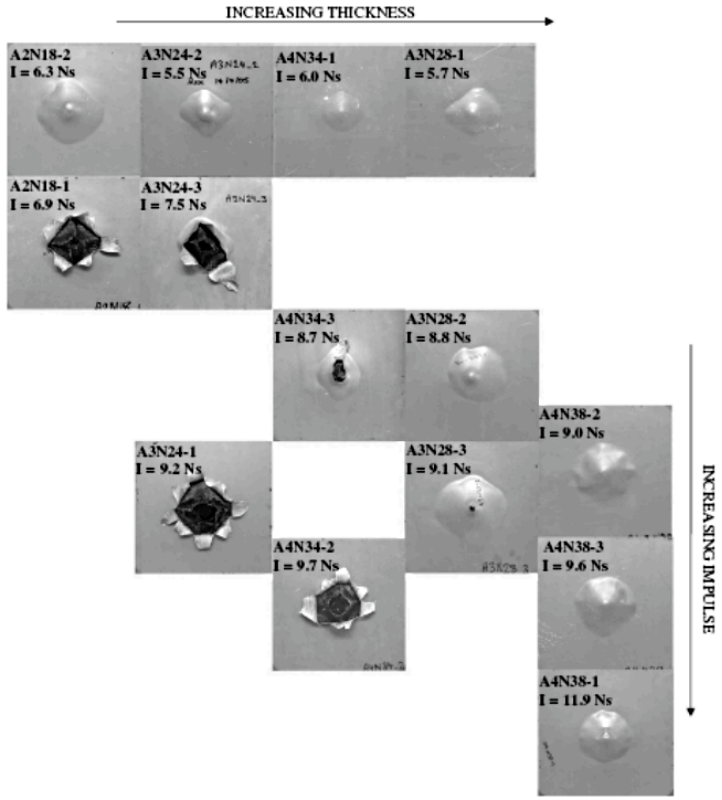

Figure 2.21: Photographs of the diamond shape observed by Cantwell et al. [57].

The diamond shaped back face damage pattern was also observed by Langdon et al. [58, 59]. An example of this is shown in Figure 2.21 and compared to Figure 2.22 observed by Langdon et al. [57] for FMLs with glass fibre polypropylene composite layers. The diamond shaped damage observed on the back face of the FMLs was attributed to fibre dominated behaviour [11, 57–59, 61]. The impulse of the blast propagated within the panel both as a compressive wave (through the panel thickness) and as a transverse shear wave, laterally away from the centre of the blast. Upon reaching the back face, the compressive wave was reflected as a tensile wave. This tensile wave usually caused debonding at the first surface it encountered making it responsible for the back face debonding. Wave propagation is described in more detail by Olsson [62]. In homogeneous materials, such as metals, the transverse shear wave would propagate radially through the material unhindered, resulting in a circular shaped damaged area. In fibre reinforced composites the wave propagated faster

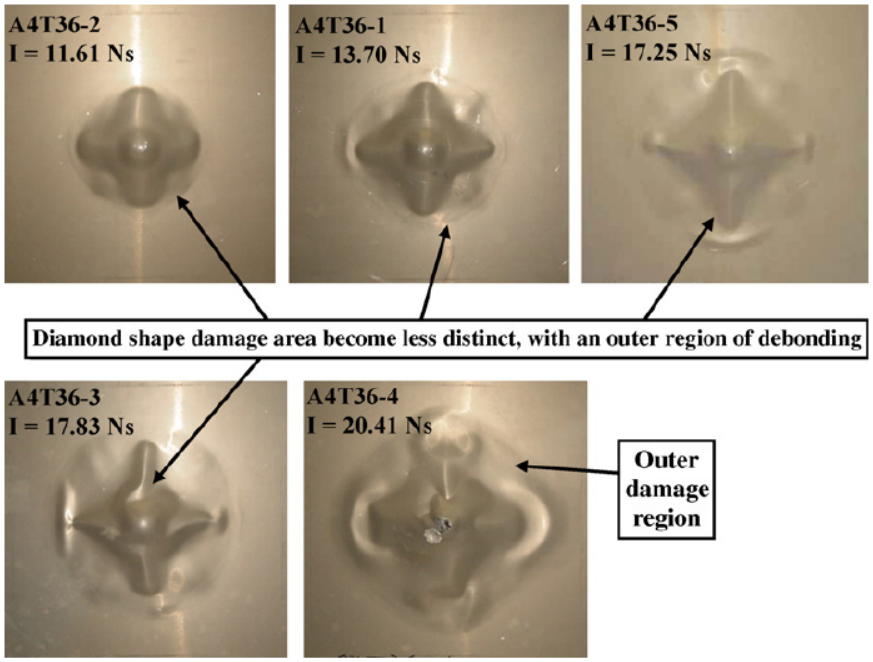

Figure 2.22: Photographs of the diamond shape observed by Langdon et al. [58, 59].

through the fibres than through the matrix. Since the fibres of the FMLs are orthogonally oriented, the stress wave propagated along these axes, resulting in the characteristic diamond shape. The thicker panels showed far less distinctive back face damage, attributed to the extra layers added to the composite structure. It is thought that in thicker panels, a larger amount of the damage is propagated radially through the metal layers and composite matrix, causing a smoothing effect leading to a less distinctive diamond shape [57, 58].

Lemanski et al. [61] performed similar experiments experiments on specimens of varying thickness and material distribution. They observed large plastic deformation, debonding, delamination, fibre fracture and matrix cracking as various energy absorption mechanisms. This study tested the blast resistance of Twintex (a woven glass fibre material) in thermoplastic resin, combined with Al2024-0. They used the same general procedure as Cantwell et al. [57] for testing. Pitting was found to occur on the front face in the region where the explosive charge was mounted as seen in Figure 2.23.

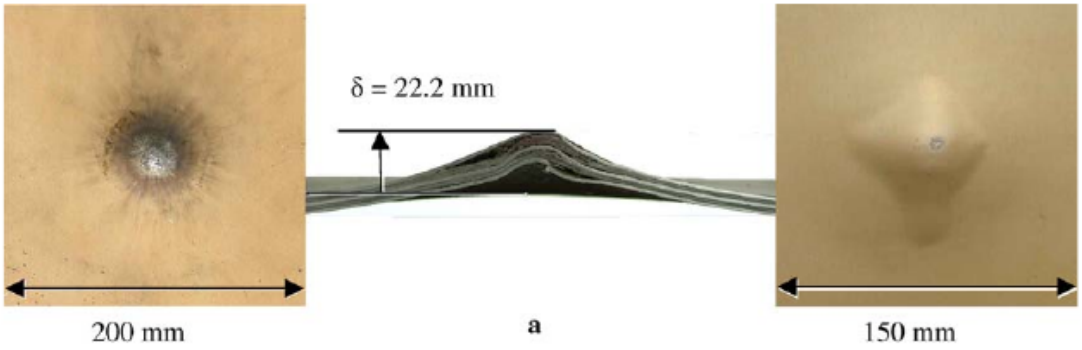

Figure 2.23: Pitting found to result on the front face by Lemanski et al. [61].

The severity of the pitting, also reported as a damage mechanism by multiple references [11, 57–59, 61, 62], was found to be dependant on the charge mass. Along with pitting, the front face was found to undergo local plastic deformation leaving a crater shaped front face delamination shown in Figure 2.24. This type of buckling was found to be more pronounced in thicker panels due to their increased stiffness. Thinner panels more often exhibited global plate bending. Similar behaviour was observed by Langdon et al. [57–59].

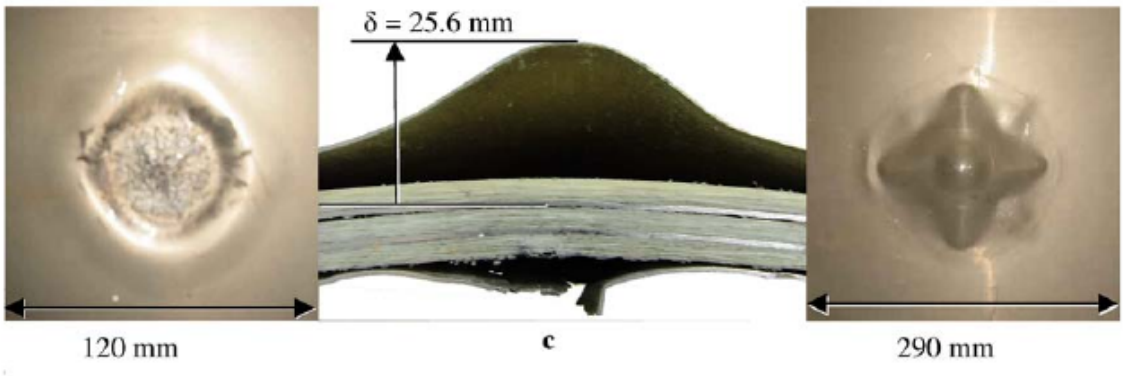

Figure 2.24: Ring buckling of the front face found in localised blast loading of FMLs [61].

The back face deformations were dominated by the characteristic diamond shaped deformations. Due to the difference in composition and structure of FMLs, when compared to monolithic plates, energy can be dissipated via different mechanisms such as matrix cracking, debonding and delamination. Behaviour in FMLs were categorised using nominal plate thickness and number of layers. Thin plates exhibited tearing of the back face at lower impulses than thicker plates. No significant difference was observed between front and back face deflections in thin panels whereas thick panels usually exhibited greater difference with larger deflections of the back face. For the same

nominal impulse, thinner panels showed large deflections and small scale debonding compared to the small deflections and widespread debonding of the thicker panels as shown in Figure 2.25.

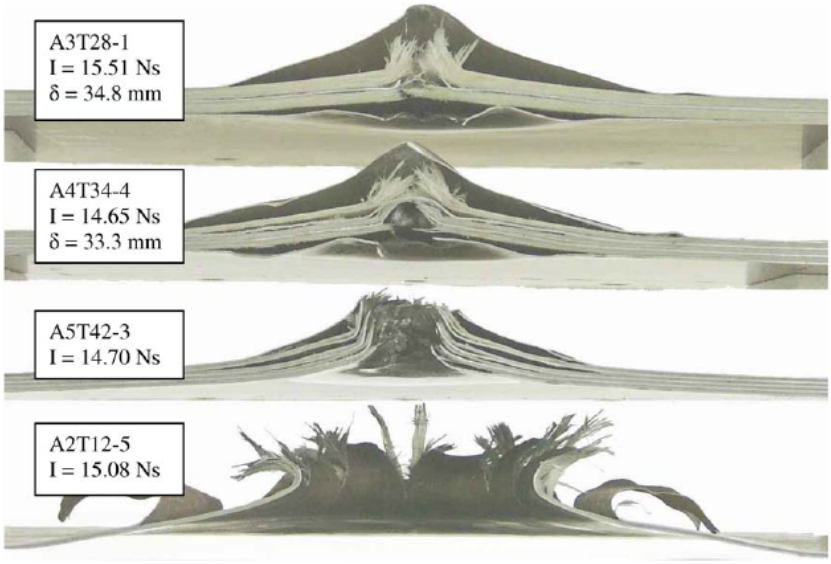

Figure 2.25: Damage variation with panel thickness [61].

Tensile tearing at the back face occurred when the local curvature led to excessive strains in the back face. In agreement with results published in literature [7, 8], interlaminar debonding was not a significant energy absorption mechanism but that both local deflection and fibre failure were. Investigating the response of layered glass fibre laminates to blast loading, Franz et al [63] further found that the layers of the back face provided support to the layers of the front face.

Langdon et al. [58,59,61] investigated the blast response of FMLs consisting of aluminium 2024-0 and woven glass fibre reinforced polypropylene layers in order to further expand the failure modes of FMLs. Localised blast tests were performed on 400 mm × 400 mm square panels with an exposed area of 300 mm × 300 mm and an explosive standoff distance of 14 mm. To promote better adhesion between the composite and metal layers a chromate coating was applied to the aluminium and a polypropylene interlayer was used.

Various configurations of FMLs were investigated, including everything from two layers of aluminium and a single layer of composite (2/1) to 5 layers of aluminium and 4 layers of composite. In each composite layer the number of plies were also varied between 2, 4, 6 and 8. Three different failure modes were defined to describe the observations in the

study. These modes included

- Mode I: Large inelastic deformations of the back face
- Mode II: Complete tearing of the back face
- Mode II*: The transition between Mode I and Mode II

The impulse at which Mode II* occurred was defined as the threshold impulse. Damage to the front face fell into two categories namely pitting/crater formation and global displacement due to the impulse loading. Pitting occurred at the center of the panels and affected a region approximately the same radius as the explosive charge, similar to the results reported thus far. For larger impulses on the thicker panels ring buckling was also observed on the front face.

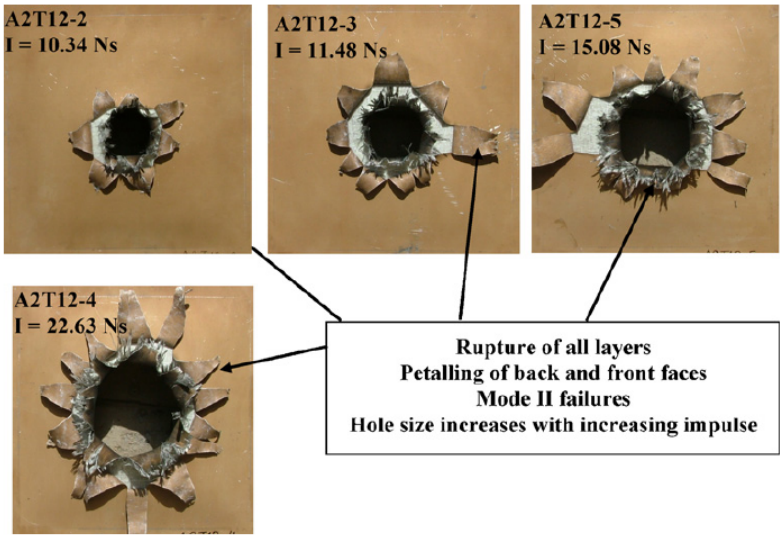

Figure 2.26: Petalling damage observed by Langdon et al. [58,59] for large charge masses.

For the thinner panels (2 layers aluminium and 1 layer composite) all tests subjected to impulses over 10 Ns exhibited rupture or petalling of the back face, seen in Figure 2.26. At lower impulses, Mode I failure was observed with the back face debonding into the characteristic diamond shape, brought on by the difference in wave speed within the different materials as reported on thus far. Increasing the amount composite plies within a composite layer proved to increase the stiffness of the panels, resulting in higher mode II threshold impulses. In summary the back face damage was characterized as follows:

- *Diamond shape debonding* - thin panels with less than 17 layers in total

- *Diamond/cross formation* - intermediate panels with less between 19 and 22 layers in total
- *Cross dominated formation* - thick panels with 28 layers in total

In order to compare the tests results quantitatively, the properties of the FML were approximated using a rule of mixtures seen in Equation (2.22) and (2.23).

$$E = \frac{E_{Al}t_{Al} + E_{comp}t_{comp}}{t} \tag{2.22}$$

$$\sigma_{UTS} = \frac{\sigma_{UTS_{Al}}t_{Al} + \sigma_{UTS_{comp}}t_{comp}}{t} \tag{2.23}$$

When these tests were subjected to non-dimensional analysis, the front and back-face displacements plotted against the impulse fell within one plate thickness of the trend line, seen in Figures 2.27 and 2.28. Various FML failure modes were defined by Langdon et al. [11] and are shown in Table 2.5.

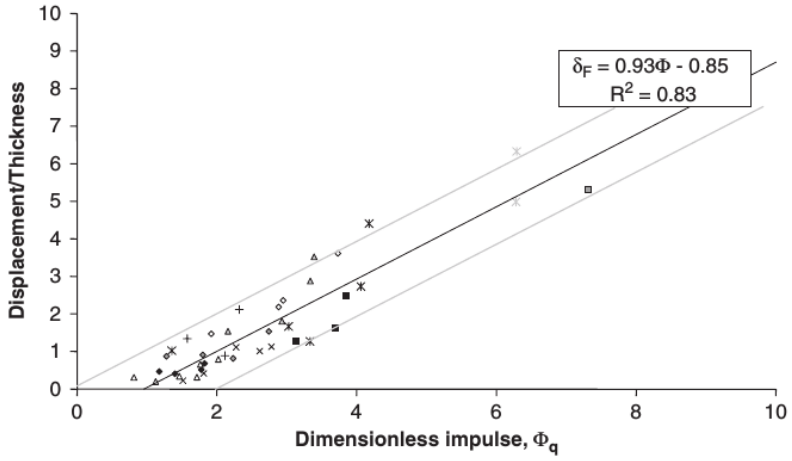

Figure 2.27: Front face displacement trend line [59].

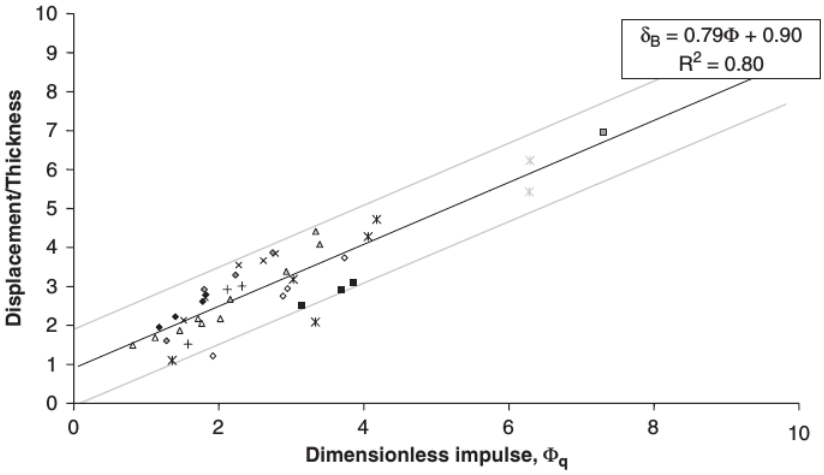

Figure 2.28: Back face displacement trend line [59].

Table 2.5: Failure modes of laminated materials under blast loading [11]

In Mode I failure category	
Mode Idb	Large inelastic deformation with debonding evident in the cross-section
Mode Idl	Large inelastic deformation with delamination of the composite plies
Mode Idbdl	Large inelastic deformation with debonding and delamination
In Mode II* failure category	
Mode IIdb	Partial tearing (no petals) with debonding evident in the cross-section
In Mode II failure category	
Mode IIsp	Symmetric petalling of the panel
Mode IIspr	Symmetric petalling of the rear surface of the laminated panel
Mode IIspf	Symmetric petalling of the front surface of the laminated panel
Mode IIsprf	Symmetric petalling of the rear and front surfaces of the laminated panel
Mode IIspe	Symmetric petalling with the petals elongated in one direction
Mode IIspre	Symmetric petalling of the panel rear surface, elongated in one direction

2.5.2 Uniform Blast Loading of FMLs

Uniformly distributed blast loading can be achieved in one of two ways. The explosive charge can either be detonated at sufficient distance from a structure to allow the blast wave time to develop fully before impinging upon it, or by uniformly distributing the explosive charge across the surface area of the structure.

Cantwell et al. [64] reported results on the response of aluminium and glass fibre FMLs with a polypropylene matrix subjected to uniform blast loading. The tests were performed to compliment the localised blast loading experiments reported in literature [58, 59, 65]. Uniform loading conditions were achieved by detonating equally distributed strips of explosive material. These strips were placed 13 mm away from the intended surface on a polystyrene pad as seen in Figure 2.29. The impulse was varied by varying the diameter of the explosive. These tests differed from the previous tests by having only 200 mm $\times$ 200 mm exposed area.

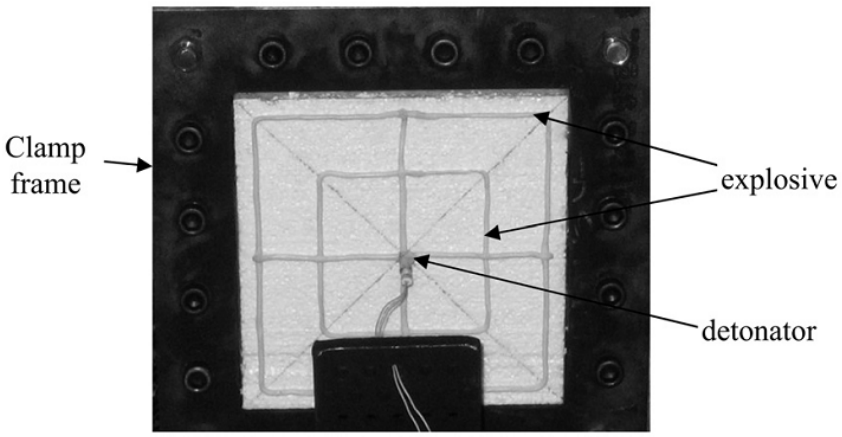

Figure 2.29: Uniform blast loading charge mass distribution used by Langdon et al. [64].

From the tests some common failure mechanisms were observed, seen in Figure 2.30. These included:

- Large plastic displacement (global deformation)
- Stretching and tearing of the aluminium
- Debonding of the back face
- Debonding of internal aluminium alloy layers
- Pitting of the front face (due to proximity of the explosive)
- Bucking of the front face

These findings, in contrast to the locally loaded panels reported on in literature [58, 59, 65], indicate that a greater amount of the panel volume is involved in the deformation and failure mechanisms. No diamond shape was observed on the back face of the panels as well as no ring buckling on the front face.

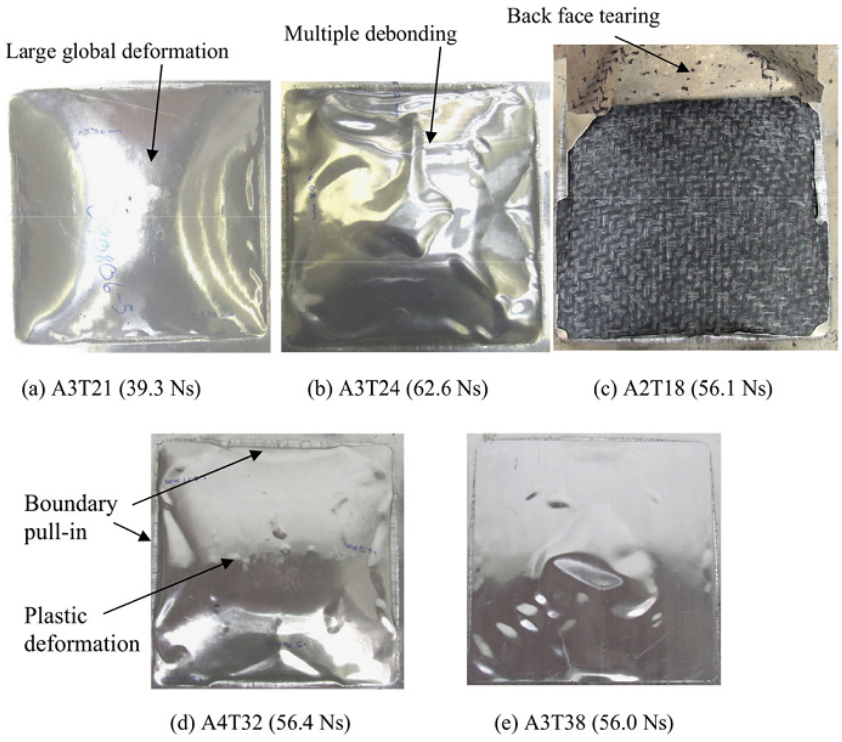

Figure 2.30: Uniform blast load damage observed by Langdon et al. [64].

Similar to localised loading an increasing impulse caused a linear increase in permanent panel deflection during uniform loading tests. Thicker panels also required higher impulses to obtain larger deflections.

2.5.3 Blast Loading of GLARE®

Langdon et al. [5] investigated the blast loading of GLARE® 3, a variant of GLARE® designed for impact loading conditions. The GLARE® 3 panels were subjected to both localised and uniform loading conditions on the blast pendulum set-up reported on by multiple references [11, 57–59, 61, 62]. Specimens had exposed areas of 200 mm × 200 mm. The tests were limited to a total of 8 panels due to the small quantity of GLARE® available. It was found that localised loading resulted in catastrophic damage of the panels due to their low thickness (1.42 mm) and the fact that composites do not perform well under localised loading conditions. This is illustrated in Figure 2.31. Large holes were observed in the centre of the panels with fibre fracture and petalling occurring on the hole perimeter.

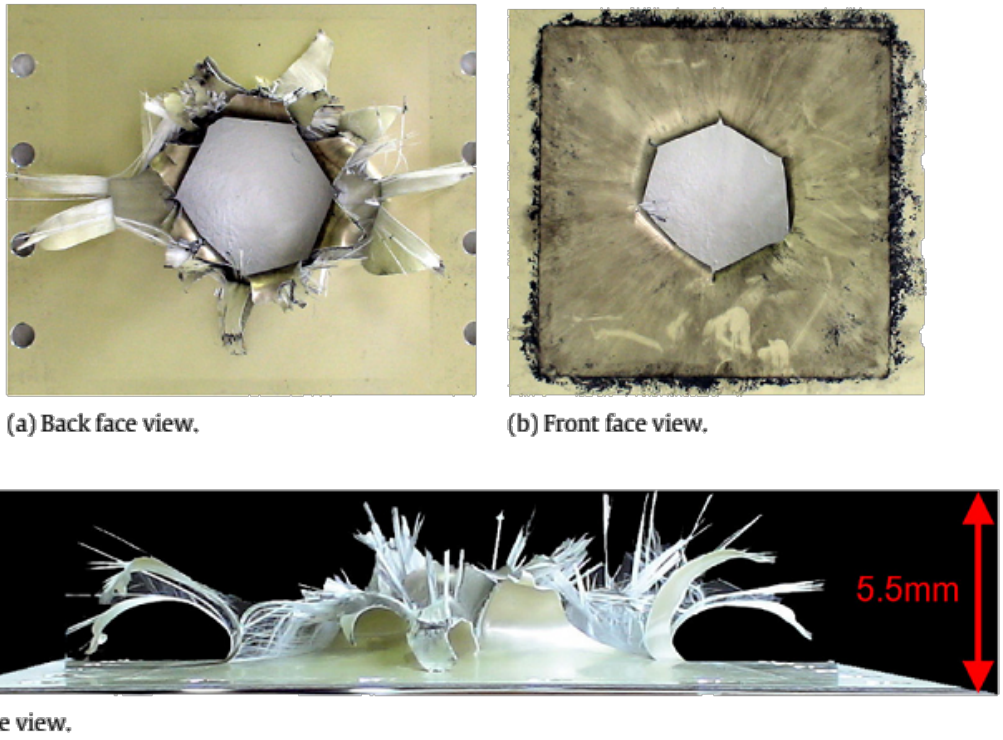

Figure 2.31: Locally blast-loaded GLARE® 3 panels (4 g PE4, 13 mm SOD) by Langdon et al. [5].

A square tube was employed with a 200 mm standoff for the explosive in order to obtain uniform loading conditions. Charge masses were varied between 4g and 14g using both 20 mm and 40 mm charge diameters. Following the experiments, large inelastic deformations were observed with yield line formation[6], seen in Figure 2.32, typical of the response of monolithic metal plates to uniformly distributed blast loading. Significant pull-in was also observed around the edges for higher charge masses which delays the onset of tearing in the material.

[6]The formation of plastic hinges

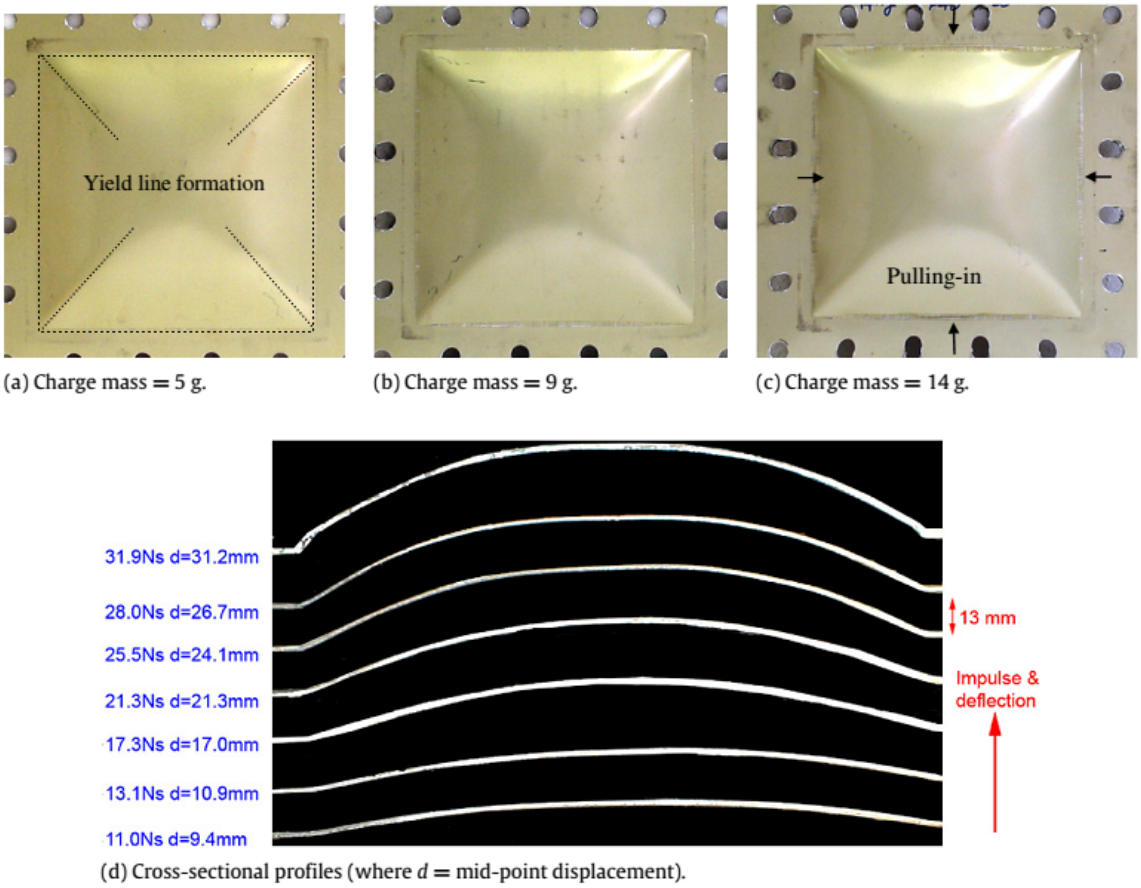

Figure 2.32: Uniform blast-loaded GLARE® 3 panels (4 g PE4, 13 mm SOD) by Langdon et al. [5].

Delamination was observed at the panel boundary indicating that boundary conditions, as with the blast loading of monolithic metal plates, played an important role in response. This can be seen in more detail in Figure 2.33.

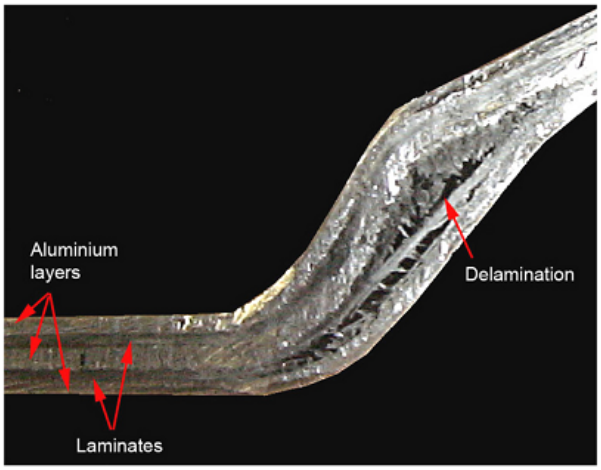

Figure 2.33: Boundary delamination of GLARE® 3 panels [5].

Comparing the non-dimensional impulse-displacement plot of the tested GLARE® 3 against that of mild steel, seen in Figure 2.34, it was found that GLARE® 3 outperformed mild steel. For a given dimensionless impulse GLARE® 3 showed up to 11% decrease in normalised displacements. This is something not found when comparing the non-dimensional data of the thermoplastic FMLs [58, 59, 64].

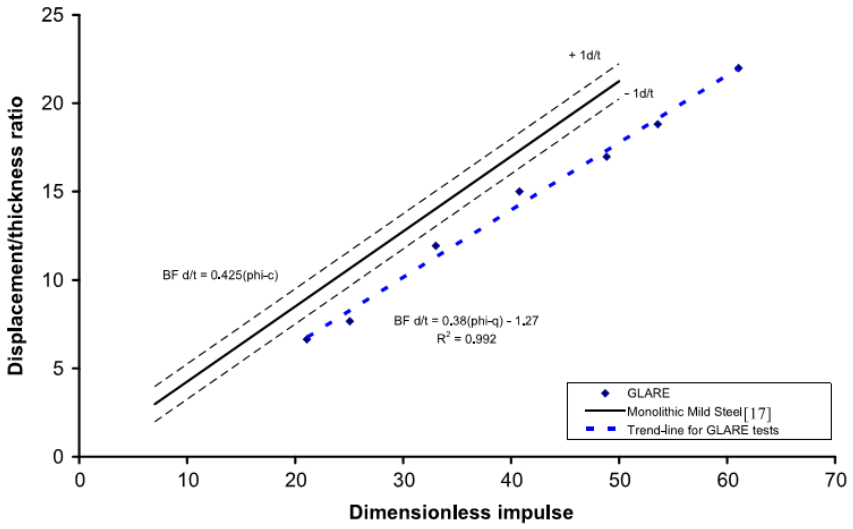

Figure 2.34: Non-dimensional impulse-displacement plot of GLARE® 3 panels [5].

Chapter 3

Materials and Manufacturing

This chapter details all the materials and methods used during the manufacture of the specimens. Section 3.1 details the mechanical properties of the constituent materials. Sections 3.2 and 3.3 cover the various surface treatment and composite layup techniques employed during manufacture. The manufacturing of the various specimens is also discussed.

3.1 Material Specifications and Sourcing

3.1.1 Aluminium Al2024-T3

Al2024 is an aluminium alloy with Copper (Cu) and Magnesium (Mg) as its primary alloy. These elements exist as 3.8 - 4.9 Wt.% Cu and 1.2 - 1.8 Wt.% Mg respectively. The T3 temper grade applies to aluminium that has been solution heat treated, cold worked to improve the material strength and then naturally aged [66].

This alloy was introduced in 1931 by ALCOA, replacing Al2017-T4 (Duralumin) as the predominant aircraft alloy [67]. Due high tensile strength and good fatigue resistance [67], Al2024 products are used in fuselage structures, wing tension members, shear webs and ribs and other areas where stiffness and fatigue performance is important. Al2024-T3 is also one of the main components used in the manufacture of GLARE®. As the focus of this study falls on comparing the blast response of the manufactures FML to that of GLARE®, Al2024-T3 was also chosen for the metal layers. The major mechanical properties of Al2024-T3 are shown in Table 3.1 [68].

Table 3.1: Aluminium 2024-T3 material properties obtained from [68].

Property	Average Value	Units (S.I.)
Density	2780	kg/m^3
Young's Modulus	73.1	GPa
Ultimate Tensile Strength	483	MPa
Tensile Yield Strength	345	MPa
Shear Modulus	28	GPa
Shear Strength	283	MPa
Poisson's Ratio	0.33	
Strain to Failure	18	%
Specific Heat	875	$J/kg \cdot K$

The Al2024-T3 was obtained from ALCLAD Sheetmetal Services CC based in Pretoria, South Africa. The metal was ordered as 0.8 mm thick sheets of 300 mm $\times$ 300 mm. This is similar in size to the GLARE® panels blast tested by Langdon et al [5], ensuring a more accurate comparison between results. Due to manufacturing constraints discussed later in this chapter, 0.8 mm thick sheets was used instead of the thinner 0.3 mm used in GLARE®.

3.1.2 Glass Fibre

Due to its low cost, high availability and high strength, the fibre grade chosen for this study is E-glass or electrical grade glass. E-glass is a low alkali glass originally developed for stand off insulators in electrical wiring, but later found to have excellent fibre forming capabilities [69].

For the purpose of this study, two different weaves of E-glass fibre were used to compare the effects of the blast loading on different fibre configurations. A simple plain weave fabric with an areal density of 400 $\mathrm{g\,m^{-1}}$ and a uni-directional glass fibre with an areal density of 220 $\mathrm{g\,m^{-1}}$ was used. The uni-directional glass fibres had a 200 $\mathrm{g\,m^{-1}}$ areal density in the warp direction and 20 $\mathrm{g\,m^{-1}}$ in the weft direction. These fibre configurations were chosen in order to match the thickness of the GFRP layer to the metal layer. Table 3.2 shows the material properties of the E-glass fibre.

Table 3.2: Material properties for E-glass, obtained from [69].

Property	Minimum Value	Maximum Value	Units (S.I.)
Density	2550	2600	kg/m^3
Young's Modulus	72	85	GPa
Ultimate Tensile Strength	1950	2050	MPa
Shear Modulus	30	36	GPa
Poisson's Ratio	0.21	0.23	
Specific Heat	800	805	$J/kg \cdot K$

3.1.3 SE 84LV Woven Prepreg

SE 84LV prepreg is an extremely versatile hot-melt epoxy prepreg developed by Gurit [70]. It is often used with heavy fibre weights where low-flow processing conditions are necessary. Its high compression strength makes it ideal for use in large, heavily loaded components, such as yacht hulls and spars. This also makes it an attractive material for use in other structural applications.

SE 84LV prepregs come in a variety reinforcing fibres. The 275 $\mathrm{g\,m^{-1}}$ plain weave, E-glass fibre reinforced, SE 84LV was chosen due to its availability and successful use as FML composite by van Tonder [12]. This fibre configuration gave the SE 84LV prepreg a total areal density of 295 $\mathrm{g\,m^{-1}}$, differing somewhat from the plain glass fibres used. As discussed in Section 2.3, the bond strength of surface treatment schedule paired with the SE 84LV prepreg proved superior to most other methods. No uni-directional SE 84LV could be obtained for this study, due to the lack of stock availability and the cost of custom material manufacture. The prepreg was obtained in roll form from AMT Composites. The material properties for a single ply of plain weave, E-glass reinforced, SE 84LV, cured at 80 °C for 12 hours are shown in Table 3.3, obtained from the manufacturer data sheet [70].

Table 3.3: SE 84LV/RE295 epoxy prepreg properties of a ply cured at 80 °C for 12 hours [70].

Property	Average Value	Units (S.I)
Cured Ply Density	1800	kg/m^3
Fibre Weight	275	$\mathrm{g\,m^{-1}}$
Tensile Modulus (0°/90°)	37	GPa
Tensile Strength (0°/90°)	633	MPa
Compressive Strength (0°/90°)	644	MPa
Tensile Laminate Fibre Vol.	51.9	%

3.1.4 Prime 20LV Epoxy Resin

Prime 20LV is a very low viscosity epoxy infusion system designed for a variety of different infusion processes [71]. The lower viscosity and longer working time make it ideal for infusing large components or for use in wet layup processes. Mechanical properties of the finished VARTM/infused laminate are claimed to lie between those of hand lamination and low-temperature cure prepreg processes. This makes it a good epoxy infusion system for comparison with the SE 84LV prepreg.

Due to its availability and successful use by van Tonder [12], Prime 20LV was chosen as the epoxy infusion system. The cured matrix properties for the Prime 20LV with Slow hardener are shown in Table 3.4, obtained from the manufacturer data sheet [71].

Table 3.4: Mechanical properties of Prime 20LV matrix cured according to prescribed schedule using slow hardener [71].

Property	LV Resin & Slow Hardener	Units (S.I)
Cured Ply Density	1144	kg/m^3
Tensile Modulus	3.5	GPa
Tensile Strength	73	MPa
Strain to Failure	3.5	%

3.1.5 Redux 609 Film Adhesive

Redux 609, developed by Hexcel, is a modified epoxy film adhesive used, most notably, in aluminium to aluminium bonding. It cures at 120 °C and is available in standard areal weights of 200 $g\,m^{-1}$ and 300 $g\,m^{-1}$. It was used by van Tonder with great success, improving the bond strength of all the composite - aluminium interfaces, discussed in Section 2.3.

3.2 Aluminium Surface Treatments

This section details the various surface treatments performed on the Aluminium 2024-T3 sheets. The surface treatment processes are listed in the order in which they were performed, namely mechanical surface roughening (through bead blasting), silane chemical surface treatment and the application of Redux 609 film adhesive.

3.2.1 Bead Blasting

As discussed in Section 2.3, the aluminium surfaces were bead blasted to achieve a macroscopic surface roughness. All aluminium plates were cleaned first using acetone, to remove any surface grease and dirt. The cleaned aluminium plates were then placed inside the bead blasting chamber.

Bead blasting was performed using 150 µm glass beads and a line air pressure of 6 bar. The bead blasting nozzle was held at a downward angle and at a 50 mm stand-off distance in order to obtain a consistent surface roughness. The nozzle was moved horizontally across the panel, until the entire surface of the metal obtained a constant opacity. In cases where both surfaces of the metal had to be roughened, such as the mid surface of the FML, the panels were turned over and the process was repeated. In all cases the aluminium plates were stabilised inside the chamber, using the built-in protective rubber gloves.

Samples of bead blasted aluminium plates was inspected using a scanning electron microscope (SEM) in order to determine the consistency of the bead blasting process. The specimens seen in Figure 3.1 show good consistency in surface roughness indicated by the size and distribution of the indentations.

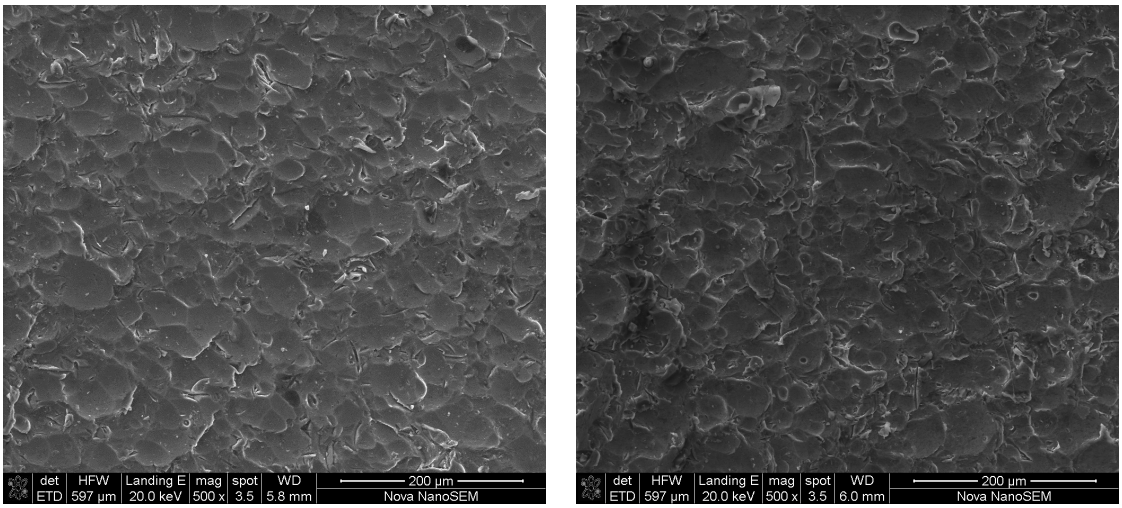

(a) SEM Sample 1 - Bead blasted. (b) SEM Sample 2 - Bead blasted.

Figure 3.1: SEM images of two different bead blasted aluminium surfaces.

3.2.2 Silane (Sol-Gel) Chemical Treatment

A silane sol-gel, known chemically as (3-Glycidyloxypropyl)trimethoxysilane, was used to treat the bead blasted aluminium surfaces in order to enhance its bond-ability with composite materials. The sol-gel was obtained from Sigma-Aldrich and selected for its enhanced hydrostatic stability and affinity to bond epoxies and metals [36, 72]. This is the same chemical used by van Tonder [12] yielding successful results. Henceforth the (3-Glycidyloxypropyl)trimethoxysilane will be referred to only as silane.

The process followed for chemical surface treatment is similar to that followed by van Tonder [12] and Fedel [38]. This surface treatment consisted of three stages, namely, hydrolysis of the silane, submersion of the aluminium in the silane solution and finally drying and curing of the treated plates. The chemical treatments were all performed at the UCT Centre for Materials Engineering (CME). This section describes all the steps involved in the surface treatment, as well as all observations, in order to elucidate the process as much as possible.

Hydrolysis of silane

Literature [12, 36, 72] suggest using an acidic solution to dissolve the silane. The method of hydrolysis is described as follows:

- A 500 ml flask was filled up with distilled water while the 5L flask was filled to the 3 l mark.
- 5 ml of Glacial acid (pure acetic acid) was added to the 500 ml flask of distilled water.
- The acetic acid solution was further dilated by titrating a small amount of the fluid in the into the larger flask with 3 l of distilled water. This was done until the pH reached 4.5. The pH was measured using a universal indicator.
- 30 g of the silane was then added to the diluted, 3 l acetic acid mixture, to obtain a 1% solution by mass.
- The mixture was then stirred, using a magnetic stirrer, until all the silane droplets had hydrolysed.

It was observed that the silane, when first added to the acidic mixture, did not dissolve but formed small droplets, sinking to the bottom of the flask. Both stirring for longer periods and at increased temperatures (40 °C), decreased the time it took for the silane to hydrolyse. It was also found that, when left unchecked for long periods, a gel deposit formed at the bottom of the flask. This deposit could not be dissolved once formed, leading to the conclusion that the mixture had to be used immediately after hydrolysis, before it was potentially no longer viable.

Submersion of aluminium plates

The hydrolysed silane mixture was poured into a large ceramic container. The plates were placed between supports, five at a time, and submerged completely in the mixture for 15 minutes, then removed and left to air dry. The supports were manufactured from high density polyethylene to prevent any reaction with the chemical treatment. The submersion of the plates is shown in Figure 3.2. This process was repeated multiple times, treating a total of 30 plates before remaking a silane solution. No visual difference was observed between the treated and untreated plates.

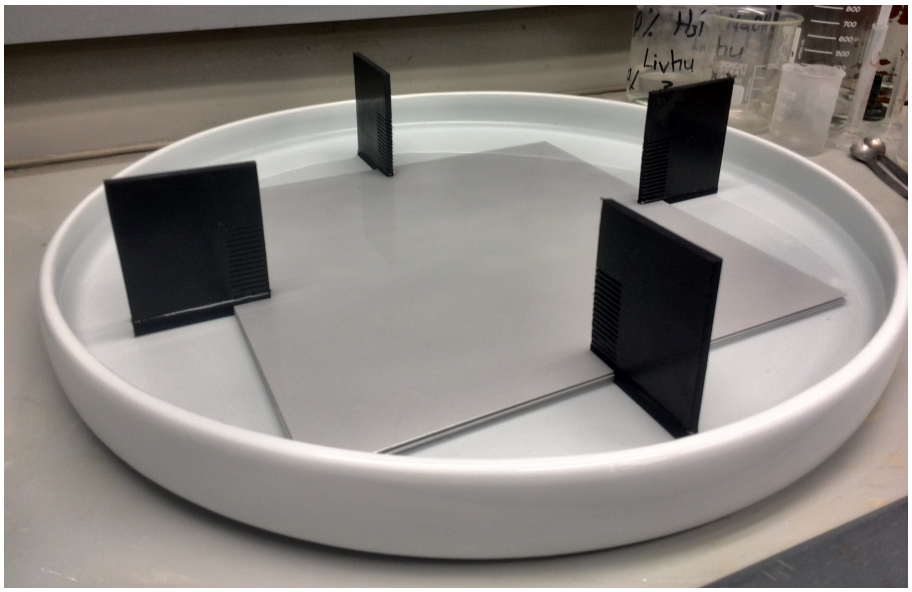

Figure 3.2: Chemical surface treatment of the Al2024-T3 plates.

Drying and curing

After air drying, the plates were placed in a temperature controlled oven and cured at 92 °C for four hours, using the temperature profile shown in Figure 3.3.

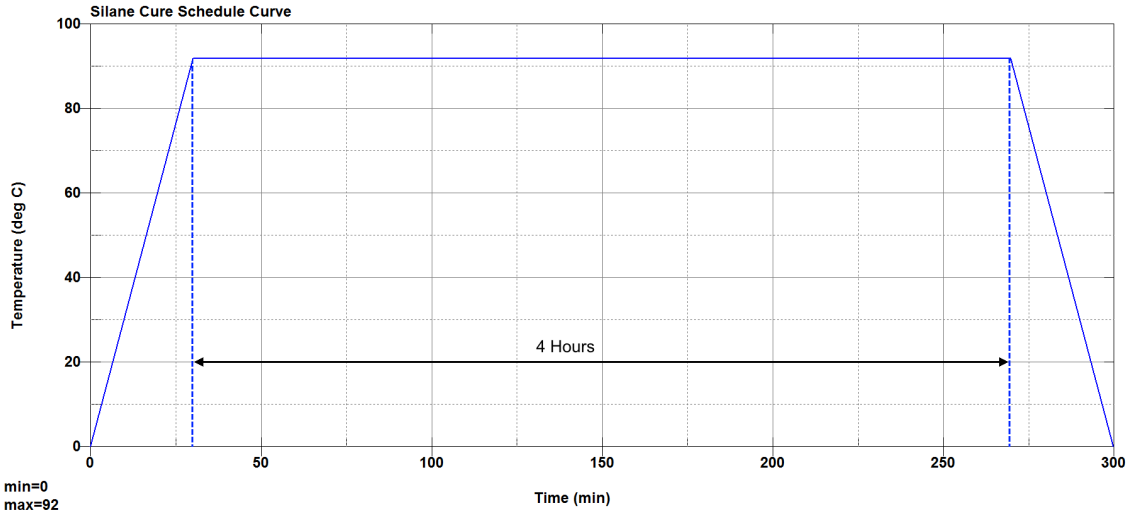

Figure 3.3: Silane cure temperature profile [12].

Samples of bead blasted and silane treated aluminium plates inspected using the SEM are shown in Figure 3.4. The specimens showed good consistency in surface roughness as well as white ridges at the edges of the indentations differing from the specimen only subjected to bead blasting, shown in Figure 3.1. The white ridges were caused by etching due to

submersion in the acidic silane solution. Etching of the aluminium substrate resulted in a more reflective surface, appearing as white lines on the SEM images.

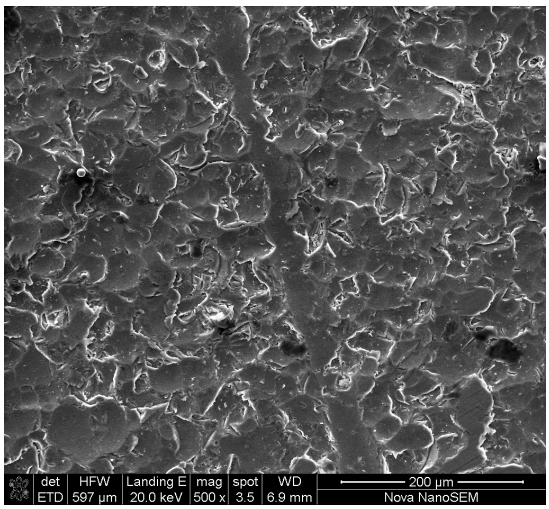

(a) SEM Sample 3 - Bead blasted and silane treated

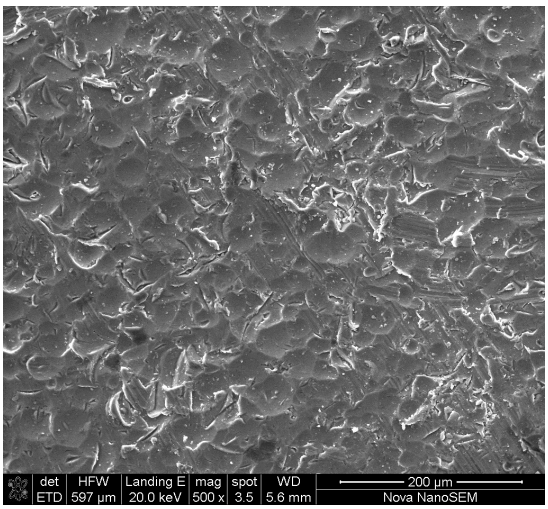

(b) SEM Sample 4 - Bead blasted and silane treated

Figure 3.4: SEM images of two different bead blasted and silane treated surfaces.

3.2.3 Film Adhesive Layup

The final surface treatment was the addition of a Redux 609 300 $\mathrm{g\,m^{-1}}$ film adhesive. In this document the film adhesive is referred to as a surface treatment. The Redux 609 was always applied directly to the aluminium after chemical treatment with the purpose of improving the bond strength between the metal and composite interfaces.

According to the manufacturer material data sheet [73], Redux 609 film adhesive has a maximum permissible outlife of three months at 5 °C to 27 °C. This required it to be stored in sealed packaging, at sub zero temperatures, to promote longevity. Before use, the film adhesive roll was removed from the freezer and left to thaw in its sealed packaging for 24 hours to ensure that the film was at a constant temperature throughout. Handling the film adhesive prematurely could result in cracking, water absorption and degradation of the film quality.

The application of the film adhesive was a simple process. Squares, the same size as the aluminium plates, were cut from the film adhesive roll. To apply these sheets, the release paper was then removed and the sheets positioned on the bonding surface. At room temperature, Redux 609 is relatively tacky making its application simple.

Once applied to the aluminium, the Redux 609 could be cured at any of the

temperatures indicated in Table 3.5 for the corresponding duration. Temperature ramp up and down cycles were not allowed to exceed 2 °C/ min. Some of the possible cycles were found to coincide with both the post-cure cycle of Prime 20LV and cure cycle of SE 84LV. Due to time constraints on manufacturing and the logistics of lab equipment, the decision was made to use combined cure and post-cure cycles wherever possible. The effects of combined cycles on interfacial bond properties were tested using during the Single Leg Bend (SLB) tests, discussed in Section 4.3. The manufacture of these test specimens are discussed in more detail in Section 3.5.

Two different processes were attempted during manufacture, these included a two-step and single step Redux bonding. During a two-step process, the Redux 609 film adhesive was first bonded to the aluminium and cured under vacuum. The product of this was then introduced as part of the composite layup. A single step process had the Redux 609 film adhesive introduced directly into the composite layup and cured following the same cure cycle used for the respective composite.

Table 3.5: Redux 609 film adhesive cure temperatures and times [73].

Temperature (°C)	180	170	160	150	140	130	**120**	110	100
Time (min)		7	8	10	20	30	**60**	120	240

3.3 Composite Layup Techniques

Two different techniques were employed to manufacture the GFRP components of the FMLs. These techniques are a wet/hand layup, discussed in Section 3.3.1, and a prepreg layup, discussed in Section 3.3.2.

3.3.1 Wet Layup

The wet/hand layup of GFRPs is a manufacturing technique wherein the resins are impregnated into the fibres manually, using rollers or brushes. The Prime 20LV epoxy resin was applied using brushes, gently distributing the resin evenly over the entire fibre surface. The entire wet layup process was completed as follows:

- Before layup, the moulding surface was cleaned thoroughly using acetone after which it was waxed and polished multiple times, to ensure a non-stick finish.

- Fabrics and consumables were cut to the appropriate size, numbered and marked to ensure a correct layer count and consistency of warp and weft direction during layup.
- The required amounts of Prime 20LV and Slow hardener were measured in separate cups, by mass, in accordance with the amount of fibre layers to be laid up and the data sheet specifications. A 1:1 ratio of resin mass to fibre mass was used to determine the mixture quantities.
- Once measured, the hardener was added to the Prime 20LV resin and stirred consistently for 3 minutes, until the both components were well mixed.
- The layup was started by applying an initial layer of resin straight onto the mould surface, to ensuring a good surface finish.
- A fibre layer was then placed on this initial layer of resin and further impregnated using a paint brush. Resin was dabbed over the entire layer until the white glass fibre turned clear, indicating that the material was wetted throughout
- Another layer was then carefully added, wetted out and the process repeated, until the layup was complete.
- Once complete, a layer of perforated release film was placed on top. This was followed by a layer of breather cloth to allow the free outflow of air under vacuum and the absorption of any excess resin.
- The last step was the addition of a vacuum bag. A large sheet of vacuum bag material was adhered to the moulding surface using tacky tape. The material covered the entire composite layup, accounting for the height of the layup, using pleats and folds in the vacuum bag.
- Finally, a vacuum of -85 kPa was drawn and maintained for 24 hours, allowing the layup to cure at room temperature.

Once the resin reached the end of its cure cycle, the composite was de-moulded and placed in the oven for a post-cure cycle.The temperature profile of the post cure cycle used during experimentation is shown in Figure 3.5.

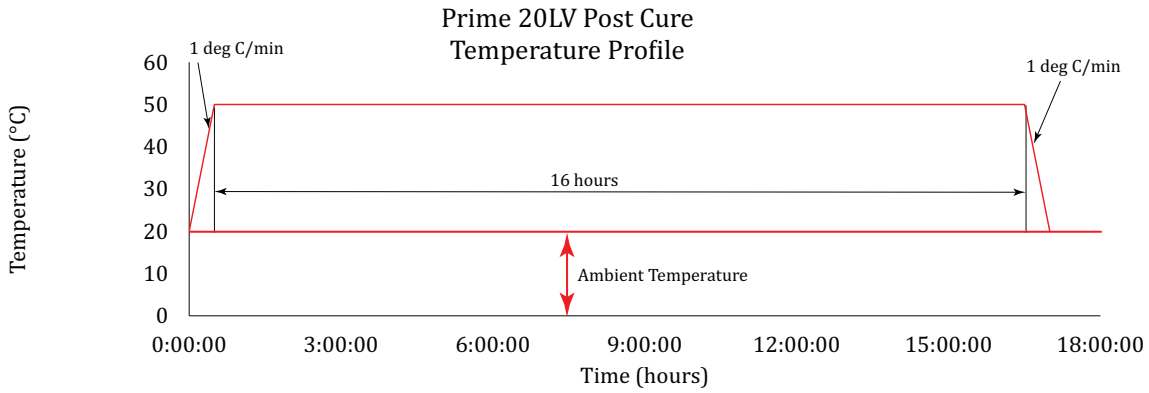

Figure 3.5: Prime 20 post cure cycle under -85 kPa vacuum [12].

3.3.2 SE 84LV Prepreg Layup

SE 84LV is a hot melt epoxy prepreg that needs to be stored at sub-zero temperatures when not in use. The prepreg was thawed to room temperature before handling to prevent cracking, water absorption and degradation of the material. The prepreg was laid up as follows:

- Before layup, the moulding surface, in this case a stainless steel plate, was cleaned thoroughly using acetone. After this the plate was waxed and polished multiple times, to ensure a non-stick finish.
- Sheets of appropriate size were cut from the roll of SE 84LV prepreg, numbered and the fibre direction marked to ensure layup consistency and correct layer count.
- Sheets were placed directly on the moulding surface. The natural tackiness of the prepreg ensured that once placed into the correct position the sheets did not move. The waxed and polished stainless steel plates ensured a good surface finish in the final product. The sheets were placed on the moulding surface and rolled to ensure the removal of any potential voids. After rolling a sheet, the layer of protective polythene was removed exposing the tacky upper surface to continue layup.
- Multiple layers were placed on top of one another in this fashion. The number of layers in the layup were dependant on the specimens being manufactured. After placing each new layer, the layup was rolled with a metal roller to ensure further compaction.
- Once complete, a layer of perforated release film was placed on top. This was also followed by a layer of breather cloth to allow the free outflow of air under vacuum and the absorption of any excess resin.

- A large sheet of vacuum bag material was then adhered to the moulding surface using tacky tape. The material covered the entire composite layup, accounting for the height of the layup, using pleats and folds in the vacuum bag.
- Finally, the moulding plates were placed in the temperature controlled oven to undergo curing. A measured vacuum of -95 kPa was drawn and kept while the composite was subjected to the cure profile shown in Figure 3.6.

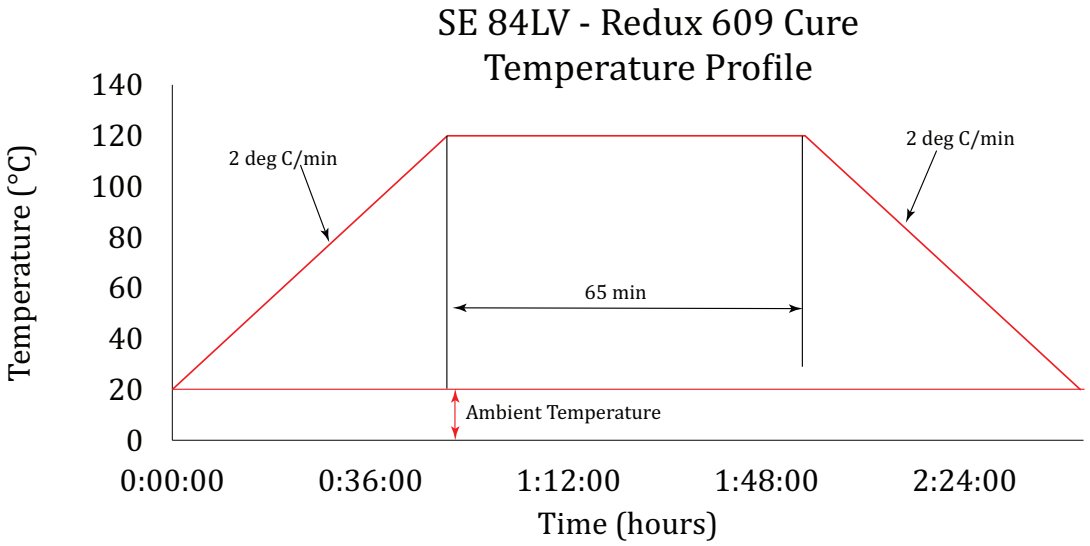

Figure 3.6: SE 84LV cure cycle under -95 kPa vacuum [12].

3.4 Material Validation Specimens

This section discusses the manufacture of specimens to test and validate material properties and the effects of the manufacturing processes used. Section 3.4.1 covers the manufacture of composite specimens for thickness determination, while the quasi-static tensile test specimens are discussed in Section 3.4.2 .

3.4.1 Composite Thickness Testing

Some samples were manufactured as a pilot test to determine the thickness of the composite layers with regard to the metal layers and number of plies used. Both resin systems were used to manufacture the different samples. Uni-directional and woven glass fibre samples were also made using the Prime 20LV resin system. The thickness of the trial pieces and fibre weights are shown in Table 3.6.

The thickness of the trial specimens were measured at various points using a micrometer. These thicknesses correlated well with the theoretical values shown in Figure 3.7. It was seen that the approximate thickness of the composite layer, for thin (less than eight layers) specimens, was given by Equation (3.1).

$$thickness(mm) = \frac{Areal\ Density\,(grams/m^2)}{1000} \tag{3.1}$$

Table 3.6: Measured thickness values of the composite specimens.

GFRP Layup Fibre	Matrix	Layer Count	Thickness (mm)
295 g m^{-1} woven Prepreg	SE 84LV	2	0.6
		8	2.1
400 g m^{-1} woven	Prime 20LV	2	0.7
		8	2.6
220 g m^{-1} uni-directional	Prime 20LV	2	0.4
		8	1.4

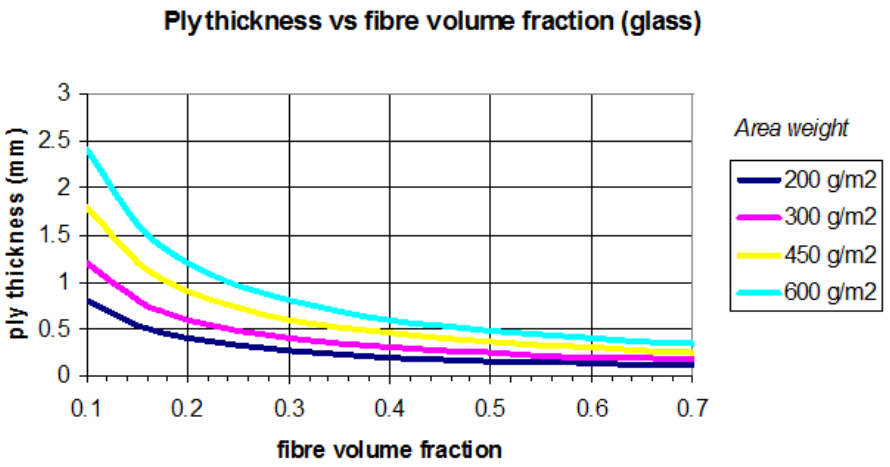

Figure 3.7: Theoretical composite layup thickness.

3.4.2 Al2024-T3 Tensile Dogbone Specimen Manufacture

Quasi-static tensile test specimens were machined to determine the properties of the aluminium alloy for numerical modelling purposes. Specimens were manufactured in accordance with the ASTM standard E8/E8M [74]. Figure 3.8 shows the design of the

dogbone specimens. The specimens were all cut from a single sheet of 0.8 mm thick Al2024-T3 at the UCT mechanical workshop. The specimens were cut both parallel and perpendicular to the roll direction to account for the response in both orientations .

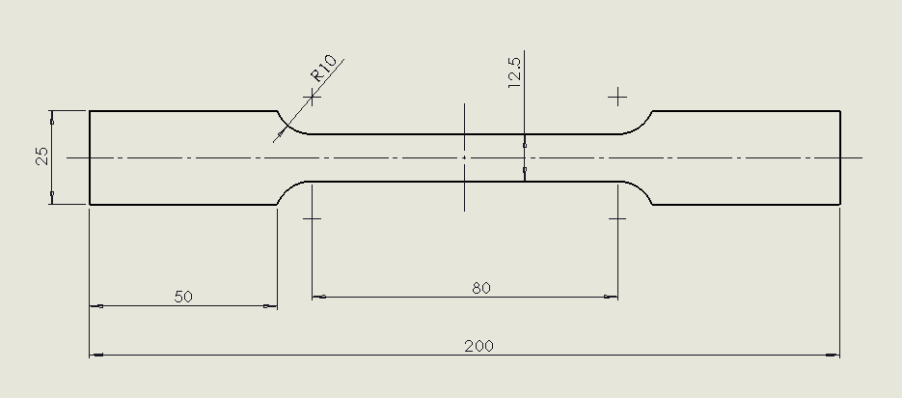

Figure 3.8: Standard dogbone specimen design (All dimensions in mm).

To determine the influence of various surface treatments on the tensile response of the alloy, specimens were tested after being subjected to varying levels of surface treatment. The specimens included a control group, with no surface treatment, a group with bead blasted surfaces and a final group that was both bead blasted and subjected to a silane treatment and cure. Table 3.7 shows the division of surface treatments for the tensile specimens.

Table 3.7: Surface treatment variation of tensile specimens.

Treatment Description	Direction (0° or 90°)	Specimens Test Number
No Surface Treatment	0° $\parallel$ to roll	1, 2, 3, 4
	90° $\perp$ to roll	5, 6, 7, 8
Bead Blasted	0°	9, 10, 11
Bead Blasted and Silande Treated	0°	12, 13, 14

3.5 Single-Leg Bend Specimen Manufacture

The purpose of the single-leg bend (SLB) tests was to characterise the bond strength of the aluminium and GFRP interface, by measuring crack growth between layers due to an applied force. As no standard exists for SLB tests, the manufactured specimens were based on the ASTM Three-Point Bend (TPB) test standard [75]. The SLB specimens

comprised of two layers of equal thickness, each of different length, with an initial crack of known length between them. The first layer was fully surface treated Al2024 including the addition of a Redux 609 interlayer while the second consisted of the glass fibre composite. The two layers were bonded together using either the wet layup or prepreg layup technique described above. A sheet of non-perforated µm thick release film was used to introduce an initial crack between the layer of aluminium and GFRP. The geometry of the manufactured SLB specimens is illustrated in Figure 3.9. The GFRP was used to manufacture the loaded (longer) side of the specimen as it has the higher stiffness.

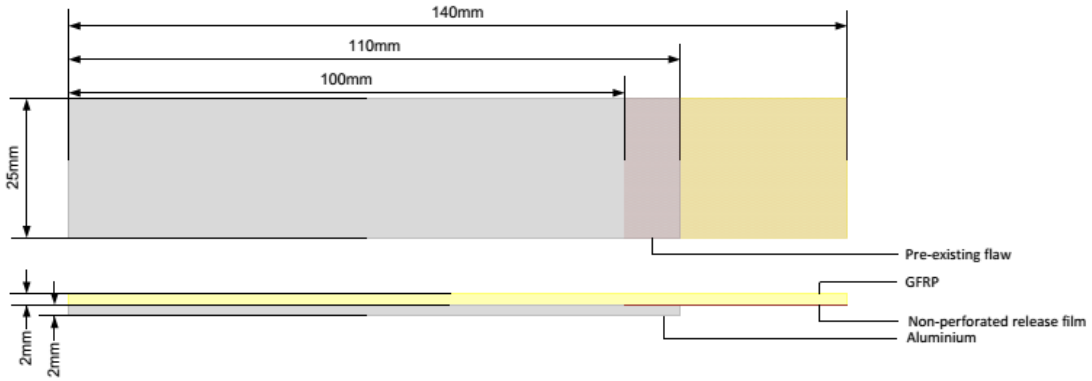

Figure 3.9: SLB coupon geometry [12].

Three sets of specimens were manufactured as follows:

- SE 84LV prepreg (295 g m^{-1} Woven E-Glass fibre) and 2 mm thick Al2024-T3 using Redux 609 in a single step layup and cure.
- Prime 20LV prepreg (400 g m^{-1} Woven E-Glass fibre) and 2 mm thick Al2024-T3 using Redux 609 in a single step layup and cure.
- Prime 20LV prepreg (400 g m^{-1} Woven E-Glass fibre) and 2 mm thick Al2024-T3 using Redux 609 in a two step layup and cure.

The layup of each process is described through the flow diagram in Figure 3.10 where each color indicates a different SLB configuration.

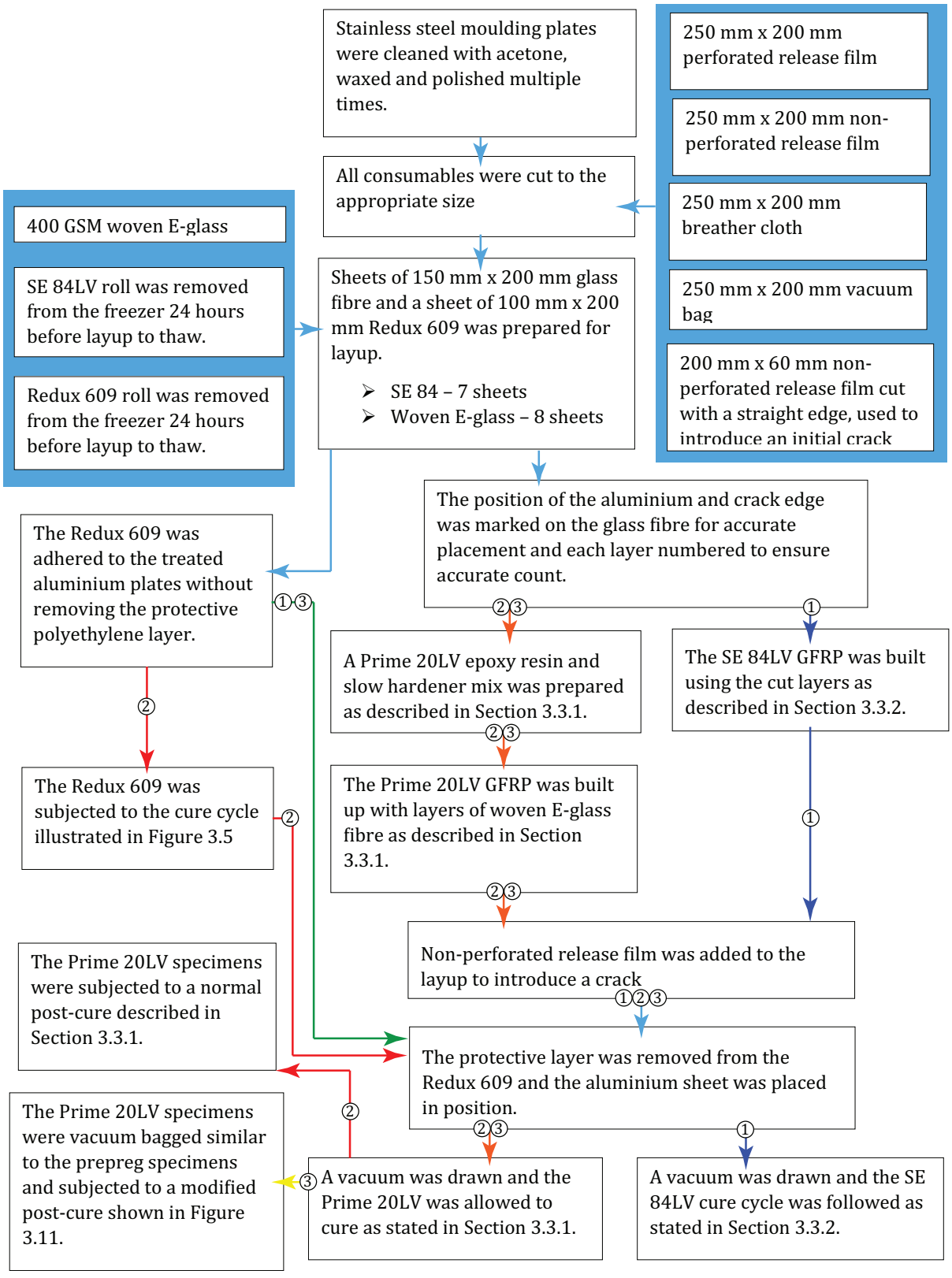

Figure 3.10: Flow diagram of SLB specimen manufacturing process.

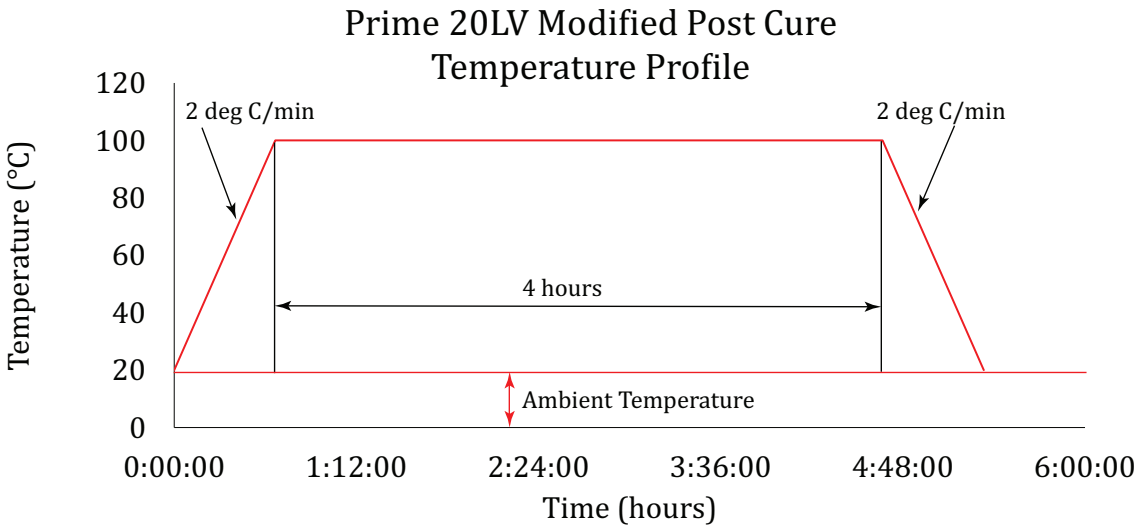

Figure 3.11: Modified Prime 20LV post cure and Redux 609 cure cycle performed with -95 kPa vacuum.

3.6 FML Manufacture

Three sets of FML panels were manufactured using two distinct layup processes. Each FML panel consisted of three layers of approximately 300 mm × 300 mm, surface treated Al2024-T3, four layers of approximately 300 mm × 300 mm Redux 609 and two layers of approximately 300 mm × 300 mm GFRP.

Of the three layers of aluminium, two were surface treated on a single side, making up the outer layers of the FML, while the third was treated on both sides, making up the middle layer of the FML. The GFRP layers of the FMLs were manufactured three different combinations, shown in Table 3.8. All panels were manufactured using the single stage layup technique discussed in preceding sections. The two processes used to manufacture the FMLs are described in more detail below, referencing the respective GFRP layups where applicable. The general layup of the FMLs is illustrated in Figure 3.12. The layup process for each FML is illustrated in the flow diagram in Figure 3.13.

Table 3.8: GFRP laminate configurations.

Fibre and Resin Configuration	Fibre Areal Density $g\,m^{-1}$	Number of Composite Layers
Simple Weave E-Glass, SE 84LV	275	1
Simple Weave E-Glass, Prime 20LV	400	1
Uni-directional E-Glass, Prime 20LV	220	2 (0° and 90°)

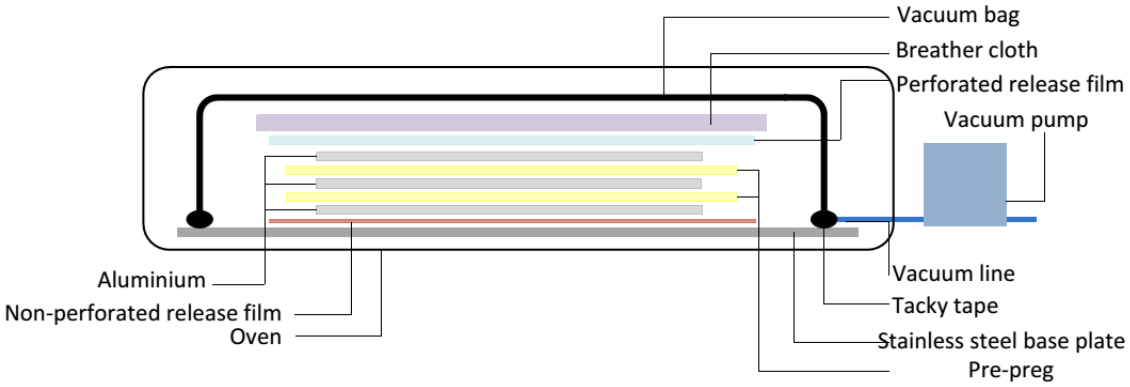

Figure 3.12: Illustration of FML layup and cure [12].

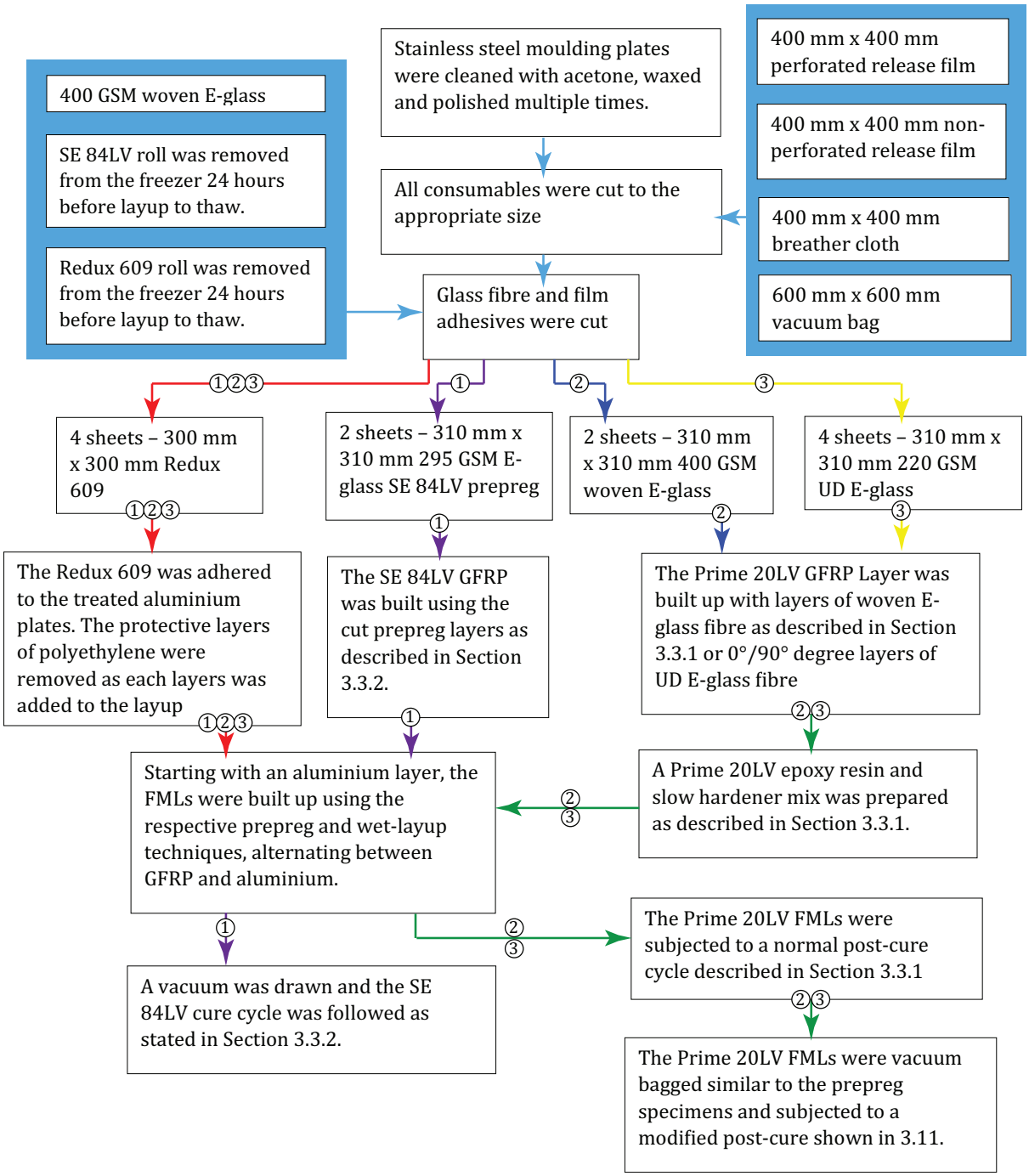

Figure 3.13: Flow diagram of FML panel manufacturing process.

Chapter 4

Material Characterization

4.1 Introduction

To assist in the numerical modelling of the FML blast tests, the constituent materials used during manufacture were experimentally characterised by performing quasi-static uni-axial tensile tests on the aluminium and single leg bend tests to characterise the interfacial bond strength of the FML. Section 4.2 details the quasi-static tensile testing and analysis and Section 4.3 describes the single leg bend tests and associated analysis.

4.2 Quasi-Static Tensile Testing

The quasi-static behaviour of the alloy was characterized by performing uni-axial tensile tests on a Zwick Roell 1484 universal testing machine. As aluminium alloys have shown very little variation in response when subjected to higher strain rates [76, 77], high strain rate characterisation was beyond the scope of the project and not a primary consideration.

4.2.1 Experimental Setup

Four sets of tensile sets were performed to ascertain the effects of the roll direction and various different surface treatments. The test sets are shown in Section 3.4.2, Table 3.7. The experimental procedure for uni-axial tensile tests was adapted from ASTM A370-05 [74]. Due to limitations of the extensometer, a gauge length of 40 mm was used instead of the standard 70 mm. The specimens were all tested up to the point of fracture. Tests were performed at crosshead speeds of 5 $\mathrm{mm\,min^{-1}}$, 10 $\mathrm{mm\,min^{-1}}$ and 20 $\mathrm{mm\,min^{-1}}$. These crosshead speeds correspond to engineering strain rates of

2.083×10^{-3} s^{-1}, 4.167×10^{-3} s^{-1} and 8.333×10^{-3} s^{-1} respectively. A pre-load of 200 N was implemented in an attempt to remove the effects of bedding-in. An extensometer was utilised to obtain the initial portion of the force-displacement curve containing data pertaining to the elastic modulus of the material.

4.2.2 Tensile Test Data Analysis

A typical force-displacement curve obtained from the tests is shown in Figure 4.1. This curve consists of an initial elastic response, measured by the extensometer, followed by a plastic response, measured from the test bed displacement.

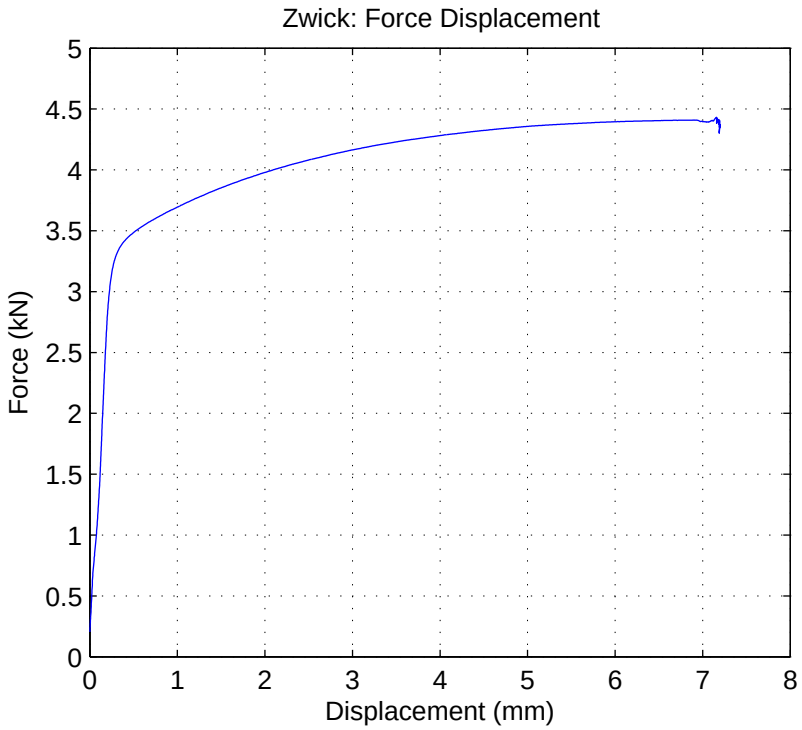

Figure 4.1: Force displacement data obtained from tensile tests.

In some of the test cases, minor slipping was observed in the elastic portion of the curve, shown in Figure 4.2. Equation (4.1) was used to determine the strain offset caused by these effects and subsequently removed from the raw displacement data.

$$\delta_s = \delta_{@maxslope} - \frac{F_{@maxslope}}{m} \tag{4.1}$$

where $\delta_{@maxslope}$ is the displacement at the point of maximum slope, $F_{@maxslope}$ is the force at the maximum slope and m represents the maximum slope.

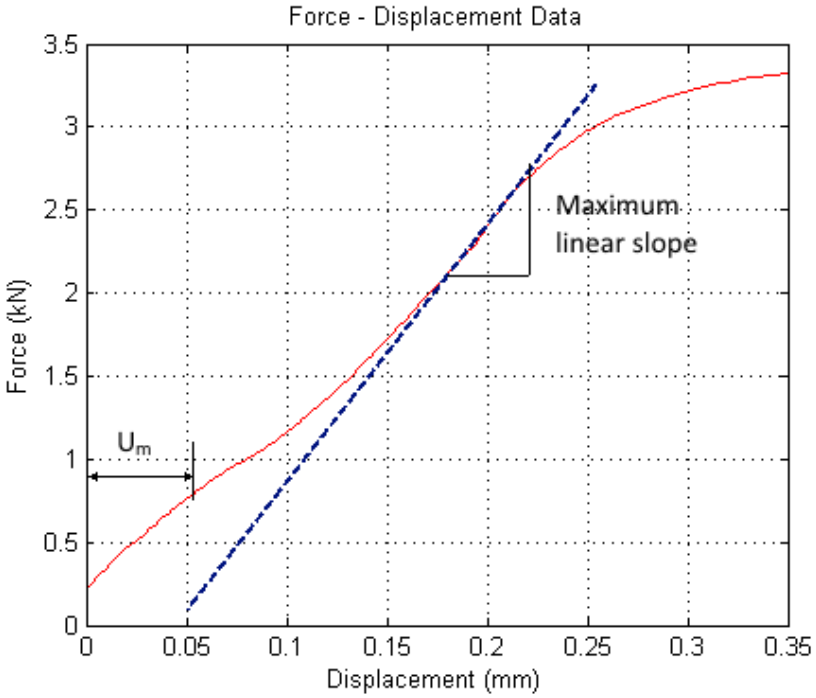

Figure 4.2: Slipping observed in the elastic portion of some tests.

Subtracting the displacements due to slipping from the captured displacement data resulted in a corrected strain displacement, Equation (4.2).

$$\delta_{corrected} = \delta_{raw} - \delta_s \tag{4.2}$$

Using the cross-sectional properties of the tensile specimen, shown in Figure 3.8, the data was converted to the engineering stress, σ_{ENG}, and the engineering strain,ε_{ENG}. This was achieved through the use of Equations (4.3) and (4.4),

$$\sigma_{ENG} = F/A_0 \tag{4.3}$$

where A_0 signifies the original cross-sectional area of the specimen and l_0 denotes the specimen gauge length.

$$\varepsilon_{ENG} = \frac{\delta_{corrected}}{l_0} \tag{4.4}$$

From the engineering stress and engineering strain data, the true stress (σ_T) and true

strain (ε_T) could be calculated through the use of Equations (4.5) and (4.6). As these equations are only valid up to the point of necking (σ_{UTS}), the tensile test data was reduced to this point during material characterisation.

$$\sigma_T = \sigma_{ENG}\left(1 + \frac{\Delta u_c}{l_0}\right) = \sigma_{ENG}\left(1 + \varepsilon_{ENG}\right) \tag{4.5}$$

$$\varepsilon_T = ln\left(1 + \varepsilon_{ENG}\right) \tag{4.6}$$

4.2.3 Quasi-Static Test Results and Discussion

Figure 4.3 shows a graph of force-displacement response for all the tensile specimens tested. No geometrical changes were observed in the specimens subjected to surface treatments. This differed from results observed by van Tonder [5] due to the difference in material temper grade. The force displacement data from the tests was converted to the engineering stress (σ_{ENG}) and engineering strain (ε_{ENG}), shown in Figure 4.4, using the methods described in Section 4.2.2. The temper grade of the material was validated by comparing the ultimate tensile strength (σ_{UTS}) and elongation at fracture (ε_f) of the tested specimens, to the material properties of Al2024-T3 reported in literature [13], shown Table 4.1. The properties of the tested specimens showed good correlation to those of Al2024-T3 found in literature [13].

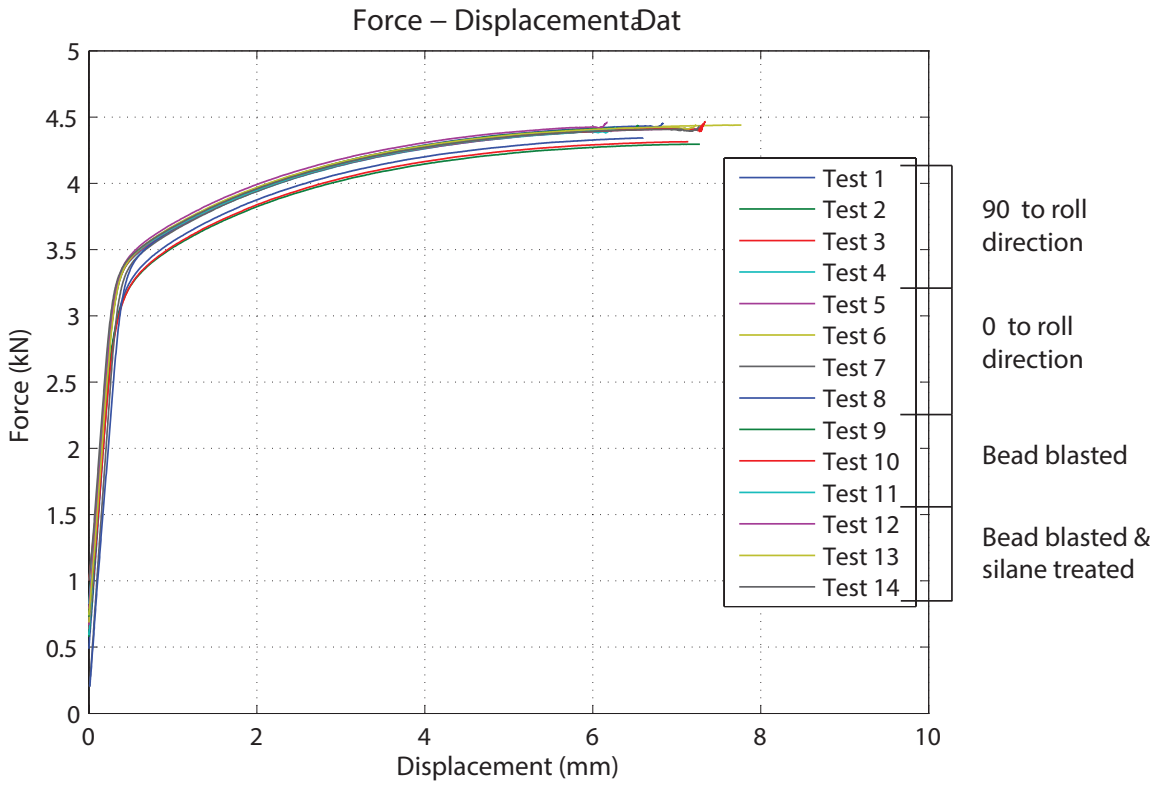

Figure 4.3: Graph of force vs displacement obtained during tensile testing.

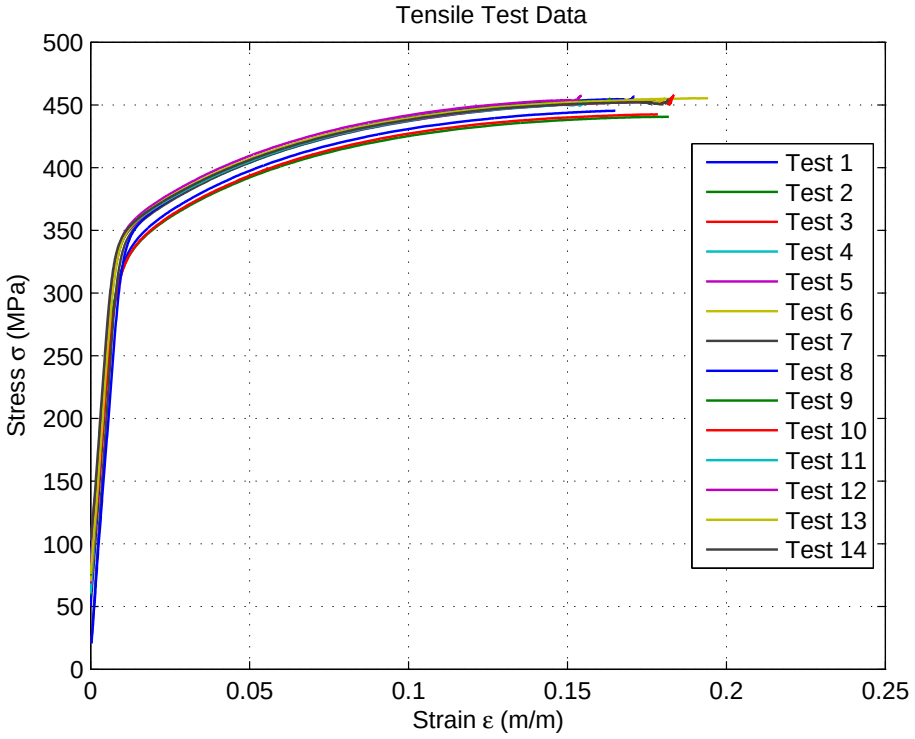

Figure 4.4: Graph of engineering stress vs engineering strain.

Table 4.1: Aluminium 2024-T3 material properties [13] (N/T - Not Tested)

Parameter	Description	Units	Literature Values	Mean Tested Values
σ_{UTS}	Ultimate Tensile Strength	MPa	483	445
σ_Y	Tensile Yield Strength	MPa	345	355
ε_f	Elongation at Fracture	%	18	17.5 - 19
E_Y	Young's Modulus	GPa	73.1	N/T
G	Shear Modulus	GPa	28	N/T
μ	Poisson's Ratio	-	0.33	N/T

The tensile responses of the various tests were then compared to one another to determine the effects of roll direction and surface treatments on the material strength. The graph in Figure 4.5 compares the tensile response of the specimens cut with the major axis at 90° to the roll direction (Tests 1 through 4) to those cut with the major axis in the roll direction (Tests 5 through 8).

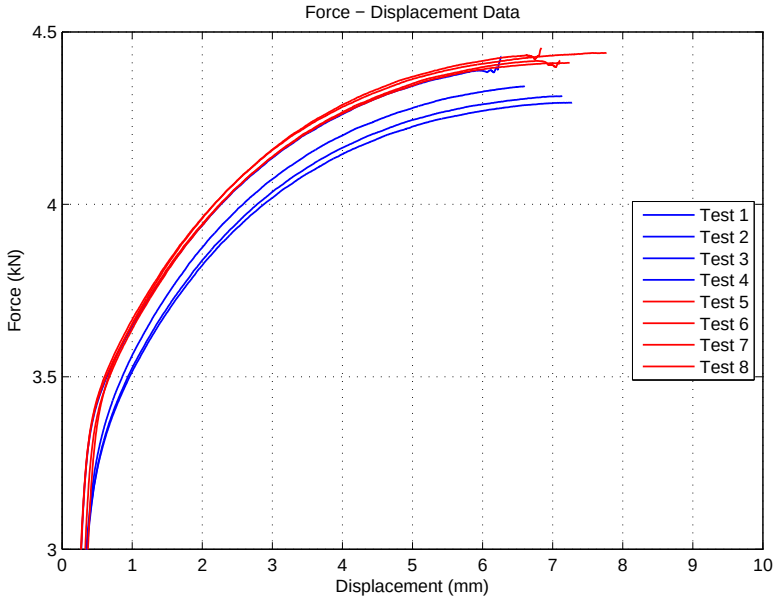

Figure 4.5: Graph indicating the effects of roll direction on material strength.

All surface treatments were performed on specimens cut with the major axis in the roll direction. The response of the mechanically surface treated (bead blasted) specimens are compared to the untreated specimens in Figure 4.6. The mechanical surface treatment of bead blasting had negligible effect on the tensile strength of the material.

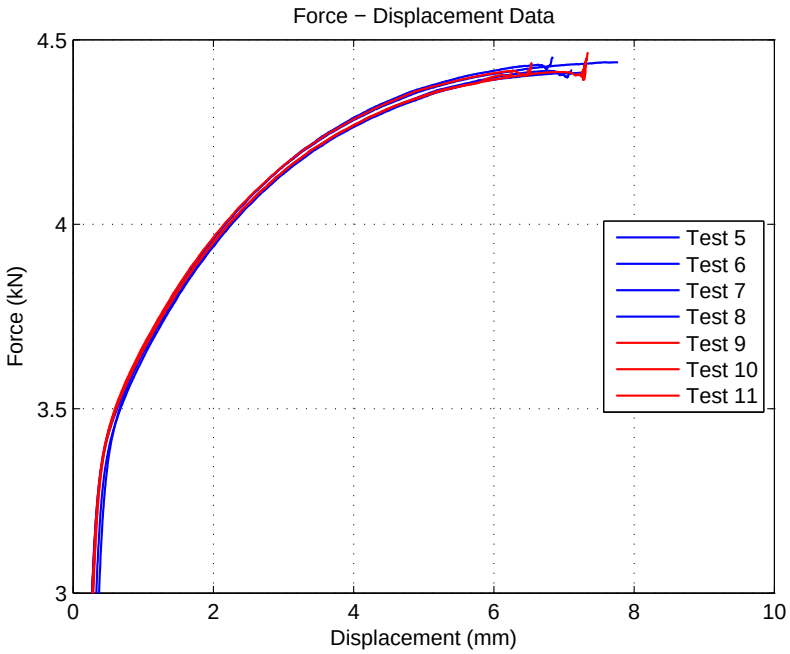

Figure 4.6: Graph indicating the effects of mechanical surface treatment on material strength.

Figure 4.7 shows a graph comparing the force-displacement behaviour of specimens subjected to silane treatment and curing (Tests 12 through 14) to the bead blasted (Tests 9 through 11) and untreated specimens (Tests 5 through 8). Very little variation was observed between the data sets. The silane treatment and curing process had no discernible effect on the material behaviour.

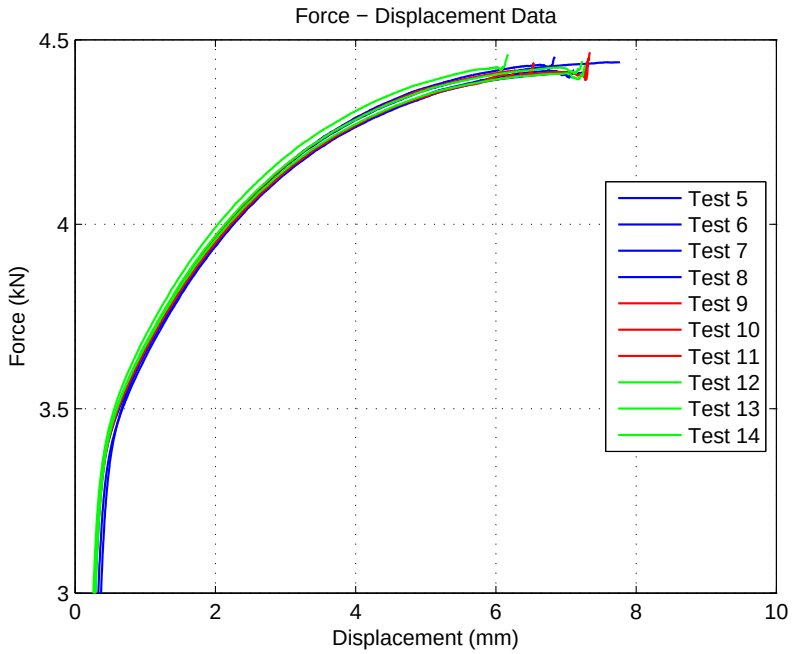

Figure 4.7: Graph indicating the effects of chemical surface treatment on material strength.

The effects of varying the quasi-static strain rates of the tests proved negligible when comparing the material response. All tests were performed up to the point of fracture. Multiple specimens failed outside the 40 mm stipulated gauge length, but still within the parallel test region. None of the specimens showed any distinct evidence of necking before fracture with no measurable reduction in stress after UTS, shown in Figure 4.3.

The engineering stress and strain values were converted to the true stress (σ_T) and true strain (ε_T) data, shown in Figure 4.8. The true stress and strain data was required to characterise the material response using a Johnson-Cook material model, Equation (4.7). Johnson-Cook is a phenomenological model, not based on classical plasticity theory, and incorporates three key material responses namely strain hardening, strain-rate effects and thermal softening. As the Johnson-Cook model also only considers the plastic response of the material the elastic response had to be removed. A 0.2% strain offset was taken and projected onto the plastic section of the material response using the linear elastic relationship and Young's modulus as the slope.

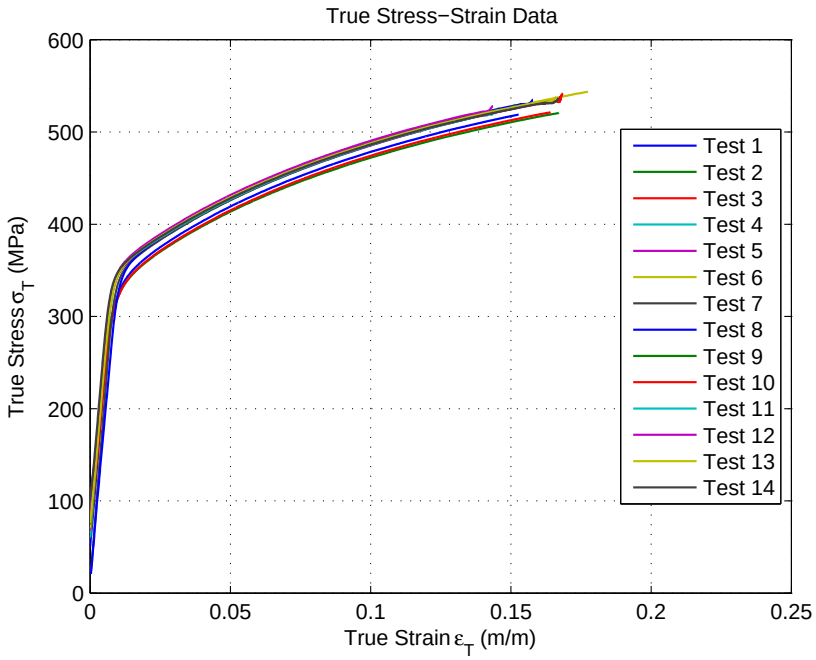

Figure 4.8: Graph of true stress vs true plastic strain.

$$\sigma = \left[A + B(\varepsilon^{p}_{eff})^{N}\right]\left(1 + Cln\dot{\varepsilon}\right)\left[1 - (T_H)^{M}\right] \tag{4.7}$$

Parameters A, B and N were obtained by fitting a curve to the true stress and true plastic strain tensile data using Equation (4.7). The curve fit is illustrated in Figure 4.9. The crosshead speed of the quasi-static tensile tests, 5 mm min^{-1} to 20 mm min^{-1}, and gauge length, l_0, was used to obtain a value for $\dot{\varepsilon}$. Values for C and m were obtained from literature [78–80]. T_H denotes the homologous temperature and is calculated as $T_H = \frac{T - T_R}{T_M - T_R}$, where T_M is the melting temperature and T_R is the reference temperature for determining A, B and N [80,81], taken as 298 K (25 °C). The Johnson-Cook material parameters obtained from testing are shown in Table 4.2 and compared to the values for Al2024-T3 available in literature [80].

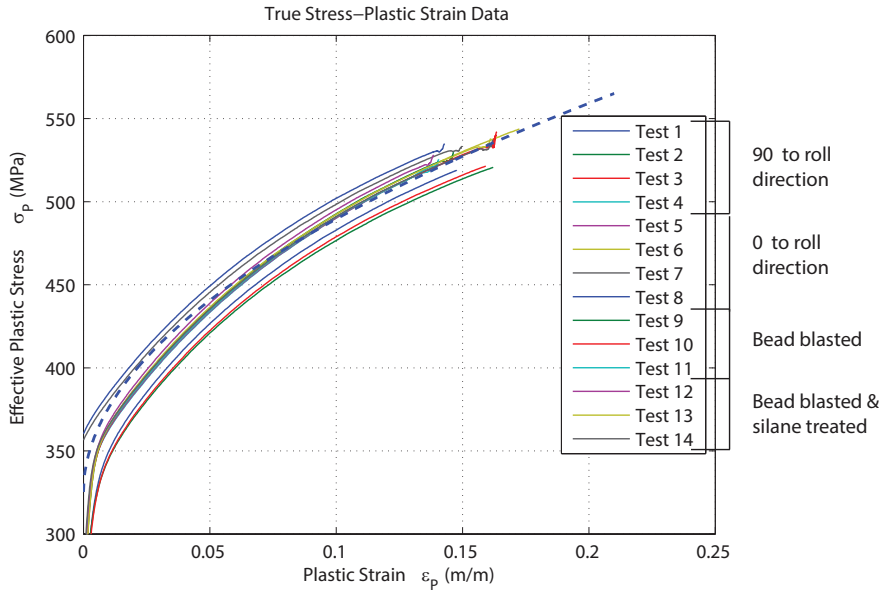

Figure 4.9: Graph showing the correlation between tensile test data and an analytical Johnson-Cook model curve fit.

Table 4.2: Johnson-Cook material properties

Parameter	A	B	N	C	ε_0	M
Units	MPa	MPa	-	-	s^{-1}	-
Test Value	345	564	0.51	-	4.1667×10^{-4}	-
Literature Values [80]	265	426	0.34	0.015	-	1

4.2.4 FEM Analysis of Tensile Tests

Further iterations of the Johnson-Cook material properties were performed by simulating the tensile tests numerically using LS-DYNA® V971. An implicit integration scheme was selected as it is unconditionally stable and better suited at solving long duration events [81, 82]. Only tensile tests performed at strain rates of 5 mm min^{-1} were simulated as the strain hardening parameters required are based on the full material response.

A quarter symmetry model was constructed using 0.5 mm, 4-node fully integrated shell elements, shown in Figure 4.10. Shell elements were used as the specimens were relatively thin, making thickness effects negligible. This had the added benefits of reducing computational cost and ensuring consistency through simulations. Appropriate

symmetry boundary conditions were used as indicated and a prescribed axial velocity boundary condition was used to simulate experimental loading. The prescribed velocity was set to half the actual test bed speed, 2.5 $\mathrm{mm\,min^{-1}}$, due to symmetry conditions. The experiment was only simulated to the point of σ_{UTS} since damage models could be required to simulate further behaviour and this fell outside the scope of the project.

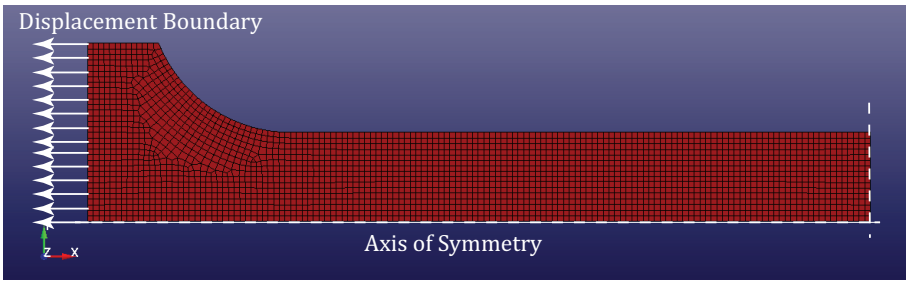

Figure 4.10: Illustration of numerical tensile test simulation.

The Al2024-T3 material was defined numerically using the Johnson-Cook material model characterized during testing. The material model, described in Equation (4.7), was implemented with the MAT_JOHNSON_COOK keyword. Initial values for A, B and N were taken from the tensile test characterisation while the values of C and M were obtained from literature.

The tensile response of the numerical specimen was obtained by measuring the nodal force values at the displacement boundary in the direction of motion. The measured response was compared to the actual tested response and the material model was altered and simulation re-run in an iterative process to determine values for A, B and N that resulted in the most accurate response. Some iterations are shown in Figure 4.11 along with the actual model and the tensile test data for comparison. The selected numerical properties for the Johnson-Cook material model are shown in Table 4.3.

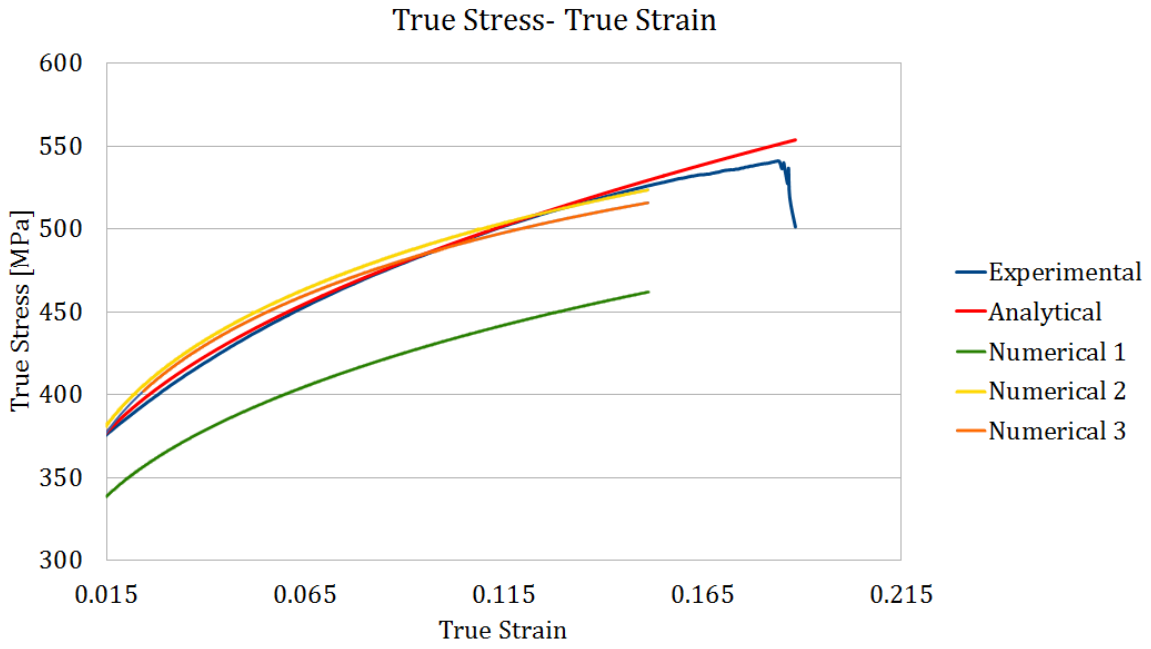

Figure 4.11: Graph showing the correlation between tensile test data and numerical simulations.

Table 4.3: Johnson-Cook material properties determined by numerical iterations.

Parameter	A	B	N	C	EPS0	M
Units	MPa	MPa	-	-	s^{-1}	-
Test Value	310	580	0.45	0.083	0.001	1

4.3 Single Leg Bend Testing

As no standards are available for Single-Leg Bend (SLB) tests, they were based on the ASTM D 7264-07 standard for Three-Point Bend (TPB) tests. The experimental procedure followed during SLB testing was proposed by Yoon and Hong [83]. Tests were performed on the Zwick Roell 1484 universal testing machine, employing the standard Three Point Bend loading head and supports, shown in Figure 4.12. Force data was captured using the built-in force transducer and the testXpert V10.11 software and stored on a personal computer.

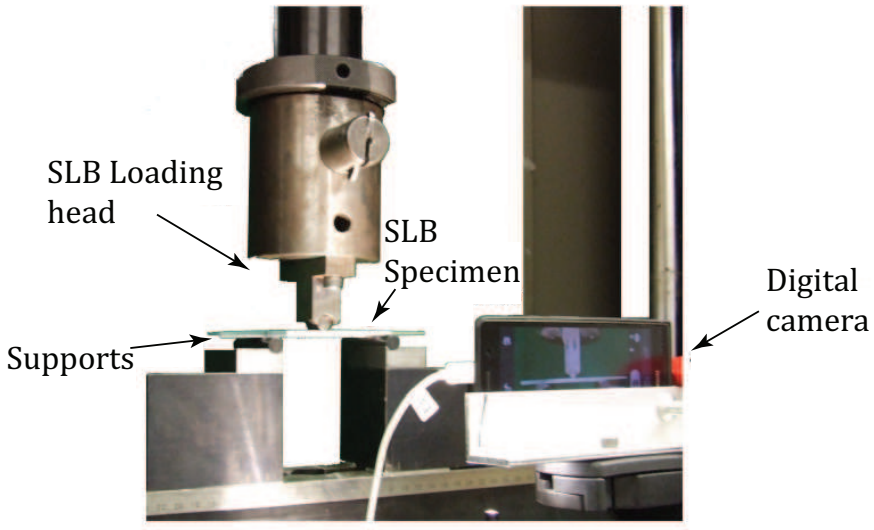

Figure 4.12: Photograph of the single leg bend test set-up.

The supports were placed a distance of 80 mm apart and offset in height by 2 mm to account for the variation in thickness of the SLB specimen layers. All specimens were marked at both the support points and in the middle to ensure accurate spacing during testing. The SLB tests consisted of two parts, namely, compliance calibration and crack propagation.

During compliance calibration, the flexure of each specimen set was determined for a given load at varying crack lengths (a). This was achieved by employing a loading protocol where the tests were ceased when a predetermined load was reached. The crack length was increased artificially by moving the specimen horizontally on the supports, increasing the distance from the right support to the crack tip. Crack lengths of 20 mm, 25 mm, 30 mm, 35 mm and 40 mm were used. As no crack initiation was allowed to take place during compliance calibration, an initial predetermined load of 40 N was used, well below the critical load for crack initiation. All compliance calibration tests were performed at a vertical crosshead speed of 1 mm min^{-1}.

Crack propagation tests were performed by loading the specimen past the point of crack initiation, continuing testing until the crack tip reached the centrally located loading head. Crack propagation tests were performed at crosshead speeds of either 1 mm min^{-1} or 2 mm min^{-1}. The test speed was slowed down after 3 tests to slow down the crack propagation rate and increase the accuracy of the photographs taken at discrete intervals. Specimen crack growth is illustrated in Figure 4.13. An external system monitored the crack growth over time visually, by taking photographs of the specimen at constant time

intervals.

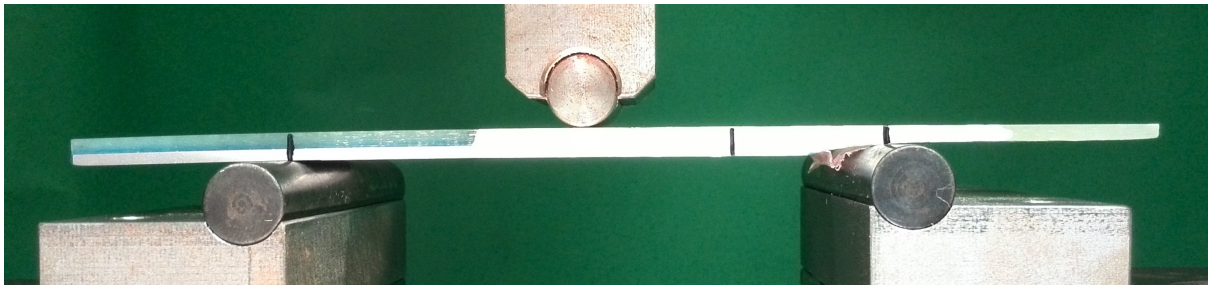

(a) Specimen before testing - crack length of 20 mm

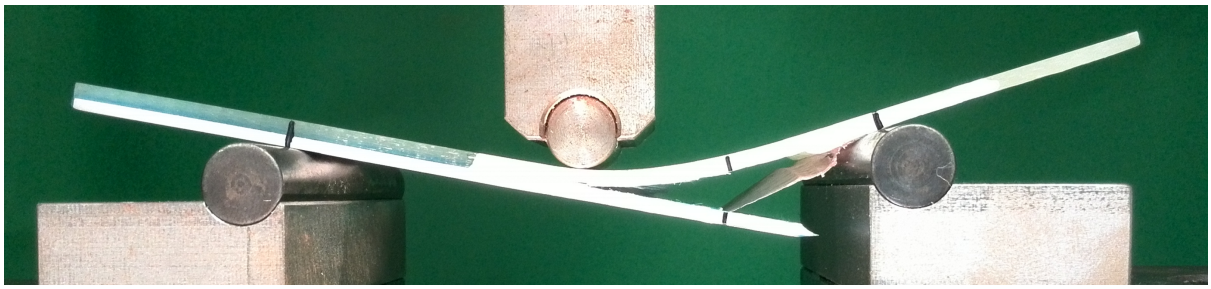

(b) Specimen after testing - crack length of 40 mm

Figure 4.13: Crack propagation during SLB testing.

4.3.1 Digital Image Data Capturing and Analysis

Digital images were used to track the growth of the induced crack between the aluminium and GFRP layers during the SLB crack propagation tests. Images were taken using a Huawei Ascend P6 digital camera phone. The camera quality was set to 8 Mega-pixel (MP), employing the high-dynamic-range (HDR) functionality which increases image detail by reproducing a greater dynamic range of luminosity. The digital camera was mounted to a tripod and placed in a central position and at a constant stand-off distance of 100 mm, well above the minimum focal distance of the camera (40 mm). Focus was maintained on the centre of the SLB specimen, in line with the loading head.

The digital camera was connected directly to a laptop computer which acted as a data capturing unit, shown in Figure 4.14. A C++ script in unison with a virtual camera trigger mobile application, ensured that images were taken at constant 3 s time intervals. All time capture data was embedded within each image. This allowed small offsets, due to electronic lag of the camera set-up, to be accounted for during analysis. The image data was stored on the digital camera and transferred to the laptop

computer after each test.

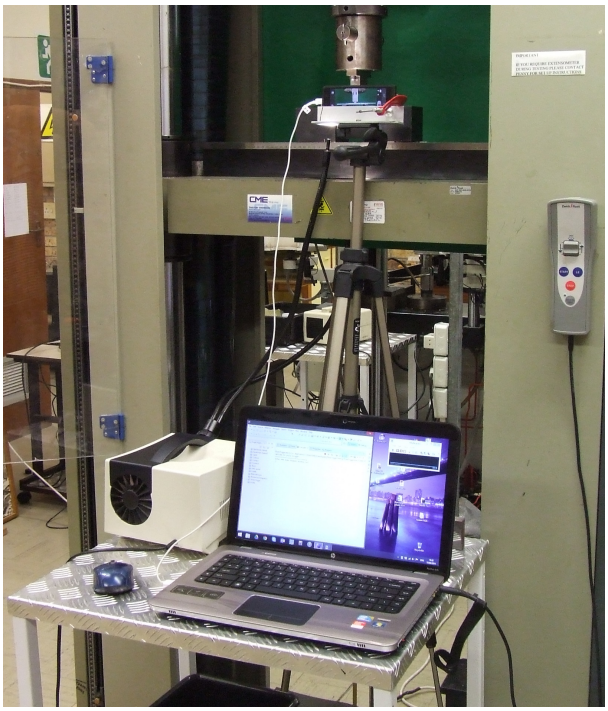

Figure 4.14: Experimental set-up of digital image data acquisition system.

The image data was analysed using a Matlab® script, to obtain the crack growth over time. The script is shown and detailed in Appendix B.1.2. The script analysed images by removing specific colour ranges. These colour ranges included background and foreground residual colours, resulting in the specimen appearing in white while all other data was blacked out. A simple pixel value count was then performed in a 10×10 pixel square box, preselected by the user, just ahead of the initial crack tip. With white pixels containing a value of 255 and black pixels a value of 0, crack length was presumed to increase when the block value dropped below a given threshold. This threshold varied between 1000 and 3000 due to minor differences in experimental lighting conditions. In cases where the crack growth could not be accurately predicted by the elementary script, the position of the crack tip was manually selected in each image. The correlation between the resultant experimental crack length and analysed crack length is illustrated in Figure 4.15. The red line illustrates the crack path as tracked by the software. The values of crack length vs time were output to a text file for further analysis.

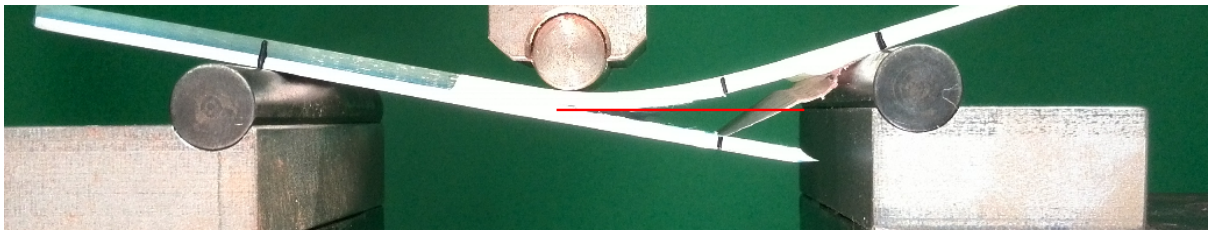

Figure 4.15: Comparison of final crack length in digital photos to numerical algorithm measurements.

4.3.2 Single Leg Bend Data Analysis

The SLB tests were used to obtain values for the mixed-mode I/II energy release rate ($G_{I/II}$) and the critical traction separation boundary conditions. The mixed-mode energy release rate could then be broken up into both G_I and G_{II} using the appropriate mode ratios. Figure 4.16 shows an illustration of the SLB geometry for analytical analysis.

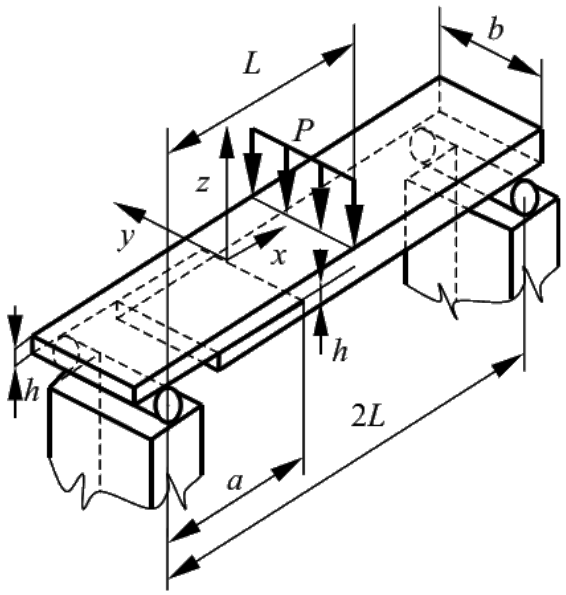

Figure 4.16: Illustration of an analytical single leg bend test configuration [84].

Equation (4.8) is known as the Irwin-Kies expression and is widely used to calculate the mixed-mode I/II energy release rate [85]. The variable P represents the force measured during crack propagation, b represents the specimen width and $\frac{\partial C}{\partial a}$, the derivative of the compliance calibration curve with regards to crack length.

$$G_{I/II} = \frac{P^2}{2b}\frac{\partial C}{\partial a} \tag{4.8}$$

From the experimental force-displacement data obtained from the compliance calibration tests, values for the compliance (C) at different crack lengths (a) were calculated using Equation (4.9).

$$C = \frac{\delta}{P} \tag{4.9}$$

A reduced third order polynomial [84], illustrated by Equation (4.10), was fitted to the calculated data points. This related specimen compliance to crack length.

$$C(a) = \frac{7a^3 + 2L^3}{8bh^3E_{11}} \tag{4.10}$$

The curve, $C(a)$, was differentiated with respect to a to obtain $\frac{\partial C}{\partial a}$. The crack growth-time curve, obtained from the digital image data capturing, was superimposed on the force-time curve, obtained during SLB testing. This resulted in the applied force as a function of crack length, $P(a)$. The function, $P(a)$, could then be combined with $\frac{\partial C}{\partial a}$ in Equation (4.8) to yield data points for the mixed-mode I/II curves. Another curve fit was then performed, using Equation (4.11), to obtain a function of $G_{I/II}$ for different crack lengths. A variety of experimental results for mode ratios are available in literature [84, 86–90]. These values are shown in Table 4.4 and were used to extract the respective values for G_I and G_{II} where comparisons were required.

$$G_{I/II}(a) = \frac{21a^2P^2}{16b^2h^3E_{11}} \tag{4.11}$$

Table 4.4: Mode ratios from i [84], ii [86, 87], iii [88], iv [89, 90], v VCCT [91]

a[mm]	20	30	40	50	60	70	
	1.676	1.557	1.500	1.465	1.443	1.427	i
	1.764	1.633	1.555	1.509	1.479	1.458	ii
	1.665	1.555	1.500	1.467	1.445	1.429	iii
	1.893	1.719	1.626	1.569	1.530	1.502	iv
	1.658	1.572	1.529	1.502	1.493	1.483	v

4.3.3 Single Leg Bend Test Results and Discussion

Single-leg bend tests were performed on three distinct sets of specimens to determine the effects of the different manufacturing techniques on interfacial bond strength. During testing, an increase in force was seen with increasing crack length in the period after stable crack growth. This section of the curve was omitted from analysis as these effects are not part of crack growth. When the crack tip reaches the central loading head, the sheets of GFRP and aluminium are simultaneously pulled apart by the crack growth mechanism and pushed together by the compressional force of the loading head. This leads to the crack tip being opened and closed simultaneously resulting in inadmissible reaction forces. This behaviour started appearing at a distance of 5 mm from the loading head. This resulted in the last 5 mm of crack propagation tests and crack growth measurements being disregarded during analysis. The full set of test data is available in Appendix B.1. Resistance of the SLB specimen interfaces to crack growth was measured using mixed Mode I/II Strain Energy Release Rate (SERR, $G_{I/II}$).

Prime 20LV Multi-Step Manufacturing SLB Tests

The initial Prime 20LV SLB specimens were manufactured using a Multi-Stage Manufacturing (MSM) technique where the Redux layer was first bonded to the aluminium and cure, then added to the GFRP layup. This layup method is discussed in detail in Section 3. Figure 4.17a shows the force - displacement curves for various crack lengths measure during compliance calibration and Figure 4.17b shows the reduced force-displacement data for the SLB specimens tested in crack propagation. In all cases de-bonding failure was observed between the Redux layer and the GFRP.

Figure 4.17a shows a steady decrease in slope with an increase in crack length. This is expected due to the difference in stiffness between the GFRP and the combined Al2024, Redux and GFRP. The force - displacement data recorded during crack propagation, Figure 4.17b, shows good correlation between the various specimens. A linear curve was fitted to each test up to the point of crack propagation. Past the point of crack propagation, a hyperbolic curve is used to achieve an accurate fit.

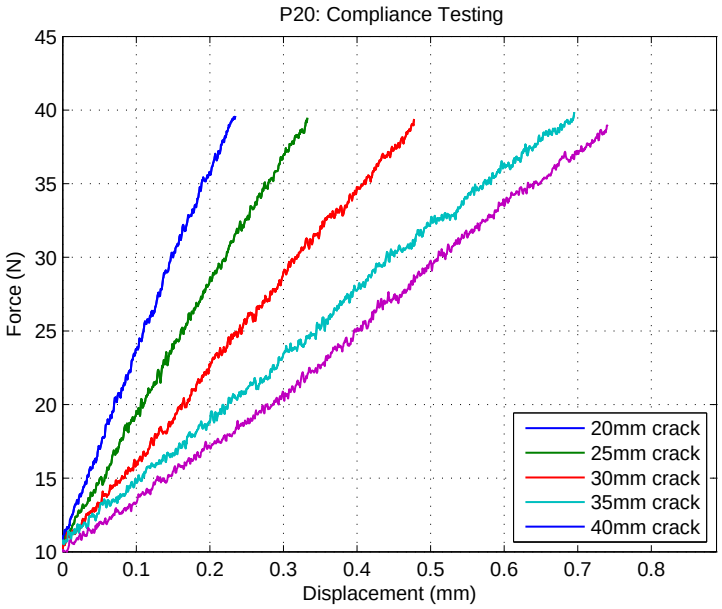

(a) Graph showing the Prime 20LV MSM compliance calibration tests.

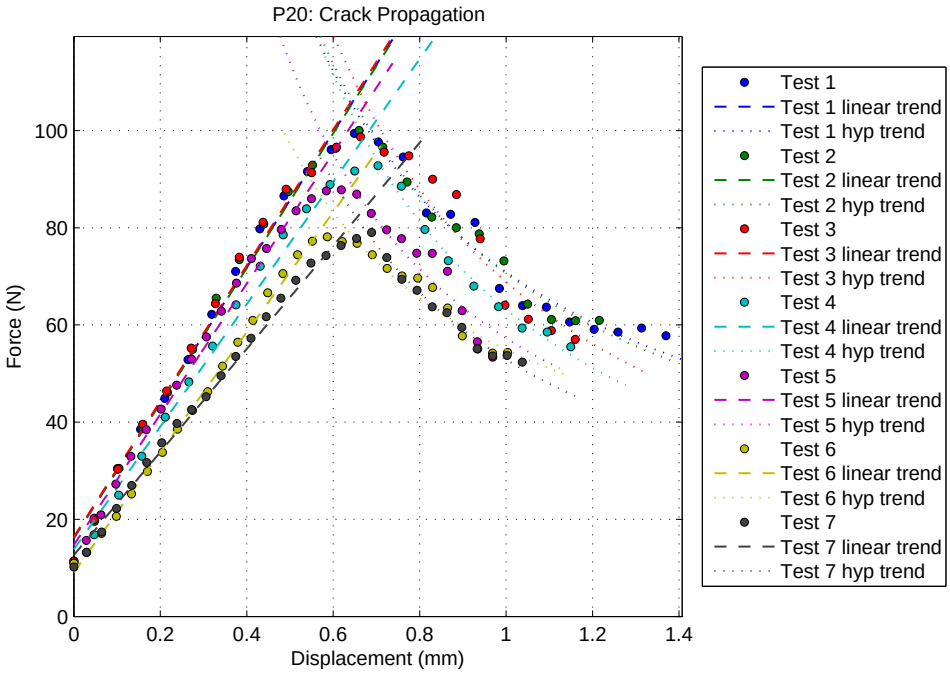

(b) Graph showing the Prime 20LV MSM crack propagation force vs displacement.

Figure 4.17: Graphs showing the experimentally captured data of the Prime 20LV MSM specimens.

The compliance, $\frac{\delta}{P}$, was plotted against crack length, obtaining a set of distinct data points, shown in Figure 4.18. As described in Section 4.3.2, a reduced third order

polynomial was fitted to this set of data points, obtaining the illustrated curve. As expected, the compliance increases with increasing crack length.

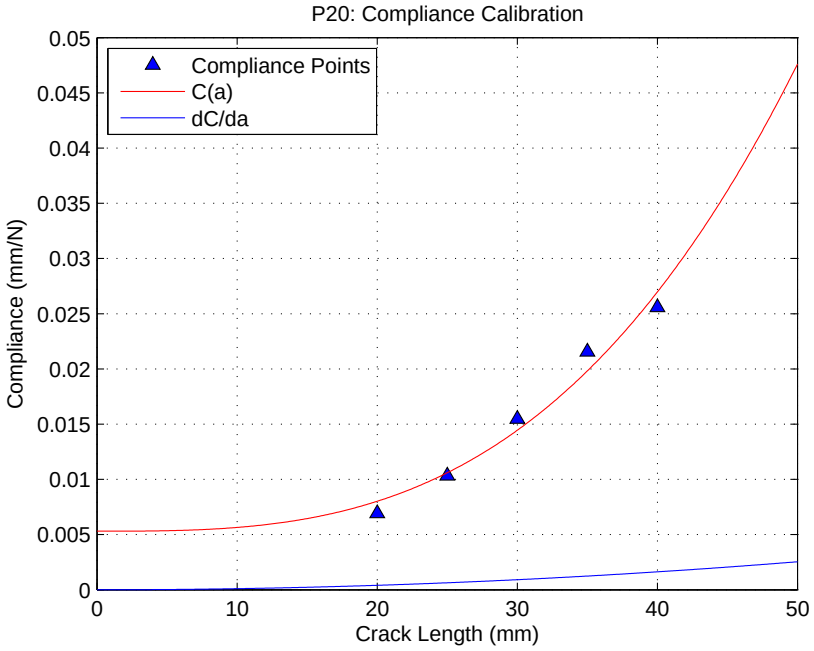

Figure 4.18: Graph showing the Prime 20LV MSM compliance calibration curve.

The Prime 20LV MSM crack growth rate data recorded from the digital image analysis is shown by the data markers in Figure 4.19 in reduced format. A linear trend curve was fitted to the data. In this specific data set, crack propagation tests number 1 through 4 were performed at 1 mm min^{-1} while tests 5 through 7 were performed at 2 mm min^{-1}.

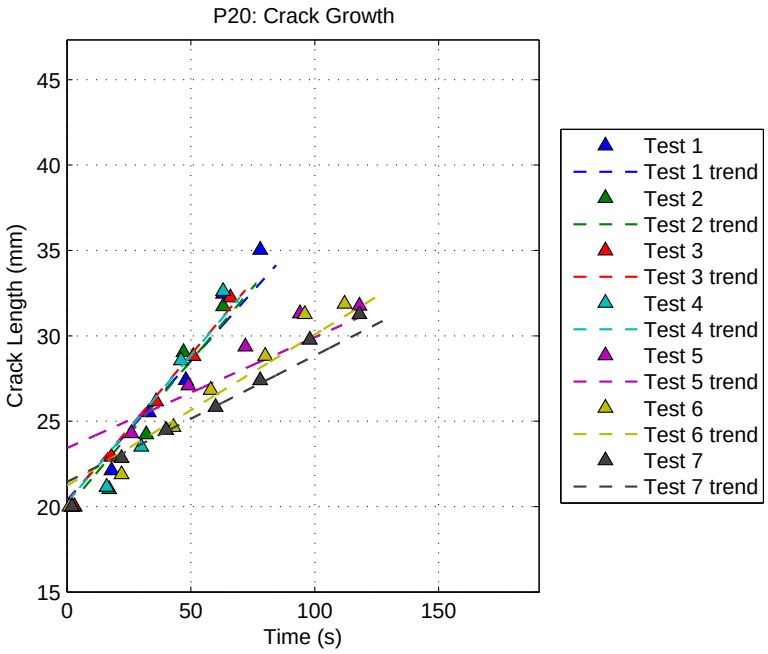

Figure 4.19: Graph showing the Prime 20LV MSM data capture crack growth curve.

Superimposing the crack growth over time from the point of crack initiation, resulted in a curve depicting the force at every respective crack length. These values were then used with the compliance calibration curves to generate the mixed mode I/II strain energy release rate, $G_{I/II}$, shown in Figure 4.20. The data shows little overall variation in $G_{I/II}$ for the respective tests. It is noted that despite being tested at varying crosshead speeds, the energy release rate for all tests remain constant, varying from the mean by no more than 15 $\mathrm{J\,m^{-2}}$. In all cases, it was found that failure took place between the layer of Redux 609 and the GFRP indicating consistent failure behaviour at the aluminium - GFRP interface. For the purpose of the SLB tests, this was defined as Failure I.

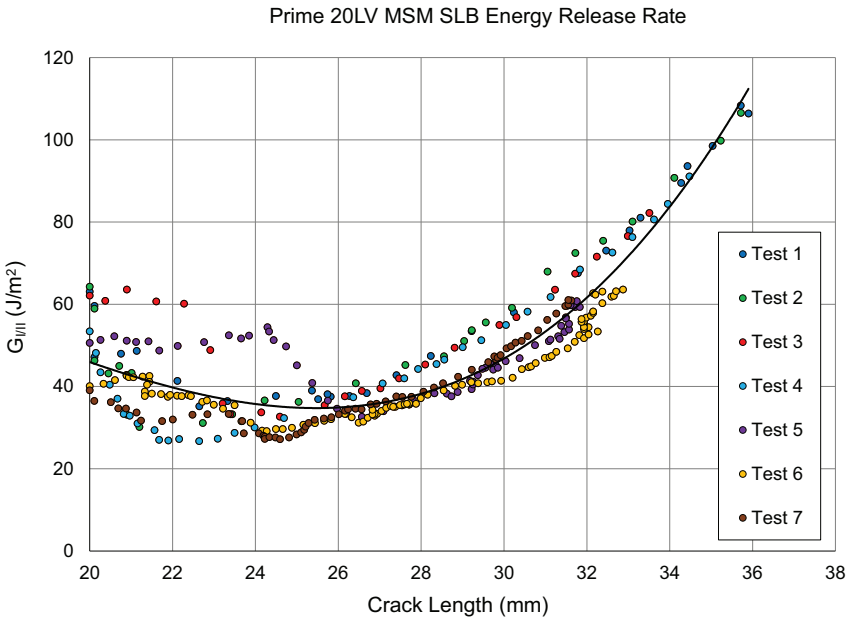

Figure 4.20: Graph showing the Prime 20LV MSM energy release rates.

Table 4.5 shows the energy release rates for the Prime 20LV specimens at various crack lengths. The data shows consistent averages with little variation in minimum and maximum values.

Table 4.5: Energy release rates of the Prime 20LV MSM specimens at various crack lengths. (Units measured in J/m^2)

	Prime 20LV MSM Failure I		
Crack length (mm)	20	30	35
Average Measured $G_{I/II}$	60	60	85
Max $G_{I/II}$	64	73	108
Min $G_{I/II}$	53	44	62

Prime 20LV Single-Stage Manufacturing SLB

In an effort to further improve the Redux 609 bond as well as decrease manufacturing times, the Prime 20LV was laid up using a Single-Step Manufacturing (SSM) process, discussed in Section 3. The single-step manufactured (SSM) specimens' force-displacement curves for both compliance calibration and crack propagation are shown in Figures 4.21a and 4.21b respectively.

The Prime 20LV SSM also shows a decreasing slope for an increasing crack length. The force displacement data for the Prime 20LV SSM during crack propagation, Figure 4.21b, show inconsistent crack initiation forces leading to inconsistent crack propagation force. These forces vary between 170 N and 300 N. As before, a linear curve was fitted to each test up to the point of crack propagation. Past the point of crack propagation, a hyperbolic curve is used to achieve an accurate fit. This was done to indicate and compare the trends of all tests. From the data is can be seen that tests 2 and 7 show good correlating and tests 3, 4 and 6 show relatively good correlation. Tests 1 and 5, however, behave like outliers, not correlation to one another or the other data. This behaviour is further discussed and compared at the end of this section.

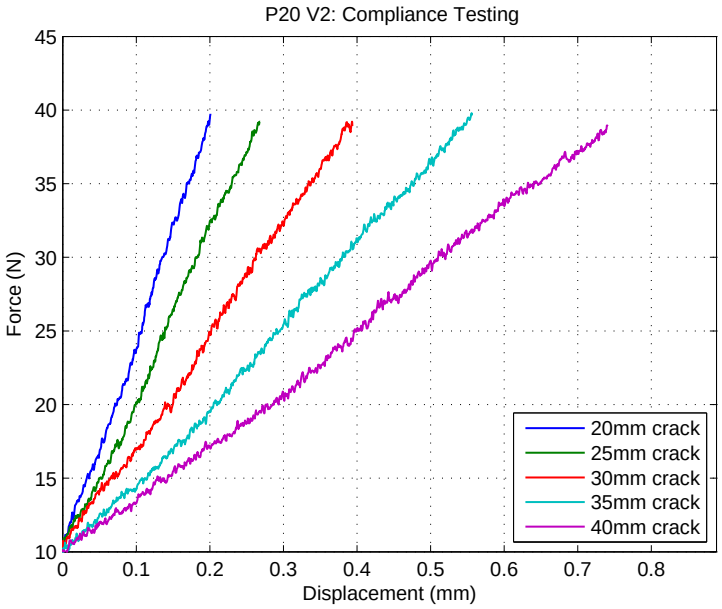

(a) Graph showing the Prime 20LV SSM compliance calibration tests.

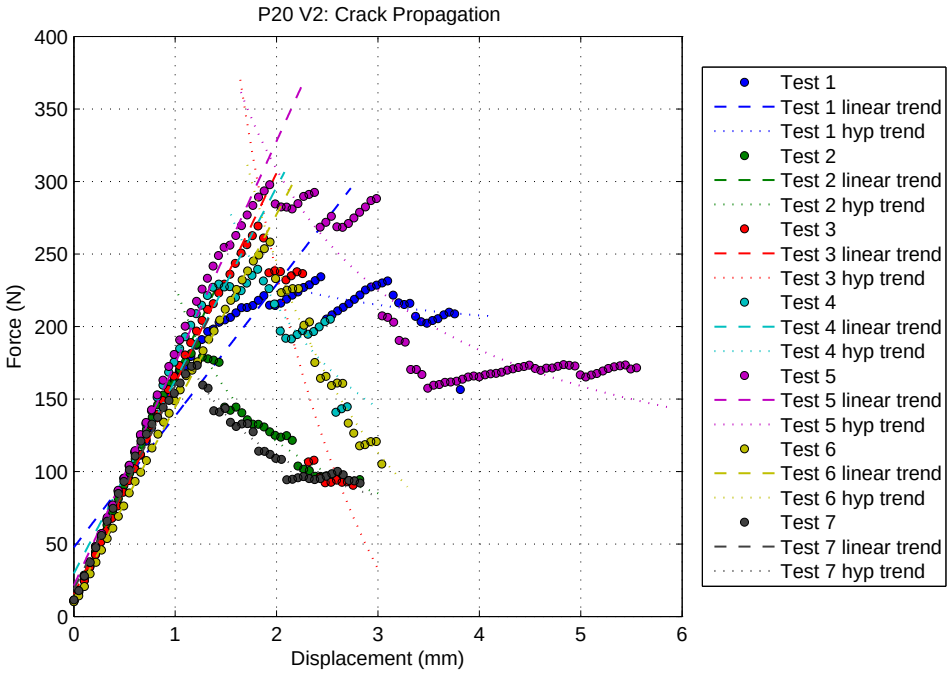

(b) Graph showing the Prime 20LV SSM crack propagation force vs displacement.

Figure 4.21: Graphs showing the experimentally captured data of the Prime 20LV SSM specimens.

The compliance calibration data and third order polynomial curve fit for the Prime 20LV SSM are shown in Figure 4.22. All the data points show good correlation with the curve

fit.

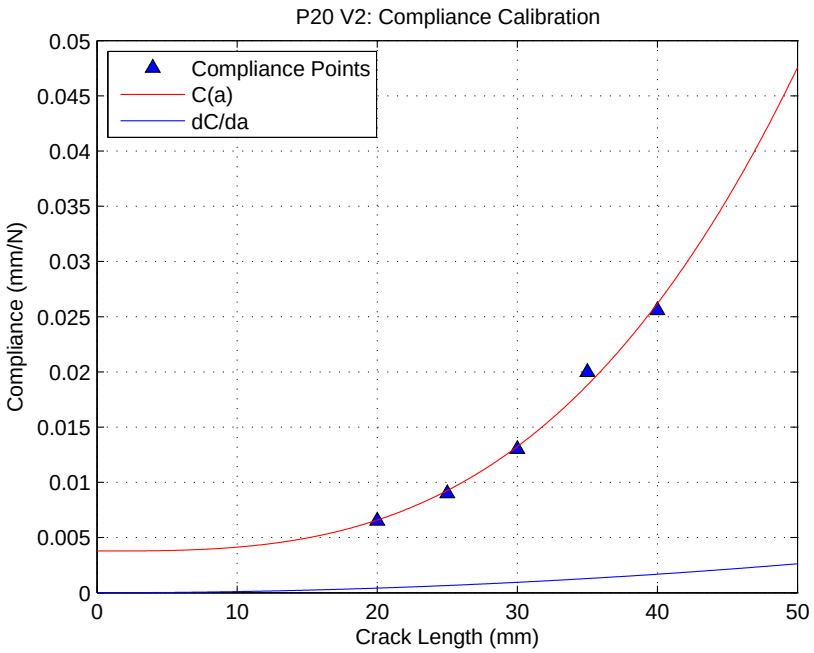

Figure 4.22: Graph showing the Prime 20LV SSM compliance calibration curve.

Figure 4.23 details the crack growth over time measured by the digital image data capturing system. The Prime 20LV SSM SLB tests exhibited inconsistent crack growth behaviour indicating that the manufacturing process had a definite effect on the aluminium - GFRP bond.

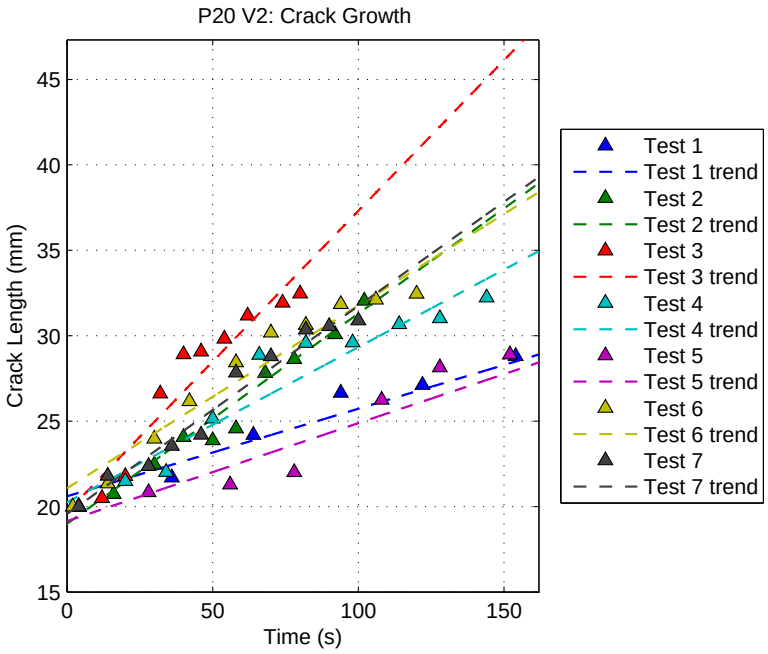

Figure 4.23: Graph showing the Prime 20LV SSM data capture crack growth curve.

The energy release rates for the Prime 20LV SSM are shown in Figure 4.24. Trends from the force - displacement data, shown in Figure 4.23, are also evident in the strain energy release rates for the respective specimens, shown in Figure 4.24. The data shows a correlation between tests 2, 3 and 7 at the lower end of the spectrum while tests 4 and 6 correlate to form the midrange. Tests 1 and 5 were initially regarded as two separate outliers when considering the crack propagation data. These two tests, however, showed reasonable correlation with one another to result in the higher energy release rates seen in Figure 4.24. Similar to the force - displacement data from the crack propagation tests, significant deviation was observed between the energy release rates of the various specimens.

Closer examination revealed that there was a variation in failure mode during tests. Test specimens 2, 3, 4, 6 and 7 showed similar crack propagation mechanisms with the Redux layer consistently debonding from the aluminium interface, defined as Failure II for these tests. This differs from the Failure I behaviour seen in the MSM SLB specimens where the Redux debonded from the GFRP layer, indicating that the SSM process influences the bond strength of the Redux to both the aluminium and GFRP layers. Test specimens 1 and 5 showed further variation in the mode of crack propagation when it was observed that the Redux layer debonded from both surfaces during testing, defined as Failure III. Patches of Redux remained on both the aluminium and GFRP surfaces of these specimens after testing. This behaviour further

illustrates the sensitivity of the Redux layer and interfacial bond strength to the various manufacturing processes.

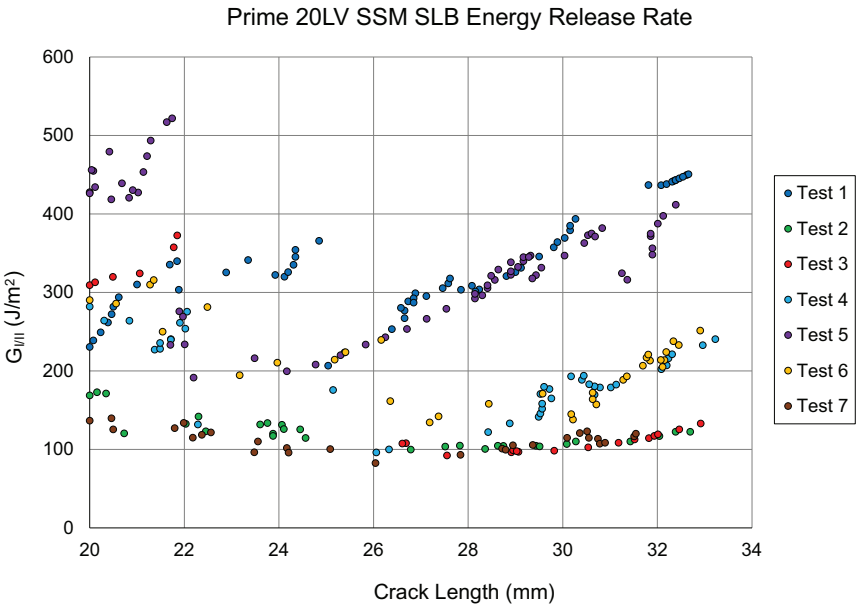

Figure 4.24: Graph showing the Prime 20LV SSM energy releases.

The energy release rates of the SSM SLB tests were further grouped and analysed according to the different failure modes seen during testing, shown in Figure 4.25a and 4.25b.

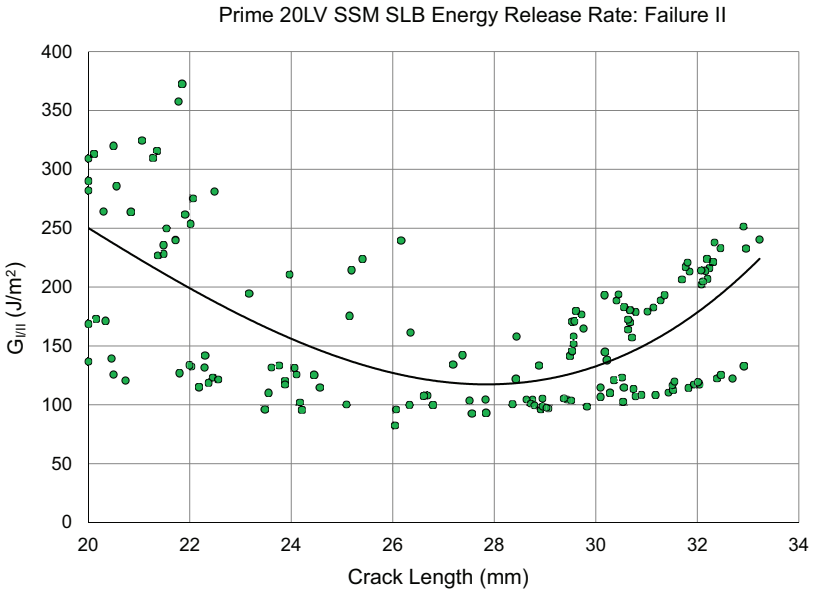

(a) Graph showing the release rates of specimens Prime 20LV SSM energy 2, 3, 4, 6 and 7.

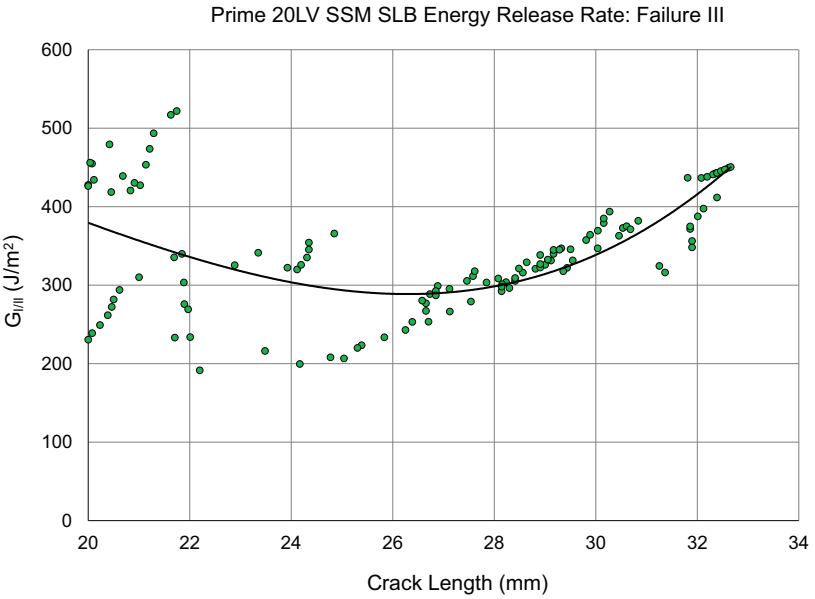

(b) Graph showing the energy release rates of Prime 20LV SSM specimens 1 and 5.

Figure 4.25: Graphs showing the average energy release rates of Prime 20LV SSM specimens for the defined failures

Table 4.6 shows the energy release rates for the Prime 20LV SSM specimens at various crack lengths. Specimens that exhibited both Failure II and III showed considerable scatter in data at crack lengths below 26 mm. Failure II consistently showed the lowest

average SERR and continued to exhibit considerable scatter in test data at crack lengths longer than 26 mm. Failure III proved to be the mode with a higher SERR of the two and exhibited more consistency in the data at crack lengths above 26 mm. Both Failure II and III showed increases in SERR for crack lengths increasing beyond 26 mm.

Table 4.6: Energy release rates of the Prime 20LV SSM specimens at various crack lengths. (Units measured in J/m^2)

	Prime 20LV SSM Failure II		Prime 20LV SSM Failure III	
Crack length (mm)	20	30	20	30
Average Measured $G_{I/II}$	237	152	329	364
Max $G_{I/II}$	309	213	427	386
Min $G_{I/II}$	136	107	136	350

SE 84LV SLB

The SE 84LV specimens were manufactured using a single step layup and cure process discussed in Section 3. The force - displacement curves for both compliance testing and crack propagation are shown in Figures 4.26a and 4.26b respectively.

The SE 84LV specimens showed a consistent decrease in slope for an increasing crack length, during compliance calibration tests, Figure 4.26a. Consistent force - displacement data and crack initiation force were also observed during crack propagation tests. The minimum and maximum crack initiation point shows a variation as large as 100 N. This variation seems large when considering the force data of the Prime 20LV specimens, however, it makes up a much smaller fraction of the average crack initiation force measured from the SE 82LV series. A consistent linear curve was fit to the initial portion of the force displacement data followed by consistent hyperbolic curve fits during the portions of crack propagation.

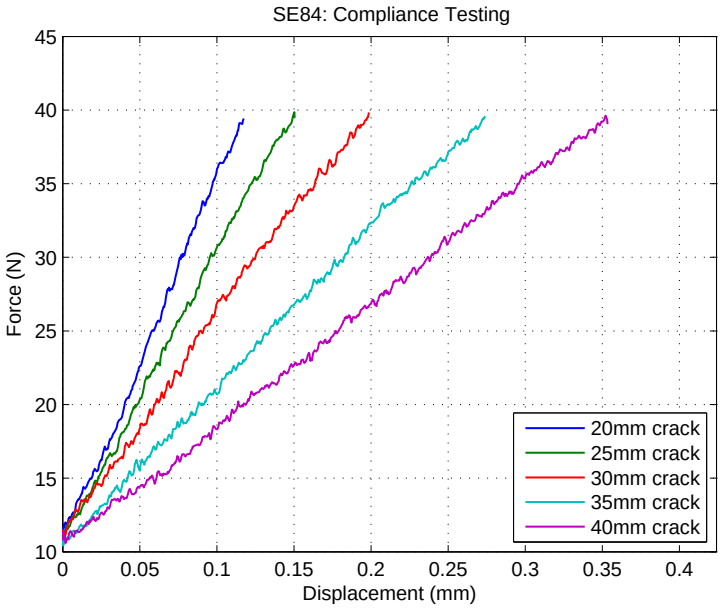

(a) Graph showing the SE 84LV compliance calibration tests.

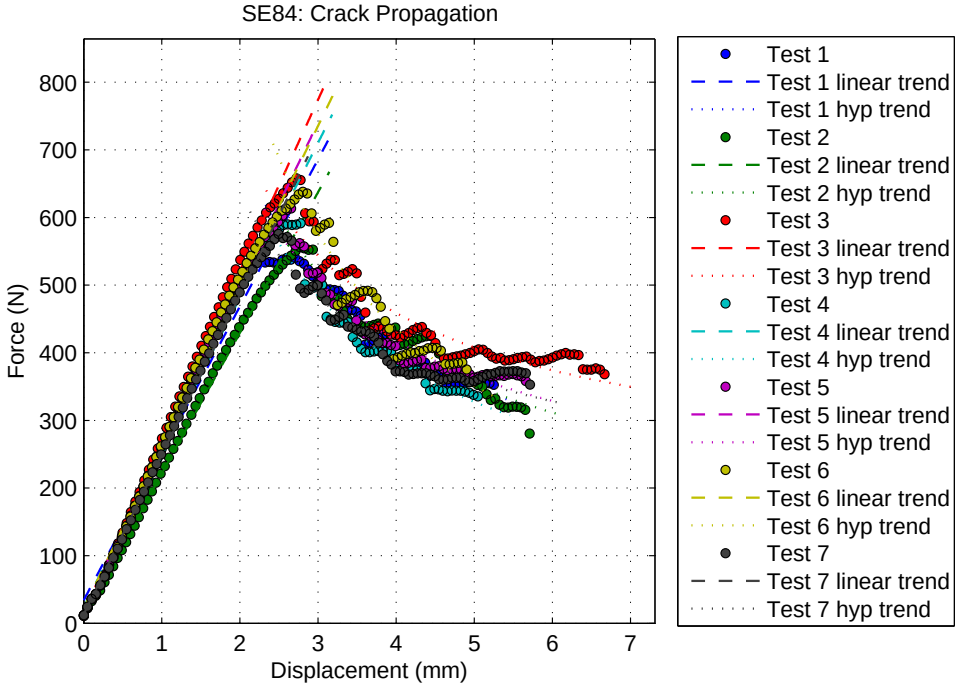

(b) Graph showing the SE 84LV crack propagation force vs displacement.

Figure 4.26: Graphs showing the experimentally captured data of the SE 84LV SLB specimens.

The compliance data points calculated for the SE 84LV based specimens as well as the 3^{rd} order polynomial curve fit is shown in Figure 4.27. All data points show a close correlation with the curve fit.

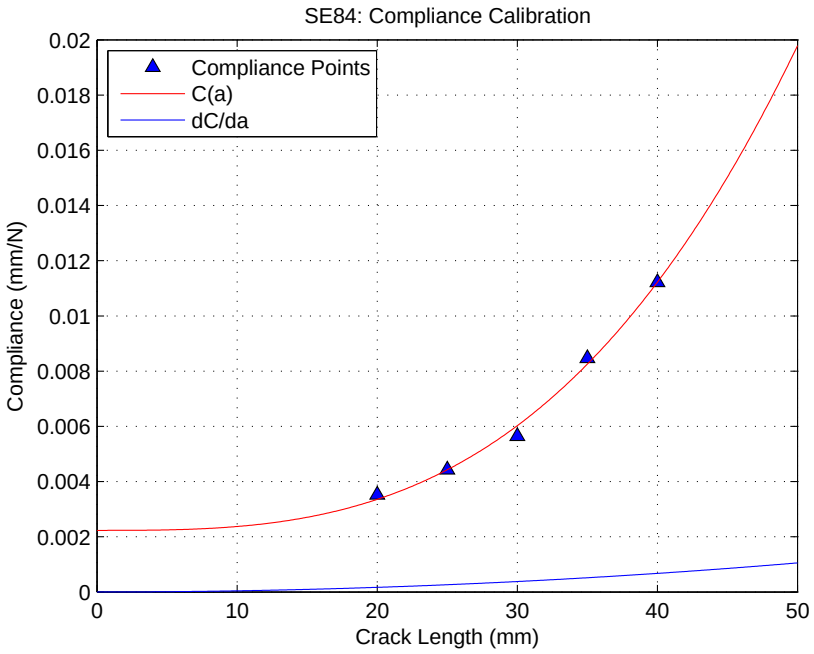

Figure 4.27: Graph showing the SE 84LV compliance calibration curve.

Figure 4.28 shows the crack growth rate for the SE 84LV tests. Very consistent crack growth was observed for all tests. Linear curves could accurately approximate the crack growth over time.

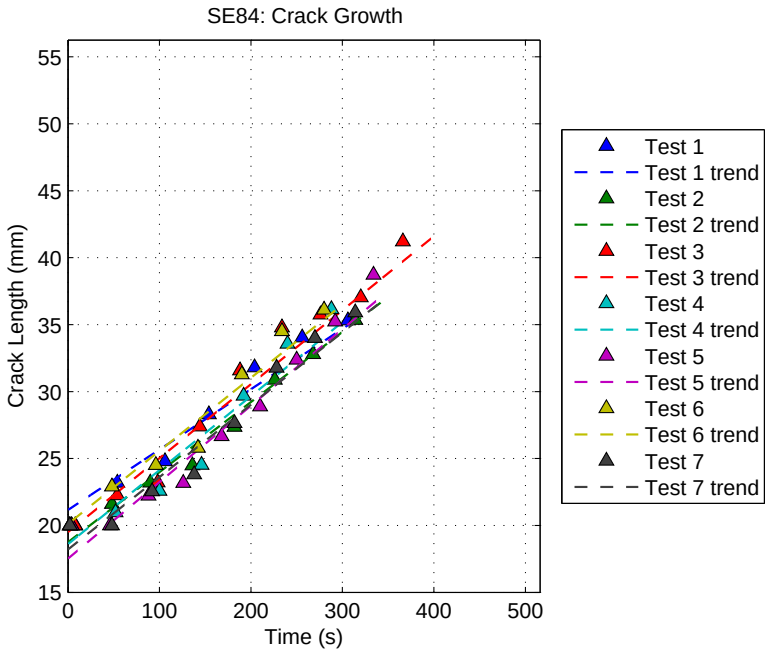

Figure 4.28: Graph showing the SE 84LV data capture crack growth curve.

The strain energy release rates, $G_{I/II}$, calculated for the SE 84LV tests are shown in Figure 4.29. The data showed great initial variation between tests while energy release rate values at crack lengths above 25 mm were grouped much closer together. Closer inspection of the specimens revealed three different crack propagation mechanisms at work at the aluminium - GFRP interface. Specimens 4, 5 and 7 exhibited similar (Failure III) crack propagation behaviour as specimens 1 and 5 from the Prime 20 SSM tests with the Redux debonding from both the aluminium and GFRP interfaces. Specimens 1, 3 and 6 showed similar crack propagation behaviour to specimens 4, 5 and 7 with the addition of composite delamination occurring at the top surface of the composite in small sections of the crack-affected zone, defined as Failure IV. This indicates that the bond strength achieved with the SE 84LV SLB specimens approach the inter-laminar bond strength of the composite material. Specimen 2 was an outlier of the test set, showing initial signs of delamination but resulting in crack propagation where the Redux debonded from the GFRP interface. This behaviour explains the initial increase in $G_{I/II}$, followed by a large decrease and lower final energy release rate.

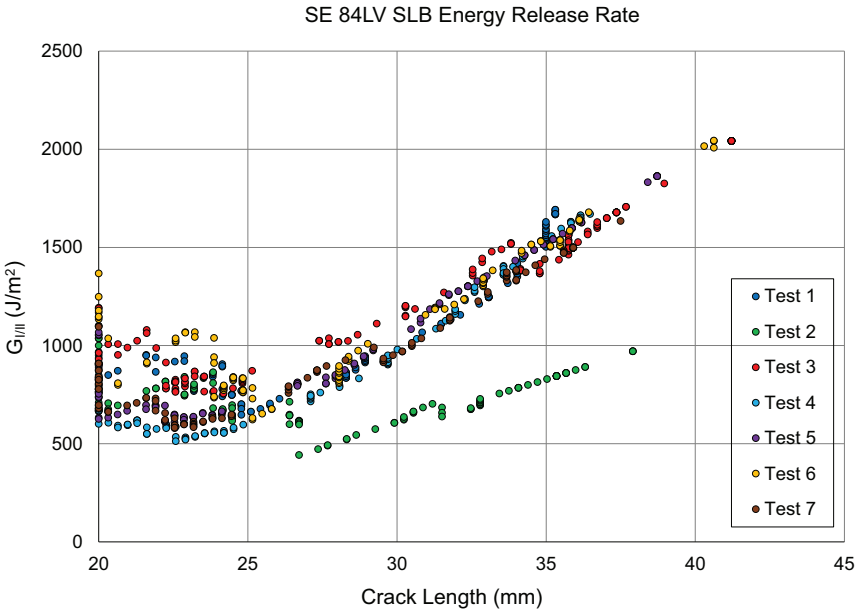

Figure 4.29: Graph showing the SE 84LV energy release rates.

The energy release rates for the two main crack propagation mechanisms in the SE 84LV specimens are shown in Figures 4.30a and 4.30b respectively. The specimens undergoing some form of delamination showed only an initial increase in $G_{I/II}$ followed by consistent crack growth, driven by debonding from both the aluminium and GFRP interfaces.

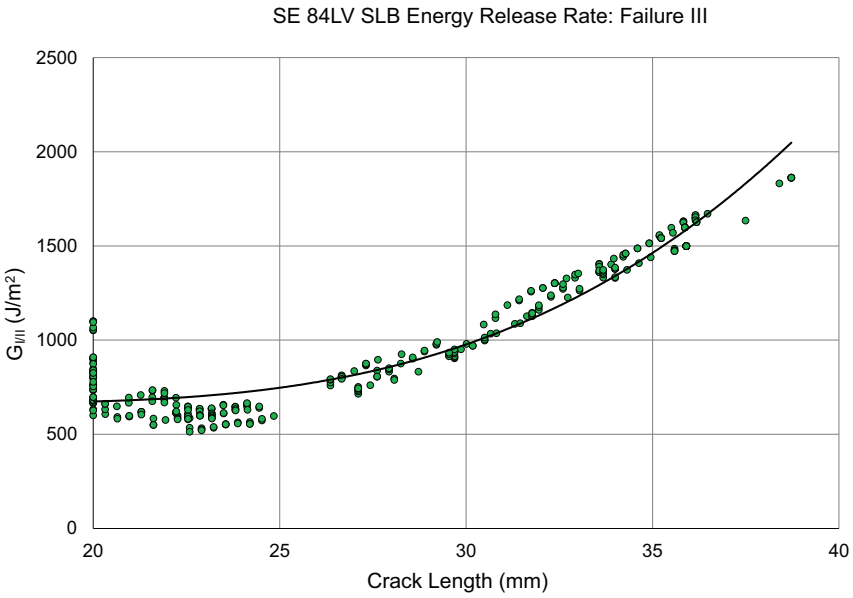

(a) Graph showing the average energy release rates of SE 84LV specimens 4, 5 and 7.

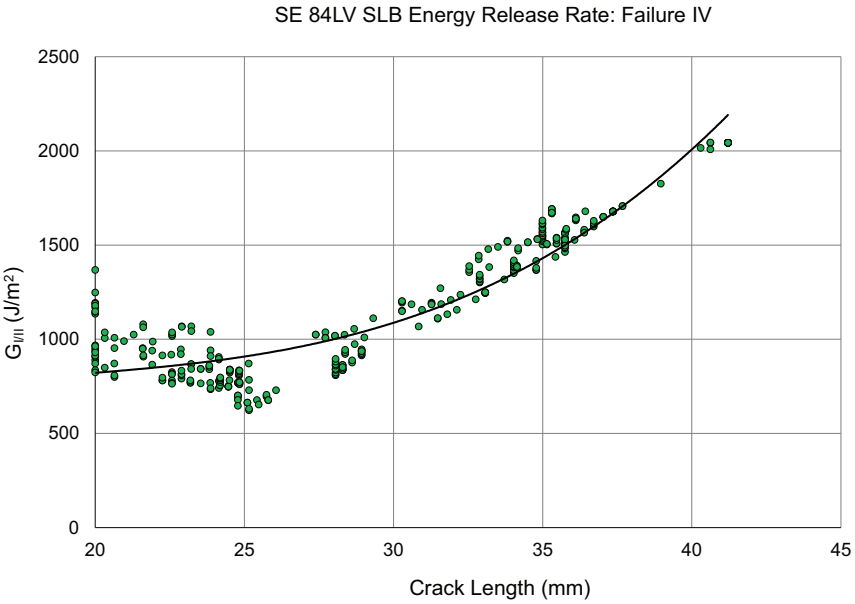

(b) Graph showing the average energy release rates of SE 84LV specimens 1, 3 and 6.

Figure 4.30: Graphs showing the average energy release rates of SE 84LV specimens for the defined failures.

Table 4.7 shows the energy release rates for the SE 84LV specimens at various crack lengths. Failure III showed the greatest increase in SERR with increasing crack length. The most consistent increases SERR was observed with Failure IV, however, this mode

also showed the greatest variation in SERR values due to the presence of delamination.

Table 4.7: Energy release rates of the SE 84LV specimens at various crack lengths. (Units measured in J/m^2)

	SE84 Failure III			SE84 Failure IV		
Crack length (mm)	20	30	35	20	30	35
Average Measured $G_{I/II}$	994	982	1494	1176	1073	1483
Max $G_{I/II}$	1101	1086	1624	1368	1271	1539
Min $G_{I/II}$	828	908	1373	967	940	1407

Comparisons to Literature

Table 4.8 shows compares the experimental critical SERR values to each other, to that of woven E-glass/epoxy composites and to GLARE®, reported by [92]. The critical SERR values calculated at crack initiation (a = 20 mm). The mixed Mode I/II failure was decomposed into Mode I and II respectively using mode ratios for SLB specimens available in the literature [86–90], shown in Table 4.4.

Table 4.8: Critical Strain Energy Release Rates of SLB tests compared to literature [92, 93].

Units	Average Measured $G_{I/II}$ J/m^2	Calculated G_I J/m^2	Calculated G_{II} J/m^2
SE 84LV SLB (Failure III)	994	368	625
SE 84LV SLB (Failure IV)	1176	435	740
P20 SSM SLB (Failure II)	237	88	149
P20 SSM SLB (Failure III)	329	121	207
P20 MSM SLB (Failure I)	60	22	38
Woven glass/Epoxy [93]		450 ±200	1400
GLARE Al/GFRP [92]	-	3067	-
GLARE GFRP 0°/90° [92]	-	3545	-

The data indicates that Failure IV occurred at the highest critical SERR, closely followed by Failure III of the SE 84LV specimens. Failure IV suggested that the critical

SERR of the bond between the aluminium and GFRP layers approached that of the GFRP laminates. This is further seen when comparing the measured experimental values to those of woven E-glass/epoxy composites available in literature [93], shown in Table 4.8. Similar critical SERRs are seen for the initiation of Mode I failure, indicating that the bond strength between the GFRP and aluminium for Mode I failure is similar to that of the GFRP laminates. Failure III in the Prime 20LV SSM specimens showed a far lower critical SERR than that observed for similar failure in the SE 84LV. Failure II was the most consistent failure mode in the Prime 20LV SSM specimens. Only Prime 20LV MSM specimens experienced Failure I which appeared to be the failure mode initiated by the lowest average critical SERR. The SSM process thus also resulted in an increase of bond strength.

None of the specimens showed critical SERR values close to that of GLARE® reported in literature [92]. It was noted, however, that Mode I critical SERR at the GFRP-aluminium interface of GLARE® was relatively similar to that of the UD-GFRP laminate. These results are similar to those seen in the SE 84LV specimens, which may result in similar responses to blast loading conditions.

This page has been intentionally left blank.

Chapter 5

Experimental Design Using Numerical Simulations

In order to obtain a suitable range of charge masses and experimental conditions, a numerical model of the FMLs was constructed and analysed using the LS-DYNA finite element code. Only FMLs manufactured using the SE 84LV prepreg (PPW series) were simulated. Their superior bond strength, observed in SLB tests, allowed the simulation of the entire FML panel as a single part with reasonable accuracy. This section details the generation of numerical blast models for both localised and uniform blast loading in LS-DYNA for the PPW FML panels, which were then used to develop the blast experimental matrix.

5.1 General Numerical Model Formulation

FML panels with clamped boundaries and a 200 mm $\times$ 200 mm exposed area were subjected to a simulated blast load using similar techniques to previous BISRU researchers [19, 82]. An Arbitrary-Lagrangian-Eulerian (ALE) mesh was used to define the air and PE4 explosives. The FML and all rigid components were modelled using a Lagrangian mesh definition. The PPW FMLs were chosen for simulations on the basis of the SLB test results. Since the prepreg SLB specimens showed exceptional interfacial bond strength with the aluminium layer, the FML was modelled as a composite part consisting of two different materials.

5.1.1 Model Geometry and Symmetry

The Lagrangian FML model was placed within the ALE air and explosive domains as shown in Figure 5.1. A multi-material group formulation for the ALE ensured that material definitions for both air and PE4 could be incorporated, and allowed for a greater measure of customization and control over the explosive conditions than other options in LS-DYNA. It also allowed for greater interaction to take place between the structure, air and explosive material. The FML panels, air and explosive were all modelled using quarter symmetry conditions, similar to work done by other researchers [82,94,95] on the blast modelling of composites.

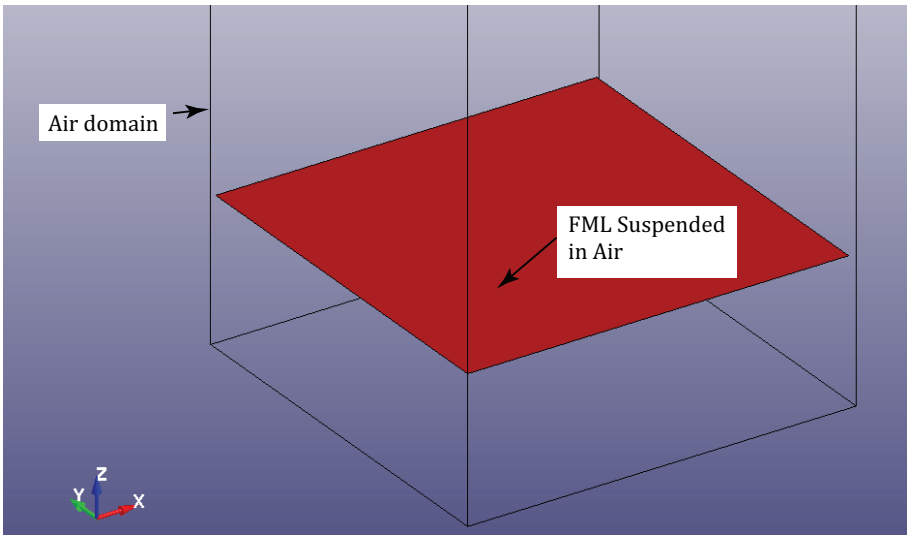

Figure 5.1: 3D View of the Lagrangian plate domain in the ALE domain.

5.1.2 Air Domain

The air domain was largest of the three main components and was approximated numerically using an Eulerian element description. An air mesh was generated using solid brick elements with a constant element size of 2 mm, determined from mesh convergence studies. The air domain was modelled up to the clamped boundary, resulting in a 100 mm $\times$ 100 mm mesh in each of the x and y axes. The height of the air mesh in the z-axis was sized to match the respective experiment being simulated. The height was modelled as the respective standoff distances of the PE4 with 50 mm added to account for explosive height, panel thickness and panel deformation. The air meshes for both localised and uniform loading is shown in Figure 5.2.

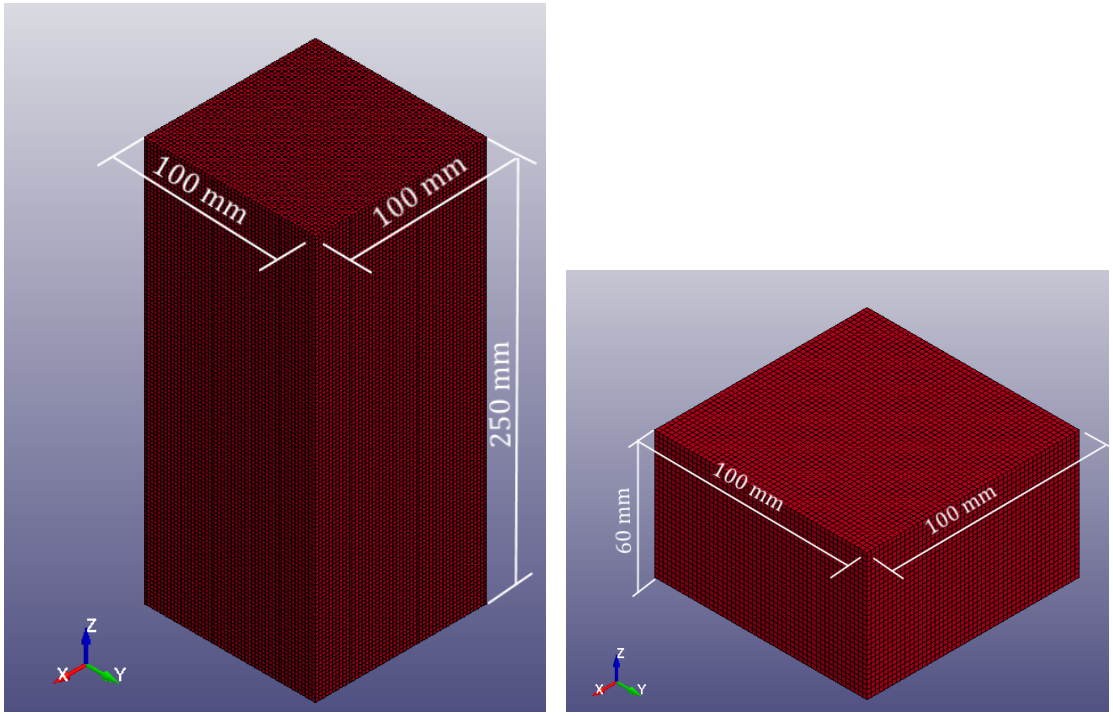

(a) Uniform blast loading air domain (b) Localised blast loading air domain

Figure 5.2: 3D Views of the LS-DYNA Uniform and Localised Solid ALE Air Domain

5.1.3 Plastic Explosive Domain

A section of the air domain was defined as PE4 using the ALE multi-material formulation. A pseudo part was created to contain all the PE4 formulations, and explosive charge was defined as part of the ALE domain through the initial volume fraction keyword. A standard charge diameter of 25 mm was used for localised loading and 40 mm for uniform loading conditions. The PE4 part definition was applied to this volume fraction geometry, effectively transforming all existing encased elements into PE4, illustrated in Figure 5.3. In order to activate the PE4 material, a virtual detonation point was placed in the centre of the PE4 cylinder, a distance of 5 mm from the top in order to simulate the inclusion of the experimental detonator.

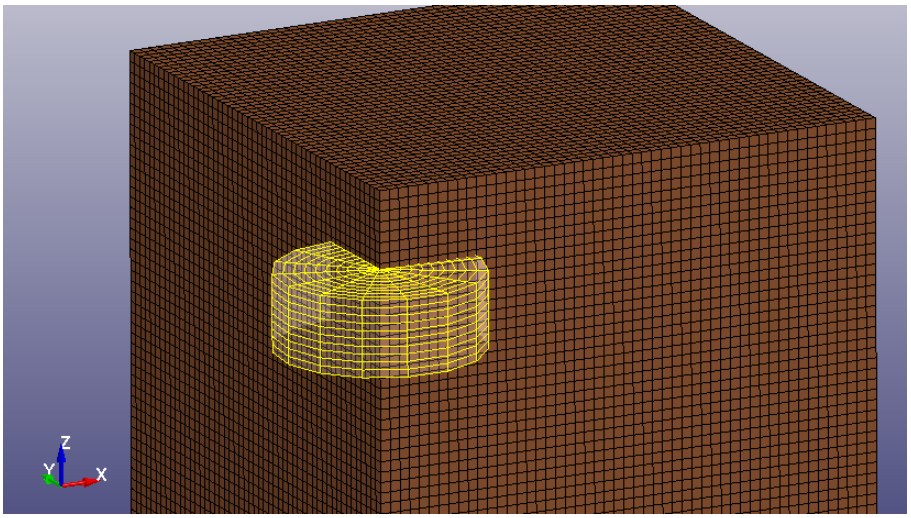

Figure 5.3: LS-DYNA Plastic Explosive Domain

5.1.4 FML Panel Formulation

The FML panel domain was modelled using the composite part definition to simulate a single layer of fully integrated shell elements as a combination of different materials, using user defined integration points. Shell elements were chosen as they exhibit good results under bending, prove stable under impulsive loading and do not require the addition of an equation of state (EOS) when being subjected to blast loading. A single integration point was defined in the centre of each constitutive layer of the FML. The panel element mesh and user defined integration points are illustrated in Figure 5.4. The thickness of the Redux layer was accounted for by increasing the thickness of the composite layers of the simulated panel. The panel was only simulated up to the clamped boundary to reduce computational cost.

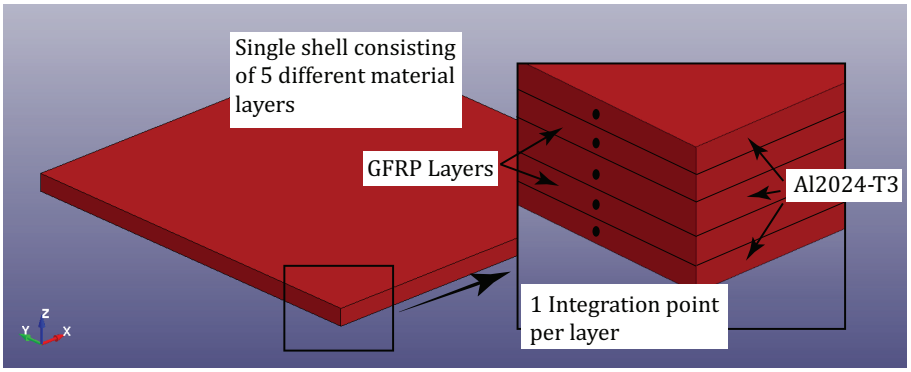

Figure 5.4: Illustration of the FML plate domain

To capture the explosive impingement on the FML, elements of the Lagrangian mesh were connected to elements in the ALE mesh using a predetermined number of coupling points [81]. Leakage [19, 81, 82] entails elements of the explosive domain passing through the plate mesh upon contact, illustrated in Figure 5.5. This was controlled by careful selection of LS-DYNA variables such as MCOUP variable, ALE-Lagrange mesh ratios and element unit normal definitions [19,81,82]. The method employed here was also used successfully by both Ozinsky [19] and Geretto [82] to prevent non-physical leakage effects. An element size ratio between the air and plate mesh of 1:2 was used to minimizing the likelihood of leakage while maintaining numerical accuracy [81].

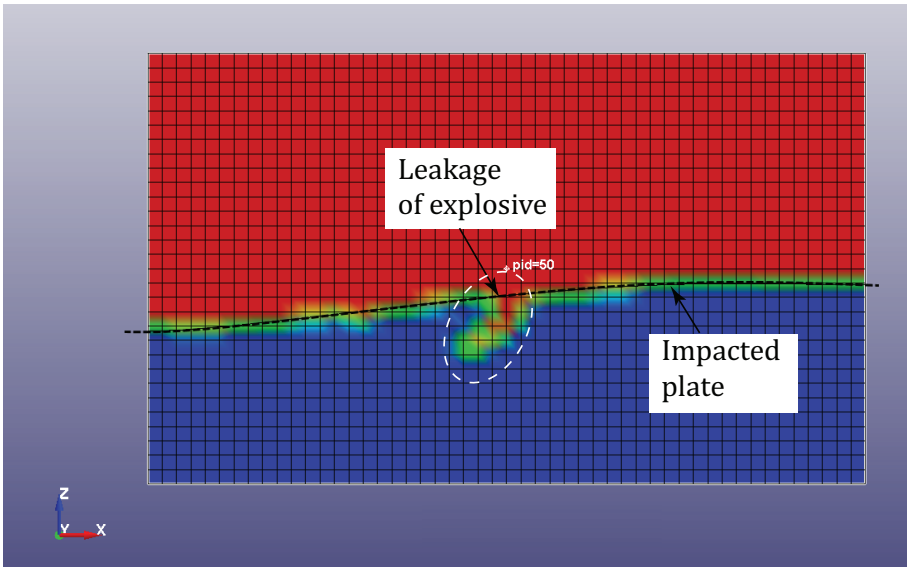

Figure 5.5: Illustration of leakage

5.2 Material Model and Equation of State Configurations

5.2.1 Explosive Material Definition

The detonation of explosive materials was defined using the MAT_HIGH_EXPLOSIVE_BURN keyword and the properties of C4 which are widely documented [19, 82]. The minimum parameters required are the detonation velocity (D), material density (ρ) and the Chapman-Jouget pressure (PCJ).

The Jones-Wilkins-Lee (JWL) EOS, Equation (5.1), was used to describe the detonation products of explosives. This equation describes the relationship between pressure P,

Table 5.1: High explosive burn material and JWL EOS parameters

ρ_0 kg/m^3	D m/s	P_{CJ} GPa	A GPa	B GPa	R_1 -	R_2 -	ω -	E_0 GJ/m^3
1601	8193	28	609.77	12.95	4.5	1.4	0.25	9

volume ratio V and E, the energy per unit volume [81]. The remaining parameters (R_1, R_2, B and ω) need to be calibrated for the specific explosive material. The calibrated values for C4 were obtained from the LLNL handbook [19] and shown in Table 5.1, using the nomenclature of LS-DYNA to denote them.

$$p = A\left(1 - \frac{\omega}{R_1 V}\right)e^{-R_1 V} + B\left(1 - \frac{\omega}{R_2 V}\right)e^{-R_2 V} + \frac{\omega E}{V} \tag{5.1}$$

5.2.2 Air Material Definition

The air domain EOS was considered without computing deviatoric stresses, defined using only the reference density (ρ_0) of air at 25 °C and atmospheric pressure. The linear polynomial EOS, Equation (5.2), was used to relate the state variable for the air definition.

$$P = C_0 + C_1\mu + C_2\mu^2 + C_3\mu^3 + (C_4 + C_5\mu + C_6\mu^2)E \tag{5.2}$$

The coefficients C_0 through C_6 are calibrated while $\mu = \rho/\rho_0 - 1$. The values ρ_0 and ρ are the initial and current configurations of the material density respectively. Setting all the coefficients to the values shown in Table 5.2, this EOS may be used to describe the behaviour of gasses through the gamma law, Equation (5.3). In Equation (5.3), γ represents the ratio of specific heats [81].

$$P = (\gamma - 1)\frac{\rho}{\rho_0}E \tag{5.3}$$

Air was considered to exhibit ideal gas behaviour, simulated numerically by defining only C_4 and C_5 of the linear polynomial [81]. As air does not offer any resistance to shear distortion, no strength model was required. Properties for both the material and EOS are shown in Table 5.2 using LS-DYNA nomenclature.

Table 5.2: Material and linear polynomial parameters for the simulation of air [81].

ρ_0	E_0	C_0	C_1	C_2	C_3	C_4	C_5	C_6
kg/m^3	kJ/kg	-	-	-	-	-	-	-
1.184	253.3	0	0	0	0	0	0.4	0.4

5.2.3 FML Material Definitions

Two different material models were used to define the constituent materials of the FML. Since the panel was constructed using shell elements, no EOS was required.

Al2024-T3

The Johnson-Cook material model determined during tensile testing was used to simulate the behaviour of the aluminium alloy using similar implementation as described in Section 4.2.4. The behaviour of the model is illustrated in Equation (4.7). The material parameters for the aluminium alloy can be found in Section 4.2.4, Table 4.3.

GFRP

The GFRP layers were simulated using an orthotropic composite model, MAT_COMPOSITE_DAMAGE in LS-DYNA. Material properties for SE 84LV based composite were obtained from the manufactures data sheet [70] where possible and calculated using the method of volume fractions where required. The relevant composite material properties can be found in Table 5.3.

Table 5.3: GFRP layer material properties obtained through MVF and literature [70].

Parameter	V_F	ρ	$E_{11} = E_{22}$	E_{33}	G_{12}	$E_{13} = E_{23}$	μ_{12}	$\mu_{13} = \mu_{23}$
Units	-	kg/m^3	GPa	GPa	GPa	GPa	-	-
Woven GFRP	0.52 0.58	1800	26.5	15.65	5.67	5.42	0.125	0.283

5.3 Boundary Condition Configurations

The model was constrained numerically to simulate the intended experimental conditions, utilise model symmetry and negate any rigid body modes. The experimental clamp frame conditions were simulated by applying a fully fixed SPC boundary at the clamp edge of the FML. This is known to give reasonable results for Mode I failure in blast loaded metal plates [95–97] and GLARE® panels [94]. Symmetry boundary conditions were applied by fixing the midplane nodal degrees of freedom at the symmetry boundaries. These conditions are illustrated for uniform loading conditions in Figure 5.6. Similar boundary conditions were applied to the FML simulated under localised loading with the exception of a clamp frame and the use of a smaller air mesh.

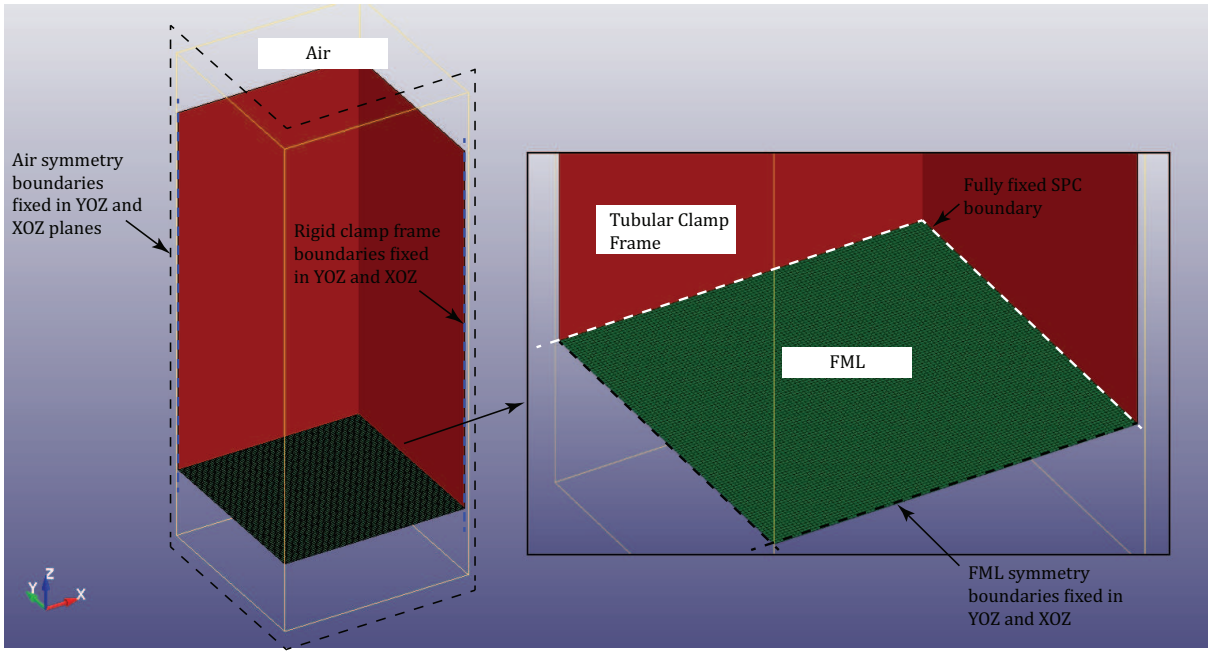

Figure 5.6: Illustration of the SPC boundary conditions employed in the numerical blast model.

The ALE air mesh was constrained on the symmetry boundaries to enable realistic detonation and motion of the explosive material within the air. In order to ensure accurate pressure dissipation after explosive detonation, a non-reflecting boundary was specified on the air surfaces not subjected to symmetry conditions. Pressure waves were allowed to move across these element boundaries, effectively simulating an infinite space. When modelling the uniform loading experiments, the tubular clamp frame was modelled using rigid shell elements fully fixed with an SPC boundary. The rigid shell mesh allowed a more accurate simulation of reflected waves caused by the tubular clamp frame.

5.4 Mesh Convergence Simulations

A mesh convergence study was performed on the ALE domain in order to determine an adequate element size. Convergence criteria was based on the stability of the simulations, run time and total experienced impulse values. The ALE mesh size was varied while a rigid plate, consisting of a constant 0.5 mm shell mesh, was used to capture the impulse of the simulated blast. The ALE element sizes were varied from 4 mm to 1.25 mm. A mesh size of 2 mm was chosen as it provided the most accurate impulse results at a reasonable computational cost.

5.5 Final Numerical Blast Model

Using the techniques and geometries described in the preceding sections, two quarter-symmetry models were generated, one for each loading condition. The standoff distance for the localised blast was 20 mm, while the uniform loading standoff distance was set at 200 mm. The uniform blast loading model consisted of the same components as the localised model with the exception of a rigid tubular clamp frame to simulate the 200 mm standoff. These final models are shown in Figure 5.7 and 5.8.

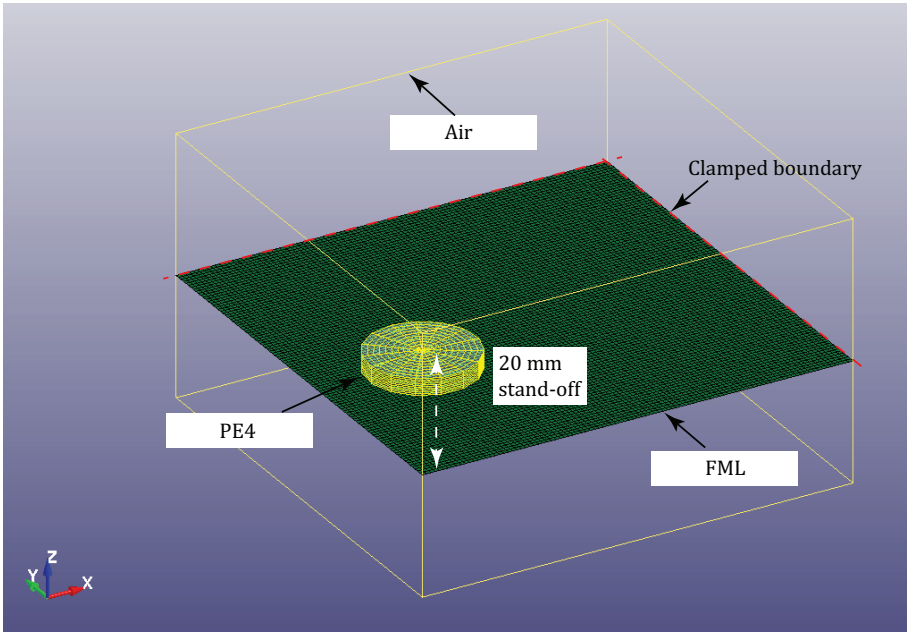

Figure 5.7: Final localised blast model.

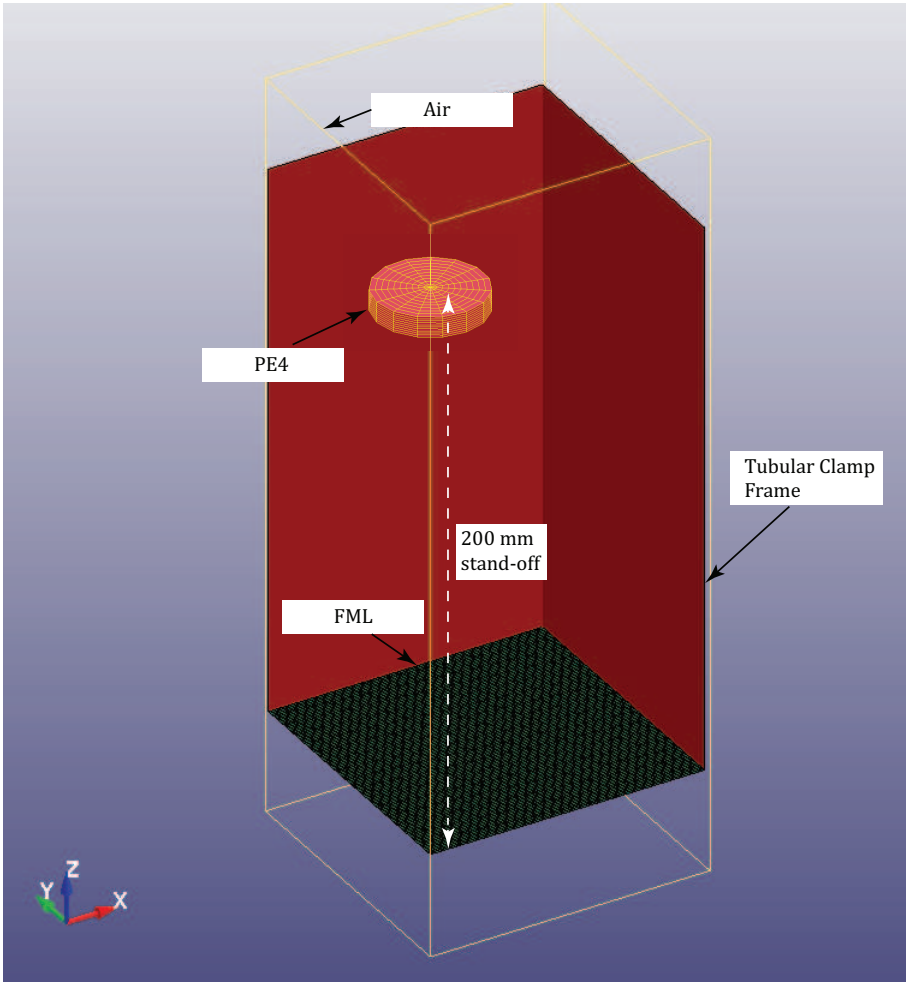

Figure 5.8: Final Uniform loading model.

5.6 Numerical Results

The uniform blast loading simulations were run for a period of 1.6 ms and the localised loading simulations for a period of 1 ms. These run times were chosen to ensure that the blast wave had adequate time to develop fully, impinge the target FML and dissipate completely, while also allowing deformation of the panel under its own inertia. The evolution of the numerical blast wave is shown in Figures 5.9 and 5.10 for uniform and localised loading simulations respectively. Under uniform loading conditions, explosive detonation (state 2-3) was followed by an initial ogive-shaped blast wave in the direction of the target panel. The blast wave propagated axially towards the target plate and radially towards the clamped boundary. After reaching the square tubular clamped boundary, the blast wave conformed to the shape of the confined area, seen in State 5. After approximately 60 µs the tip of the fully developed pressure wave impacted the target panel (state 7) followed 10 µs later by the remainder of the square pressure wave distributed

uniformly across the surface of the panel. Under localised loading with a 20 mm standoff, the target panel was impacted directly after detonation resulting in a highly localised pressure wave, as shown in Figure 5.10.

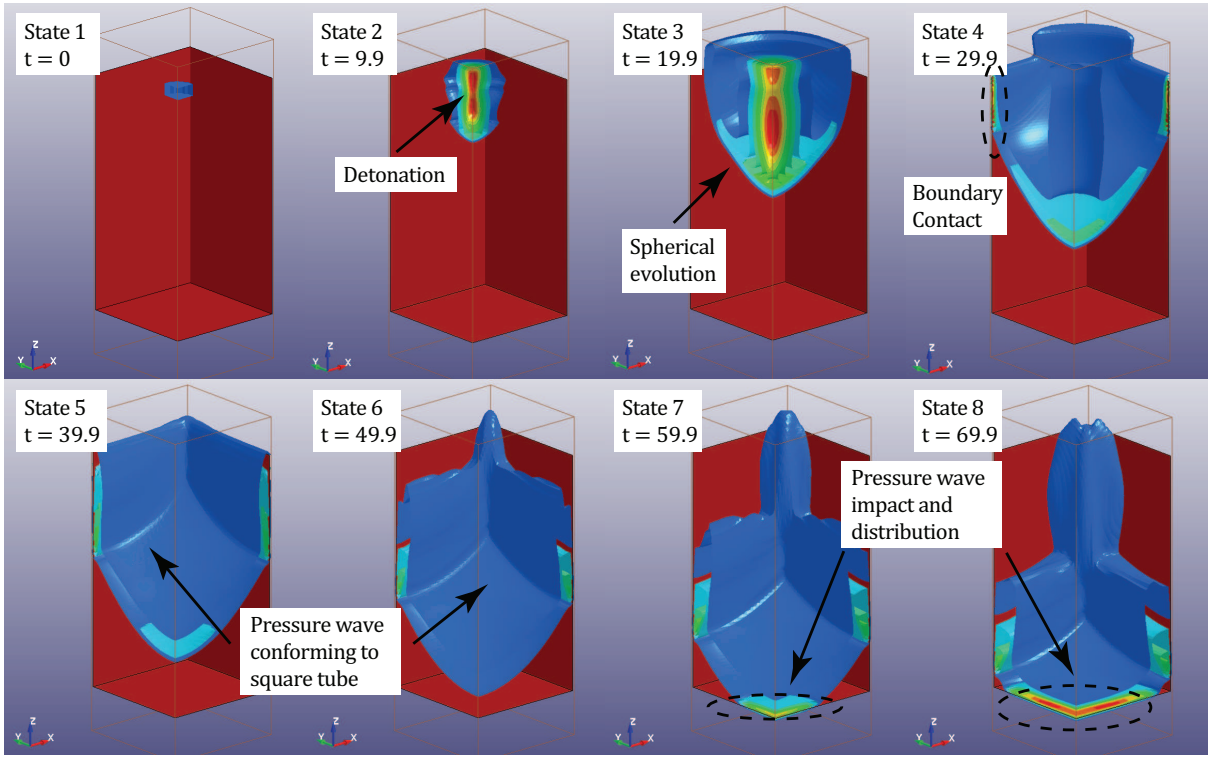

Figure 5.9: Illustration of pressure evolution during uniform blast loading simulations.

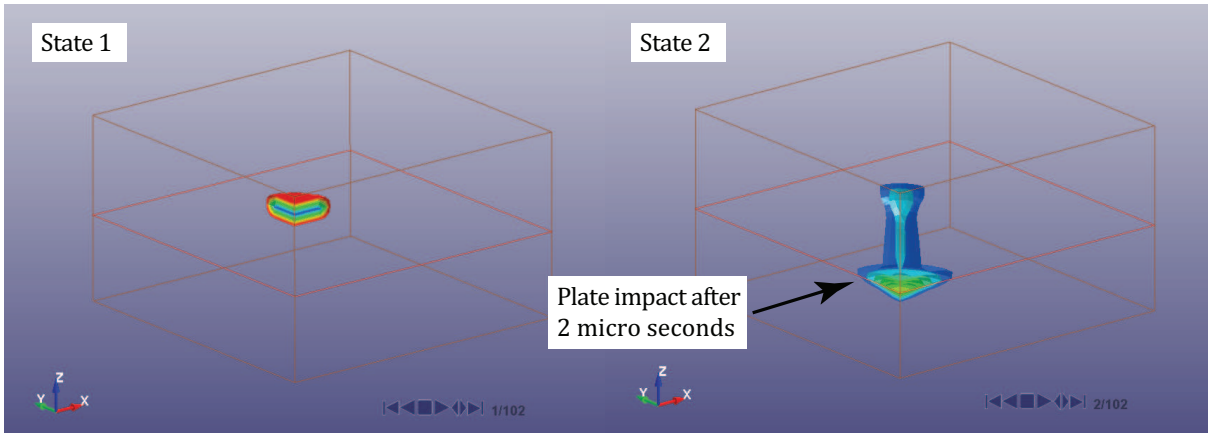

Figure 5.10: Illustration of pressure evolution during localised blast loading simulations.

The resultant numerical impulse for each simulated charge mass was measured using the dbfsi[1] parameter and is illustrated in Figure 5.11. The numerical impulses measured for

[1]database fluid structure interaction

both localised and uniform loading conditions follows a linear trend of approximately 2 N s for each gram of charge mass.

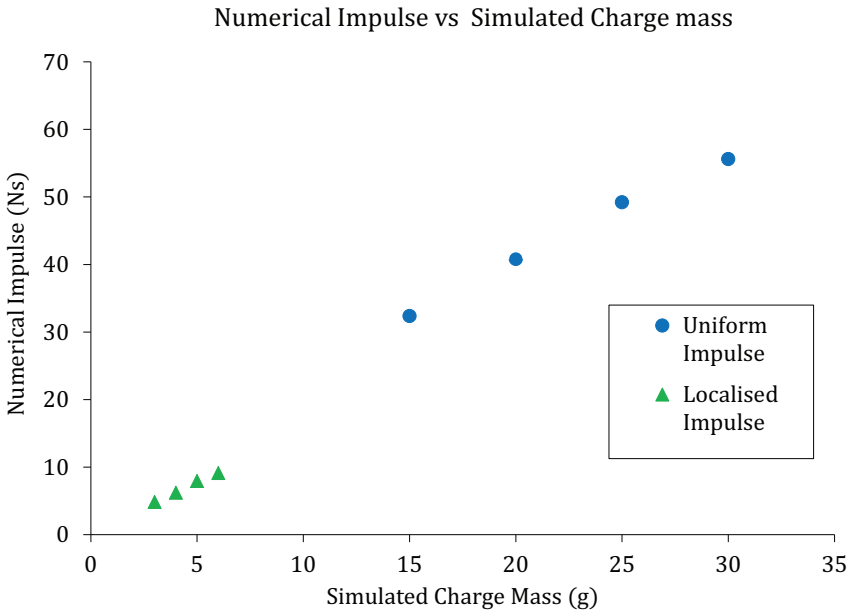

Figure 5.11: Graph showing the numerical impulse versus simulated charge mass.

Due to the elastic nature of the composite and the absence of a damage model, the deflection response of the numerical FMLs was dominated by elastic vibrations. This is illustrated in Figure 5.12 which shows the measured midpoint deflection and surface profile of the FML, subjected to a 30 g charge mass, at two different time steps. The midpoint deflection of the FML was obtained by calculating the mean value of the vibration. The measured impulses, mean- and maximum- deflections is shown in Table 5.4 for each simulated charge mass. Full deflection versus time graphs for each FML are shown in Appendix C.1.

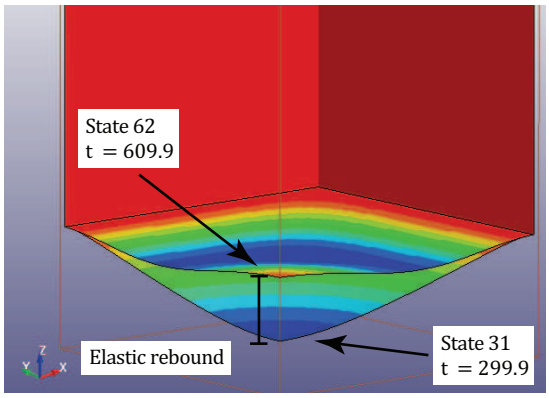

(a) Illustration of the variation in displacement due to elastic rebound.

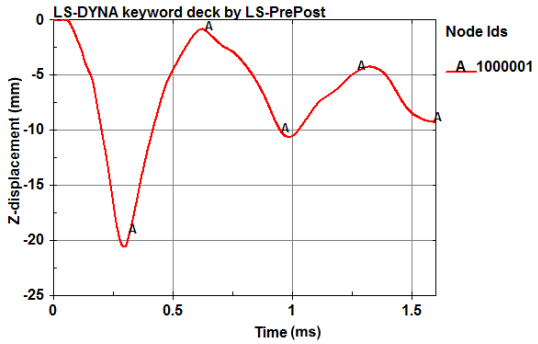

(b) Graph showing the midpoint displacement versus time for the 30 g charge mass simulation.

Figure 5.12: Illustrations of the elastic behaviour of the numerical FMLs.

Table 5.4: Numerical blast simulation results showing the obtained numerical properties.

Charge Mass (g)	Full Numerical Impulse (Ns)	Mean Final Deflection (mm)	Max Deflection (mm)	Max Plastic Strain Midpoint	Max Plastic Strain Boundary
Localised blast loading numerical simulation					
3	4.84	2.15	8.57	0.095	0.065
4	6.20	4.03	10.3	0.116	0.079
5	7.96	7.15	11.9	0.134	0.097
6	9.12	9.57	13.1	0.151	0.112
Uniform blast loading numerical simulation					
15	32.4	8.05	14.0	0.078	0.143
20	40.8	8.34	16.7	0.116	0.196
25	49.2	6.45	18.9	0.155	0.213
30	55.6	7.52	20.6	0.19	0.229

To acquire an idea of the response of the FMLs to blast loading, the evolution of plastic strain in the target panel was considered. As the FML is a multi-layered structure simulated using a single layer of shell elements, the strain values indicated represent the plastic strain exhibited in the entire cross-section of the panel. These parameters give an indication of the resistance of the constituent materials to the respective blast loads. Figure 5.13 illustrates the plastic strain (ε_p) evolution across the quarter-symmetry of the simulated FML subjected to uniform blast loading. States 10 and 12 show the first plastic strain appearing at the clamped boundaries. Plastic strain in the surface the

FML started close to the corner of the clamp frame and gradually evolved and propagated towards the center of the panel, seen in State 12 through 18. Initially, plastic strain took on the square shape of the exposed panel area, seen in State 18 through 28. The square-shaped damage then evolved into a diamond-shaped damage region (quarter diamond in the quarter symmetry model), seen in State 42, due to the orthotropic nature of the GFRP laminates. The maximum plastic strain occurred at the fully clamped boundary, starting close to the corner of the square tubular clamp frame and gradually propagating towards the middle of the boundary, seen in States 22 through 42.

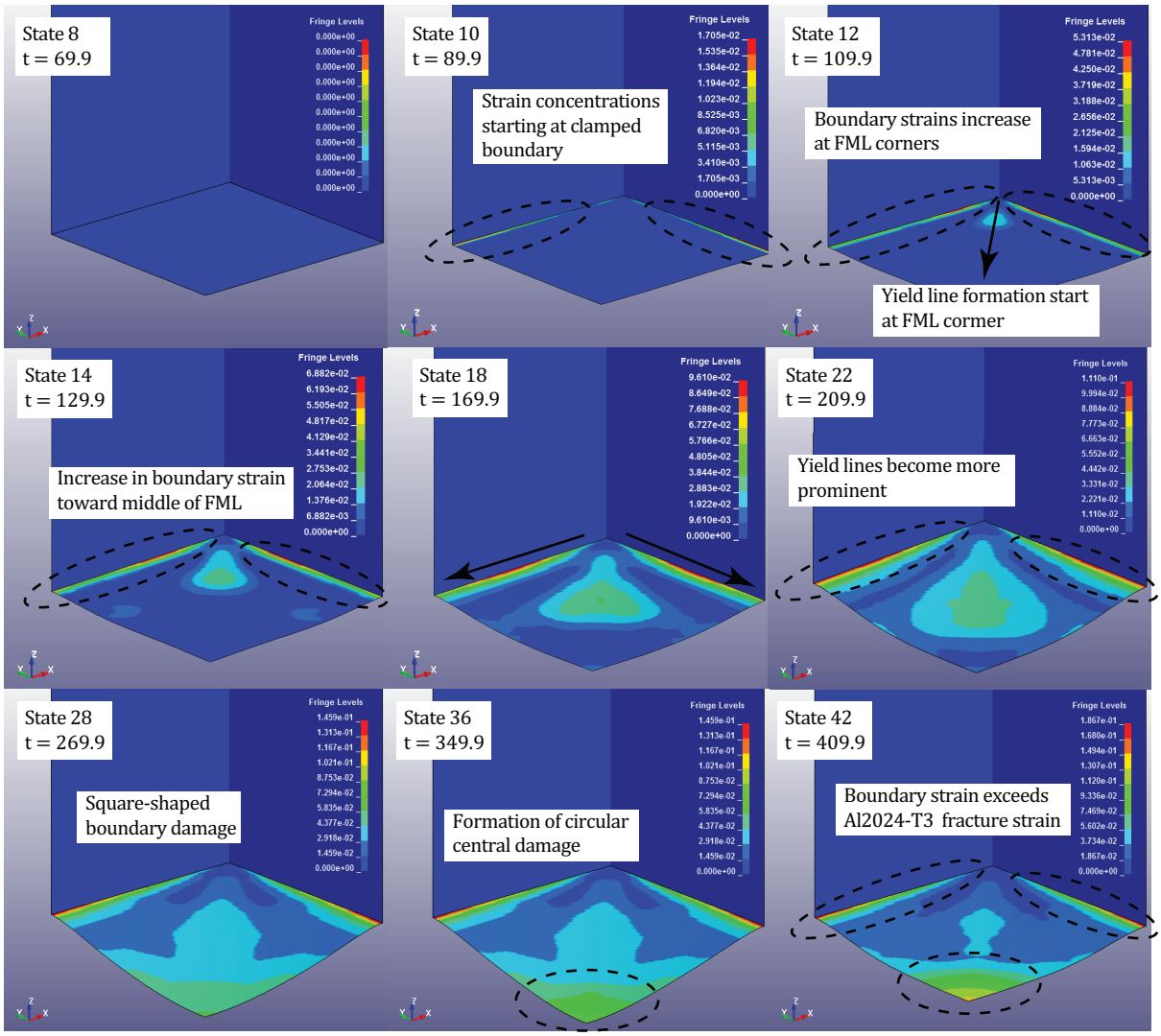

Figure 5.13: Contour plot showing the plastic strain evolution in the entire FML during uniform blast loading, simulation using 30 g charge mass.

Figure 5.14 shows the evolution of plastic strain in the simulated FMLs subjected to localised blast loading. Due to the highly localised nature of the blast wave, strains

were concentrated primarily in the centre of the target panel. State 3 through 9 shows plastic strain initially propagating radially from the point of impact. State 16 through 26 show the development of both strain at the clamped boundary and a larger diamond shaped plastic strain region due to the orthotropic influence of the GFRP.

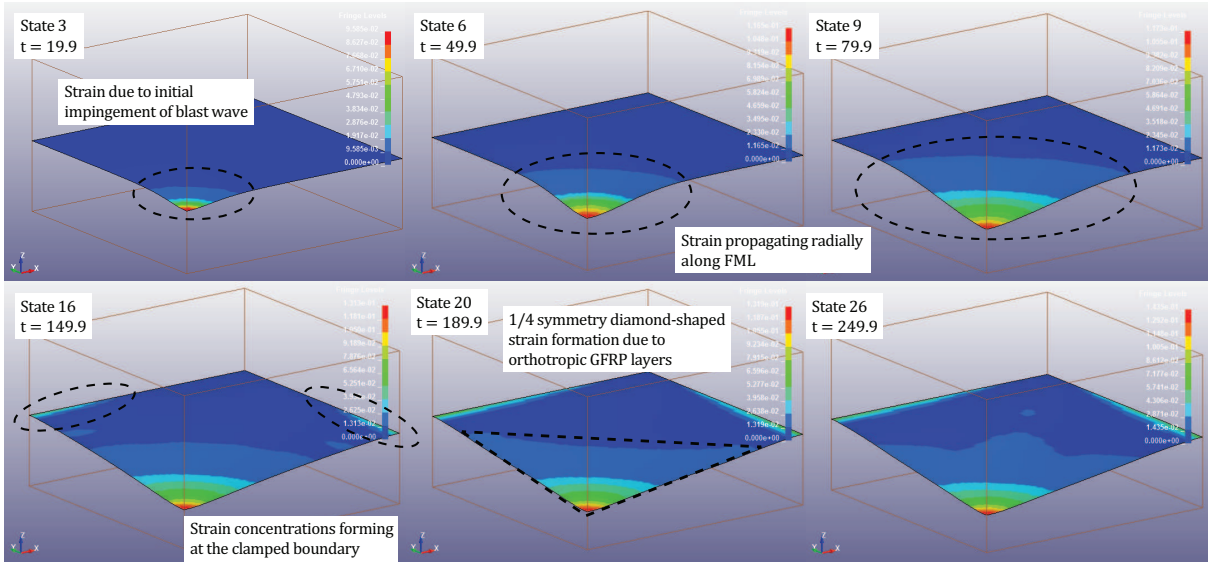

Figure 5.14: Contour plot showing the plastic strain evolution in the entire FML during localised blast loading, simulation using 6 g charge mass.

The maximum strain data for both the midpoint and boundary regions for each simulation is shown in Table 5.4. Graphs for the stress and plastic strain versus simulation time for each damage region is shown in Appendix C.2. The plastic strain data obtained from the localised loading simulations was still within the allowable range of the aluminium alloy, indicating that failure during localised loading would likely not occur at charge masses lower than 6 g. It was also observed that failure in the FMLs subjected to localised loading would most likely occur in the centre of the target panel, closer to the explosive charge. The uniform blast loading simulations showed that failure would most likely occur at the clamped boundary through tearing, due to high concentrations of plastic strain observed in these regions. For charge masses greater than 20 g, plastic strains exceeding that of the aluminium alloy was observed at the clamped boundary of the target panel. This results in the possibility of failure in the PPW series at charge masses as low as 20 g.

The results of the numerical simulations were used to design an experimental test matrix. As the simulations neglected the effects of debonding and simplified the boundary conditions, the results were assumed to be conservative estimates. Charge

masses similar to the simulated conditions were chosen. In the cases where the numerical models showed failure, extra test sets were included at lower charge masses to ensure an adequate number of data points. In the cases where the models did not indicate failure, test sets included higher charge masses. Each test series had to be subjected to similar loading conditions and charge masses to ensure consistency. The proposed experimental test schedule for all three test sets is shown in Table 5.5.

Table 5.5: Proposed experimental charge masses and loading conditions.

Loading Conditions	Mass PE4 g
Localised (20 mm SOD)	3,4,5,6,8,10
Uniform (200 mm SOD)	10,15,20,25,30

Chapter 6

Experimental Blast Set-up and Testing Procedures

Two different test series were conducted to ascertain the blast response of the manufactured FMLs. The stand-off distance was varied in order to obtain a response to both localised and uniform blast loading. Localised tests were performed under unconfined conditions while fully vented conditions were employed during uniform loading tests.

All blasts were generated by detonating a cylindrically shaped charge of PE4 explosive. The explosive disk was placed on a polystyrene bridge at stand-off distances of 20 mm and 40 mm for localised loading (using a charge diameter of 20 mm to 25 mm) and a polystyrene pad at 200 mm for uniform loading(using a charge diameter of 40 mm). The properties of the PE4 explosive is shown in Table 6.1. PE4 is nearly identical to the well-known C4, varying only in the type and proportion of plasticizer[1].

Table 6.1: PE4 material properties [98, 99]

Detonation Velocity	m/s	8193
Density	kg/m^3	1603
TNT Equivalence	%	130

[1]PE4 - 88% RDX, 11% Lithium Grease - Plasticizer, 1% Penta-erythritol dioleate [98]
C4 - 91% RDX, 2.1% Polyisobutylene - Plasticizer, 1.6% Motor Oil, 5.3% 2-ethylhexyl sebacate [99]

6.1 Ballistic Pendulum

All experiments were performed on the ballistic pendulum set-up in the blast chamber at the BISRU. This set-up, shown in Figure 6.1, has been successfully used and well documented in the literature [1, 5, 11, 19, 57–59, 61, 64, 65, 82] as a method for obtaining the impulse transferred to an intended target plate.

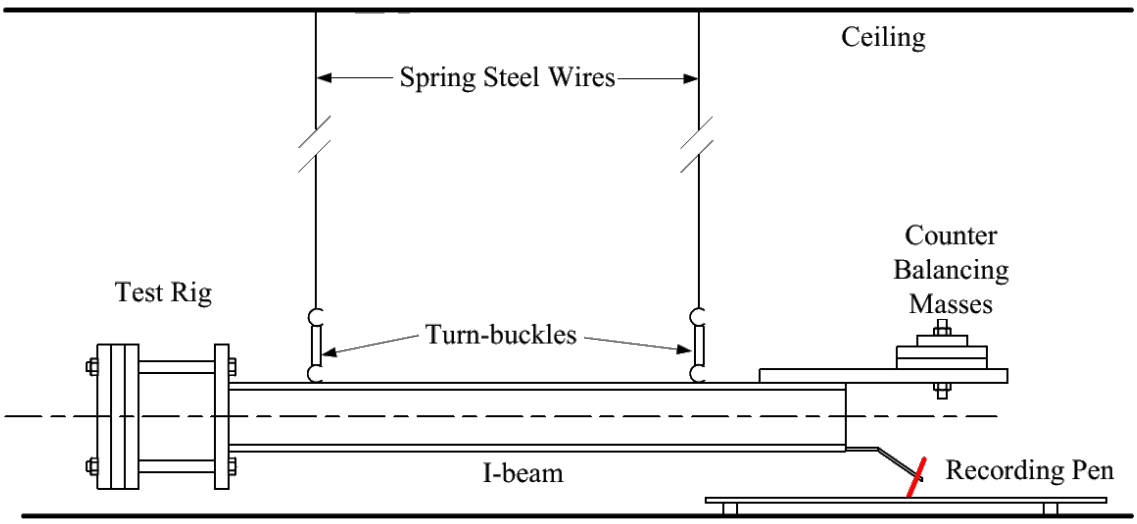

Figure 6.1: Illustration of ballistic pendulum experimental set-up [82].

The pendulum set-up consists of an I-beam suspended from the roof by four steel cables. The one end of the beam contains the target plate assembly, held in place by two steel clamp frames. These are offset from a backing plate by four 100 mm spacers. The backing plate allows impulse to be transferred to the pendulum even if the target plate fails during loading. To counteract the mass of the backing plate, spacers, clamp frame and target plate, counterbalance masses were placed on the opposite side of the pendulum. The impulse experienced by the target plate was calculated using the amplitudes of pendulum swing, ie. ΔL and ΔR.

6.1.1 Ballistic Pendulum Theory

Simple pendulum theory was applied to analyse the behaviour of the ballistic pendulum. The mass of the cables were assumed to be negligible while any rotational inertia was disregarded. In pendulum theory, the maximum angle of the pendulum swing is regarded as small so as to satisfy the condition $\sin(\theta) \approx \theta$. The problem is reduced to a two-dimensional, single degree of freedom problem. Adjusting the mass of

the pendulum either increases or decreases the amplitude of the swing. It is important that the pendulum should be balanced in order to maintain motion purely in a two-dimensional plane. Equation (6.1) expresses the linearised equation of motion of a 2-D, single degree of freedom, pendulum with the addition of viscous damping.

$$\ddot{x} + 2\beta\dot{x} + \omega_n^2 x = 0 \tag{6.1}$$

Where $\beta = \frac{C}{2m_p}$ and $\omega_n = \frac{2\pi}{T}$. The variable C is the damping coefficient, m_p is the pendulum mass and T is the period of the pendulum swing. A solution to Equation (6.1) is given by Equation (6.2).

$$x(t) = \frac{(e^{\beta t})\dot{x}_0 sin(\omega_d t)}{\omega_d} \tag{6.2}$$

where $\dot{x}_0$ is the initial velocity of the pendulum and ω_d the damped frequency, calculated using Equation (6.3).

$$\omega_d = \sqrt{\omega_n^2 - \beta^2} \tag{6.3}$$

Taking into account that the maximum positive displacement of the pendulum (x_1) occurs at $t = \frac{T}{4}$ while the maximum negative displacement (x_2) occurs at $t = \frac{3T}{4}$, Equation (6.2) reduces to,

$$x_1 = \frac{\dot{x}_0 T}{2\pi} e^{\frac{-1}{4}\beta T} \tag{6.4}$$

and

$$x_2 = \frac{\dot{x}_0 T}{2\pi} e^{\frac{-3}{4}\beta T} \tag{6.5}$$

The value of β is determined by dividing x_1 by x_2 and writing the result in terms of β, as seen in Equation (6.6).

$$\beta = \frac{2}{T} ln\left(\frac{x_1}{x_2}\right) \tag{6.6}$$

Rearranging Equation (6.4), an expression for $\dot{(x_0)}$ can be obtained.

$$\dot{x}_0 = \frac{2\pi}{T} x_1 e^{\frac{1}{4}\beta T} \tag{6.7}$$

The total impulse impacted to the ballistic pendulum can be calculated using Equation (6.8).

$$I = m_p \dot{x}_0 \tag{6.8}$$

Figure 6.2 illustrates the pendulum swing. The measured horizontal distances ΔR and ΔL are dissimilar to the distances x_1 and x_2 due to the rotational motion of the measuring pen assembly relative to the pendulum.

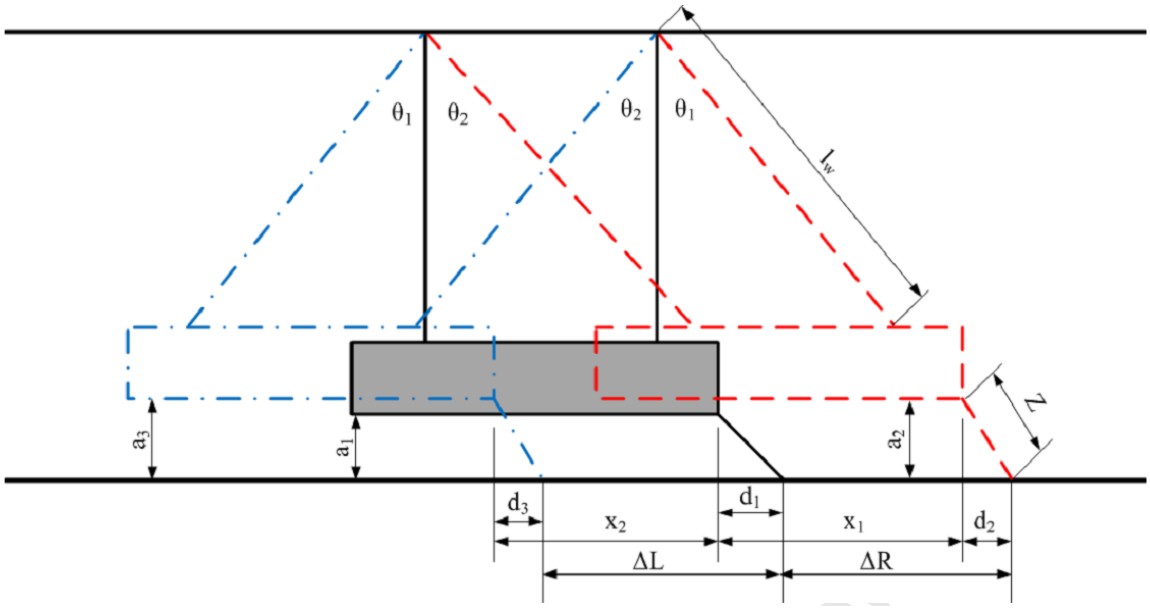

Figure 6.2: Illustration of data measurement using pendulum swing [82].

These differences are accounted for using the geometrical measurements of the pendulum. The measurable quantities in Figure 6.2 are wire length (l_w), the height of the pendulum above the measurement board (a_0), the length pen arm (Z) and the length of the forward and backward pen measurements ΔR and ΔL. Using simple trigonometry, the value of d_0, d_1 and d_2, the differences between the pen stroke and pendulum swing can be calculated, as shown in Equation (6.9).

$$d_i = \sqrt{Z^2 - a_i^2} \qquad (i = 0:2) \tag{6.9}$$

where the values of a_1 and a_2 are related to a_0 by

$$a_1 = l_w(1 - \cos(\theta_1)) + a_0$$
$$a_2 = l_w(1 - \cos(\theta_2)) + a_0$$

The values of x_1 and x_2 are also determined from Figure 6.2 using trigonometry thus giving Equation (6.10) and (6.11).

$$x_1 = l_w \sin(\theta_1) \tag{6.10}$$

and

$$x_2 = l_w \sin(\theta_2) \tag{6.11}$$

Writing the measurable distances in terms of ΔR and ΔL, yields Equations (6.12) and (6.13).

$$\begin{aligned} \Delta R &= x_1 - d_0 + d_1 \\ &= l_w \sin(\theta_1) - \sqrt{Z^2 - a_0^2} + \sqrt{Z^2 - \left(l_w(1 - \cos(\theta_1)) + a_0\right)^2} \end{aligned} \tag{6.12}$$

and

$$\begin{aligned} \Delta L &= x_2 + d_0 - d_2 \\ &= l_w \sin(\theta_2) + \sqrt{Z^2 - a_0^2} - \sqrt{Z^2 - \left(l_w(1 - \cos(\theta_2)) + a_0\right)^2} \end{aligned} \tag{6.13}$$

Values for a_0, l_w, Z and T were measured directly from the pendulum set-up. T was taken as the average pendulum period over 10 oscillations. Solving Equations (6.12) and (6.13) simultaneously, the values of θ_1 and θ_2 could be obtained. Using θ_1 and θ_2, the values of x_1 and x_2 can be determined in turn, using Equations (6.10) and (6.11). These values were then used to obtain the value of β from Equation (6.6). Once β is known, the initial velocity of the pendulum can be obtained through Equation (6.7). The initial velocity can then be multiplied by the pendulum mass to obtain the impulse transferred to the pendulum for a given blast load using Equation (6.8).

6.1.2 Ballistic Pendulum Set-up

The pendulum was balanced correctly to minimize lateral sway. This increased the accuracy of the pen stroke measurements and the validity of the assumption of a 2D,

single degree of freedom problem. Balance was achieved by weighing the front test rig components and counterbalancing at the rear. Once the masses were balanced, the pendulum was levelled to ensure equal tension in all four spring steel cables and allow the pendulum swing to act through its centroid.

A photograph of the standard ballistic pendulum set-up is shown in Figure 6.3. The mass of the pendulum was varied for different test series. For uniform loading, charge masses of up to 40 g were used, which would also cause large movements of the pendulum without the addition of extra mass to the standard set-up. Side masses were added, increasing the total mass m_p, to obtain reasonable ΔR and ΔL values which enabled the accurate measurements but were small enough to allow the small angle assumption to be maintained, while retaining balance. For localised loading, smaller charge masses were used (less than 10g) and the side masses were not employed. A small number of tests were performed using a secondary pendulum set-up. The secondary set-up was initially employed to perform DIC work on some of the tested panels, but was later abandoned due to errors affecting the high-speed cameras. Table 6.2 shows the values of the measured constants for the various pendulum set-ups.

Table 6.2: Experimental blast pendulum set-up configurations

Pendulum Set-Up	m_p kg	a_0 mm	l_w mm	Z mm
Standard Uniform Loading Pendulum	189.5	0.156	2.945	0.212
Standard Localised Loading Pendulum	117.5	0.156	2.945	0.212
Secondary Pendulum	175	0.1	2.784	0.15

Figure 6.3: Photograph of the standard ballistic pendulum.

6.2 Unconfined Localised Blast Loading

An unconfined blast load refers to the detonation of an explosive in free air where the blast wave can propagate freely and impinge upon the intended target without any prior reflection or amplification. The blast wave subjects the target plate to a short duration, high magnitude impulsive load. A localised blast load refers to the detonation of an explosive within close proximity of the target plate, in this case stand-off distances of 20 mm and 40 mm. Figure 6.4 shows an illustration of the unconfined localised blast loading arrangement.

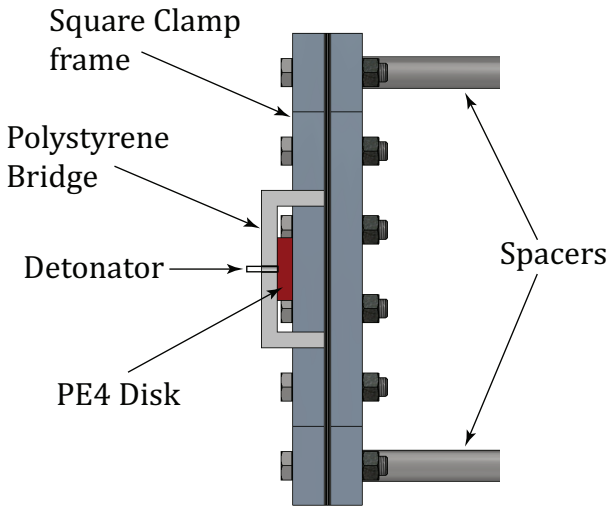

Figure 6.4: Sectioned view illustrating the unconfined localised blast load clamp-frame set-up.

The 300 mm × 300 mm FML panels were tightened between two square clamp frames with an exposed area of 200 mm × 200 mm. Once sandwiched between the clamp frames, the clamp frame arrangement was mounted onto the ballistic pendulum, shown in Figure 6.5.

The explosive was placed on the FML side of the polystyrene bridge at a stand-off distances of either 20 mm or 40 mm. The polystyrene bridge containing the explosive charge was centred on the target plate using a stencil. As the explosive charge was placed on the FML side of the polystyrene bridge, it was assumed the effects of the polystyrene on the blast load propagation was negligible. The detonator was inserted into the centre of the PE4 disk through a small hole drilled in the polystyrene bridge. A measurement pen was used to record the swing of the pendulum on a sheet of tracing paper.

Figure 6.5: Photograph of the unconfined localised blast load pendulum set-up.

6.3 Partially Confined Uniform Blast Loading

The uniform loading conditions were classified as partially confined due to the presence of a square tubular clamp frame. While this allowed a constant stand-off distance of 200 mm, it also resulted in some reflection and potential amplification of the impulsive pressure wave before impinging on the panel. The square tubular clamp frame consisted of four walls of 10 mm thick mild steel welded together at the corners. The clamp frame resulted in an exposed panel area of 200 mm × 200 mm. The cylindrical PE4 explosive disk was detonated on a polystyrene pad, placed snugly into the end of the tube. This configuration of explosive and clamp frame can be seen in Figure 6.6.

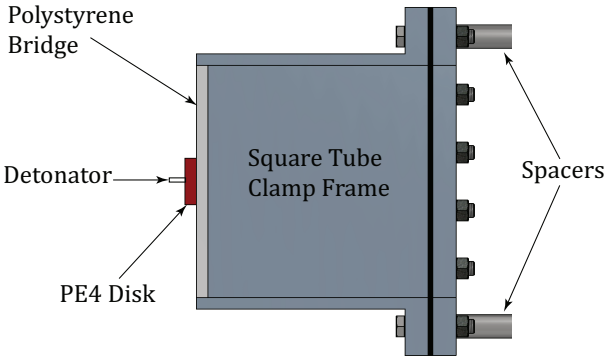

Figure 6.6: Section view illustrating the uniform blast loading clamp-frame set-up.

The uniform loading experiments were conducted on the same standard pendulum set-up described in previous sections. The target panel was clamped between the clamp frames and fastened to the pendulum set-up, shown in Figure 6.7. The detonator was inserted into the cylindrical PE4 charge and kept in a steady position using an arrangement of steel struts as with the localised loading.

Figure 6.7: Photograph of uniform blast loading pendulum set-up.

Chapter 7

Experimental Results and Observations

Following the blast experiments described in Section 6, the various blast loaded FMLs were documented and analysed. Tests were divided into three main series depending on matrix and fibre configuration, shown in Table 7.1. The test specifications and general results, such as pendulum impulse and midpoint deflections, are detailed in Table 7.3 and 7.2.

Table 7.1: Description of test series designation

Test Series Designation	Epoxy Matrix and Manufacturing method	Fibre Configuration
PPW	SE 84LV Prepreg	1 Layer of 295 $g\,m^{-1}$ Woven E-Glass
WLW	Prime 20LV Wet layup	1 Layer of 400 $g\,m^{-1}$ Woven E-Glass
WLUD	Prime 20LV Wet layup	2 Layers(0°/90°) of 220 $g\,m^{-1}$ Uni-Directional E-Glass

Table 7.2: Localised blast loading test results performed at 20 mm and 40 mm standoff distances with 20 mm and 25 mm load diameters with * indicating rupture of the respective surface.

Panel	Charge Mass (g)	SOD (mm)	Load Radius (mm)	Panel Mass (g)	Measured Impulse (Ns)	Mean Thickness (mm)	Back Face Deflection (mm)	Front Face Deflection (mm)
Summary of test results for 295 $\mathrm{g\,m^{-1}}$ woven SE 84LV & Al2024-T3 FMLs								
PPW02	3	20	12.5	789.4	6.94	4.45	13.56	13.20
PPW06	3	20	12.5	799.3	5.47	4.55	*	13.54
PPW08	10	40	10.0	790.8	14.9	4.46	10.53	10.48
PPW09	7	40	10.0	797.9	12.3	4.53	5.98	5.91
Summary of test results for 400 $\mathrm{g\,m^{-1}}$ woven Prime 20LV & Al2024-T3 FMLs								
WLW05	10	20	12.5	838.8	18.5	4.98	*	*
WLW03	5	20	12.5	833.4	8.83	4.96	*	*
WLW04	3	20	12.5	847.8	6.59	5.14	14.80	13.57
WLW08	10	40	10.0	840.9	15.3	5.08	13.44	12.42
Summary of test results for 0deg/90deg 220 $\mathrm{g\,m^{-1}}$ uni-directional Prime 20LV & Al2024-T3 FMLs								
WLUD07	10	40	10.0	875.5	16.2	5.10	12.68	12.15

Table 7.3: Uniform blast loading test results performed at 200 mm standoff and 40 mm load diameter with * indicating tearing of the respective surface.

Panel	Charge Mass (g)	Panel Mass (g)	Measured Impulse (Ns)	Mean Thickness (mm)	Back Face Deflection (mm)	Front Face Deflection (mm)
Summary of test results for 295 $\mathrm{g\,m^{-1}}$ woven SE 84LV & Al2024-T3 FMLs						
PPW01	15	796.2	33.87	4.59	17.53	17.48
PPW03	30	793.2	56.40	4.50	*	*
PPW04	10	789.1	21.96	4.53	11.94	11.88
PPW05	20	797.8	37.22	4.48	20.88	20.78
PPW07	25	788.3	52.69	4.51	23.20	23.17
PPW10	30	790.9	52.28	4.58	27.78	27.78
Summary of test results for 400 $\mathrm{g\,m^{-1}}$ woven Prime 20LV & Al2024-T3 FMLs						
WLW01	15	835.1	33.87	5.08	16.15	15.65
WLW02	30	840.8	58.61	4.91	23.53	23.48
WLW06	35	852.2	61.23	5.01	29.31	29.26
WLW10	20	832.2	39.24	4.97	18.33	18.34
Summary of test results for 0deg/90deg 220 $\mathrm{g\,m^{-1}}$ uni-directional Prime 20LV & Al2024-T3 FMLs						
WLUD02	30	876.4	56.02	4.92	23.25	23.21
WLUD03	20	872.2	42.35	5.05	18.47	18.46
WLUD04	15	886.2	34.30	5.28	13.98	13.93
WLUD05	10	886.2	25.79	5.33	10.54	10.03
WLUD06	25	878.9	48.62	5.07	20.42	20.36
WLUD09	35	887.1	58.86	5.08	27.56	27.51
WLUD10	40	875.1	64.92	5.11	28.14	27.94

7.1 Relation Between Charge Mass and Impulse

Figure 7.1 illustrates the relation between explosive charge mass and measured impulse. The impulse data was obtained using the pendulum analysis method described in Section 6.

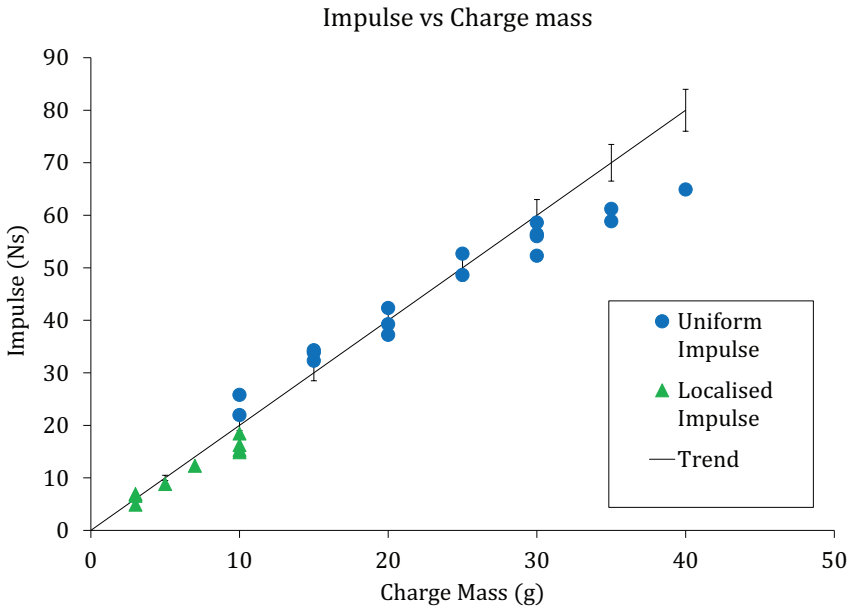

Figure 7.1: Graph showing impulse versus charge mass.

7.2 FML Damage Characteristics

The types of damage evident in the FML panels varied depending on charge mass, geometry, standoff distance and FML configuration. The damage was categorized by its location on the FML and is described in this section.

7.2.1 Front Face Damage

The most common damage effect observed for the front face (face closest to the explosive disk) was large inelastic deformation. Crater formation and tearing were commonly observed in locally loaded panels. This behaviour was caused by excessive localised deformation of the aluminium front face. For large localised charge masses (greater than 3 g) at 20 mm SODs, the tearing behaviour was replaced by hole-punching in the front face of the panel, shown in Figure 7.2.

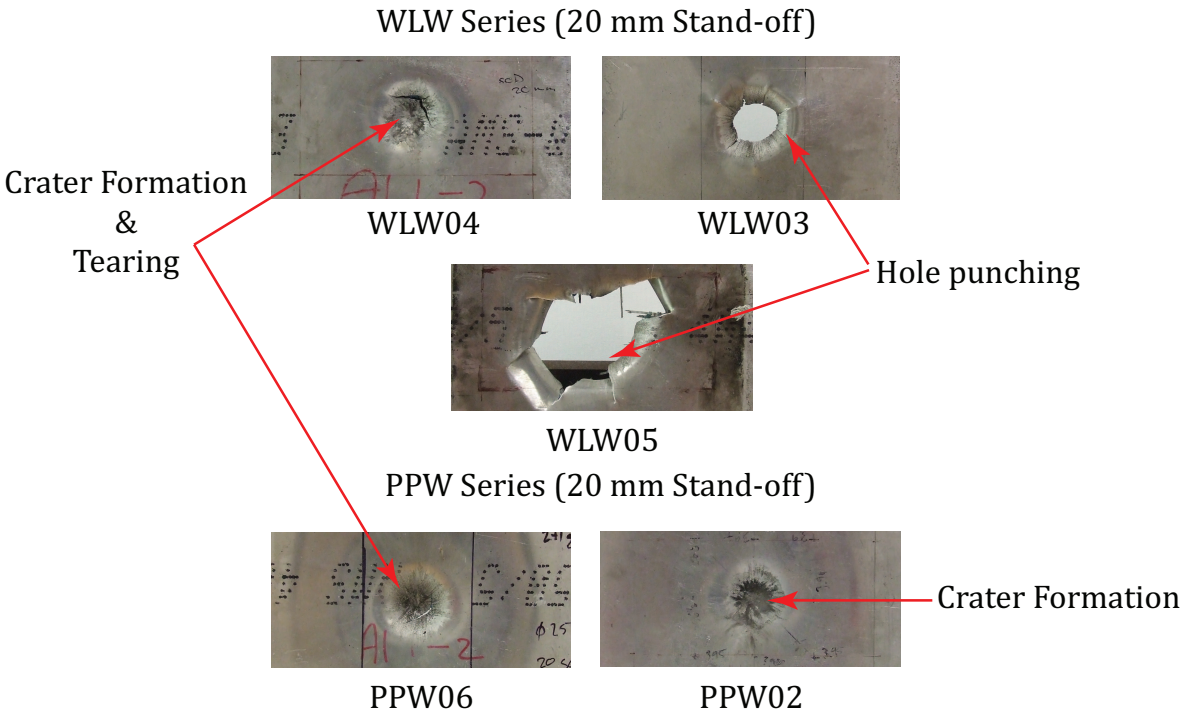

Figure 7.2: Photographs showing strain damage to the FML front face due to localised loading.

In most cases where the explosive was detonated within close proximity of the FML, the generated heat and pressure resulted in pitting of the aluminium layer, as shown in Figure 7.3. Figure 7.3 shows only the pitting observed in two panels, however this behaviour was exhibited throughout the localised loading series. Figure 7.3 also shows the minor ring buckling observed in some FMLs during localised loading at higher charge masses. The ring buckling seemed to be affected by the bond strength between the aluminium and GFRP as well as charge mass. A lack of observed ring buckling suggested very little debonding in the FMLs prior to failure.

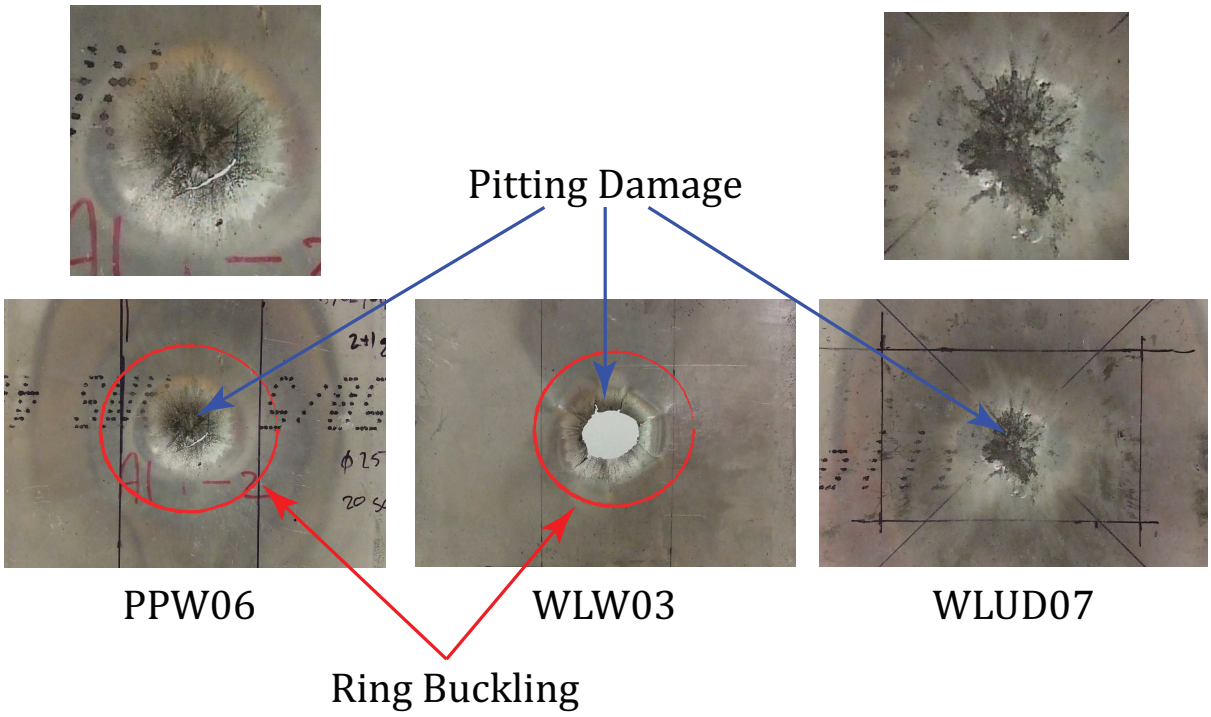

Figure 7.3: Photograph showing buckling and pitting damage on the front face due to localised loading.

A secondary cause of localised damage was found to be detonator shrapnel. At close range and for charge masses below 10 g, the copper shrapnel generated by the PE4 detonator exploding resulted in severe damage to the front face, in some cases penetrating the entire FML. This damage was highly localised and unpredictable. At larger standoff distances and greater charge masses, however, this behaviour was no longer evident due to more shrapnel being disintegrated by the explosive blast. The effects of the shrapnel damage are evident in Figure 7.4.

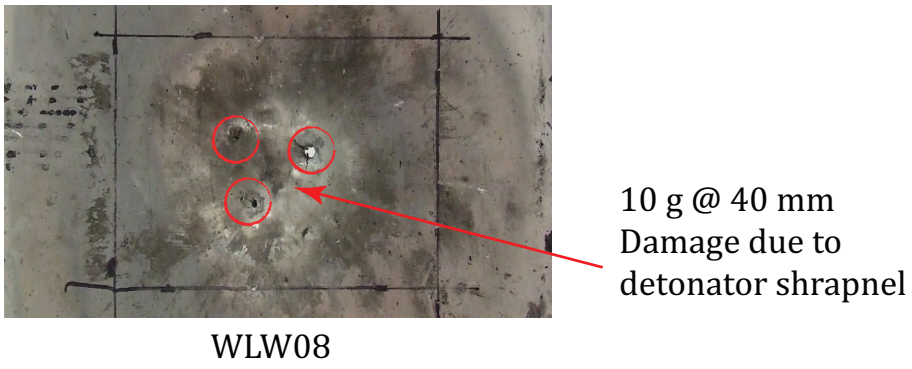

Figure 7.4: Photograph showing shrapnel damage during localised loading and low charge masses.

The most common front face damage occurrence during uniform loading was observed to be that of large inelastic deformation. The degree of deformation was found to increase with an increase in charge mass. The damage affected zones on the uniformly loaded FMLs were square shaped due to the use of a square tubular clamp frame. This led to the formation of yield lines on the diagonals of the FML, shown in Figure 7.5 for the case of 20 g explosive at 200 mm. In the uniform loading cases where debonding occurred, a secondary, smaller bulge was observed superimposed on the large inelastic deformation of the FML. Debonding reduced the effective stiffness of the materials undergoing deformation resulting in greater superimposed deflections. In some cases, these increased deflections were caused by the reflected pressure wave, resulting in a superimposed bulge in the opposite direction as the mean panel deflection, shown in Figure 7.6. Pitting damage of the aluminium surface was also observed at higher charge masses.

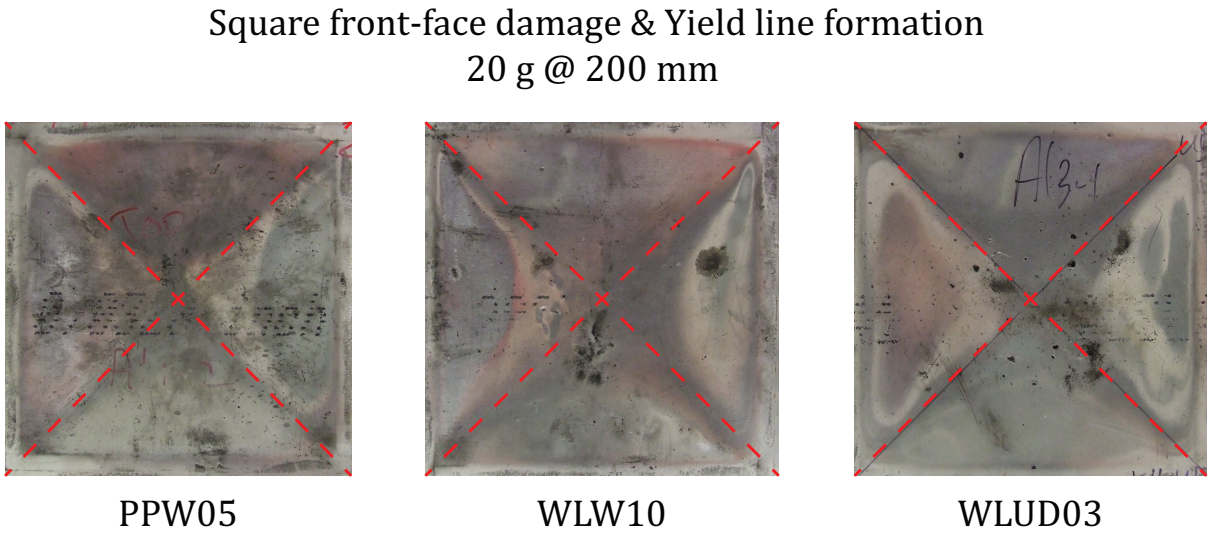

Figure 7.5: Photograph showing the formation of yield lines along the aluminium diagonals.

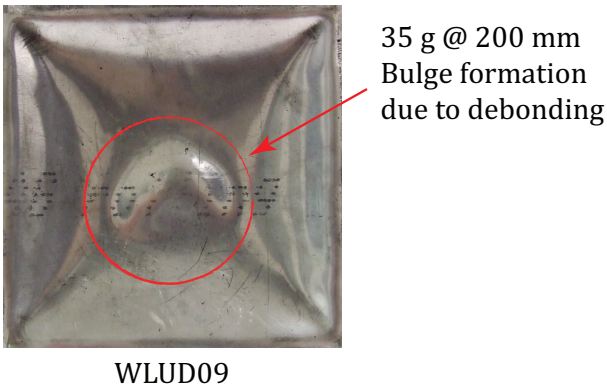

Figure 7.6: Photograph showing bulging caused by debonding of the FML layers.

7.2.2 Back Face Damage

The back face damage of the FMLs was mostly characterised by large inelastic deformation. During localised loading, at higher charge masses, this behaviour was replaced by rupture and petalling, shown in Figures 7.7. Petalling damage in the PPW series was observed on the aluminium back face as soon as the front face experienced any tearing or rupture with no transition being observed between these two damage modes. In contrast to the WLW series exhibited tearing of the front face which resulted

in inter-laminar damage but no petalling. The characteristic diamond- or cross-shaped inelastic deformation was not observed in any of the FMLs, indicating a largely aluminium dominated material response. Petalling, however, seemed to occur in a diamond shape before spreading throughout the back face, indicating that once the aluminium layers tore, the GFRP layer played a larger role in damage propagation.

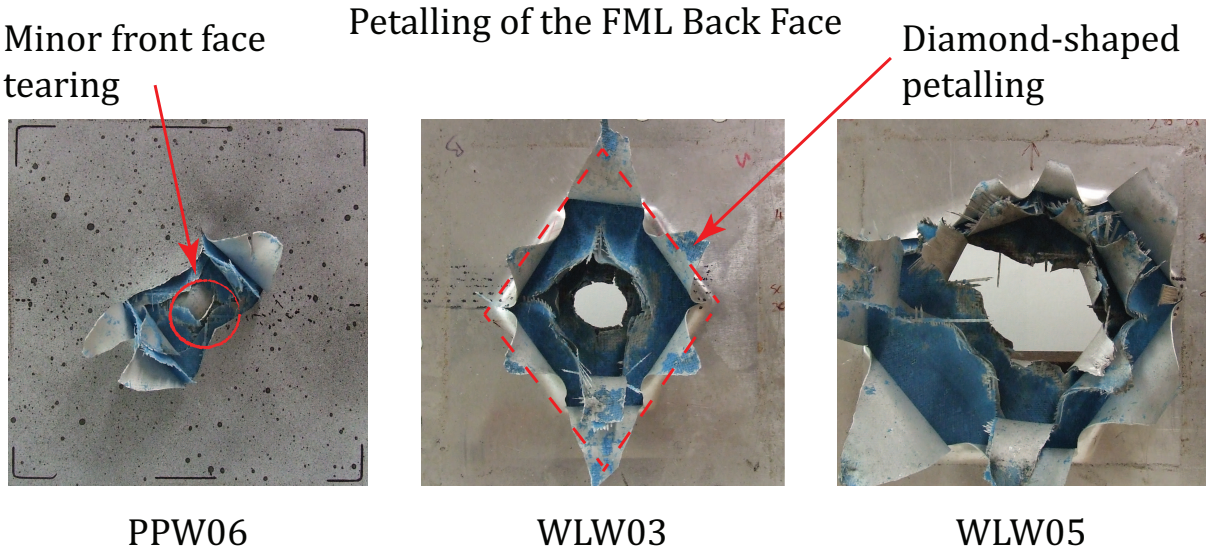

Figure 7.7: Photograph showing petalling of the FML back face during localised loading.

In the cases where debonding was observed, the aluminium back face damage remained circular indicating that fibre directionality had little effect on the blast wave propagation after debonding. Figure 7.8 shows the circular back face damage observed during localised loading.

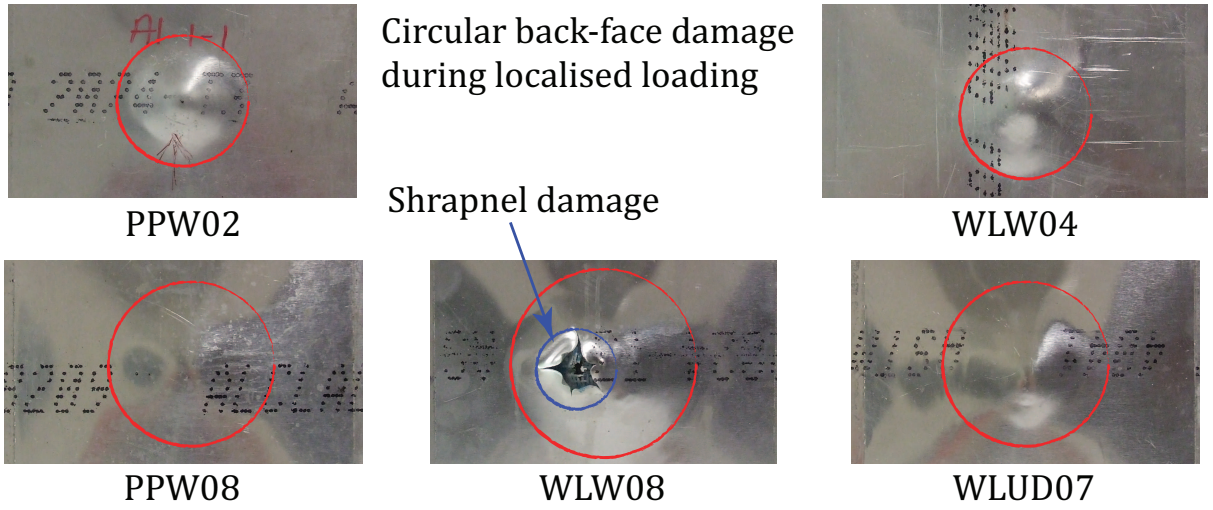

Figure 7.8: Photograph showing circular back face damage during localised loading.

All FMLs subjected to uniform loading conditions experienced global inelastic displacements varying in degree with the respective charge mass. As with the front face damage, the panels exhibited typical yield line formation, shown in Figures 7.9. In some cases, smaller local bulges were observed centrally superimposed on the larger global displacements. This behaviour is attributed to localised debonding of the metal from the GFRP layers.

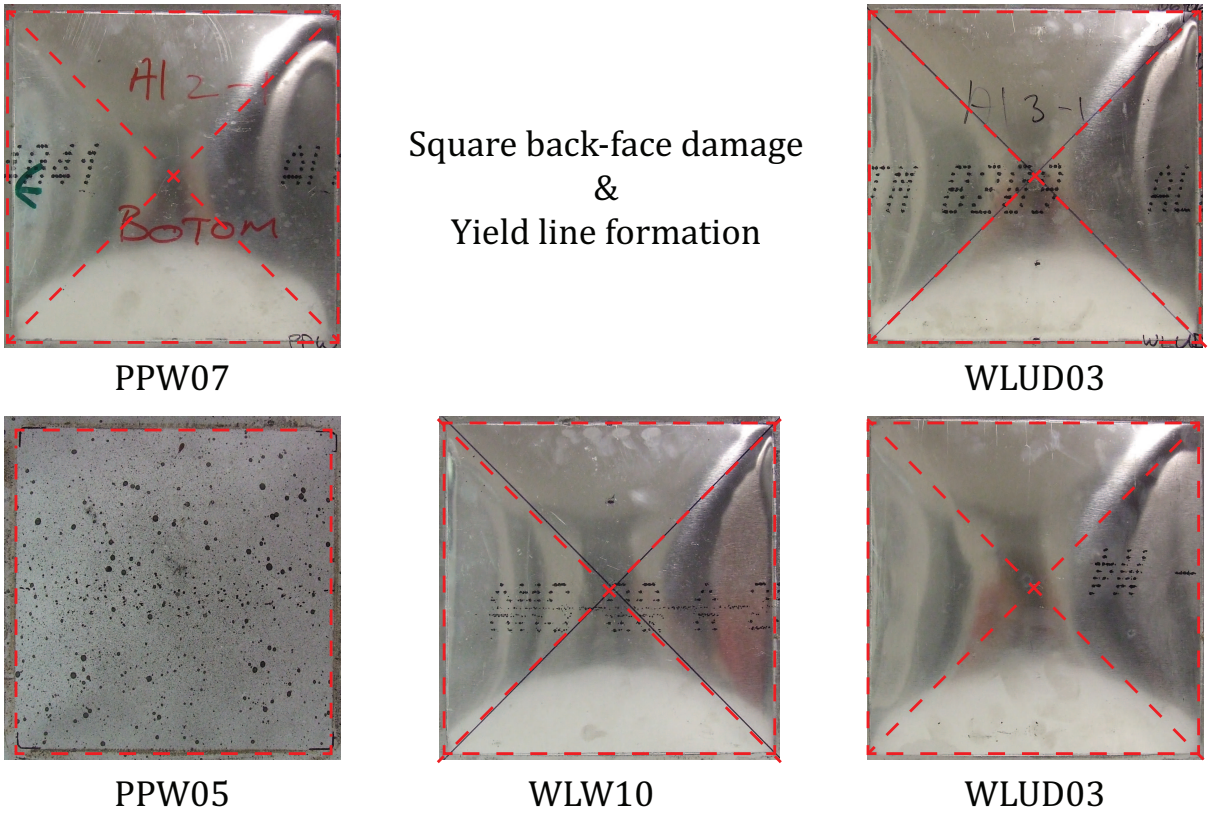

Figure 7.9: Photograph showing square-shaped back-face damage due to uniform loading (red dotted lines indicate plastic hinge formation).

7.2.3 Displacement Contour Plots

The front and back surfaces of all FMLs that did not experience rupture or petalling were digitized using a 3D scanner. The data was used to measure the variation between front and back face displacement in order to determine the onset of debonding. The results of these scans are represented as contour plots for both localised and uniform loading conditions.

Localised Loading

Only two panels were viable for scanning for the PPW series subjected to localised loading. For both a 20 mm and 40 mm standoff distance these panels exhibited similar displacements of both the front and back faces indicating negligible debonding. Figure 7.10 shows clear signs of localised loading with a circular, highly localised damage region on both the front and back face. A large amount of inelastic deformation

was observed in the centre of the FML reducing quickly when moving away from the blast affected zone. In contrast to this panels subjected to localised loading at 40 mm SODs showed a lower peak deflection and larger overall damage region resembling a more uniform blast load, shown in Figure 7.11. The contour plot also indicates the a more square shape to the damage region indicating some clamp frame effects playing a role in damage propagation.

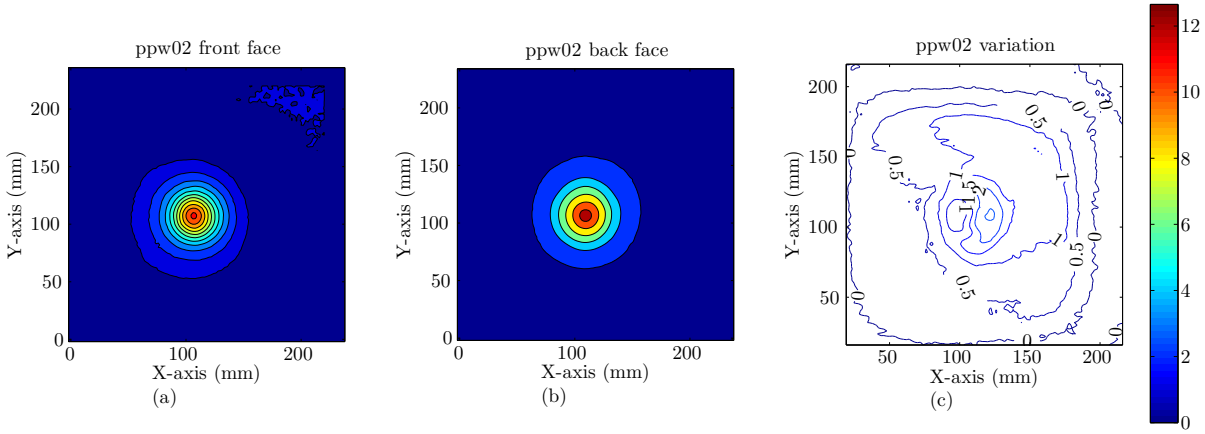

Figure 7.10: Contour plots of (a) front face displacements, (b) back face displacements and (c) variation of section thickness of a PPW panel subjected to 3 g at 20 mm standoff distance.

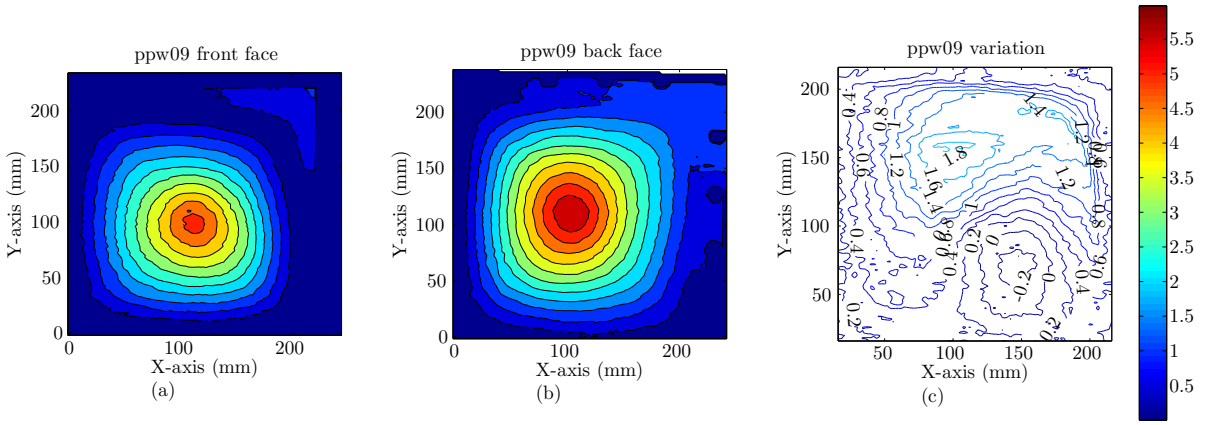

Figure 7.11: Contour plots of (a) front face displacements, (b) back face displacements and (c) variation of section thickness of a PPW panel subjected to 7 g at 40 mm standoff distance.

Although a total of four WLW panels were tested in localised loading, only those tested at an SOD of 40 mm yielded panels viable for scanning. In both cases, widespread debonding was observed. The WLW FML, shown in Figure 7.12, shows distinct variation in back and front face displacements indicative of debonding. A small highly localised

region can also be seen on both faces, and also debonding in the centre indicated by the large section thickness difference shown in Figure 7.12 (c). This damage appeared as pitting damage on the back face due to detonator shrapnel perforating the panel surface.

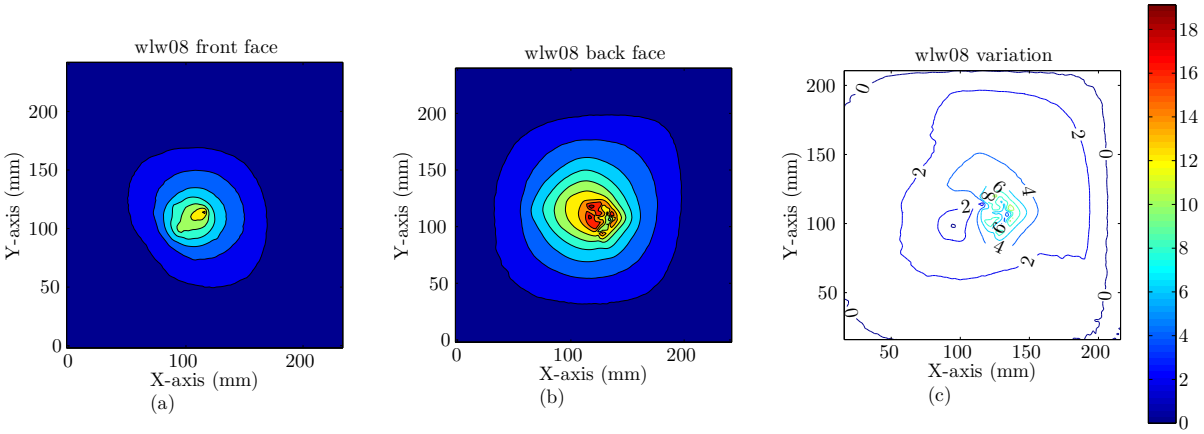

Figure 7.12: Contour plots of (a) front face displacements, (b) back face displacements and (c) variation of section thickness of a WLW panel subjected to 10 g at 40 mm standoff distance.

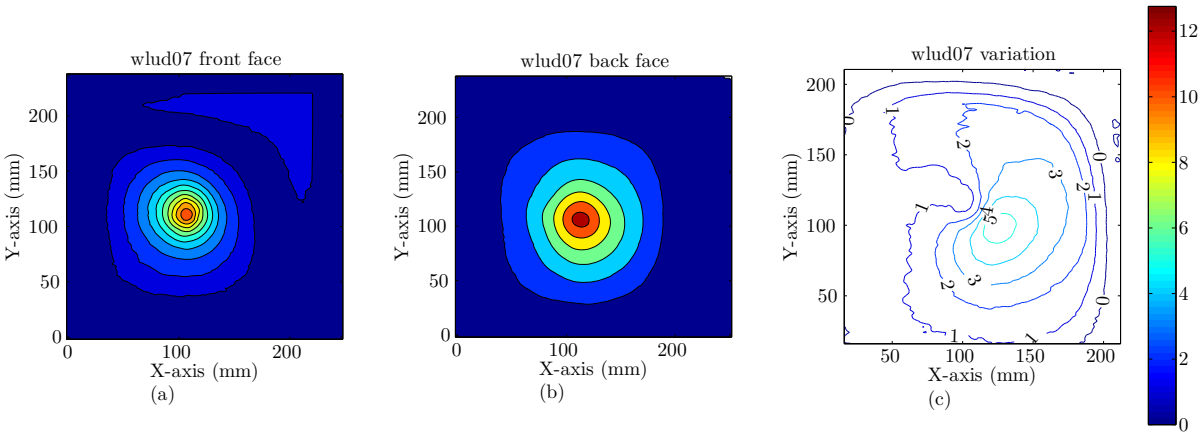

Figure 7.13: Contour plots of (a) front face displacements, (b) back face displacements and (c) variation of section thickness of a WLUD panel subjected to 10 g at 40 mm standoff distance.

Figure 7.13 shows the displacement contours of a WLUD series panel tested with 10 g of PE4 at 40 mm SOD. Only one panel of the WLUD series was successfully tested under localised loading conditions. The remainder of the localised tests failed due to detonator malfunctioning or shrapnel damage. Evidence of debonding can be seen in the variation in deflection between the front and back faces, shown in Figure 7.13 (c). The WLUD FML showed very similar characteristics to the WLW FML tested under similar conditions. It also exhibiting a circular, localised damage region on the front and back

faces. Deformation on the back face of the FML was spread over a wider region of the panel

Uniform Loading

More of the uniform loading tests were completed successfully due to larger charge masses resulting in more consistent detonation. As these tests exhibited little tearing or rupture, the tested panels could all be scanned. The displacement contour plots for all three test series, PPW, WLW and WLUD are shown in Figures 7.14 to 7.20. Some contour plots were not discussed due to their similarity to the rest of the plots from the respective test series. These plots can be found in Appendix D.

The contour plots of the typical panels for the PPW series are shown in Figure 7.14 and 7.15. Similar back and front face displacement contours for specimens throughout the test series. This is evidence of negligible to no debonding, similar to the results found during localised loading experiments. The contour plots more clearly show the square-shaped damage regions on both the front and the back faces of the FMLs and the larger peak inelastic deflection region with a more gradual decline towards the clamped boundary. The central, more circular damage regions fanned out into square-shaped damage affected areas towards the clamped boundary. The square damage region indicates the formation of yield lines that was observed during post test inspection, described in Section 7.2. This type of damage is indicative of a metal-driven response in square clamped plates subjected to uniform blasts. The larger peak deflection regions and gradual decrease in deformation towards the boundary indicate a more dome-shaped overall damage resulting from a larger blast affected area. The deformation at the centre of the panel appears circular and becomes square towards the panel boundaries. The same pattern is evident in both the front (a) and back (b) face deformations of the panels as seen in Figure 7.14 and 7.15.

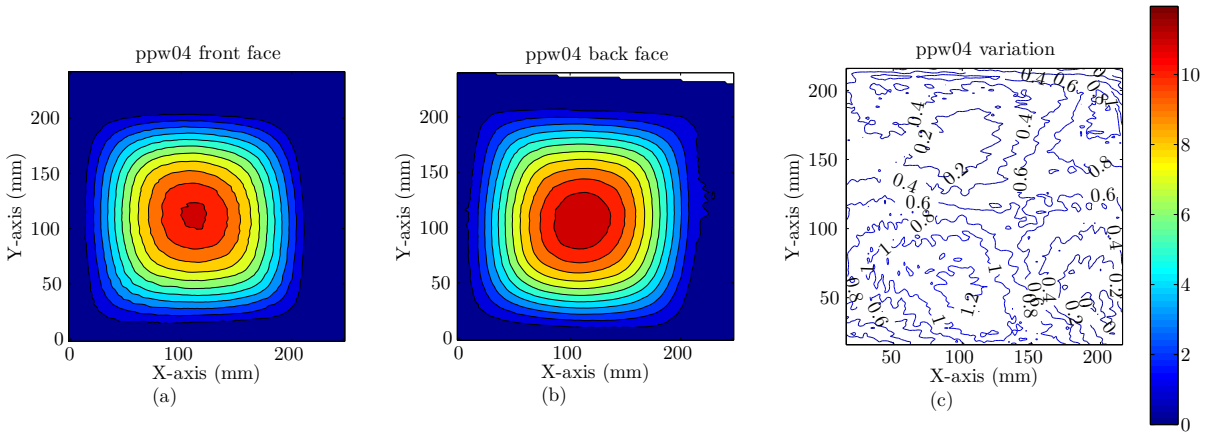

Figure 7.14: Contour plots of (a) front face displacements, (b) back face displacements and (c) variation of section thickness of a PPW panel subjected to 10 g at 200 mm standoff distance.

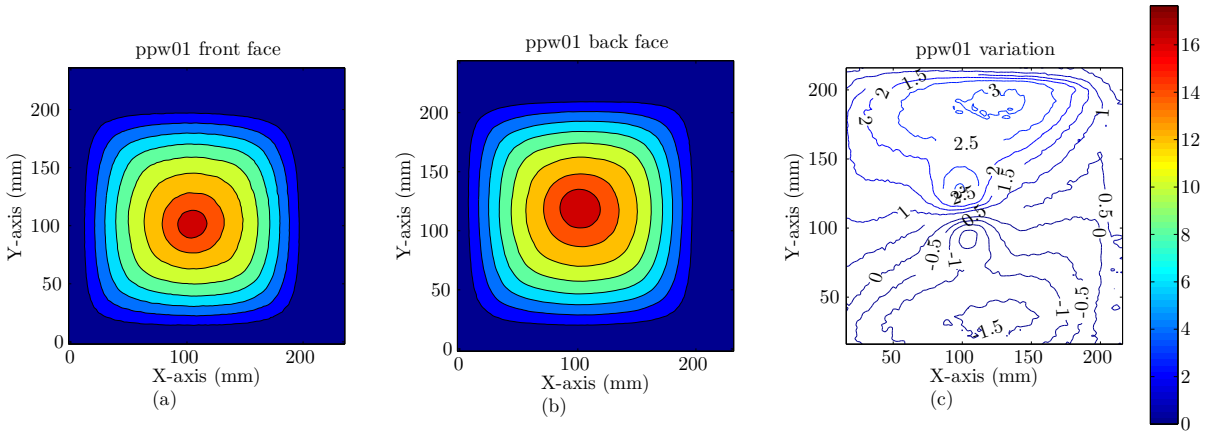

Figure 7.15: Contour plots of (a) front face displacements, (b) back face displacements and (c) variation of section thickness of a PPW panel subjected to 15 g at 200 mm standoff distance.

The WLW uniform loading series showed similar results to PPW uniform series with the addition of debonding in regions of the panels. This can be seen from the difference in front and back face displacements (c) shown in Figure 7.16 and 7.17. This debonding increased with charge mass and in some cases it even manifested as secondary bulges superimposed on the primary large inelastic deflection. Once again, the characteristic square-shaped damage and yield line formation was evident on both the front (a) and back (b) faces of the FMLs, seen in Figure 7.16 and 7.17, with the addition of a small round area of debonding in the plate centre. Large overall central damage regions were also observed with a gradual decline in deflection towards the panel boundary. Deformation in the back face was spread over a slightly larger area than the that of the front face.

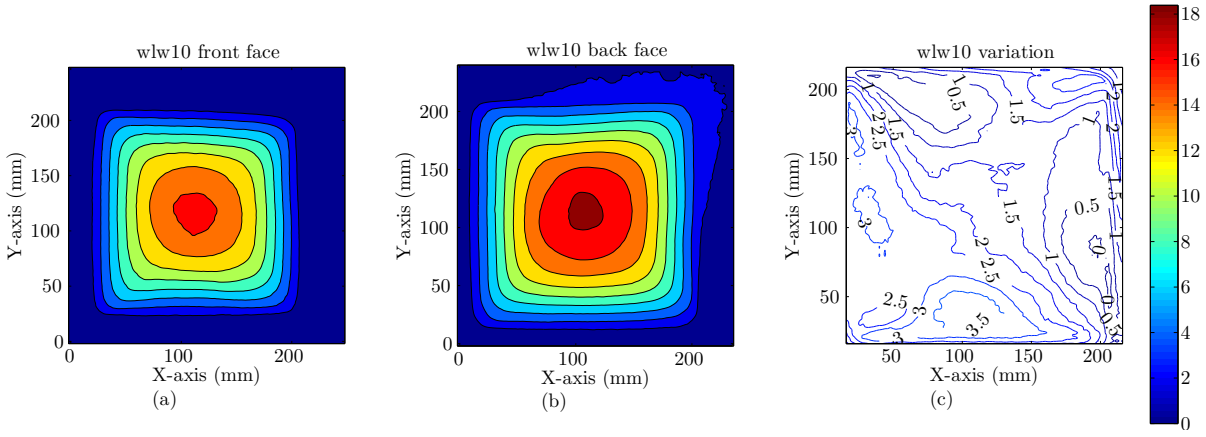

Figure 7.16: Contour plots of (a) front face displacements, (b) back face displacements and (c) variation of section thickness of a WLW panel subjected to 20 g at 200 mm standoff distance.

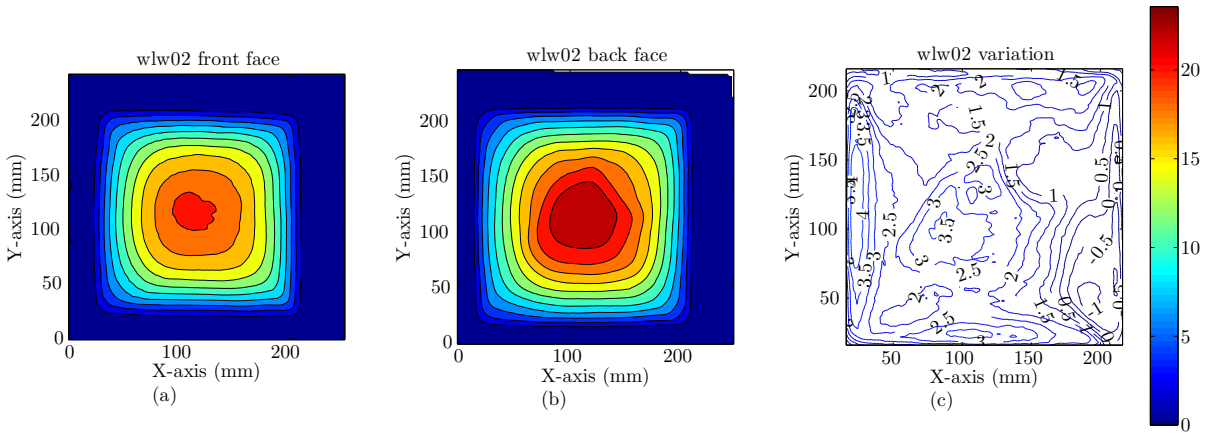

Figure 7.17: Contour plots of (a) front face displacements, (b) back face displacements and (c) variation of section thickness of a WLW panel subjected to 30 g at 200 mm standoff distance.

The WLUD series exhibited the same large square-shaped damage pattern of yield line and plastic hinge formation as the other two configurations. Circular damage was again observed in the centre of the panel transforming to a square contour towards the panel boundary. Debonding was observed in all of the WLUD panels, seen in the variation (c) of front and back face deflections in Figures 7.18 to 7.20. Similar to the WLW series, this behaviour amplified with increasing charge mass. A case of front face bulging was also observed in the WLUD series at at 35 g charge mass, shown in Figure 7.20. Figure 7.20 (c) shows the section thickness varying by up to 8 mm in the centre of the panel.

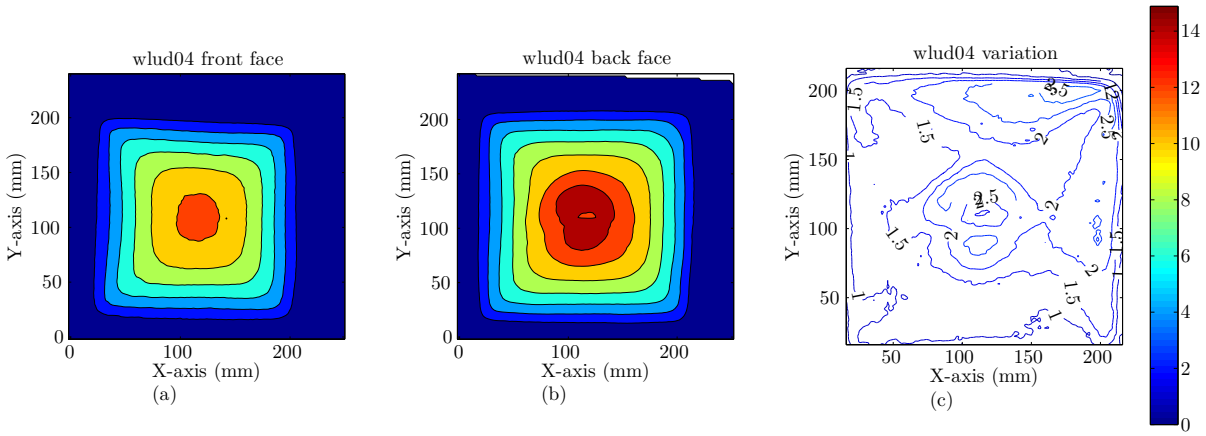

Figure 7.18: Contour plots of (a) front face displacements, (b) back face displacements and (c) variation of section thickness of a WLUD panel subjected to 15 g at 200 mm standoff distance.

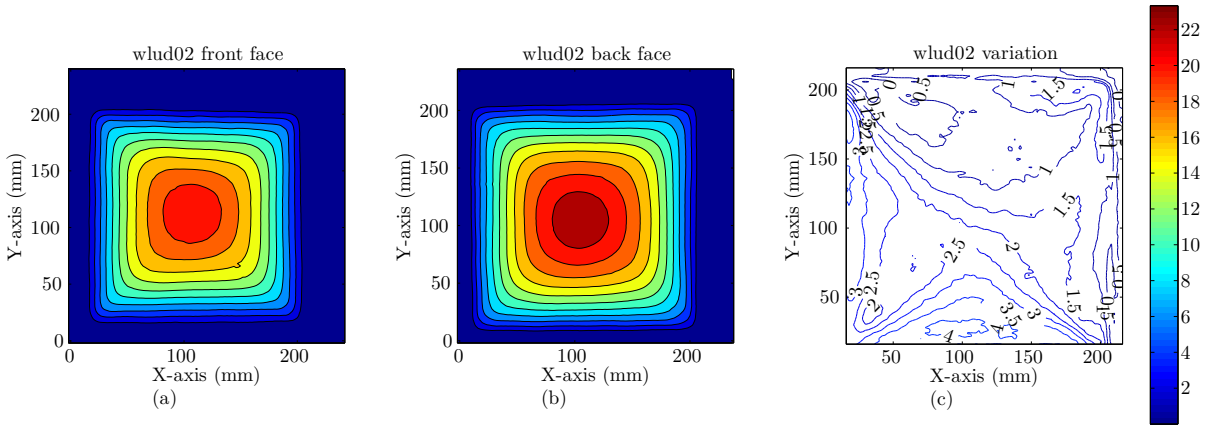

Figure 7.19: Contour plots of (a) front face displacements, (b) back face displacements and (c) variation of section thickness of a WLUD panel subjected to 30 g at 200 mm standoff distance.

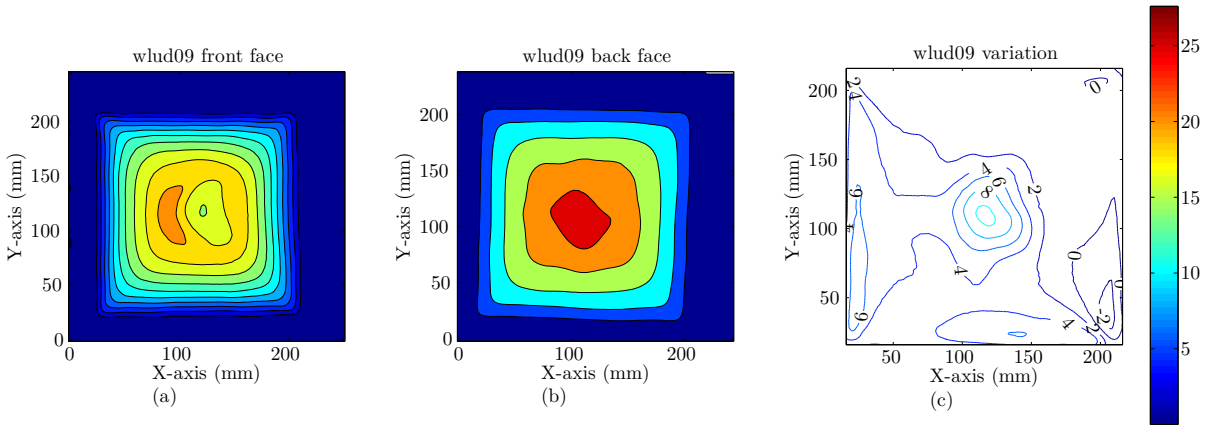

Figure 7.20: Contour plots of (a) front face displacements, (b) back face displacements and (c) variation of section thickness of a WLUD panel subjected to 35 g at 200 mm standoff distance.

7.2.4 Debonding Failure and Inter-Laminar Damage

The blast loaded FMLs were sectioned, cleaned and photographed to determine the extent of debonding and inter-laminar damage.

Localised Loading

The primary damage during localised loading was the large inelastic deformation concentrated centrally at the position of the explosive charge, shown in Figures 7.21 to 7.23. The damage radius also coincided with the radius of the explosive charge, similar to results found by other researchers [58, 59, 61].

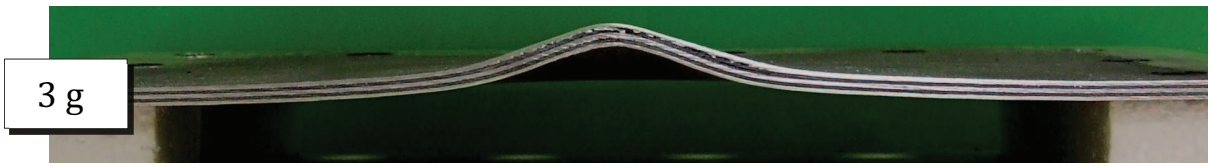

Figure 7.21: Photograph showing cross sectional views of the PPW series for 20 mm standoff localised loading.

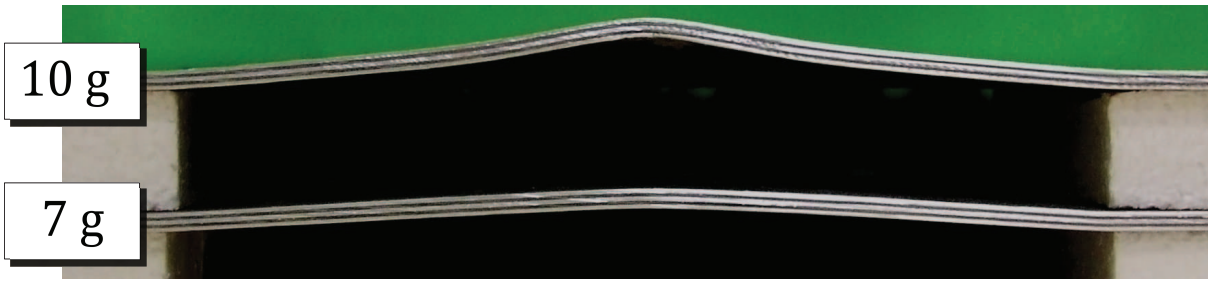

Figure 7.22: Photograph showing cross sectional views of the PPW series for 40 mm standoff localised loading.

The PPW test specimens exhibited no signs of debonding when subjected to localised loading as seen from the cross-sectional views in Figures 7.21 and 7.22. This confirmed the results reported in Section 7.2.3 from the surface scanning. The only damage to the panel was large inelastic deformation of central region exposed to the localised blast load.

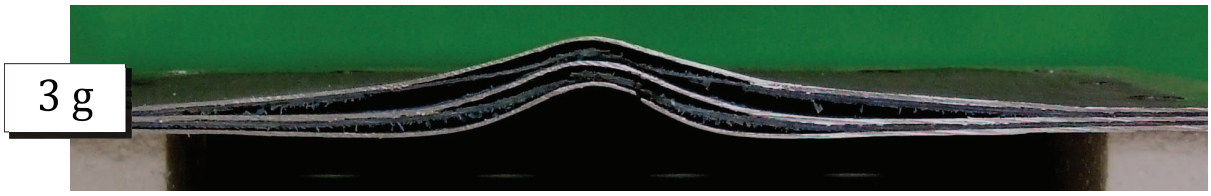

Figure 7.23: Photograph showing cross sectional views of the WLW series for 20 mm standoff localised loading.

The WLW series subjected to localised loading at 20 mm SOD underwent debonding throughout the panel area exposed to the blast. The primary inelastic deflection can be seen on the aluminium front face with the presence of tearing. This translates to the large scale debonding observed in Figure 7.23 and a gradual increase in radius of the inelastic deformation zone. Two different forms of debonding was observed including debonding of the GFRP laminate from the aluminium face directly in front of it or from the aluminium face directly behind it relative to the blast load.

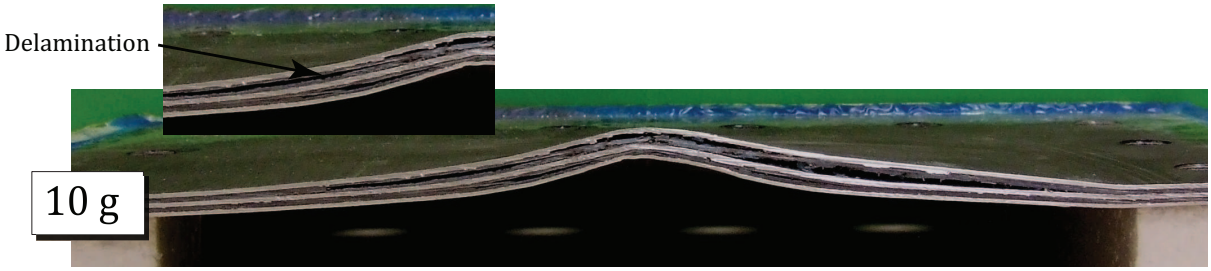

Figure 7.24: Photograph showing cross sectional views of the WLUD series for 40 mm standoff localised loading.

Figure 7.24 shows a cross-sectional view of a WLUD panel tested under localised loading conditions. The panel shows minor debonding throughout the area exposed to the blast. Debonding of the GFRP layer from both the front and back faces is observed througout the FML, similar to the WLW series. In addition some delamination is also evident in the WLUD panel.This could only take place in the WLUD FMLs due to the multi-layered uni-directional GFRP laminate. The delamination occurred primarily in the centre of the FML, the region affected most by the high strains of the localised load.

Uniform Loading

Cross sections of the uniformly loaded FMLs for each test series are shown in Figures 7.25 to 7.27. The cross sections were arranged according to increasing charge mass to show the damage increase.

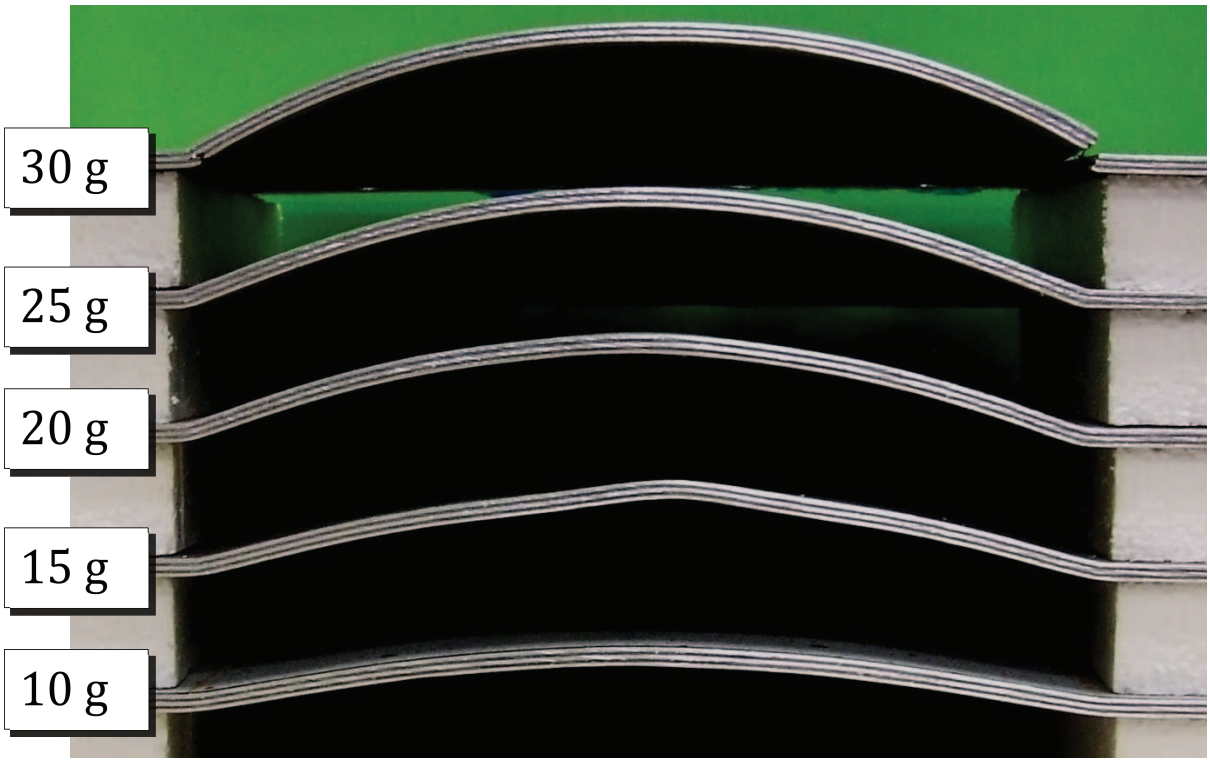

Figure 7.25: Photograph showing cross sectional views of the PPW series for 200 mm standoff uniform loading.

The PPW series shows a gradual increase in large inelastic deformation with increasing charge mass. No debonding was observed in the PPW series, leading to similar deformation in all layers. Rupture at the panel boundary occurred at 30 g charge mass.

This failure is consistent with failure modes observed in monolithic metal plates by Nurick et al. [52–54], seen in Table 2.4, and is discussed further in Section 8.1.

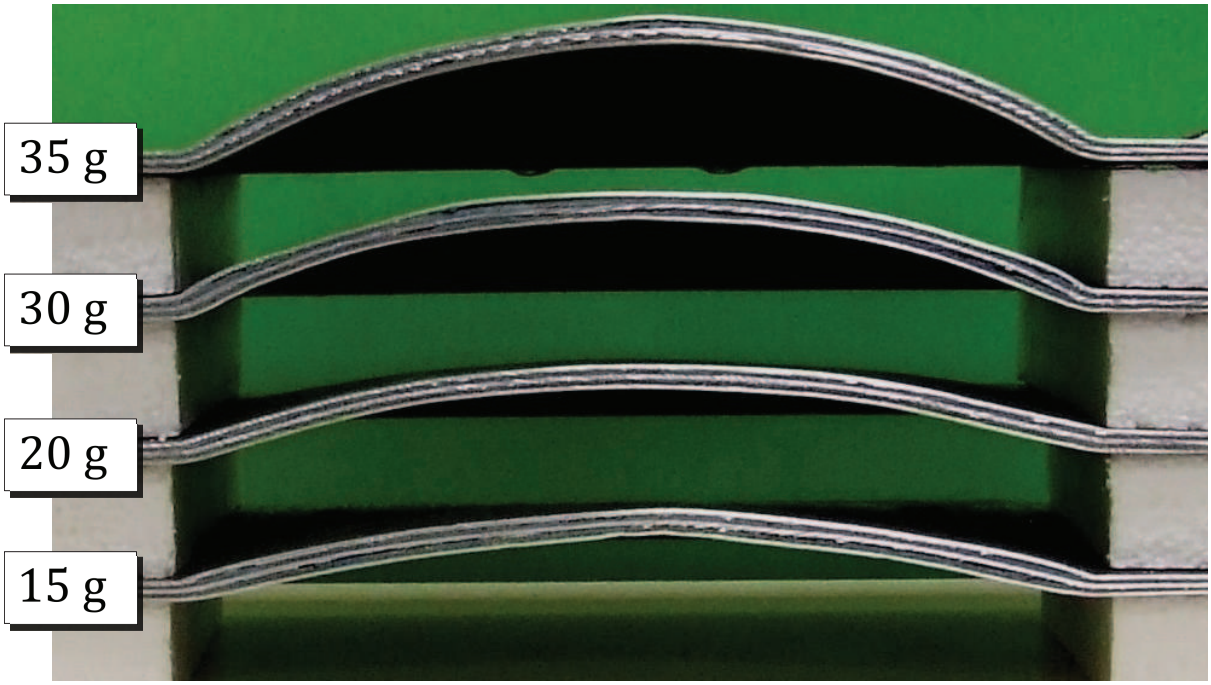

Figure 7.26: Photograph showing cross sectional views of the WLW series for 200 mm standoff uniform loading.

The uniformly loaded WLW series shows signs of debonding at relatively low charge masses. Debonding was observed at varying levels in the entire area exposed to the blast. From the cross-sectional photographs in Figure 7.26 it is evident that the level of debonding did not increase significantly with charge mass. The level of large inelastic deflections, however, increased similar to that observed in the PPW series. Debonding of the aluminium from the GFRP layers may have resulted in a slightly different distribution of damage in WLW panels compared to the PPW series. This is best seen in debonding of the laminates in the region of the clamped boundary. This resulted in a different cross-sectional profile than was observed in the PPW series. No rupture occurred even at a charge mass of 35 g.

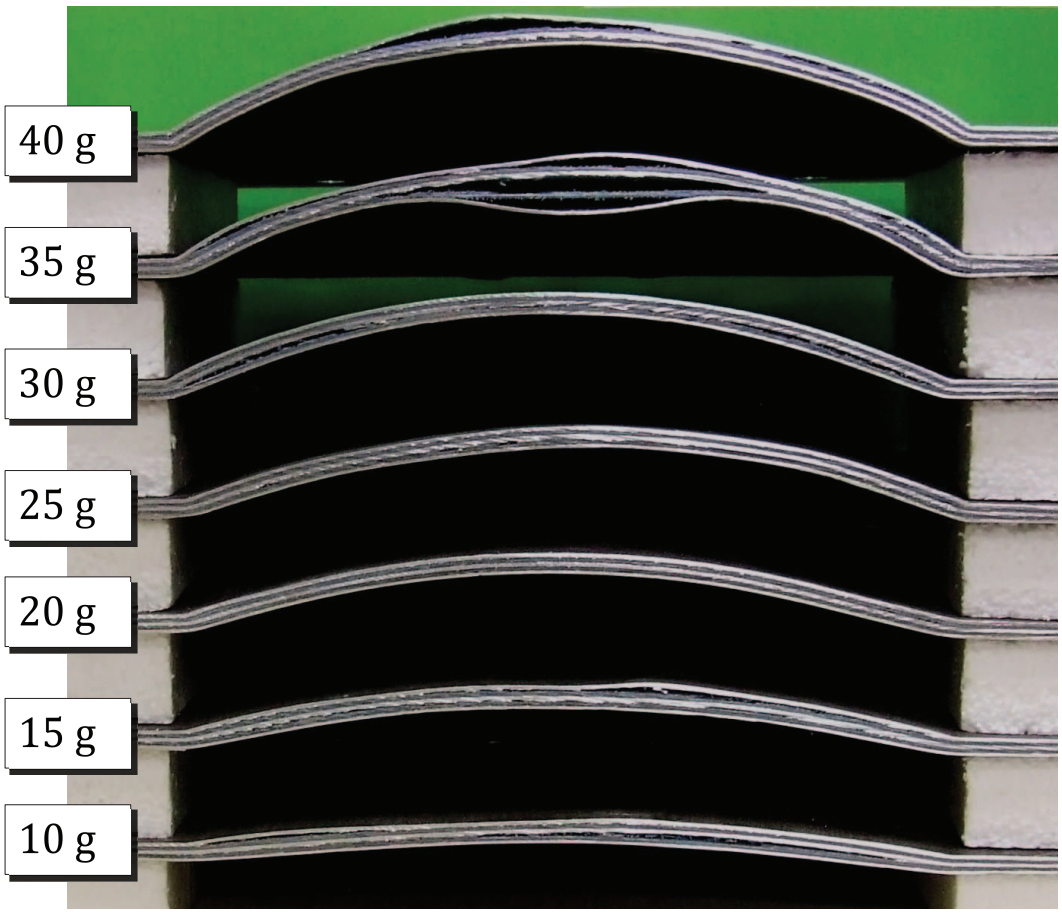

Figure 7.27: Photograph showing cross sectional views of the WLUD series for 200 mm standoff uniform loading.

From the cross-sectional photograph in Figure 7.27, it is evident that the WLUD panels exhibited similar behaviour to the WLW series when subjected to uniform loading. This included the presence of debonding even at low charge masses as well as large inelastic deformations. Similar to the WLW series, the WLUD series also experienced more prominent regions of debonding closer to the panel boundaries. In some cases, smaller separate deformation of the aluminium layers was seen superimposed on the larger inelastic deformation of the FML taking the form of aluminium bulges. This behaviour presented in areas where greater amounts of debonding occurred. Tearing was also not observed in any of the WLUD series aluminium layers even at charge masses as high as 40 g.

7.2.5 Panel Boundary Damage

Hole elongation or "pulling in" was observed as the prevalent damage mechanism at the clamped boundary, shown in Figure 7.28. At higher charge masses an inadequate clamping force at the boundary of the blast loaded panel resulted in the material being pulled inwards towards the centre as it deformed. This caused the elongation of the bolt holes. This phenomena was observed for all charge masses from 25 g, and might partly be the cause of the absence of rupture in the WLW/WLUD panels.

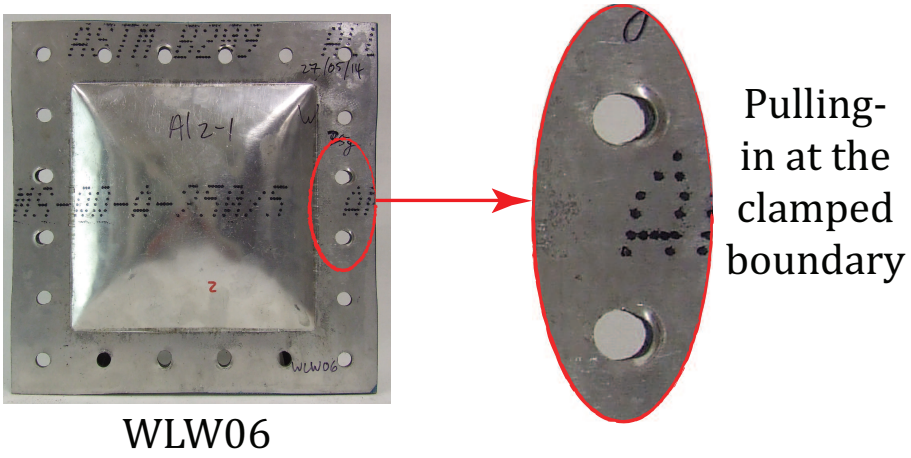

Figure 7.28: Photograph showing pulling in at the clamped boundary.

Rupture along the boundary edge was observed only in the PPW series, shown in Figure 7.29. This was observed on two separate occasions, using a 30 g charge in both cases. Different degrees of tearing was observed for both panels with PPW10 showing only partial tearing at the boundary and PPW03 exhibiting total tearing of the exposed panel area. The panel exhibiting only partial tearing also showed a greater degree of pulling-in at the boundary which likely resulted in enough energy being absorbed to stop further tearing of the panel. Tearing at the boundary is reminiscent of the behaviour of monolithic plates subjected to blast loading. This is indicative of an extremely good bond strength, allowing equal engagement of all layers of the FML.

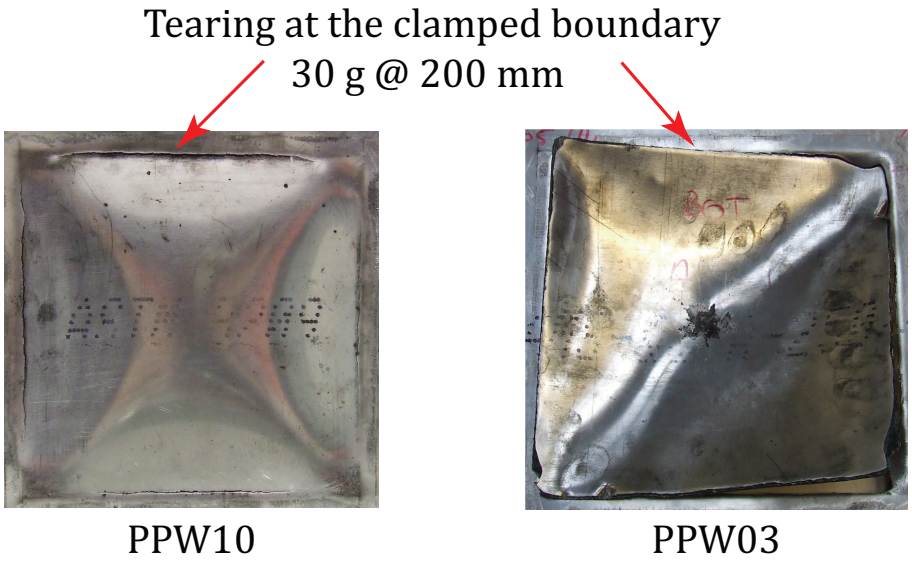

Figure 7.29: Photograph showing tearing at the clamped boundary.

Chapter 8

Experimental Analysis and Discussion

The behaviour of the FMLs were analysed by identifying the respective failure modes and performing dimensionless analysis on the recorded data. The results are indicated Tables 8.1 and 8.2 for the localised and uniform loading test series respectively. The respective methods of analysis are detailed Sections 8.1 and 8.2.

Table 8.1: Dimensionless analysis of localised blast loading results with * indicating rupture

Panel Designation	Charge Mass (g)	stand-off (mm)	Load Radius (mm)	Dimensionless Impulse ϕ_{ql}	BF d/t	Failure Mode
Tesults for 295 g m^{-1} woven SE 84LV & Al2024-T3 FMLs						
PPW02	3	20	12.5	2.34	3.01	Mode I[i]
PPW06	3	20	12.5	1.65	*	Mode IIspre[ii]
PPW08	10	40	10	3.31	2.33	Mode I
PPW09	7	40	10	2.74	1.25	Mode I
Test results for 400 g m^{-1} woven Prime 20LV & Al2024-T3 FMLs						
WLW05	10	20	12.5	4.90	*	Mode IIsprf[iii]
WLW03	5	20	12.5	2.34	*	Mode IIspe[iv]
WLW04	3	20	12.5	1.75	2.84	Mode IIdb[v]
WLW08	10	40	10	2.69	2.65	Mode Idb[vi]det[vii]
Test results for 0°/90° 220 g m^{-1} UD Prime 20LV & Al2024-T3 FMLs						
WLUD07	10	40	10	2.85	2.46	Mode Idbdl[viii]

[i] Large inelastic deformations.

[ii] Symmetric petalling of the panel rear surface, elongated in one direction.

[iii] Symmetric petalling of the rear and front surfaces of the laminated panel.

[iv] Symmetric petalling with the petals elongated in one direction.

[v] Partial tearing (no petals) with debonding evident in the cross-section.

[vi] Large inelastic deformation with debonding evident in the cross-section.

[vii] An Indication of detonator shrapnel affecting the failure mode.

[viii] Large inelastic deformation with debonding and delamination.

Table 8.2: Dimensionless analysis of uniform blast loading results

Panel	Charge Mass (g)	Dimensionless Impulse ϕ_q	BF d/t	Failure Mode
Test results for 295 g m^{-1} woven SE 84LV & Al2024-T3 FMLs				
PPW01	15	4.99	3.79	Mode I
PPW03	30	8.30	*	Mode II pi[i]
PPW04	10	3.23	2.52	Mode I
PPW05	20	5.48	4.38	Mode I
PPW07	25	7.76	5.08	Mode I pi
PPW10	30	7.70	5.78	Mode II*[ii] pi
Test results for 400 g m^{-1} woven Prime 20LV & Al2024-T3 FMLs				
WLW01	15	3.75	3.04	Mode Idb
WLW02	30	6.80	4.51	Mode Idb pi
WLW06	35	7.11	5.68	Mode Idb pi
WLW10	20	4.55	3.39	Mode Idb pi
Test results for 0°/90° 220 g m^{-1} UD Prime 20LV & Al2024-T3 FMLs				
WLUD02	30	6.50	4.38	Mode Idb pi
WLUD03	20	4.92	3.42	Mode Idb
WLUD04	15	3.98	2.61	Mode Idb
WLUD05	10	2.99	1.93	Mode Idb
WLUD06	25	5.64	3.96	Mode Idb pi
WLUD09	35	6.83	5.19	Mode Idb pi
WLUD10	40	7.53	5.37	Mode Idb pi

[i] An indication of where pulling-in was also observed.

[ii] Partial tearing failure observed at the clamped boundary.

8.1 Failure Mode Identification

Varying degrees of failure were observed throughout the different test sets. In order to better quantify failure in the FMLs, uniformly loaded panels were classified separate to panels subjected to localised loading. Existing failure modes for both monolithic plates [52–54] and laminated structures [11], defined by previous researchers, were used to categorise the observed failure of the tested FMLs. These modes are denoted and described in Tables 2.4 and 2.5 in Sections 2.4 and 2.5 respectively. In addition to the

predefined failure modes, indications were added to the failure modes of the panels where pulling-in (pi) and detonator shrapnel damage (det) was observed.

8.1.1 Mode I

As described in Section 2.5, Mode I failure and its derivatives are related primarily to large inelastic deformation. This includes deformation with debonding and delamination in laminated structures. This mode of damage was observed in the majority of localised and uniformly loaded panels. Photographs of the front and back faces of the panels which exhibited Mode I failure are shown in Figures 8.1, 8.2 and 8.3 for the PPW, WLW and WLUD series respectively.

The observed deformation for the localised blast tests is limited to the middle region of the panels, in the vicinity of the charge mass, as previously shown in the contour plots in Figures 7.10 and 7.11. Yield line formation becomes more evident at higher charge masses in the uniformly loaded panels, as expected, and indicated in the contour plots in Figures 7.14 and 7.15. There is little evidence of localised front face damage (particularly pitting) in the uniformly loaded panels since the standoff distances were much greater.

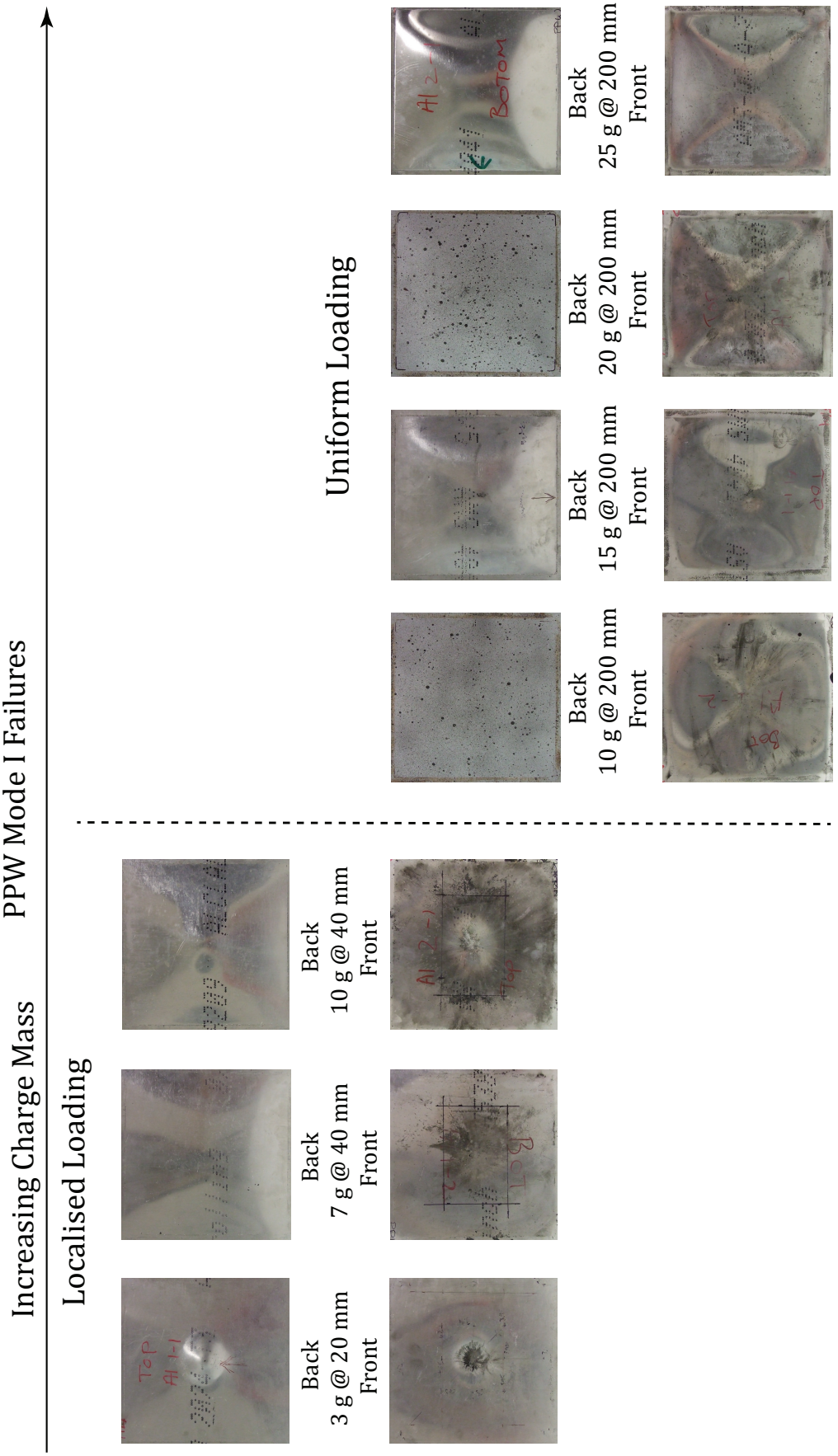

Figure 8.1: Photographs of PPW test series - Mode I failures.

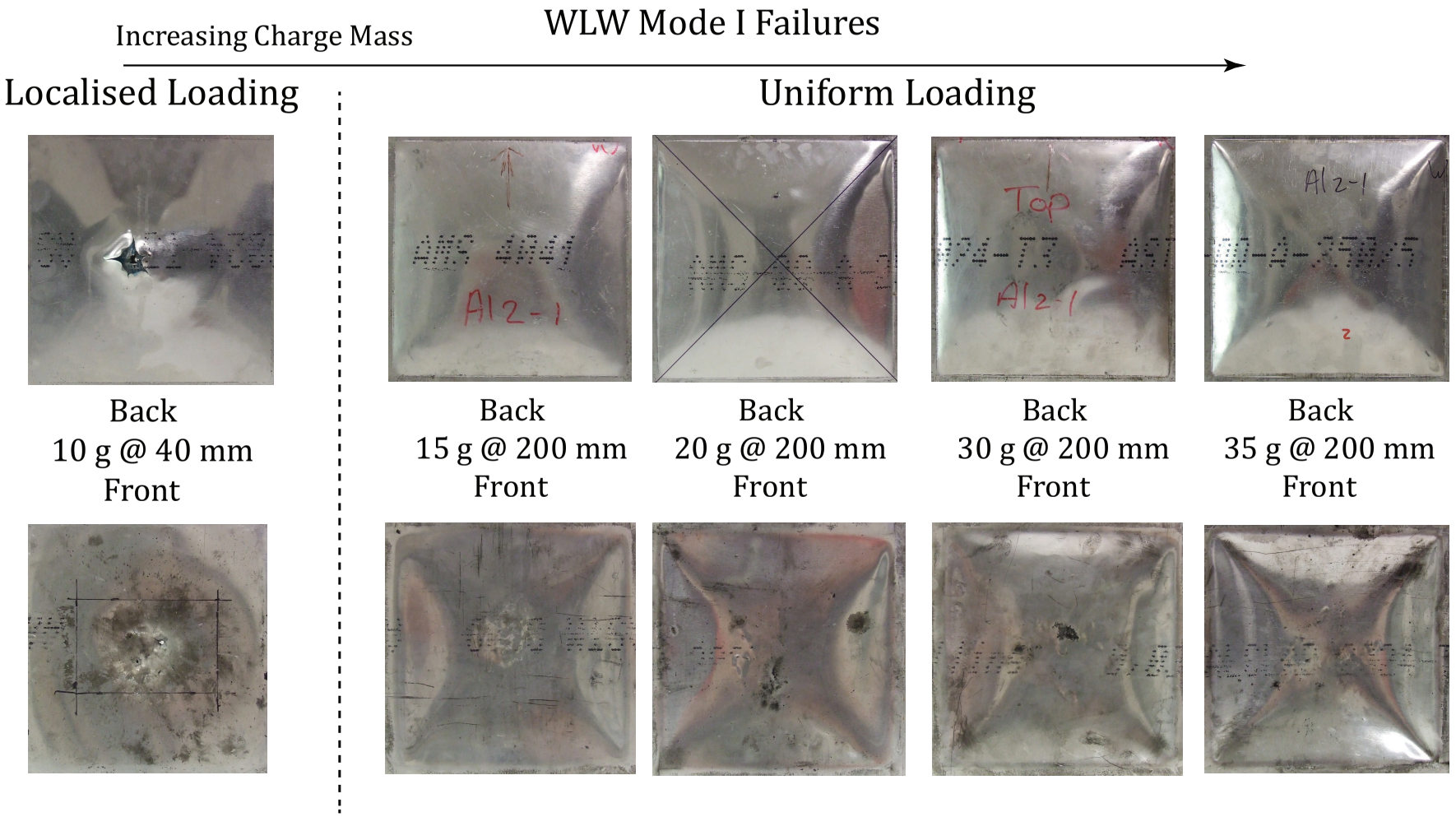

Figure 8.2: Photographs of WLW test series - Mode I failures.

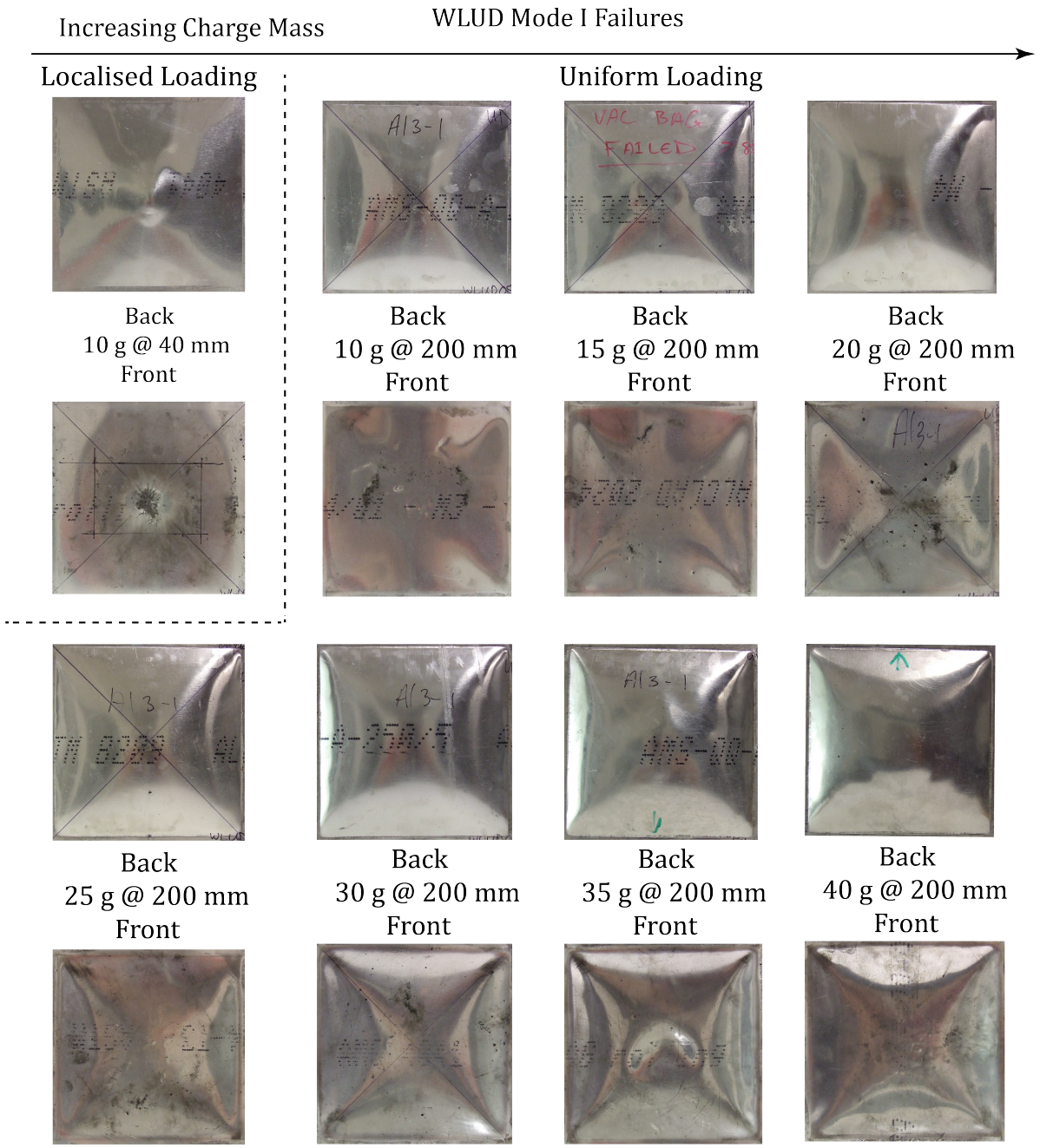

Figure 8.3: Photographs of WLUD test series - Mode I failures.

8.1.2 Mode II*

Mode II* failure is a transition mode where a combination of Mode I and Mode II failure is exhibited. In this transition mode, the large inelastic deformations of Mode I leads to partial tearing. This mode was only observed in the PPW10 (30 g PE4 at 200 mm) and WLW04(3 g PE4 at 20 mm) panels shown in Figure 8.4.

The PPW panel exhibited Mode II* failure closely resembling that of monolithic metals, detailed by Nurick et al. [2, 52–54], with partial tearing through the entire thickness of the panel along sections of the clamped boundary. The tearing seemed to originate in the middle of the boundary and move towards the corners. No difference in the degree of tearing was observed between the front and back faces. From the cross-sectional view of the panel, shown in Figure 7.25, the boundary rupture in the PPW panel appears to resemble shear failure, but is defined as Mode II* because of the large inelastic deformation of the panel. Work by Langdon et al. [100], including a microstructure analysis, showed that even Mode II failures in aluminium alloy plates exhibited a shear component in the actual failure mechanism.

The WLW panel exhibited Mode II* failure similar to that defined by Langdon et al. [11] with partial tearing of only the front face of the FML. Debonding was also observed in the cross-section view, shown in Figure 7.23, with large inelastic deformation of the rest of the panel layers.

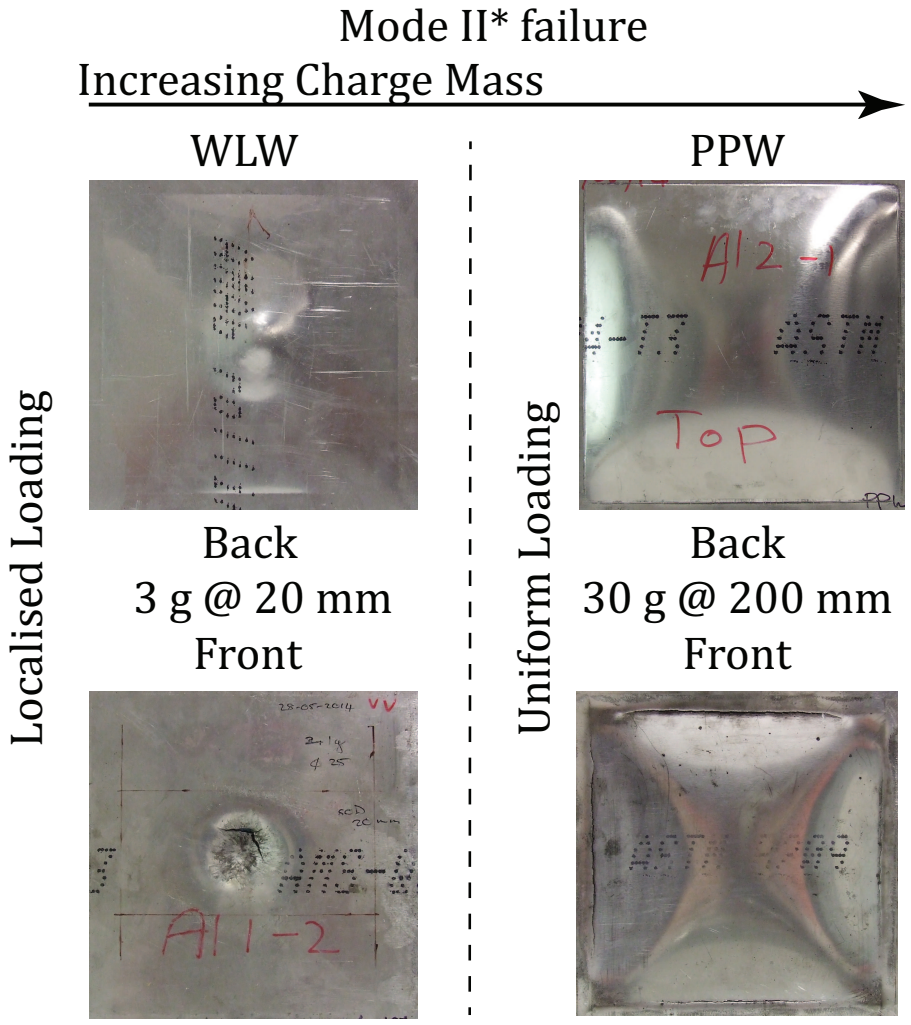

Figure 8.4: Photographs of PPW test series - Mode II* failure.

8.1.3 Mode II and Derivatives

Panels from the PPW and WLW series underwent different variations of Mode II failure. These ranged from pure Mode II (seemingly tensile tearing at the boundary as observed in monolithic metals) to Mode II sprf (symmetric petalling of the front and rear surfaces). Figures 8.5 and 8.6 illustrate the various Mode II failures observed during testing. No Mode II failures were observed in the WLUD series.

Failure of the PPW panel subjected to 30 g PE4 at 200 mm, showed rupture at the clamped boundary resulting in tearing of the entire exposed area, shown (b) in Figure 8.5. This failure was classified as Mode II due to the presence of large inelastic deformation in the torn section of the panel as discussed during Mode II* identification.

The PPW series exhibited Mode II failure when subjected to localised and uniformly distributed loading. Petalling was characteristic of the locally loaded panels (both in PPW and WLW responses). One of the PPW locally loaded panels exhibited rupture at the back face at a lower charge mass (3 g at 20 mm) than its WLW counterpart tested under similar conditions. Insufficient WLUD data was obtained under localised loading for fair comparisons.

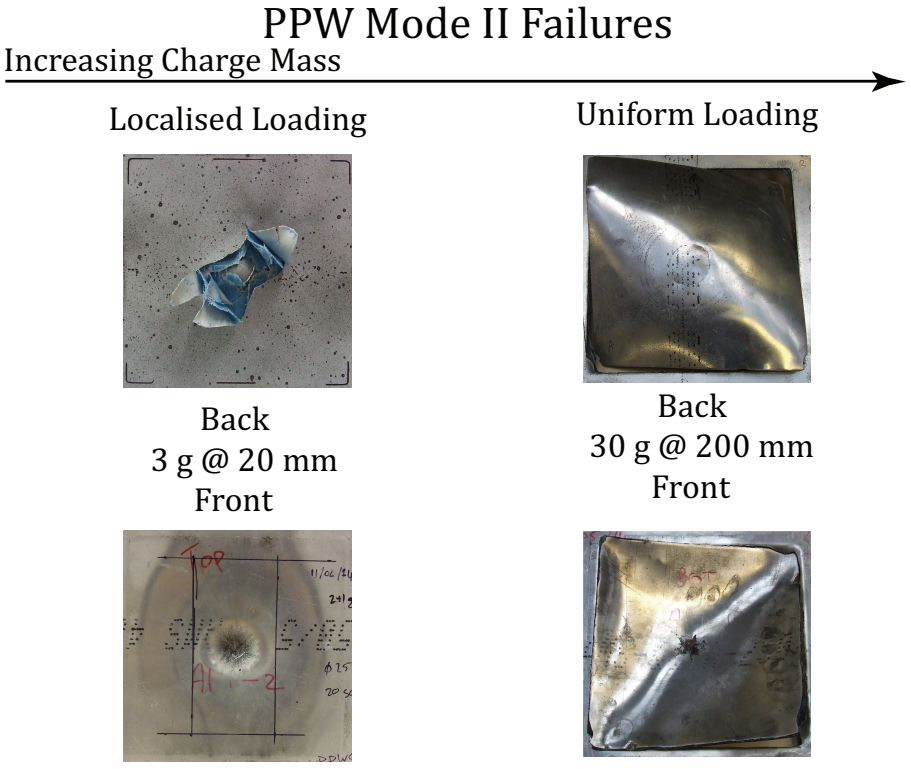

Figure 8.5: Photographs of PPW test series - Mode II failures.

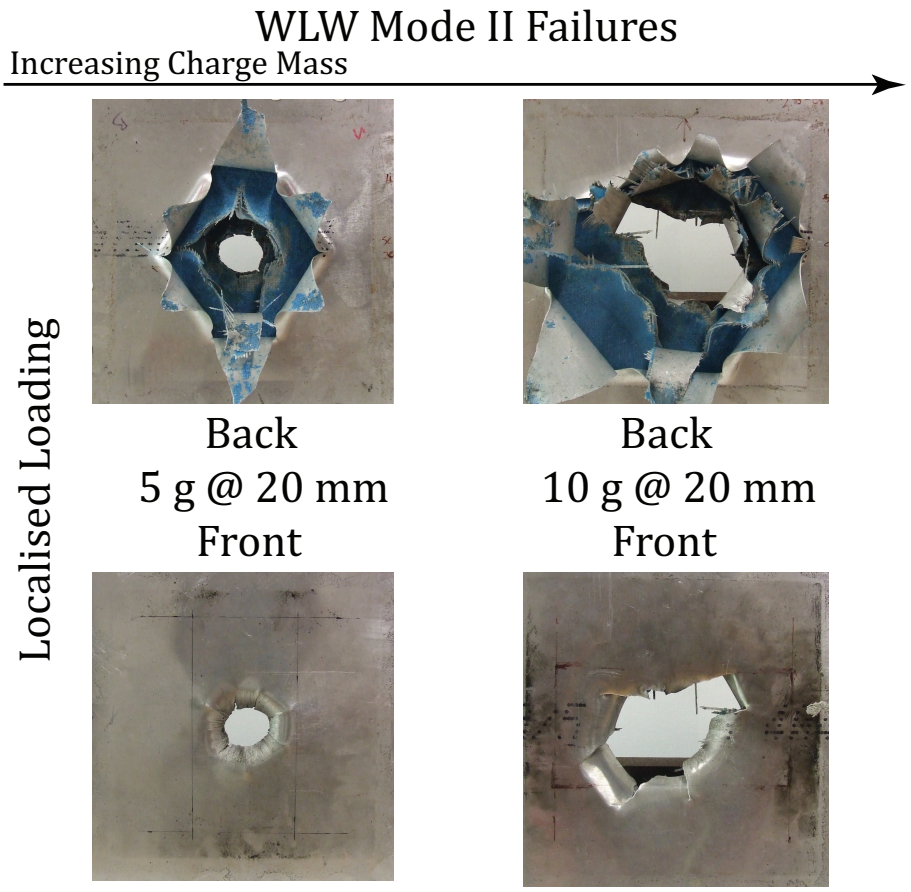

Figure 8.6: Photographs of WLW test series - Mode II failures.

8.2 Dimensionless Analysis

Dimensionless analysis techniques are used in this section to enable comparisons of the response of the current FMLs to other materials. Nurick and Martin [101] derived Equation (8.1) to compare quadrangular plates subjected to air-blast loading. The formula was based on Johnson's damage number [102] and has been used successfully in literature [1, 5, 11, 19, 57–59, 61, 64, 65, 82] for plates of different geometries and material properties. Equation (8.1) was modified by Nurick and et al. [60, 103] to account for localised loading, Equations (8.2), and loading at larger SODs, Equation (8.3).

$$\phi_q = \frac{I}{2t^2 \left(BL\rho\sigma\right)^{1/2}} \tag{8.1}$$

$$\phi_{ql} = \frac{I\left(1 + \ln \frac{BL}{\pi R_0^2}\right)}{2t^2 \left(BL\rho\sigma\right)^{1/2}} \tag{8.2}$$

Where I is the measured impulse, and B, L and t denote the plate width, length and thickness respectively. The variables ρ and σ represent the density and characteristic material stress respectively, and R_0 is the load radius of the centrally located explosive disk.

$$\phi_q = \frac{I\left(1 + \ln \frac{BL}{\pi R_0^2}\right)}{2t^2\left(1 + \ln \frac{S}{\pi R_0}\right)(BL\rho\sigma)^{1/2}} \tag{8.3}$$

With the addition of the variable S, the stand-off distance, Equation (8.2) is modified to calculate the dimensionless impulse for structures where the load is generated by detonating explosive disks at greater standoff distances. The material properties used in these equations are smeared values, calculated using the rule of mixtures described in Section 2.1 and detailed in Table 8.3. The variable σ denotes the static yield strength of the material when considering monolithic metals, but has also been defined as the global ultimate tensile strength for thermoplastic FMLs. The value of σ was calculated as a smeared value of the aluminium alloy σ_{UTS} using the method of volume fractions, shown in Equation (8.4), where t represents the respective thicknesses. Using the dimensionless impulses, results from the different test series could be compared to one another as well as to the documented blast response of other FMLs [57–59, 64, 104].

$$\sigma = \frac{t_{Al_{total}}}{t_{GFRP_{total}}}\sigma_{UTS_{Al}} \tag{8.4}$$

Table 8.3: FML material properties calculated using the rule of mixtures.

		PPW	WLW/WLUD
Average Total Thickness t	mm	4.5	5.1
Density ρ	kg/m^3	1890	1850
Yield strength σ	MPa	237	209
Young's modulus E	GPa	50.9	48.5

Plotting the calculated dimensionless impulses, ϕ_q, against the inelastic displacement thickness ratios (d/t) obtained from the locally and uniformly loaded panels, yielded the graphs shown in Figures 8.7 and 8.8 respectively.

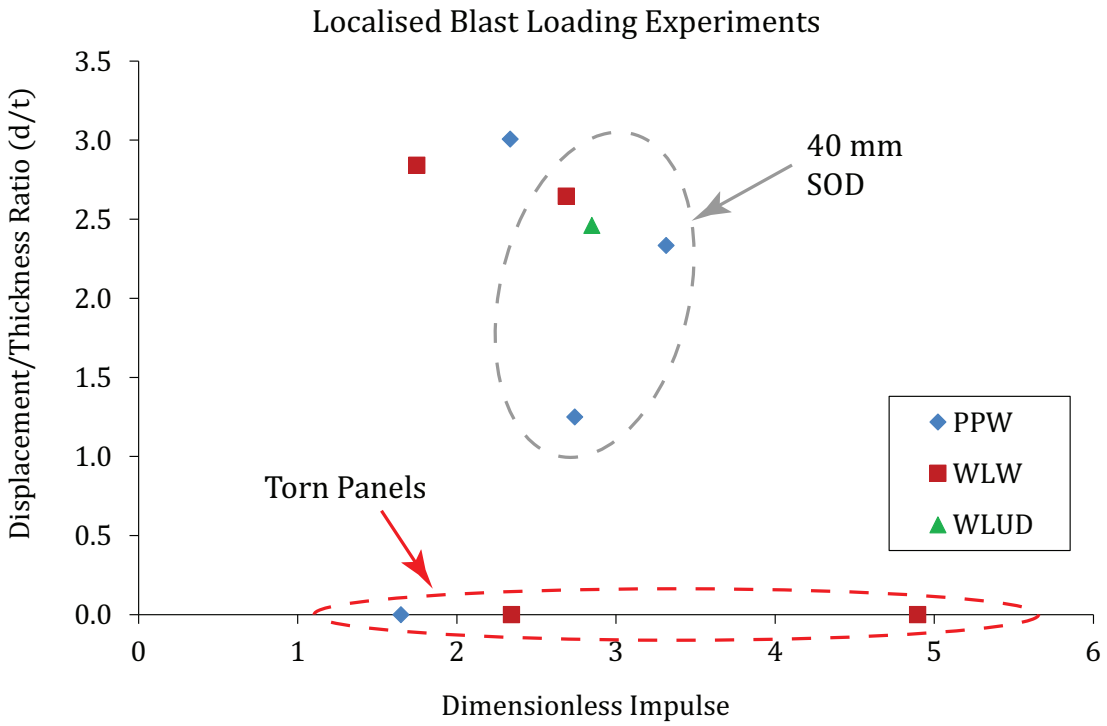

Figure 8.7: Graph of dimensionless impulse vs displacement/thickness ratio - localised loading.

No distinct pattern can be seen from the localised loading results. This was a due to the degree of damage experienced by the FMLs by the close proximity of the charge and detonation. No inelastic displacement reading could be obtained from the FMLs undergoing petalling, resulting in an unattainable displacement/thickness ratio, indicated as zero in Figure 8.7. The response was largely affected by localised damage caused by shrapnel which obscures any trends. Additionally the variation in displacement was ±5mm which is small in absolute terms, but represents a large percentage variation because of small overall inelastic deformation and the elastic nature of the composite. Hence, it is not possible to make a definite conclusion about the response of the FML types to localised loading due to the inconsistent loading and insufficient test data. Further tests were not performed due to the high degree of shrapnel damage.

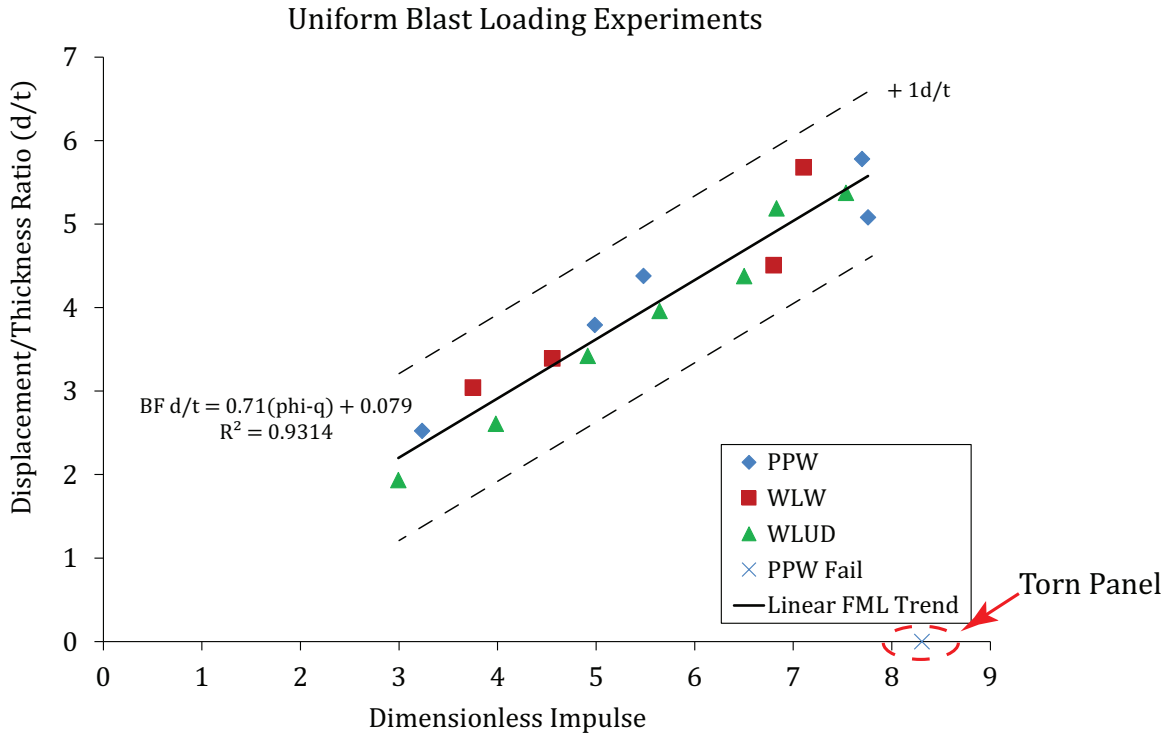

Figure 8.8: Graph of dimensionless impulse vs displacement/thickness ratio - uniform loading.

Dimensionless analysis of the uniformly loaded FMLs show far more consistent results with similar trends in all three test series. Displacement-thickness ratio values for each series falls within 1 unit value of the respective trend line, shown in Figure 8.8. The inelastic displacements of all three FML test series subjected to uniform loading, were largely aluminium dominated and relatively insensitive to the weave and matrix types. This is indicated by the similar trends shown for each of the three test series.

8.3 Failure Mode Mechanisms and Thresholds

It is difficult to quantify the various mechanisms that play a role in the failure of laminated structures such as FMLs. Research suggests, however, that debonding does not act as significant absorption mechanism of the overall energy [7, 8, 58, 59]. The energy absorbed by the various failure mechanisms during ballistic impact testing of GLARE®, was estimated by Hoo Fatt et al. [6] using an analytical model. The model suggested that 85% to 92% of the energy was absorbed by bending and membrane deformation of the FML. Hence it is not surprising that the three different composite configurations had little influence on the dimensionless displacements of the uniformly

loaded panels.

The behaviour of unbonded, stacked glass fibre panels was investigated by Franz et al. [63] in order to determine the energy absorption effects of debonding. Their findings suggested that layers towards the back of the structure provide extra support resulting in smaller front face displacements. This behaviour is similar to the results observed during the highly localised loading experiments, where greater variations in displacement were observed between the FML front and back faces. This is illustrated in Figure 8.9 as well as the contour plots discussed in Section 7.2.3.

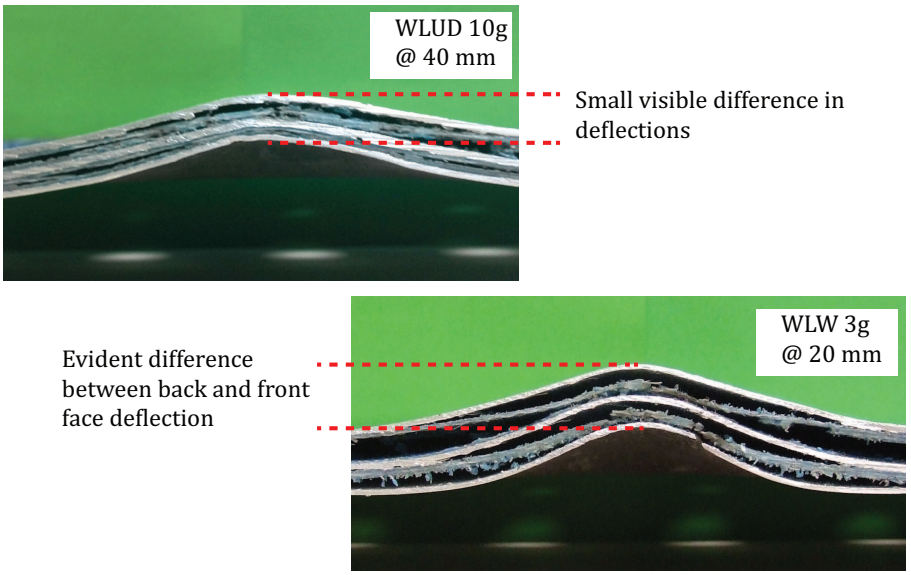

Figure 8.9: Photographs showing back face support resulting in smaller front face deflection.

Thin FMLs generally exhibit deformation throughout the panel due to fewer back layers lending structural support. Similar sized displacements are thus observed on both the front and back faces of thin FMLs. Distinct variations in response were observed between the different test series. The PPW series underwent no debonding, transitioning directly from large inelastic displacements to tearing at the clamped boundary, shown in Figure 8.10. This behaviour is similar to that of monolithic metal plates, meaning that the energy required to cause debonding within the FML exceeded the energy required to cause rupture. Even in the case where the entire exposed area was torn out of the FML, no debonding was evident. Although proving exceptional bond strength, this characteristic may not be beneficial to the FML as it results in less damage being absorbed as well as the formation of a high velocity projectile, which could result in further damage to objects behind the panel.

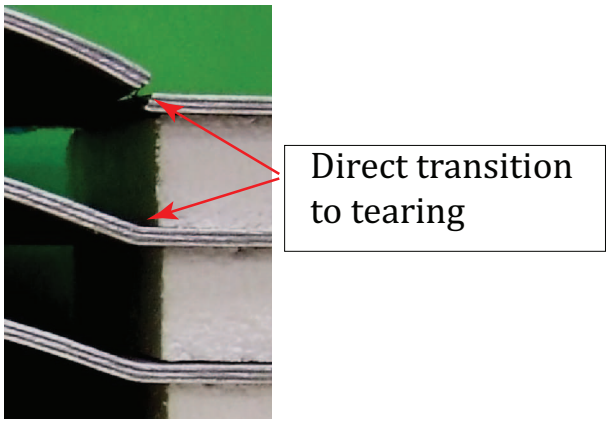

Figure 8.10: Photographs showing transition from inelastic displacements to tearing.

In contrast with this, both the WLW and WLUD series experienced debonding even at lower charge masses. Debonding, however, was not evenly distributed over the surface of the FML. Even in the presence of debonding, the specimens of both series still deformed relatively evenly. In some cases, distinct smaller deformations were observed in the different metal layers superimposed on the large inelastic deformations of the FML, see Figure 8.11. This is as a result of more energy being required to cause further debonding than deformation of the already debonded metal section.

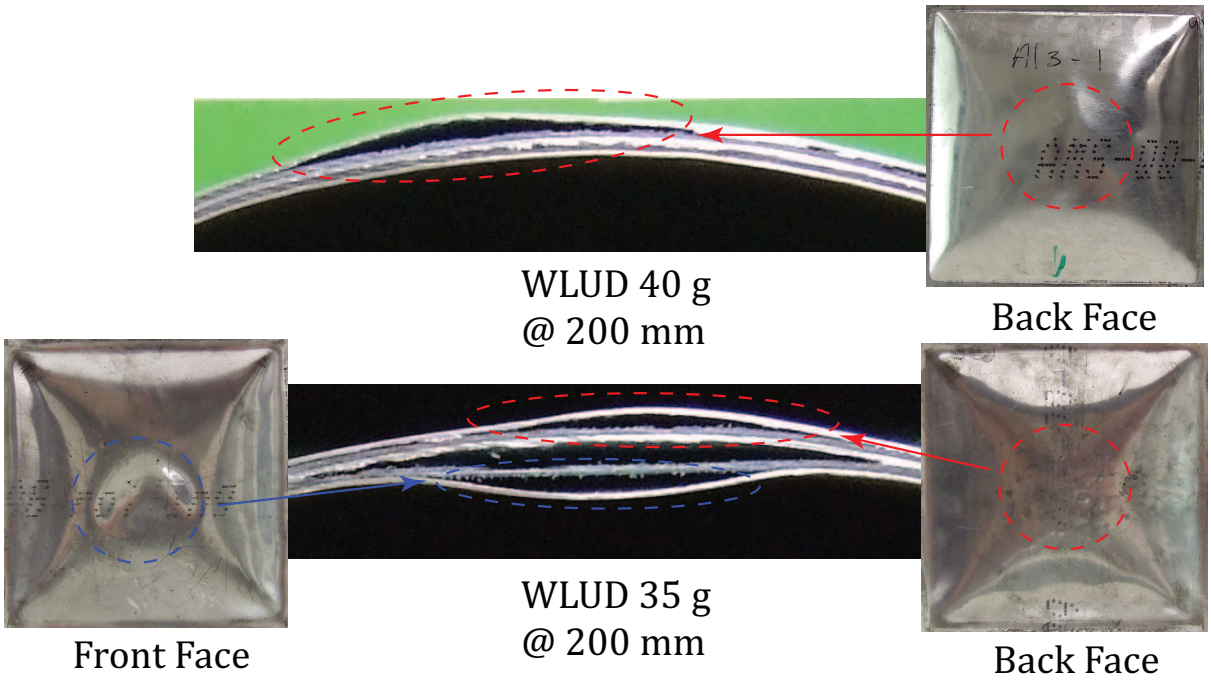

Figure 8.11: Photographs showing superimposed deformation of aluminium laminates.

In both the WLW and WLUD series, consistent debonding failure was observed at or close to the clamped boundary, shown in Figure 8.12a. The metal sections at the clamped boundary are prone to the highest amount of deformation. After the FML underwent initial deformation due to the compressive blast wave, the tensile wave reflected off the back layer caused debonding between the composite and metal layers. The elasticity of the composite caused the front layers of the FML to rebound, leaving the back layer more deformed than the front. This behaviour presented itself more prominently at the clamped boundary. This also supports the claims by Hoo Fatt et al. [6] that bending and membrane deformation play the greatest role in energy absorption. The behaviour may also explain the dissimilar gradient of the deformed plate profile as seen in Figure 8.12b, in the cases where this debonding was observed. Debonding at the clamped boundary also showed a decrease with an increase in pulling-in, suggesting that pulling-in might serve to mitigate a significant amount of energy.

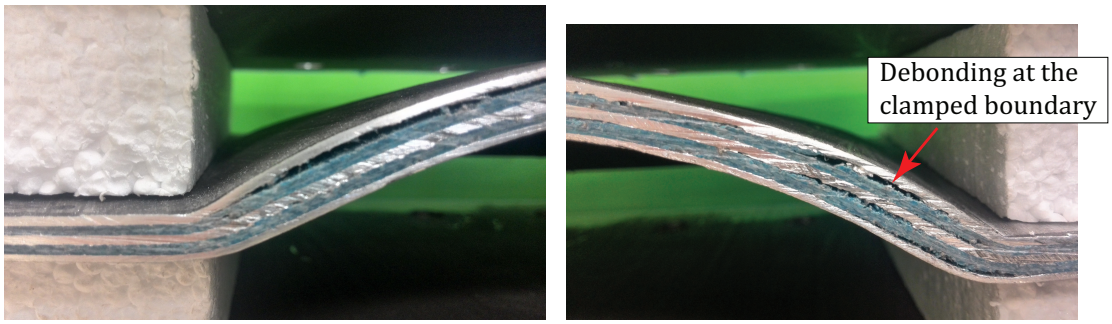

(a) Photograph of WLW debonding at the clamped boundary.

(b) Photograph of WLUD debonding at the clamped boundary.

Figure 8.12: Photographs showing boundary deformation and debonding failure in WL series panels subjected to uniform loading.

8.4 Influence of Composite Type on FML Failure

The different components of each test series caused slightly different FML responses to damage. The general trends, however, suggest that the response of all the FMLs were largely aluminium based. The slight variations due to matrix and fibre configuration are explored in this section.

8.4.1 Influence of GFRP Matrix and Weave Density on Failure Modes

The greatest difference in response was due to the use of different matrix materials and curing processes. These differences are best illustrated by considering the PPW series which contained a 295 $g\,m^{-1}$ plain weave SE 84LV prepreg, and the WLW series which contained 400 $g\,m^{-1}$ plain weave E-Glass fibre with Prime 20LV epoxy. The respective GFRP layers differed in epoxy matrix and weave density. The SE 84LV prepreg matrix based FMLs showed a significant increase in bond strength when compared to the Prime 20LV wet-layup FMLs. These differences are best illustrated when considering the cross-sectional images of the PPW and WLW series seen in Figures 7.25 and 7.26.

The significant increase in bond strength leads to a more monolithic plate type response to damage observed in the PPW series with the onset of tearing at the clamped boundary. The debonding of the WLW series lead to an apparent increased damage resistance as the FML only underwent Mode I failure, as opposed to tearing which can be classified as a more catastrophic failure event. Larger weave densities resulted in a slightly thicker and stiffer composite layer in the WLW series. This increased stiffness resulted in larger elastic rebound of the composite laminates, further adding to the effects of debonding.

8.4.2 Influence of Glass Fibre Configuration on Failure Modes

The effect of fibre configuration was investigated by comparing the WLW and WLUD test series. Both series were manufactured using the Prime 20LV epoxy as matrix. WLW FMLs were manufactured using a single layer of 400 $g\,m^{-1}$ woven E-glass fibre while WLUD FMLs were manufactured using 2 layers of $0°/90°$ 220 $g\,m^{-1}$ uni-directional E-glass fibre. The effects of the slight difference in weave density of these fibre configurations were assumed negligible. Both test series showed fairly similar responses to uniform loading conditions with large inelastic deformation of the entire blast affected area, yield line and plastic hinge formation as well as widespread debonding of the GFRP laminate from the aluminium layer. The similar large inelastic deformations and yield line formation indicated an aluminium driven response to the uniform loading. Dimensionless analysis indicated that the WLUD series had a slightly better response to uniform damage than the WLW series with a lower d/t ratio throughout. Concentrated areas of debonding were observed in regions close to the clamped boundary in both test series indicating similar debonding mechanisms at work. The cross-sections views of the FMLs in Figures 7.26 and 7.27, however, indicate that the WLUD series had a greater tendency to debond and form superimposed aluminium

bulges on the surface of the FML.

During localised loading, the WLUD series also experienced delamination along with debonding, shown in Figure 7.24. This indicated that, under highly localised conditions, the interlaminar bond behaved similar to the bond between GFRP layers. This adds another mechanism of damage absorbtion to the WLUD FMLs. In general, the effects of fibre weave appear to be less significant than bond strength and panel thickness.

8.5 Comparison of Tested FMLs to Numerical Simulations

Figure 8.13 shows a comparison of the simulated uniform blast load to the experimentally achieved uniform blast load. The trend line shown is a one-to-one linear relationship between the numerical model and experimental configuration. The graph in Figure 8.13 shows good correlation between the simulated uniform loading impulses and the actual experimental impulses for all simulated charge masses. This indicates that the correct experimental loading conditions were simulated in the numerical model.

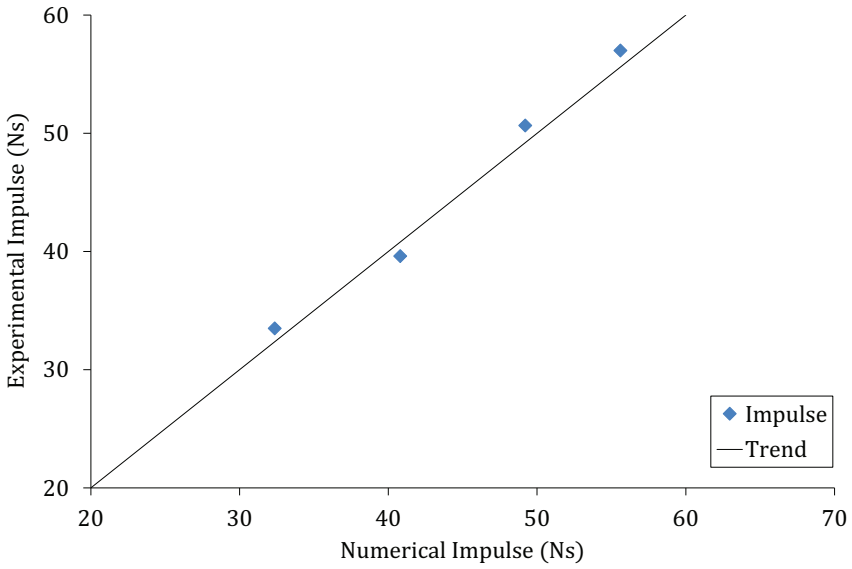

Figure 8.13: Graph showing a comparison of the experimentally achieved impulse to the numerically simulated uniform blast impulse.

Due to the good consistency of the experimental data throughout the different test series and the limited debonding in both the WL series (in charge masses smaller than

30 g), displacement/thickness (d/t) ratios from all three test series were compared to the numerically obtained values, shown in Figure 8.14. The peak numerical deflection values used for comparison show much better correlation to the experimental values than the mean values obtained in the initial analysis of the simulations. This was attributed to the aluminium dominated response of the actual FMLs resulting in much less elastic rebound (which is a composite driven response) than seen in the numerical simulations. Less rebound and the highly plastic nature of the aluminium would result in a much more accurate prediction of actual specimen deflection from the simulated initial peak displacement.

The graph shows that the predicted peak d/t ratio of the numerically simulated FMLs underestimate the actual d/t ratio of the PPW series. This was the result of simplification of the boundary conditions. Since no allowance was made for slip or fibre pulling at the clamped boundary, the simulated response of the FMLs was overly stiff in comparison to the actual response of the PPW series. This resulted in larger deflections and consequently larger d/t ratios. It is also evident that the WLUD and WLW series show much closer correlation to the simulated data than the PPW series. This was the result of slightly thicker composite layer in both WL series causing a larger elastic rebound of the actual tested FML thereby reducing the experimental d/t ratio.

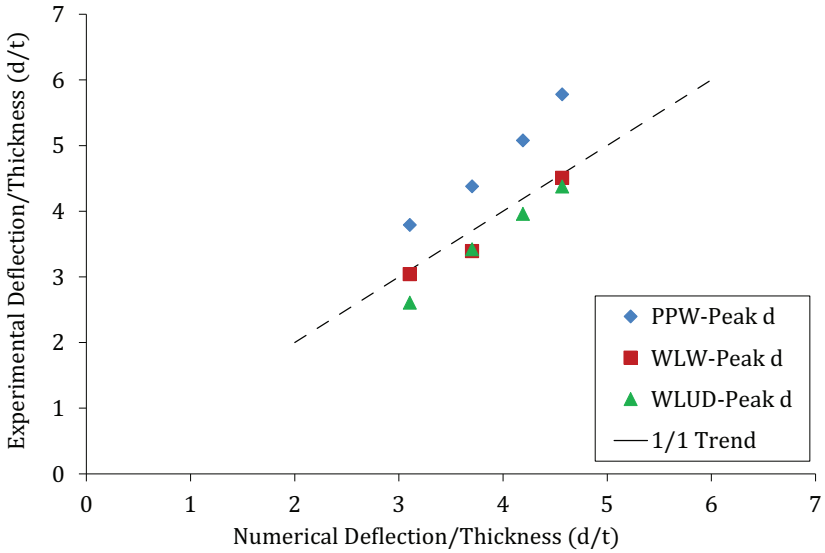

Figure 8.14: Graph showing a comparison of the experimental dimensionless back face deflection to the numerically simulated dimensionless deflections resulting from uniform blast loading.

8.6 Comparison of FMLs with Literature

The experimental results were plotted against the reported results of both GFPP and GFPA based FMLs subjected to various degrees of blast loading, obtained from literature [57–59, 64, 104]. This was done to determine how the tested FMLs compared to other current technologies. The current FMLs show a similar response to blast loading as GFPP and GFPA based FMLs responses reported by Langdon et al. [57–59, 64, 104]. A slightly lower backface d/t ratio was seen in all three test series subjected to uniform loading conditions, which is considered favourable. The large amounts of scatter in the data from references [57–59, 64, 104] is due to the large differences in stacking configurations of the FMLs. The current FMLs exhibited far less scatter as there was no significant difference in the stacking configuration.

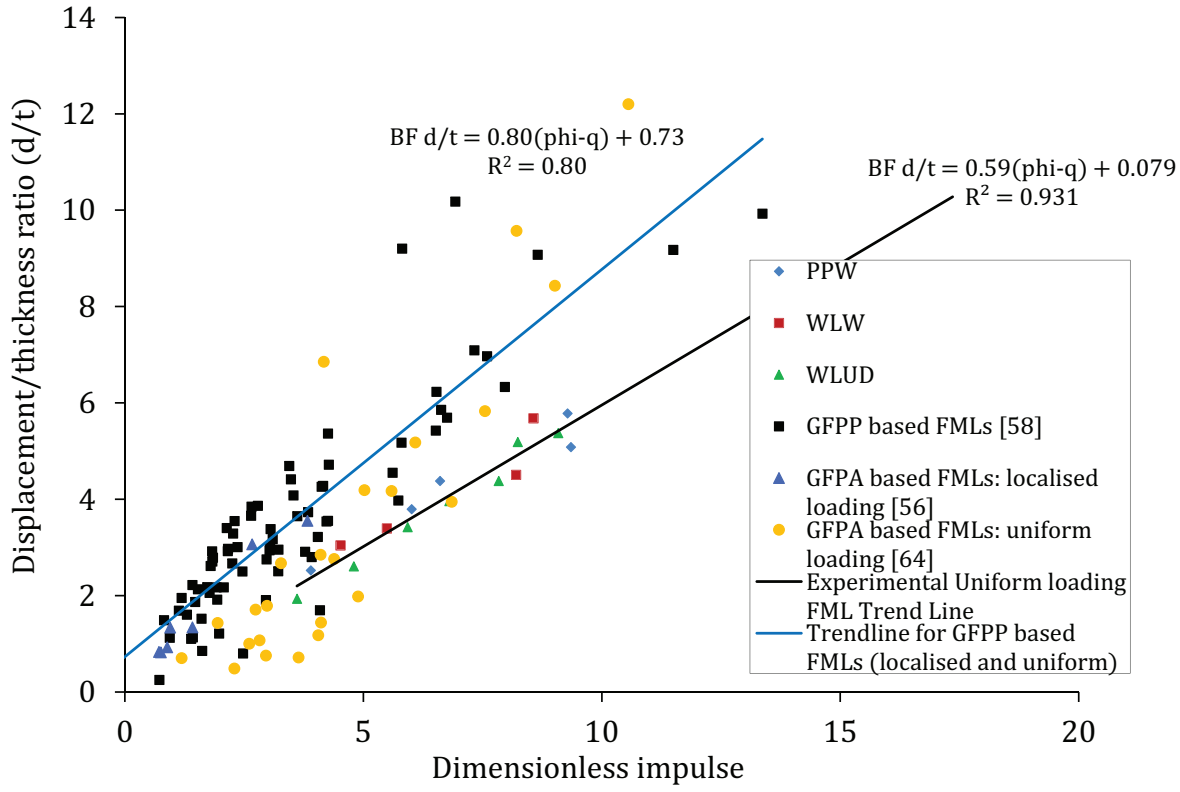

Figure 8.15: Graph showing a comparison of the experimental FML series to GFPP and GFPA based FMLs from literature [57–59, 64, 104].

8.7 Comparison of FMLs with GLARE®

Figure 8.16 shows a graph of d/t vs dimensionless impulse, comparing the current test results to experiments on GLARE® 3. Langdon et al. [5] performed tests on GLARE® 3 and found that it behaves similarly to monolithic metal plates when subjected to blast loading. This is seen in the large inelastic deformation and yield line formation, similar to that of the PPW test series. Although undergoing failure at a lower dimensionless impulse than GLARE®, the response was largely aluminium dominated. It should be noted that the dimensionless impulse range of the current FMLs is much smaller than that of GLARE® while also resulting in higher dimensionless displacements. The current FMLs are approximately three times thicker than GLARE® 3 due to the use of thicker constituent materials. If the constituent materials are thus scaled down equally while the thickness ratio and bond strength between the aluminium and GFRP interface remain the same, the response would remain aluminium dominated while not debonding. A reduction in thickness could lead to an increased dimensionless impulse range, see Equation (8.3), resulting in the manufactured FMLs becoming more competitive with the tested GLARE® 3.

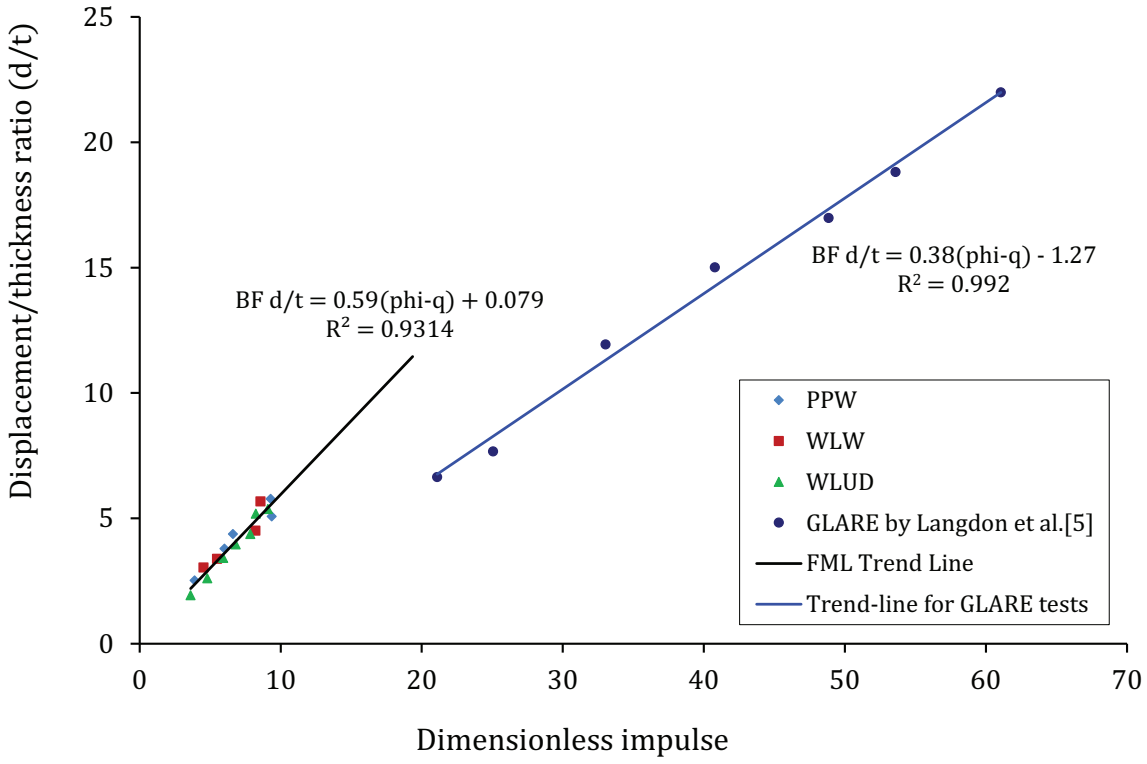

Figure 8.16: Graph showing a comparison of the experimental FML series to GLARE® 3 tester by Langdon et al. [5].

In terms of displacements, there is little difference between the PPW, WLW and WLUD panels, when examining Figure 8.16. This is despite the presence of debonding in the wet-layup panels (WLW and WLUD).

Chapter 9

Concluding Remarks and Recommendations

This study aimed to manufacture and test FMLs consisting of similar constituent materials as GLARE®, in order to further investigate the blast response of glass-fibre epoxy-based FMLs. Tensile and SLB specimens were manufactured to characterise the aluminium alloy and Al/GFRP interfacial bond strength respectively. The SLB specimens were manufactured using different layup techniques and cure schedules in order to determine the best manufacturing method for the FMLs. Numerical modelling was employed to plan the experimental conditions and determine the probable limits of loading. The manufactured FMls were tested under both localised and uniform loading conditions and analysed with regard to damage and failure modes. The response of the tested FMLs was compared to that other blast loaded FMLs form literature [57–59, 64, 104] and GLARE® 3 [5].

9.1 FML and Specimen Manufacturing and Surface Treatment

FMLs and test specimens were manufactured using AL2024-T3 and glass-fibre reinforced epoxy, employing the surface treatment techniques recommended by van Tonder [12]. These techniques consisted of a combination of bead blasting, Silane chemical treatment and the addition of a Redux 609 film adhesive. Cure cycles of the manufacturing and surface treatment techniques were adapted to allow for concurrent layup and cure/post-cure, reducing manufacturing time. Material properties of the constituent materials were determined from the available literature.

9.2 Material and Bond Strength Characterisation

The temper grade of the aluminium alloy (Al2024-T3) was confirmed by comparing the material response of the tensile specimens to the response of Al2024-T3 available in the literature. The measured yield strength (σ_Y), ultimate tensile strength (σ_{UTS}) and elongation at fracture (ε_f) show good correlation with literature values [13]. The properties obtained from the aluminium sheets showed good consistency, important for the manufacture of FMLs with consistent material properties. The true stress and true plastic strain of the aluminium was used to characterise the alloy with Johnson-Cook material model. Dependant parameters of the model that were not characterised, were obtained from the available literature [80].

Single-leg bend tests provided the interfacial SERRs of the Al/GFRP bond for three sets of specimens (Prime 20LV MSM, Prime 20LV SSM and SE 84LV). The surface treatment schedule (Bead blasting, Silane and Redux 609) in combination with the SE 84LV prepreg resulted in specimens with the highest critical SERR. These specimens showed consistent debonding of the Redux layer from both the aluminium and GFRP interfaces. Delamination between the GFRP layers of the SE 84LV in some specimens, indicated an interfacial bond strength close to that of the composite laminates. This was confirmed when the Mode I critical SERR of the specimens were compared to that of woven E-glass/epoxy laminates.

Specimens manufactured using the SSM method, showed the highest critical SERRs of the two sets Prime 20LV based SLB specimens, along with the greatest variation in failure modes. The SSM process appeared to degrade the bond strength between the aluminium and Redux layer while improving the bond strength between the Redux and GFRP layer. The resultant failure modes included debonding of the Redux from the aluminium surface alone and mixed debonding from both the aluminium and GFRP surfaces. The Prime 20LV MSM specimens showed the most consistent failure modes and lowest average critical SERR. The Redux layer consistently debonded from the GFRP layer indicating that the MSM process greatly reduced the bond strength specifically between the Redux and GFRP layers.

None of the specimens showed bond strengths close to that of GLARE® reported in literature [92], indicating that the bond strength of the tested specimens at the Al/GFRP interface was not equal to that of GLARE®. GLARE® showed a substantially larger critical SERR than the tested specimens, however, it appeared that bond strength between the Al/GFRP interfaces was similar to the bond strength between the layers of UD E-glass/epoxy. Similar behaviour was observed in the SE

84LV specimens, indicating that the primary method of improving laminated material performance is to achieve consistency in bond strength in all layers of the laminate. Any further increase in bond strength of the SE 84LV specimen Al/GFRP interface would be redundant.

9.3 Blast Test Design

The blast experiments were designed through numerical modelling, simplifying conditions by assuming a fully clamped boundary. The effects of debonding were neglected due to the exceptional bond strength of the PPW series. The localised loading simulations showed that damage under these conditions was concentrated in the centre of the target panel, suggesting failure could occur though large inelastic deformation, tearing and eventually petalling. The uniform loading simulations indicated that the largest concentration of damage was at the clamped boundary. Large plastic strain values in this region indicated that the most probable mode of failure, following large inelastic displacement, would be tearing/rupture at the clamped boundary. Charge masses for testing were determined by comparing strain data from the numerical model to the available data for the constituent materials, assuming conservative prediction from the simulations. Results from the experiments were similar to the predictions from the design simulations, although the final displacements of the FMLs were generally higher than predicted. This may be due to the absence of debonding and simplification of the boundary conditions in the numerical models. Further investigation is required to determine the effects of each.

9.4 Blast Testing and Analysis

Localised and uniform blast loading tests were performed on three sets of FMLs using the test plan determined through numerical modelling. The FML sets varied in composite layup technique (varying the composite matrix) and fibre configuration to determine the effects of these processes and constituent materials on their blast response.

None of the test series performed well under highly localised blast loading (20 mm SOD). These conditions generally resulted in tearing of the FML surface layers, petalling and hole punching. Variations in consistency was observed due to the included

damage of detonator shrapnel. When the stand-off distance was increased to 40 mm, the FMLs showed more consistent damage and deformation, however, results were still affected by the detonator shrapnel causing damage to the FML front face. Consistent debonding was observed in both WLW and WLUD panels under localised loading conditions. The woven SE 84LV series showed no debonding, transitioning directly from inelastic deformations to tearing and petal formation, shown in Section 8.1, Figure 8.5. The aluminium dominated response of the FMLs resulted in the absence of the characteristic diamond-shaped back face damage in FMLs subjected to localised loading, reported by other researchers [57–59].

Debonding was again observed in both series wet-layup panels (WLW and WLUD) subjected to uniform loading, appearing at even the lowest charge masses (10 g) and showing minor growth with increasing impulse. At higher impulses, superimposed inelastic deformation was observed in the debonded regions of the WLUD series. The PPW series experienced no trace of debonding, similar to GLARE® 3, even when subjected to charge masses as high as 30 g. The PPW series showed deformation behaviour and failure modes similar to that of monolithic metal, transitioning directly from large inelastic deformations to tearing at the clamped boundary. The FML response to uniform loading was also dominated by the aluminium laminates, showing large inelastic deformation and yield line formation. Dimensionless analysis on the data supported this as the similar dimensionless responses were seen from all three test series. Pulling-in at the clamped boundary was observed at all charge masses above 25 g, with the exception of the WLW series which started showing this behaviour from 20 g. The degree of pulling-in also increased with increasing charge mass. Analysis of the FMLs revealed that pulling-in may have absorbed enough energy in some cases to stop the occurrence of certain failure modes.

The tested FMLs showed a slight reduction in the experienced d/t ratios, when compared to the dimensionless response of GFPP and GFPA based FMLs available in literature [57–59, 64, 104], indicating a more favourable response. Data from the tested FMLs were also more consistent due to the consistency of stacking throughout the series. When compared to GLARE® 3 [5], all the tested FMLs showed a lower tolerance to blast damage. The FMLs were tested at a lower dimensionless impulse range and resulted in higher dimensionless displacements. Due to the dependence of dimensionless impulse on thickness ($1/t^3$), a decrease in constituent material thickness could produce an FML with properties comparable to that of GLARE® 3, should the bond strength be retained.

9.5 Research Outcomes

The quasi-static tests were successfully simulated numerically and used to obtain material models for blast test design simulations. It was determined that, similar to results by van Tonder [12], the SE 84LV and surface treatment schedule had superior bond strength compared to the Prime 20LV and surface treatment schedule. The different SLB configurations resulted in different modes of crack propagation each affecting critical SERR. Specimens manufactured sing the SE 84LV prepreg showed interfacial bond strengths approaching that of the GFRP laminates indicating that further increase of this bond strength would be redundant. Critical SERRs of all the specimens were lower than that of GLARE®, indicating the Al/GFRP interfacial bond strength is not similar to that of the commercial product.

Experimental blast conditions were successfully designed using numerical simulations. The FMLs were successfully subjected to blast loading and the effects of various components analysed. The fibre areal density appeared to only affect the composite layer thickness which could have added to the degree of debonding. The effects of this was found to be far less significant than bond strength and panel thickness. The Prime 20LV FMLs (WLW and WLUD) showed evidence of debonding in all experiments but were however able to withstand charge masses larger than the SE 84LV (PPW) series. The woven SE 84LV FMLs exhibited behaviour similar to that of monolithic metals, showing tearing at the clamped boundaries without debonding, indicating exceptional bond strength between laminates. Trends from dimensionless analysis of the FML response were too close to indicate a clearly superior configuration. The PPW series exhibited the most catastrophic failure mode (tearing at the clamped boundary), but showed the most superior bond strength. The WL series showed the most consistent failure, but exhibited widespread debonding in all tests as well as greater pulling-in at high charge masses.

Considering the interfacial bond strength and blast response, the PPW series shows the closest resemblance to GLARE®. Hence, should further studies be attempted, using thinner constitutive materials, this is the most likely candidate to result in material properties comparable to that of GLARE®. The wet-layup series (WLW and WLUD), however, also showed good blast resistance and could improve with further development. Both wet-layup series (WLW and WLUD) requires further investigation into the damage absorption effects of pulling in and debonding.

9.6 Recommendations

- Investigate the effects of increasing the post-cure cycle temperature in the combined single-stage manufacturing process. An increase in post-cure cycle temperature would result in the redux 609 being cured at the recommended temperature which could lead to improvements in interfacial bond strength with the Prime 20LV based FMLs.
- Reducing the thickness of the aluminium laminate would reduce the effect of the aluminium on the material response and the overall thickness which would in turn increase the experienced dimensionless impulse. It would allow a more evident difference in response between woven and uni-directional fibre configurations.
- Reducing the thickness of all the material layers equally would reduce the overall thickness which would increase the experienced dimensionless impulse. It would allow a accurate comparison to GLARE®.
- Improving the boundary clamping of the FMLs when subjecting them to blast loading would result in less pulling-in and a more accurate measure of failure mode thresholds.
- The use of a uni-directional SE 84LV prepreg to determine the difference in response between uni-directional and woven fibres with superior bond strength.
- The use of cohesive elements or tiebreak contacts to expand the numerical blast model beyond the PPW simulations. Employing multiple element layers would help in identifying the debonding mechanisms at work during blast loading.
- Increasing the accuracy of the clamped boundary in simulations in order to increase the accuracy of the response of the FMLs.

References

[1] M. Yazid Yahya, W.J. Cantwell, G.S. Langdon, and G.N. Nurick. The blast behavior of fiber reinforced thermoplastic laminates. *Journal of Composite Materials*, 42(21):2275–97, 2008.

[2] B. Cozzi. Clipper maid of the seas: Flight 103 - Lockerbie, Scotland. Technical report, PanAm Air, 2011. `http://www.panamair.org/~accidents/~lockerbievictims.htm`.

[3] M. Cox and T. Foster. *Their Darkest Day: The Tragedy of Pan Am 103 and It's Legacy of Hope*. Grove Pr, 1992.

[4] H.J. Fleischer. Design and explosive testing of a blast resistant luggage container. In *Structures Under Shock and Impact Conference IV*, 1996.

[5] G.S. Langdon, Y. Chi, G.N. Nurick, and P. Haupt. Response of GLARE panels to blast loading. *Engineering Structures*, 31(12):3116–3120, 2009.

[6] M.S. Hoo Fatt, C. Lin, D.M. Revilock Jr, and D.A. Hopkins. Ballistic impact of GLARE fibermetal laminates. *Composite Structures*, 61(1-2):73–88, 2003.

[7] G. Reyes Villanueva and W.J. Cantwell. The high velocity impact response of composite and fml-reinforced sandwich structures. *Composite Sciences and Technology*, 64(1):35–54, 2004.

[8] Z. Guoqi, W. Goldsmith, and C.K.H. Dharan. Penetration of laminated Kevlar by projectiles I. experimental investigation. *International Journal of Solids and Structures*, 29(4):399–420, 1992.

[9] J.K. Kim, L. Leung, S. Lee, and Y. Hiray. Impact performance of a woven fabric cfrp laminate. *Polmers and Polymer Composites*, 4:549–561, 1996.

[10] J.K. Kim and M.L. Sham. Impact and delamination failure of woven-fabric composites. *Composites Science and Technology*, 60(5):745–761, 2000.

[11] G.S. Langdon, W.J. Cantwell, and G.N. Nurick. The blast response of novel thermoplastic-based fibremetal laminates some preliminary results and observations. *Composite Sciences and Technology*, 65(6):861–72, 2005.

[12] T. van Tonder. Adhesive properties of thermoset fibre metal laminates. MSc Dissertation, University of Cape Town, 2014.

[13] F.C. Campbell. *Structural Composite Materials*, chapter Introduction to Composite Materials. ASM International, 2010.

[14] A.K. Kaw. *Mechanics of Composite Materials SE*. Mechanical and Aerospace Engineering Series. CRC Press, 2005.

[15] D. Roylance. Introduction to composite materials. Technical report, Massachusetts Institute of Technology, 2000.

[16] W. Kaufmyn. Fiber-reinforced composites. Technical report, City College of San Francisco, July 2009.

[17] V.V. Vasiliev and E.V. Morozov. *Advanced Mechanics of Composite Materials and Structural Elements TE*. Elsevier Science, 2013.

[18] H.F. Wu and L.L. Wu. Mil-hdbk5 design allowables for fibre/metal laminates: Arall 2 and arall 3. *Journal of Materials Science*, 13(8):582–585, 1994.

[19] A. Ozinsky. The response of partially-confined right-circular cylinders to internal blast loading. MSc Dissertation, University of Cape Town, 2012.

[20] C.A.J.R. Vermeeren. *Applied Composite Materials*, chapter An Historic Overview of the Development of Fibre Metal Laminates. Kluwer Academic Publishers, 2003.

[21] A. Vlot, L.B. Vogelesang, and de Vries T.J. Towards application of fibre metal laminates in large aircraft. *Aircraft Engineering and Aerospace Technology: An International Journal*, 71(6):558–570, 1999.

[22] L.B. Vogelesang and A. Vlot. Development of fibre metal laminates for advanced aerospace structures. *Journal of Materials Processing Technology*, 103(1):1–5, 2000.

[23] L.B. Vogelesang, F.E.H.M. Smulders, and D. Chen. Process for manufacturing a laminate of metal sheets and filaments-reinforced synthetic layers, July 1989. `http://www.google.com/~patents/~EP0323660A1?cl=en`EP Patent App. EP19,880,202,813.

[24] G. Roebroeks. Towards GLARE the development of a fatigue insensitive and damage tolerant aircraft material. Masters Dissertation, Delft University of Technology, 1991.

[25] L.B. Vogelesang, J. Schijve, and R. Fredell. *Case Studies in Manufacturing with Advanced Materials Vol. 2*, chapter Fibremetal laminates: damage tolerant aerospace materials. Elsevier, 1995.

[26] G. Roebroeks. Fiber metal laminates - recent developments and applications. In A. Beukers, T. de Jong, J. Sinke, A. Vlot, and L.B. Vogelesang, editors, *Fatigue of Aircraft Materials*. Delft University Press, Delft, 1993.

[27] A. Vlot. *Low velocity impact loading on fibre reinforced aluminium laminates*. PhD thesis, TU Delft, 1991.

[28] A. Vlot, E. Kroon, and G. La Rocca. Impact response of fibre metal laminates. In J.K. Kim and T.X. Yu, editors, *Impact Response and Dynamic Failure of Composites and Laminate Materials*. Trans Tech Publishers, Switzerland, 1998.

[29] V. Silvestrov and A. Plastinin. High-strain-rate behavior of several types of epoxy-based composites. *Journal de Physique IV*, 7(C3):459–464, 1997.

[30] A. Kinloch. *Adhesion and Adhesives: Science and Technology*. Cambridge University Press, 1987.

[31] W. Brockmann, P. Gei, J. Klingen, and K. Schroder. Adhesive bonding: Materials. In *Applications and Technology*. John Wiley and Sons, Weinheim, 2009.

[32] S. Park, W. Choi, H. Choi, and H. Kwon. Effects of surface pre-treatment and void content on GLARE laminate process. *Journal of Materials Processing Technology*, 210(8):1008–16, 2010.

[33] W. Brockmann, O.D. Hennemann, and C. Matz. Adhesion in bonded aluminium joints for aircraft construction. *International Journal of Adhesion and Adhesives*, 6(3):115–143, 1986.

[34] G. Critchlow, K. Yendall, D. Bahrani, A. Quinn, and F. Andrews. Strategies for the replacement of chromic acid anodising for the structural bonding of aluminium. *International Journal of Adhesion and Adhesives*, 26(6):419–453, 2006.

[35] M. Davis and D. Bond. Principles and practices of adhesive bonded structural joints and repairs. *International Journal of Adhesion and Adhesives*, 19(2-3):91–105, 1999.

[36] Shin-Etsu Silicone. Silane coupling agents. Technical report, Shin-Etsu Chemical Co., Ltd., 2011.

[37] S.Y. Park, W.J. Choi, H.S. Choi, H. Kwon, and S.H. Kim. Recent trends in surface treatment technologies for airframe adhesive bonding processing: A review (1995-2008). *The Journal of Adhesion*, 86(2):192–221, 2010.

[38] M Fedel. *Environmentally Friendly Hybrid Coatings for Corrosion Protection: Silane Based Pre-treatments and Nanostructured Waterborne Coatings*. PhD thesis, University of Trento, 2010.

[39] A. Higgins. Adhesive bonding for aircraft structures. *International Journal of Adhesion and Adhesives*, 20(5):367–376, 2000.

[40] R. Atkinson. Hexcel, June 2004. `http://www.hexcel.com/~news/~archive/~news-20040616`.

[41] W.E. Baker. *Explosions in Air*. University of Texas Press, 1973.

[42] S. Glasston and P. J. Dolan. *The Effect of Nuclear Weapons*, chapter Air Blast Phenomena in Air and Surface Bursts. United States Department of Defense, 1977.

[43] H. Draganic and V. Sigmund. Blast loading on structures. *Tehnicki Vjesnik*, 19(3):643–652, 2012.

[44] R. J. Martin, A. Reza, and L. W. Anderson. What is an explosion? a case history of an investigation for the insurance industry. *Journal of Loss Prevention in the Process Industry*, 13(6):491–497, 2000.

[45] C.R. Wilkinson and J.G. Anderson. An introduction to detonation and blast for the nonspecialist. Technical report, Australian Government Deprartment of Defenece: Defence Science amd Technology Organization, 2003.

[46] P.W. Cooper. *Explosives Engineering*. Wiley-VCH, 1996.

[47] J. A. Zukas, W. Walters, and W.P. Walters. *Explosive Effects and Applications*, chapter High Pressure Shock Compression of Condensed Matter. Springer New York, 2002.

[48] T. Ngo, P. Mendis, A. Gupta, and J. Ramsay. Blast loading and blast effects on structures - an overview. *Electronic Journal of Structural Engineering Special Issue: Loading on Structures*, pages 76–91, 2007.

[49] G. C. Mays and P. D. Smith. Blast effects on buildings - design of buildings to optimize resistance to blast loading, 2001.

[50] Health and Safety Executive Staff. The effects of simplification of explosion pressure-time history. Technical report, Steel Construction Institute, 1992.

[51] S.B. Menkes and H.J. Opat. Tearing and shear failures in explosively loaded clamped beams. *Experimental Mechanics*, 13(11):480–486, 1973.

[52] M.D. Olson, G.N. Nurick, and J.R. Fagnan. Deformation and rupture of blast loaded square plates–predictions and experiments. *International Journal of Impact Engineering*, 13(2):279–291, 1993.

[53] G.N. Nurick and G.C. Shave. The deformation and tearing of thin square plates subjected to impulsive loads - an experimental study. *International Journal of Impact Engineering*, 18(1):99–116, 1996.

[54] R.G. Teeling-Smith and G.N. Nurick. The deformation and tearing of thin circular plates subjected to impulsive loads. *International Journal of Impact Engineering*, 11(1):77–91, 1991.

[55] G.N. Nurick, M.E. Gelman, and N.S. Marshall. Tearing of blast loaded plates with clamped boundary conditions. *International Journal of Impact Engineering*, 18(7–8):803–827, 1996.

[56] G.N. Nurick and A.M. Radford. *Recent developments in computational and applied mechanics - a volume in honour of John B. Martin.*, chapter Deformation and tearing of clamped circular plates subjected to localised central blast loads, pages 277–301. CIMNE: Barcelona, 1997.

[57] G.S. Langdon, G.N. Nurick, and W.J. Cantwell. Localised blast loading of fibremetal laminates with a polyamide matrix. *Composites Part B: Engineering*, 38(7-8):902–913, 2007.

[58] G.S. Langdon, S.L. Lemanski, G.N. Nurick, M.C. Simmons, W.J. Cantwell, and G.K. Schleyer. Behaviour of fibremetal laminates subjected to localised blast loading: Part I experimental observations. *International Journal of Impact Engineering*, 34(7):1202–22, 2007.

[59] S.L. Lemanski, G.N. Nurick, G.S. Langdon, M.C. Simmons, W.J. Cantwell, and G.K. Schleyer. Behaviour of fibremetal laminates subjected to localised blast loading - Part II: Quantitative analysis. *International Journal of Impact Engineering*, 34(7):1223–45, 2007.

[60] N. Jacob, G.N. Nurick, and G.S. Langdon. The effect of stand-off distance on the failure of fully clamped circular mild steel plates subjected to blast loads. *Engineering Structures*, 29(10):2723–2736, 2007.

[61] S.L. Lemanski, G.N. Nurick, G.S. Langdon, M.C. Simmons, W.J. Cantwell, and G.K. Schleyer. Understanding the behaviour of fibre metal laminates subjected to localised blast loading. *Composite Structures*, 76(1-2):82–87, 2006.

[62] R. Olsson. Mass criterion for wave-controlled impact response of composite plates. *Composites Part A: Applied Science and Manufacturing*, 31(8):879–87, 2000.

[63] T. Franz, G.N. Nurick, and M.J. Perry. Experimental investigation into the response of chopped-strand mat glassfibre laminates to blast loading. *International Journal of Impact Engineering*, 27(6):639–667, 2002.

[64] G.S. Langdon, W.J. Cantwell, and G.N. Nurick. The response of fibre-metal laminates subjected to uniformly distributed blast loading. *European Journal of Mechanics - A/Solids*, 27(2):107–115, 2008.

[65] G.S. Langdon, G.N. Nurick, S.L. Lemanski, M.C. Simmons, W.J. Cantwell, and G.K. Schleyer. Failure characterisation of blast-loaded fibremetal laminate panels based on aluminium and glassfibre reinforced polypropylene. *Composites Science and Technology*, 67(7-8):1385–1405, 2006.

[66] Engineers Edge. Aluminium tempers, specifications and designations. Technical report, Engineers Edge LLC, 2014.

[67] ALCOA MILL PRODUCTS. Clipper maid of the seas: Flight 103 - lockerbie, scotland. Technical report, ALCOA, 2011. `http://www.alcoa.com/~millproducts/~catalog/pdf/~alloy2024techsheet.pdf`.

[68] ASM Aerospace Specification Metals Inc. Aluminium 2024-T3. http://asm.matweb.com/search/ SpecificMaterial.asp?bassnum=MA2024T3 Accessed: 2014-09-25.

[69] AZOM.com. E-glass fibre. `http://www.azom.com/~article.aspx?ArticleID=764`Accessed: 2014-09-26.

[70] Gurit. Se 84lv: Low temperature cure epoxy prepreg. `http://www.gurit.com/~files/~documents/~se-84lvv16pdf.pdf`.

[71] Gurit. Prime 20lv: Epoxy infusion system. `http://www.gurit.com/~files/~documents/prime-20lvv11pdf.pdf`.

[72] United Chemical Technologies. Silane coupling agent guide. Technical report, United Chemical Technologies, 2011.

[73] Hexcel Composites. Redux 609: Adhesive film for bonding metallic and composite components, March 2010. http://www.hexcel.com/~Resources/~DataSheets/~Adhesives-Data-Sheets/609eu.pdf.

[74] ASTM E8 / E8M-13a. Standard test methods for tension testing of metallic materials. Technical report, ASTM International, West Conshohocken, PA, 2013. www.astm.org.

[75] ASTM D790-10. Standard test methods for flexural properties of unreinforced and reinforced plastics and electrical insulating materials. Technical report, ASTM International, West Conshohocken, PA, 2010. www.astm.org.

[76] A.S. Khan and H Liu. Variable strain rate sensitivity in an aluminum alloy: Response and constitutive modeling. *International Journal of Plasticity*, 36:1–14, 2012.

[77] J.D. Seidt. Characterization of 2024-T351 aluminum for dynamic loading applications. In *Society for Experimental Mechanics Inc: XIth International Congress and Exposition*, 2008.

[78] M.J. Loikkanen, M. Buyuk, C. Kan, and N. Meng. A computational and experimental analysis of ballistic impact to sheet metal aircraft structures. In *5th European LS-DYNA Users Conference*, 2005.

[79] U.S. Department of Transportation: Federal Aviation Administration. Explicit finite element analysis of 2024-T3/T351 aluminum material under impact loading for airplane engine containment and fragment shielding. Technical report, Air Traffic Organization Operations Planning Office of Aviation Research and Development, 2008.

[80] G.R. Johnson and W.H. Cook. A constitutive model and data for metals subject to large strains, high strain rates and high temperatures. In *Seventh International Symposium on Ballistics*, 1983.

[81] Livermore Software Technology Corporation. *LS-DYNA Keyword User's Manual*, version 970/971 edition, April 2003.

[82] C Geretto. *The effects of different degrees of confinement on the deformation of square plates subjected to blast loading*. PhD thesis, University of Cape Town, 2010.

[83] S.H. Yoon and C.S. Hong. Modified end notched flexure specimen for mixed mode interlaminar fracture in laminated composites. *International Journal of Fracture*, 43(1):R3–R9, 1990.

[84] A. Szekrényes. *Delamination of Composite Specimens*. PhD thesis, Budapest University of Technology and Economics, March 2005.

[85] G.R. Irwin and J.A. Kies. Critical energy release rate analysis of fracture strength. *Welding Journal*, 33:193–8, 1954.

[86] D. Bruno and F. Greco. Mixed mode delamination in plates: a refined approach. *International Journal of Solids and Structures*, 38(50-51):9149–77, 2001.

[87] D. Bruno and F. Greco. Delamination in composite plates: influence of shear deformability on interfacial debonding. *Cement and Concrete Composites*, 23(1):33–45, 2001.

[88] G. Bao, S. Ho, Z. Suo, and B. Fan. The role of material orthotropy in fracture specimens for composites. *International Journal of Solids and Structures*, 29(9):1105–16, 1992.

[89] L.A. Carlsson, J.W. Gillespie, and R.B. Pipes. On the analysis and design of the end notched flexure (ENF) specimen for mode II testing. *Journal of Composite Materials*, 20:594–604, 1986.

[90] R. Olsson. A simplified improved beam analysis of the dcb specimen. *Composites Science and Technology*, 43(4):329–338, 1992.

[91] P. Elisa. *Advances in Composite Materials - Analysis of Natural and Man-Made Materials*, chapter Virtual Crack Closure Technique and Finite Element Method for Predicting the Delamination Growth Initiation in Composite Structures. CC BY-NC-SA, 2011.

[92] A. Airoldi, M. Vesco, S. van der Zwaag, A. Baldi, and G. Sala. Damage in GLARE laminates under indentation loads: experimental and numerical results. In *Proceedings of the 17th international conference on composite materials*, 2009.

[93] J.K. Kim and M.L. Sham. Impact and delamination failure of woven-fabric composites. *Composites Science and Technology*, 60(5):745–761, 2000.

[94] C. Soutis, G. Mohamed, and A. Hodzic. Modelling the structural response of GLARE panels to blast load. *Composite Structures*, 94(1):267–276, 2011.

[95] H.R. Tavakoli and F. Kiakojouri. Numerical dynamic analysis of stiffened plates under blast loading. *Latin American Journal of Solids and Structures*, 11(2):185–199, 2014.

[96] B.M. Thomas. The effects of boundary conditions on the failure of thin plates subjected to impulsive loading. MSc Dissertation, University of Cape Town, 1995.

[97] R.E. Bimha. Response of thin circular plates to central blast loading. MSc Dissertation, University of Cape Town, 1996.

[98] R.K. Wharton, S.A. Formby, and R. Merrifield. Airblast tnt equivalence for a range of commercial blasting explosives. *Journal of Hazardous Materials*, 79(1-2):31–39, 2000.

[99] B.M. Dobratz and P.C. Crawford. LLNL handbook of explosives: Properties of chemical explosives and explosive simulants. Technical report, Lawrence Livermore National Laboratory, January 1985.

[100] G.S. Langdon and G.K. Schleyer. Inelastic deformation and failure of clamped aluminium plates under pulse pressure loading. *International Journal of Impact Engineering*, 28(10):1107–1127, 2003.

[101] G.N. Nurick and J.B. Martin. Deformation of thin panels subjected to impulsive loading a review. Part II: Experimental studies. *International Journal of Impact Engineering*, 8(2):171–186, 1989.

[102] W. Johnson. *Impact strength of materials*. UK: Edward Arnold (Pubs) Ltd, 1972.

[103] N. Jacob, S. Chung Kim Yuen, D. Bonorchis, S.A. Desai, and D. Tait. Quadrangular plates subjected to localised blast loads an insight into scaling. *International Journal of Impact Engineering*, 30(8–9):1179–208, 2004.

[104] G.S. Langdon, G.N. Nurick, S.L. Lemanski, M.C. Simmons, W.J. Cantwell, and G.K. Schleyer. Failure characterisation of blast-loaded fibre-metal laminate panels based on aluminium and glass-fibre reinforced polypropylene. *Composites Science Technology*, 67(7–8):1385–405, 2007.

This page has been intentionally left blank.

Appendices

Appendix A

Materials and Manufacturing

Risk assessments for all the processes performed during manufacturing are contained in this Appendix.

This page has been intentionally left blank.

This page has been intentionally left blank.

This page has been intentionally left blank.

This page has been intentionally left blank.

Appendix B

Material Characterisation

All relevant data obtained from materials testing, not shown in Section 4 is contained in this appendix. This includes raw data from the SLB tests, matlab code used in data analysis as well as process data from image analysis and data correlation.

B.1 Raw Single Leg Bend Data

The raw data obtained from the zwick universal testing machine performing single leg bend tests are shown in Figure B.1. The graphs show the force versus displacement data for the SLB tests performed in the zwick universal testing machine.

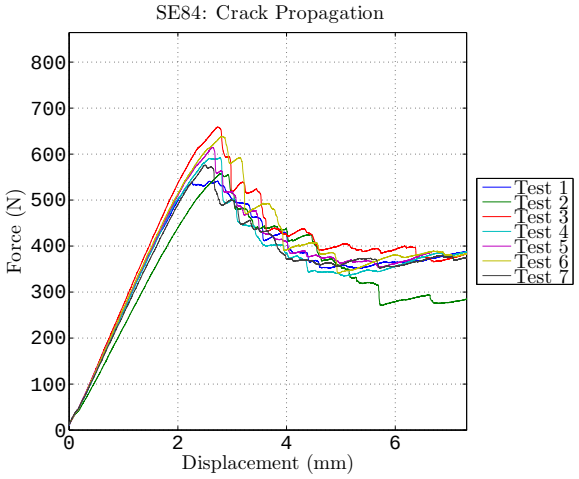

(a) SE 84LV based SLB tests raw force versus displacement data.

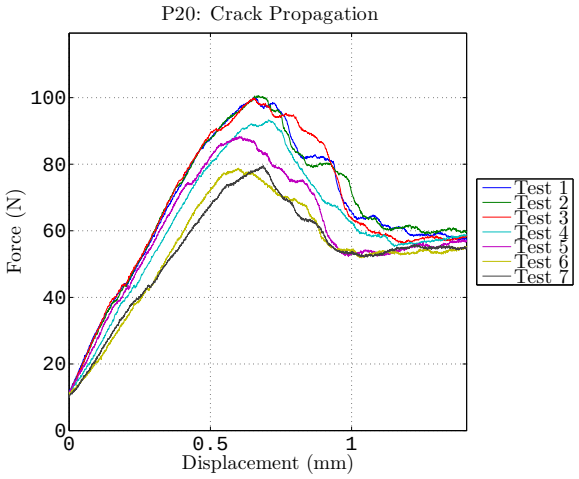

(b) Prime 20LV MSM based SLB tests raw force versus displacement data.

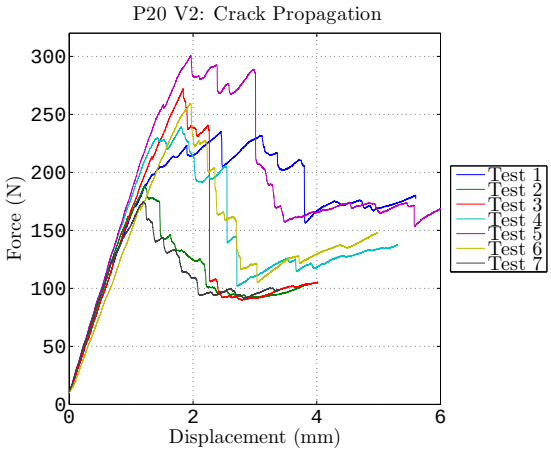

(c) 5 g Simulated charge mass.

Figure B.1: Prime 20LV SSM based SLB tests raw force versus displacement data.

B.1.1 Tensile Test Data Analysis

The force displacement data obtained from the zwick testing machine was analysed using the matlab script detailed bellow. The script consistes of two files: `analysis.m` and `zwickanalyse.m`. The specific analysis of each specimen is contained in the `zwickanalyse.m` file. This process of analysis is then run through a loop for the number of specimens tested. This loop and the various formatting options is contained in `analysis.m`.

```
function [Y,StdForce, StrainDisp, stress, strain, stress_T, strain_T,
    ↪ stress_P, strain_P] = zwickanalyse(data)

%data from the zwick output files (.TRA) is read into variable in matlab
[StdForce, StrainDisp] = textread(data,'',-1,'delimiter',',',
    ↪ 'headerlines',1,'emptyvalue',NaN);

%Tensile specimen geometries are defined
w = 12.5e-3; %m
t = 0.78e-3; %m
l = 40; %mm
A = w*t;
E = 73.8e9; %MPa

%Determining the mamaximum tensile force
[UTF,utf_id] = max(StdForce);

%offset values for calculating slope and machine compliance to negate
    ↪ specimen slip
m_min = 1000;
m_max = 3000;

%determining indexes for calculation of gradient in the elastic range
[~,minx] = min(abs(StdForce-m_min));
[~,maxx] = min(abs(StdForce-m_max));

%determining the maximum value of the gradient in the elastic range
[m,mx] = max((StdForce(minx:maxx)-StdForce(1))./StrainDisp(minx:maxx));

%Calculation of slipping
us = StrainDisp(mx)-StdForce/m;

%removal of slipping from strain data
```

```
StrainDisp = StrainDisp - us;
uc = StrainDisp;

%calculation of the engineering stress and strain
stress = StdForce./A./1e6;
strain = uc./l;

%claculation of the true stress and true strain
stress_T = stress.*(1+strain);
strain_T = log(1+strain);

%strain offset value for determining the yield point
strain_offset = 0.5/100;

%calculating m in Y=mX+C - curve intersection with yield point
[mm,mmx] = max((stress_T(10:length(strain_T)) -
    ↪ StdForce(1)/A/1e6)./strain_T(10:length(strain_T)));
%display(mm);

%calculating C in Y=mX+C
C = -mm*strain_offset;
%display(C)
%Creating linear offset line
Y = mm*(strain_T+strain_offset)+C;

%calculation of index for elastic strain data removal
[~,mnx] = min(abs(stress_T-Y));

%calculation of true plastic strain and true stress data
strain_P = strain_T-strain_T(mnx)-strain_offset;
stress_P = stress_T;
end
```

```
close all
clear all
clc

seq = 14; %numer of tensile tests
CM = lines(seq); %color sequence for the tensile tests
tests = cell(seq-4,1);

```

```
%for loop to print the entire tensile test sequance
for n = 1:seq
    %reading in file data
    fileName = ['12mm' num2str(n) '.tra'];
    [Y,force, disp, stress, strain, stress_T, strain_T, stress_P, strain_P] =
        ↪ zwickanalyse(fileName);

    color = 'b';
    if n>8
        color = 'r';
        if n > 11
            color = 'g';
        end
    end

    tests{n} = ['Test ' num2str(n)];

    [~,id_uts] = max(force);
    %[~,equal] = min(abs(stress-Y));

    %plot of stress vs strain
    figure(1)
    plot(strain(1:id_uts),stress(1:id_uts),
        ↪ 'LineWidth',1,'color',CM(n,:)),hold on
    grid on
    xlabel('Strain \epsilon (m/m)'), ylabel('Stress \sigma (MPa)')
    axis([0 0.25 0 500])

    %plot of true stress vs true strain
    figure(2)
    plot(strain_T(1:id_uts), stress_T(1:id_uts),
        ↪ 'LineWidth',1,'color',CM(n,:)),hold on
    grid on
    xlabel('True Strain \epsilon_T (m/m)'), ylabel('True Stress \sigma_T
        ↪ (MPa)')
    axis([0 0.25 0 600])

    %plot of plastic strain vs effective plastic stress
    figure(3)
    plot(strain_P(1:id_uts),stress_P(1:id_uts),
        ↪ 'LineWidth',1,'color',CM(n,:)),hold on
```

```
    grid on
    xlabel('Plastic Strain \epsilon_P (m/m)'), ylabel('Effective Plastic
        ↪ Stress \sigma_P (MPa)')
    axis([0 0.25 0 600])

    %default force displacement plot
    figure(4)
    plot(disp(1:id_uts),force(1:id_uts)/1000,
        ↪ 'LineWidth',1,'color',color),hold on
    grid on
    xlabel('Displacement (mm)'),ylabel('Force (kN)')
    axis([0 10 3 4.5])

    %Plot of the initial portion of the force displacement curve to show
    %slipping
    figure(5)
    plot(disp(1:id_uts),force(1:id_uts)/1000,
        ↪ 'LineWidth',1,'color',color),hold on
    grid on
    xlabel('Displacement (mm)'),ylabel('Force (kN)')
    axis([0 0.35 0 3.5])
end

%% Johnson cook material model parameters
strain_JC = linspace(0,0.21,1000);

A = 310;
B = 586;
n = 0.45;
C = 0.0083;
e0 = 0.001;

stress_JC =(A+B*strain_JC.^n).*(1+C*log(e0));

% plot of JC model agains effective plastic stress and plastic strain
figure(3)
plot(strain_JC,stress_JC,'--','LineWidth',2),hold on
axis([0 0.25 300 600])

%further formatting of plotted data
figure(1)
```

```
title('Tensile Test Data')
legend(tests,'location','East')
hold off

figure(2)
title('True Stress-Strain Data')
legend(tests,'location','East')
hold off

figure(3)
title('True Stress-Plastic Strain Data')
legend(tests,'location','East')
hold off

figure(4)
title('Force - Displacement Data')
legend(tests,'location','East')
hold off

figure(5)
title('Force - Displacement Data')
legend(tests,'location','East')
hold off
```

B.1.2 Digital Image Data Capture Analysis Using Matlab

The `Matlab` script used to analyse the captured images is detailed below. The script includes two different methods of analysis. The first method is user driven where a crack tip needs to be selected. The second method employed a pixel count algorithm to determine whether a crack exists in a certain region, automatically selecting the crack tip.

```
clear all
close all
clc

%% Obtain Images
srcFiles = dir('./Specimen #/*.jpg'); % the folder in which the images exists
[Year, Month, Day, Hour, Min, Sec] = datevec({srcFiles.date});
tempfilename = strcat('./Specimen #/',srcFiles(1).name);
```

```
I = imread(tempfilename);

%% Calibration
%The region to be captured was calibrated using a reference image &
%allowing the selection of a smaller viewing range
imshow(I);
%rect = getrect;
[I2, rect] = imcrop(I);
close all
imshow(I(rect(2):(rect(2)+rect(4)),rect(1):(rect(1)+rect(3)),:));
 %% Draw the bend head circle
 %The loading head was selected in order to relate millimetres to pixels
 [H xy] = imcrop(I(rect(2):(rect(2)+rect(4)),rect(1):(rect(1)+rect(3)),:));

 r = (xy(3)+xy(4))/2;

 sf = 2*r/10; %image scaling factor
%% Initial pick
% The inital pick made to indicate the position of the crack tip
% I2ref = rgb2gray(I2); %Reference image
% imshow(I2ref);
% Cref = round(ginput(1)); %Referece coordinate input
% close all

%% Calculate Time
%calculation of time from image reference data
tref = Min(1)*60+Sec(1);
time = Min*60+Sec - tref;

coord = zeros(length(srcFiles),2);
sumsum = zeros(length(srcFiles),1);
counter = 0;
%% Calculate crack tip
for i = 1 : length(srcFiles)
    %All .jpg files from the folder was imported and cycled through
    filename = strcat('./Specimen #/',srcFiles(i).name);
    I = imread(filename);

    B =I(rect(2):(rect(2)+rect(4)),rect(1):(rect(1)+rect(3)),:);
    imshow(B);

```

```
50      %The user was prompted to select the crack tip befor moving on to the
51      %next image. The coordinate data was stored in an array
52      coord(i,:) = ginput(1);
53
54  %************************************************************************
55  % In the cases where it was possible to easily determine the crack tip
56  % position, an image recognition algorithm was employed
57  %************************************************************************
58      % A color mask was applied and the image was transformed into a
59      % two-tone image
60      M = masking(B);
61      C = rgb2gray(M);
62
63      %Using the selected refernce coordinates, a square region of interest
64      %was determined and used to calculate the combined pixel value
65      square = C(Cref(1,2)-30:Cref(1,2)+30,Cref(1,1)-20:Cref(1,1)+20);
66      var = I2ref(Cref(1,2)-30:Cref(1,2)+30,Cref(1,1)-20:Cref(1,1)+20) - square;
67
68      %summation of pixel values in the refernce region
69      sumsum(i) = sum(sum(var));
70
71      %If the difference between the summed value and the reference was larger
72      % than a predetermined threshold, the pixels in the region were darkening
73      % and cracking was starting.
74      while(sumsum(i)>60000)
75              %The refernce value was move along a number of pixels until the
76              %value once more exceded the threshold
77              Cref(1,1) = Cref(1,1)-5;
78
79              square = C(Cref(1,2)-30:Cref(1,2)+30,Cref(1,1)-20:Cref(1,1)+20);
80              var = I2ref(Cref(1,2)-30:Cref(1,2)+30,Cref(1,1)-20:Cref(1,1)+20) -
                    ↪ square;
81              sumsum(i) = sum(sum(var));
82      end
83
84      %The current loop refernce coordinate was added to the coordinate count
85      coord(i,:) = Cref;
86  end
87
88  imshow(I2),hold on
89  plot(coord(:,1),coord(:,2),'Color','r','LineWidth',2)
```

```
90 Data = [time, coord/sf];
91
92 csvwrite('SLB_SPEC0#.dat',Data)
```

B.1.3 Single Leg Bend Test Data Analysis

Alalysis of the single leg bend tests was performed by the `Matlab` script detailed in this section. The script used various techniques to reduce the collected data, determine best fit curves and correlate graphs where necessary.

```
1  function slb_zwickanalyse(set_name)
2    %Defining the number of tests
3    cali = 5;
4    test = 7;
5
6    L = 40; %length to middle of specimen
7    b = 25; %width of specimen
8    c0 = 20; %initial crack length
9    h = 2; %initial thickness
10
11   CM1 = lines(cali);
12   CM2 = lines(test);
13
14   slbtests = cell(test,1);
15   calibration = cell(cali,1);
16   trend = cell(test*2,1);
17   trend2 = cell(test*3,1);
18
19 %% Compliance clibration
20 %reading and plotting the compiance data
21   for n = 1:cali
22         caliFile = ['./' set_name ' CALI/' set_name ' CALI' num2str(n) '.TRA'];
23         [cali_time, cali_displacement, cali_force] =
               ↪ textread(caliFile,'',-1,'delimiter',',','headerlines',1,'emptyvalue',NaN);
24         x(n) = (n+3)*5;
25         calibration{n} = [num2str(x(n)) 'mm crack'];
26         compliance(n) = mean(cali_displacement./(cali_force-10));
27         figure(1)
28         plot(cali_displacement,cali_force,'LineWidth',1,'Color',CM1(n,:)),hold
               ↪ on
```

```
 end

%Fitting a modified third order polynomial to compliance data
      t = x';
      X = [t.^3 zeros(size(t)) zeros(size(t)) ones(size(t))];
      A0 = X\compliance';

      a_length = linspace(0,50,500)';
      Compl = [ a_length.^3 zeros(size(a_length)) zeros(size(a_length))
          ↪ ones(size(a_length))]*A0;

      %determining dC/da - compliance differentiated with respect to
      %crack length
      B0 = A0.*[3 0 0 0]';
      dComp = [ a_length.^2 zeros(size(a_length)) zeros(size(a_length))
          ↪ zeros(size(a_length))]*B0;
%% Analysis of test data
 for i = 1:test
      testFile = ['./' set_name ' SLB/' set_name ' SLB' num2str(i) '.TRA'];
      imgFile = ['./' set_name ' IMG/SLB_SPEC0' num2str(i) '.dat'];

      % applies a smoothing factor to the curve,
      % taking every 100th point - only affects display
      smoothF = 100;

      [test_time, test_displacement, test_force] = textread(testFile,'',
          ↪ -1,'delimiter',',','headerlines',1,'emptyvalue',NaN);
      [img_time, img_x, img_y] = textread(imgFile,'',-1,'delimiter',',',
          ↪ 'headerlines',1,'emptyvalue',NaN);

      c_length = max(img_x)-img_x;
      %correction for previous error in measurement + addition of c0
      c_length = c_length/8*10+20;

      slbtests{i} = ['Test ' num2str(i)];
      trend{2*i-1} = ['Test ' num2str(i)];
      trend{2*i} = ['Test ' num2str(i) ' trend'];
      trend2{3*i-2} = ['Test ' num2str(i)];
      trend2{3*i-1} = ['Test ' num2str(i) ' linear trend'];
      trend2{3*i} = ['Test ' num2str(i) ' hyp trend'];

```

```
66          % Obtains the point of maximum force for crack initiation and
67          % minimum force past that to exclude non-physical crack propagation
68          % effects
69          [mx_force,id] = max(test_force);
70          [min_force,minid] = min(test_force(id:length(test_force)));
71
72          mod_test_force = test_force(1:(id+minid));
73
74          % Employs scale factor on force and disp data
75          s_F = mod_test_force(1:smoothF:length(mod_test_force));
76          s_d = test_displacement(1:smoothF:length(mod_test_force));
77
78  %% Force Curve Fitting
79
80          % Linear curve fit to initial part of force curve
81          test_d = test_displacement(1:id);
82          X = [test_d, ones(size(test_d))];
83          A0 = X\test_force(1:id);
84
85          d_fit = linspace(0,test_d(id)+max(test_displacement)/20,500)';
86          P_fit = [d_fit ones(size(d_fit))]*A0;
87
88          % hyperbolic curve fit
89          h_test_d = test_displacement((id+1):(id+minid));
90          X = [1./h_test_d, ones(size(h_test_d))];
91          A0 = X\test_force((id+1):(id+minid));
92
93          h_d_fit = linspace(h_test_d(1)-max(test_displacement)/
                ↪ 20,h_test_d(minid)+max(test_displacement)/20,500)';
94          h_P_fit = [1./h_d_fit ones(size(d_fit))]*A0;
95
96          %Plotting the force and displacement data
97          figure(2)
98          plot(s_d,s_F,'o','MarkerFaceColor',CM2(i,:),'Color',CM2(i,:),
                ↪ 'MarkerEdgeColor','k','MarkerSize',4),hold on
99          plot(d_fit,P_fit,'--','LineWidth',1,'Color',CM2(i,:)),hold on
100         plot(h_d_fit,h_P_fit,':','LineWidth',1,'Color',CM2(i,:)),hold on
101
102         %correlation of image and test time
103         t0 = test_time(id);
104         tf = test_time(id+minid);
```

```
105         [~,endid] = min(abs(img_time-tf));
106
107         % Fitting curve to crack length - same number of data points as
108         % tests
109         CL = polyfit(img_time,c_length,1);
110         cx = linspace(0,test_time(id+minid),length(test_time))';
111         cy = polyval(CL,cx);
112
113         %Derivative of compliance calibration containing same number of
114         %data points as test data
115         Delta_dComp = [ (cy).^2 zeros(size(cx)) zeros(size(cx))
                ↪ zeros(size(cx))]*B0;
116
117         %Derivative of compliance calibration containing same number of
118         %data points as image data
119         dCda = [ (c_length(1:endid)).^2 zeros(size(c_length(1:endid)))
                ↪ zeros(size(c_length(1:endid)))
                ↪ zeros(size(c_length(1:endid)))]*B0;
120
121         %reduction of force data
122         force = zeros(size(img_time(1:endid)));
123
124         %Matching crack data to force data using time
125         for z = 1:length(img_time(1:endid))
126             [~,temp] = min(abs(test_time - t0 - img_time(z)));
127             force(z) = test_force(temp);
128         end
129
130         % Using reduced data
131         GI_II = (force.^2)/(2*b).*dCda*1000;
132
133         %application of smoothing factor to images
134         img_smooth = 15;
135
136         figure(3)
137         plot(img_time(1:length(img_time)/img_smooth:endid),
                ↪ c_length(1:length(img_time)/img_smooth:endid),'^','Color',CM2(i,:),
                ↪ 'MarkerFaceColor',CM2(i,:),'MarkerEdgeColor','k'),hold on
138         plot(cx,cy,'--','LineWidth',1,'Color',CM2(i,:)),hold on
139
140         figure(5)
```

```
141         plot(c_length(1:endid),GI_II,'o','MarkerFaceColor',CM2(i,:),
                ↪ 'MarkerSize',4,'Color',CM2(i,:),'MarkerEdgeColor','k'),hold on
142  end
143
144 %% format plot data
145         figure(1)
146         grid on
147         xlabel('Displacement (mm)'),ylabel('Force (N)')
148         axis([0 max(cali_displacement)+max(cali_displacement)/5 10 45])
149         axis square
150         legend(calibration,'Location', 'SouthEast')
151         title([set_name ': Compliance Testing']), hold off
152
153         figure(2)
154         grid on
155         xlabel('Displacement (mm)'),ylabel('Force (N)')
156         axis([0 max(h_d_fit)*1.2 0 (max(test_force)*1.5)])
157         axis square
158         legend(trend2,'Location', 'EastOutside')
159         title([set_name ': Crack Propagation']), hold off
160
161         figure(3)
162         grid on
163         xlabel('Time (s)'),ylabel('Crack Length (mm)')
164         axis([0 img_time(endid)*1.5 15 c_length(endid)*1.5])
165         axis square
166         legend(trend,'Location', 'EastOutside')
167         title([set_name ': Crack Growth']), hold off
168
169         figure(4)
170         plot(x,compliance,'^','MarkerFaceColor','b','MarkerEdgeColor','k'),hold
                ↪ on
171         plot(a_length,Compl,'r'), hold on
172         plot(a_length,dComp,'b')
173         axis square
174         grid on
175         xlabel('Crack Length (mm)'),ylabel('Compliance (mm/N)')
176         legend({'Compliance Points' 'C(a)' 'dC/da'},'Location', 'NorthWest')
177         title([set_name ': Compliance Calibration']);
178         hold off
179
```

```
180         figure(5)
181         grid on
182         xlabel('Crack Length (mm)'),ylabel('G_{I/II} (J/m^2)')
183         legend(slbtests,'Location', 'NorthWest')
184         title([set_name ': Energy Release Rate']), hold off
185 end
```

This page has been intentionally left blank.

Appendix C

Numerical Simulations

Analysis was performed on specific sections of the numerical simulations subject to large amounts of deformation, plastic strain and stress concentrations. The data obtained from each numerical simulation is shown in the corresponding sections of this appendix.

C.1 Nodal Deflection Output

The nodal deflection output provides a deflection versus time curve for the midpoint of the numerical simulations. This data was used to determine the dimensionless displacement data and analyse the response of each simulated panel. Deflection data from the simulations of the localised loading conditions are shown in Figure C.1 and data obtained from the uniform loading simulations are shown in Figure C.2

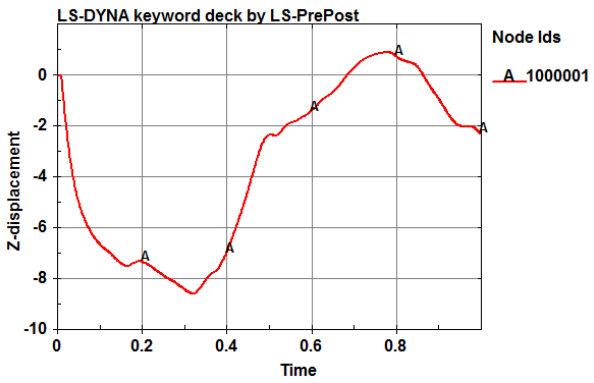

(a) 3 g Simulated charge mass.

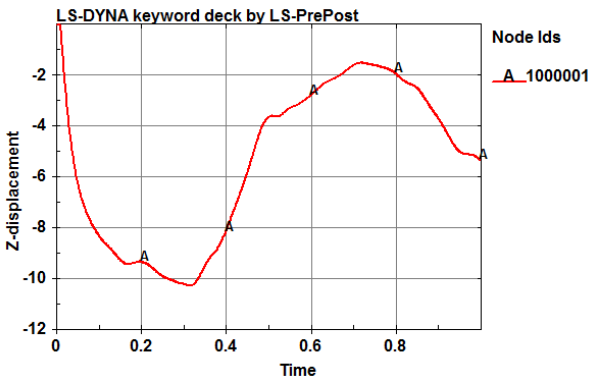

(b) 4 g Simulated charge mass.

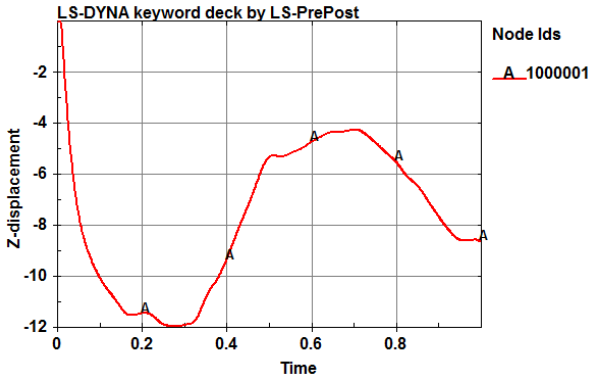

(c) 5 g Simulated charge mass.

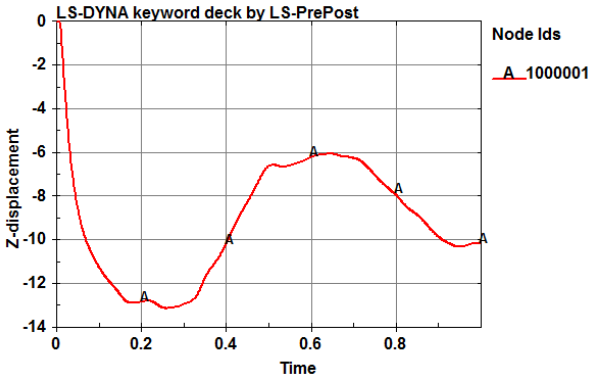

(d) 6 g Simulated charge mass.

Figure C.1: Simulated nodal midpoint deflections of FMLs subjected to localised loading.

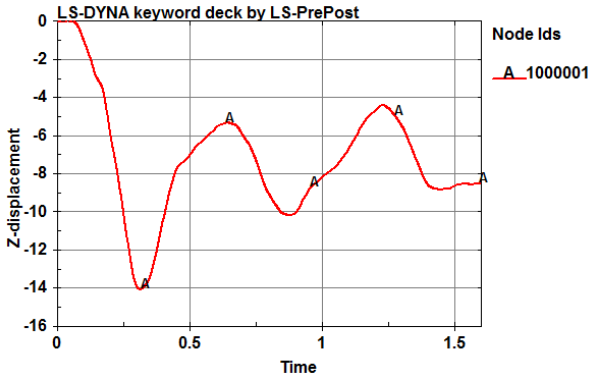

(a) 15 g Simulated charge mass.

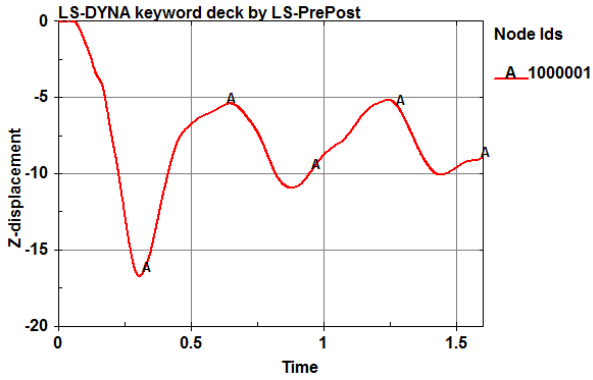

(b) 20 g Simulated charge mass.

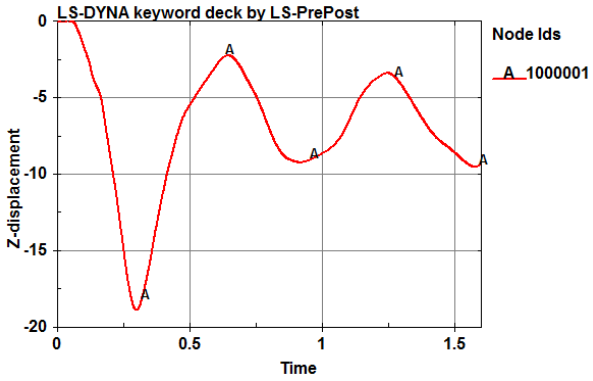

(c) 25 g Simulated charge mass.

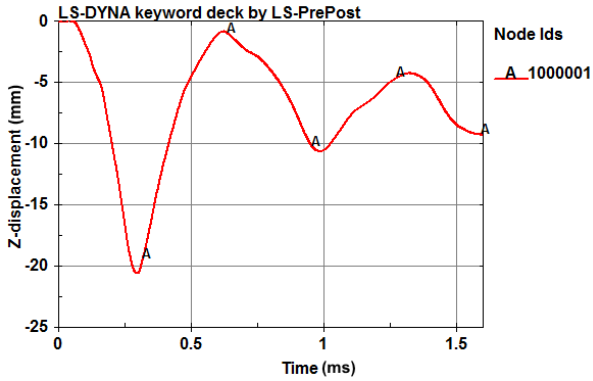

(d) 30 g Simulated charge mass.

Figure C.2: Simulated nodal midpoint deflections of FMLs subjected to uniform loading.

C.2 Stress and Plastic Strain Simulation Data

Plastic strain and stress data was measured at elements placed at both the clamped boundary (curve A) and panel midpoint (curve B) in order to determine the method of failure and the effects of the various loading conditions on failure parameter development.

C.2.1 Plastic Strain

Plastic strain was an important parameter in determining possible failure or failure regions of the FML. The measured plastic strains were compared to the elongation at failure of the aluminium alloy contained in the FML. Plastic strain data from the simulations of the localised loading conditions are shown in Figure C.3 and data obtained from the uniform loading simulations are shown in Figure C.4.

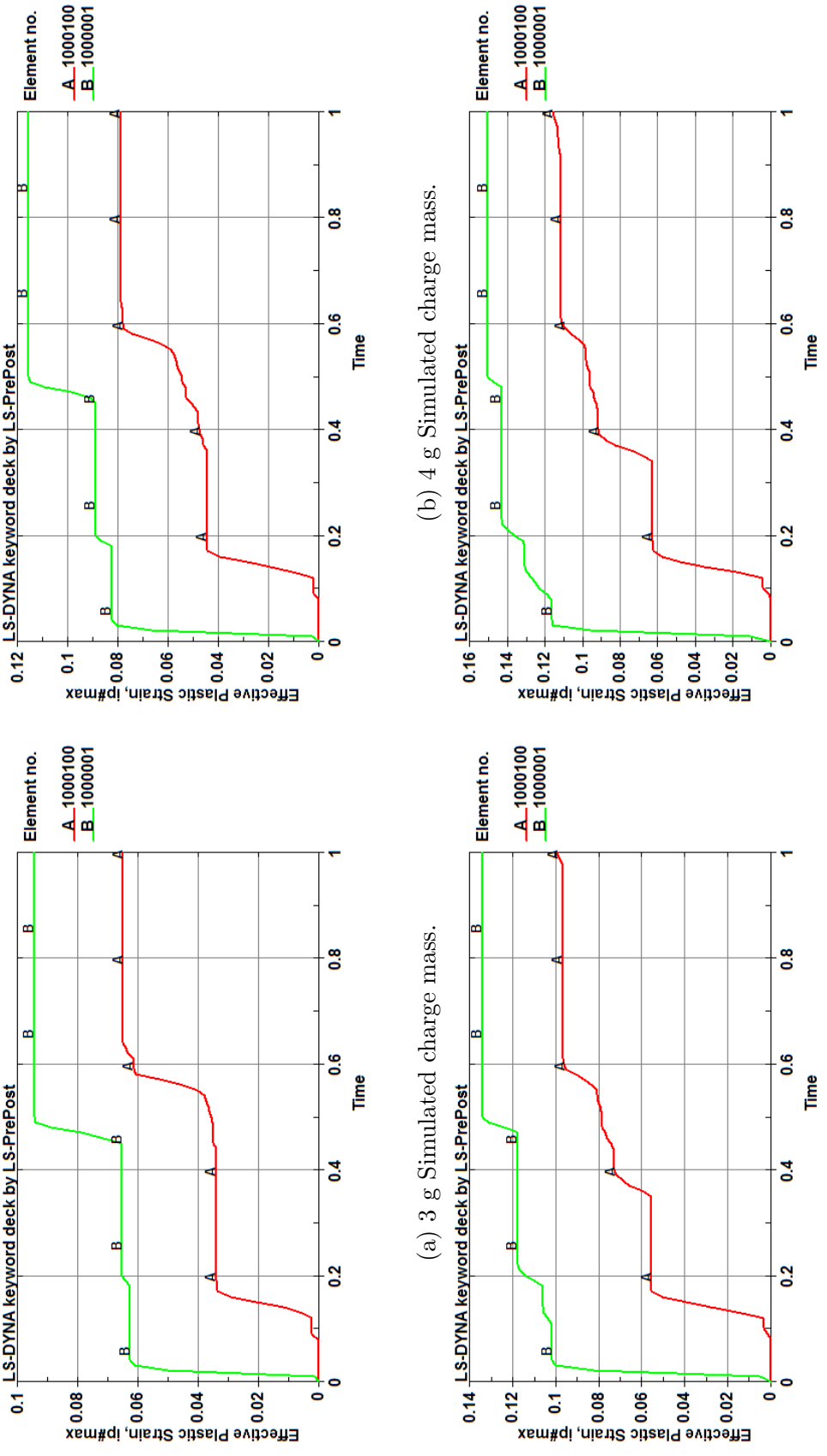

(a) 3 g Simulated charge mass.

(b) 4 g Simulated charge mass.

(c) 5 g Simulated charge mass.

(d) 6 g Simulated charge mass.

Figure C.3: Plastic strain development under localised blast loading at A - the clamped boundary and B - panel midpoint for various simulated charge masses.

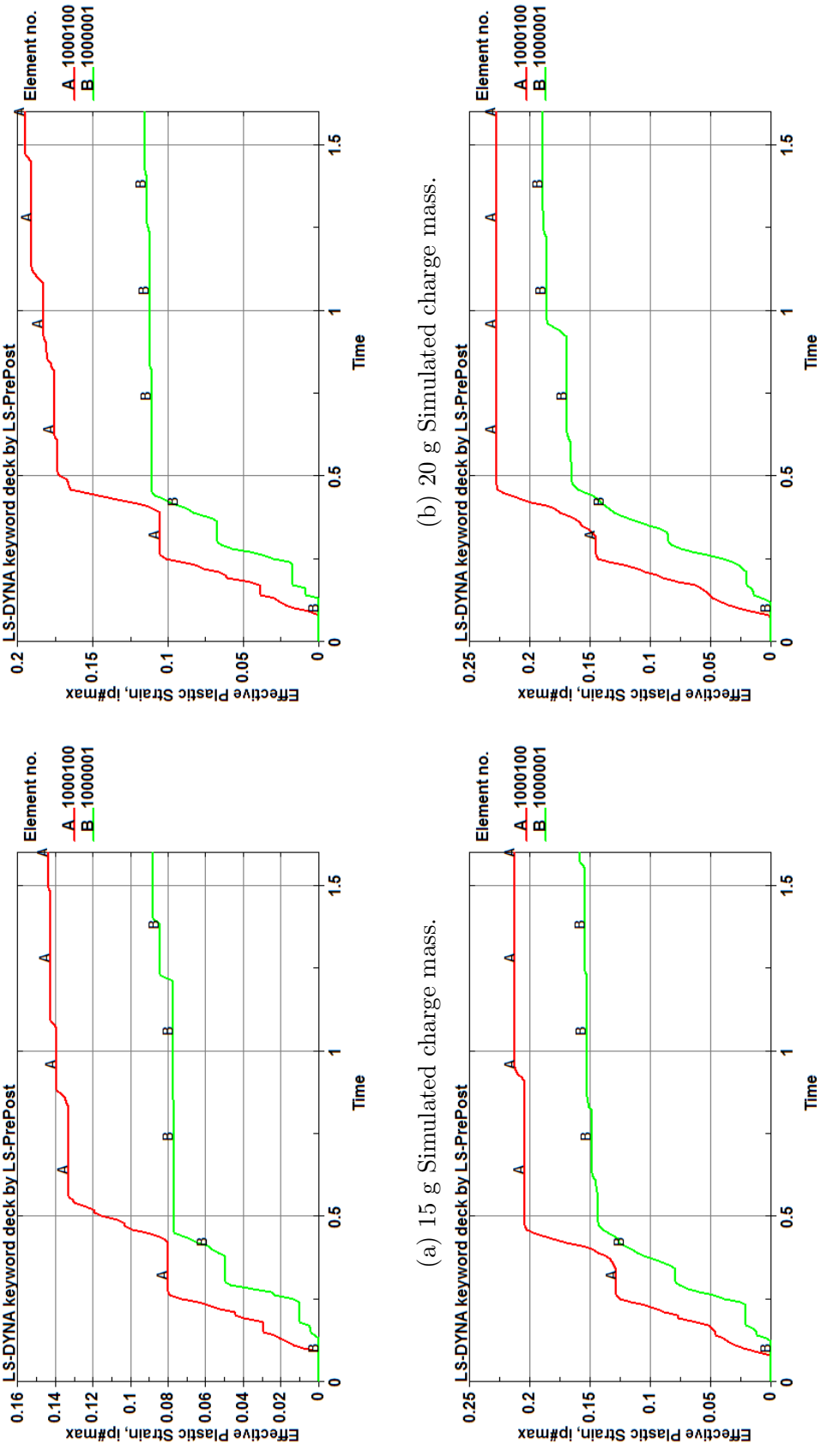

(a) 15 g Simulated charge mass.

(b) 20 g Simulated charge mass.

(c) 25 g Simulated charge mass.

(d) 30 g Simulated charge mass.

Figure C.4: Plastic strain development under uniform blast loading at A - the clamped boundary and B - panel midpoint for various simulated charge masses.

C.2.2 Von-Mises Stresses

Von-Mises stress is a good measure of ductile material resistance to complex loading conditions. As the FMLs consist of both aluminium and GFRP, the Von-Mises stress values over time serve more to indicate the evolution of stress in the FML. The Von-Mises stress data from the simulations of the localised loading conditions are shown in Figure C.3 and data obtained from the uniform loading simulations are shown in Figure C.4.

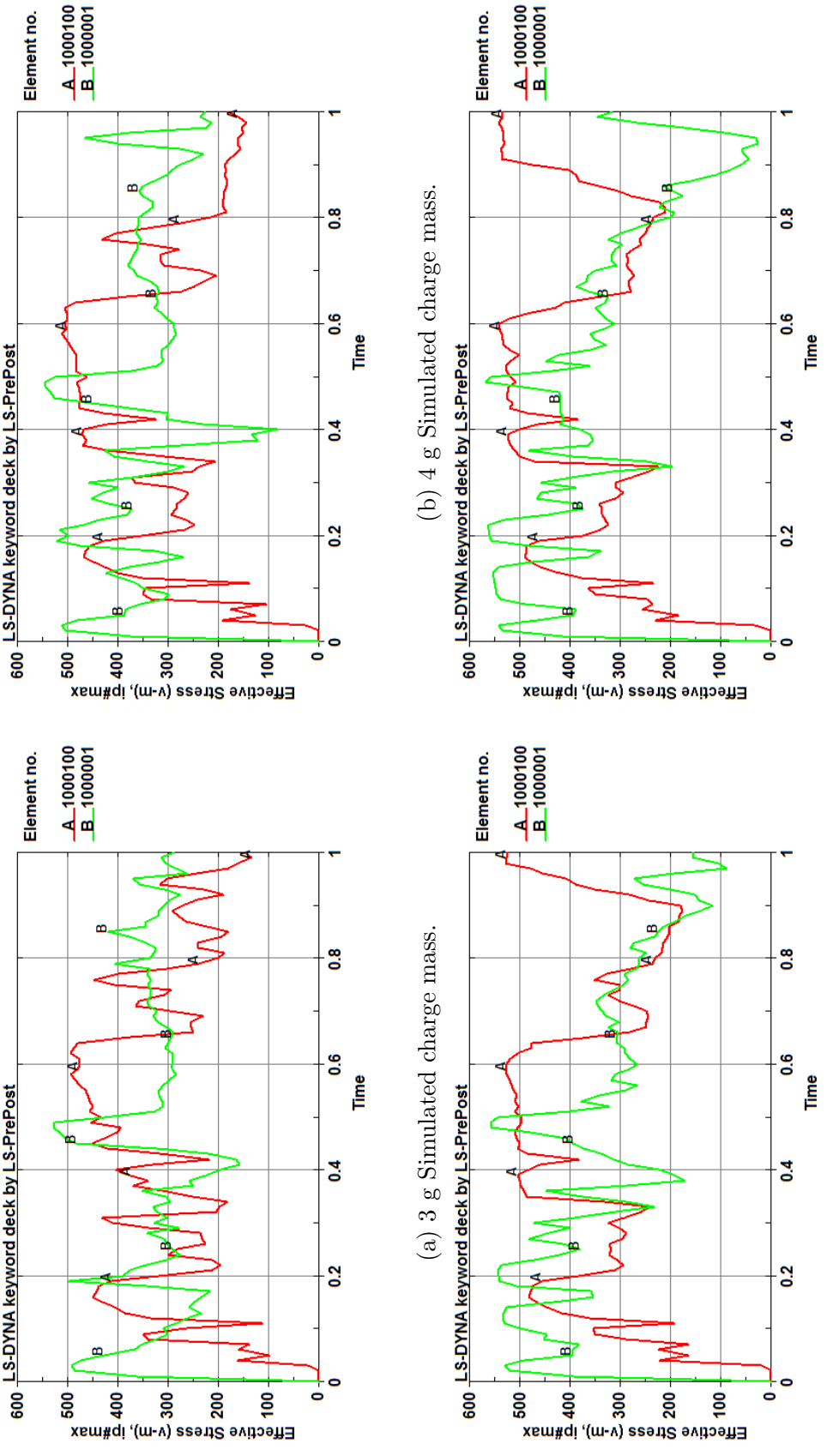

(a) 3 g Simulated charge mass.

(b) 4 g Simulated charge mass.

(c) 5 g Simulated charge mass.

(d) 6 g Simulated charge mass.

Figure C.5: Von-Mises stress development under localised blast loading at A - the clamped boundary and B - panel midpoint for various simulated charge masses.

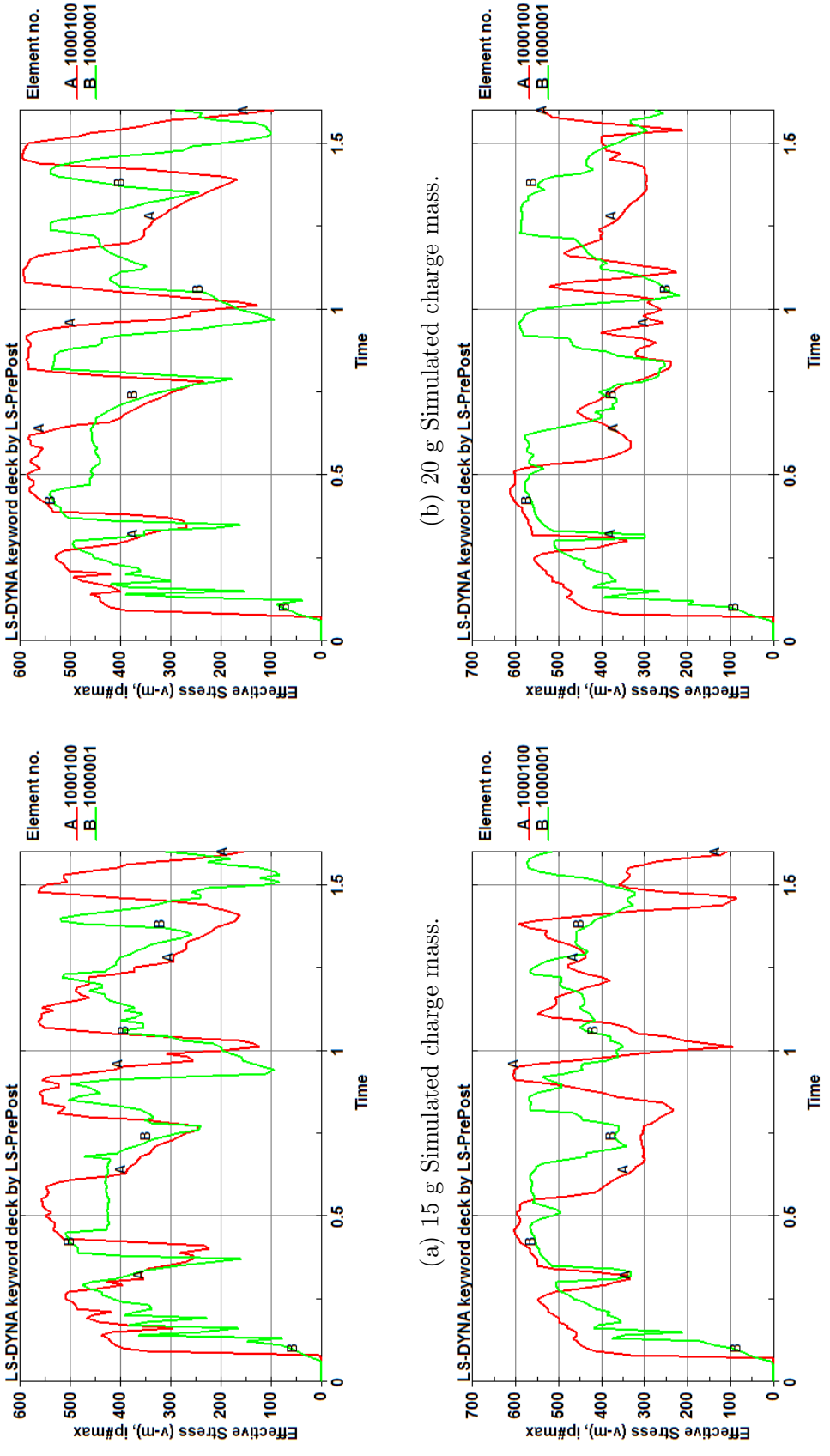

(a) 15 g Simulated charge mass.

(b) 20 g Simulated charge mass.

(c) 25 g Simulated charge mass.

(d) 30 g Simulated charge mass.

Figure C.6: Von-Mises stress development under uniform blast loading at A - the clamped boundary and B - panel midpoint for various simulated charge masses.

Appendix D

Blast Testing Results

D.1 Pendulum and Specimen Measurements

The data for all blast tests is detailed in Table D.1. This includes the charge mass, stand-off distance pendulum measurements and panel thickness.

D.2 Displacement Contour Plots

Contour plots that were not discussed in Section 7.2.3 are shown in Figures D.1 to D.9. These plots indicate the displacement response of the various FMLs to uniform loading conditions.

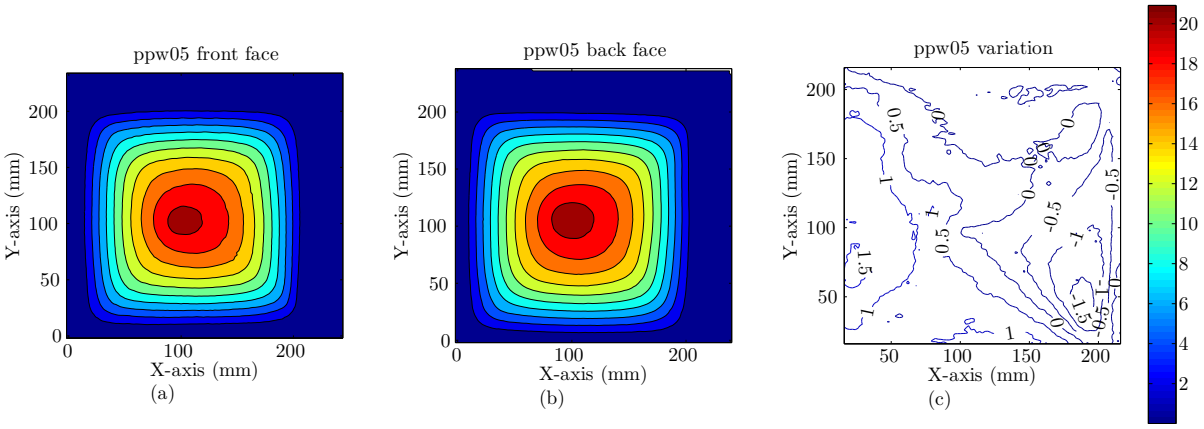

Figure D.1: Contour plots of (a) front face displacements, (b) back face displacements and (c) variation of section thickness of a PPW panel subjected to 20 g at 200 mm standoff distance.

Table D.1: Blast pendulum data

Test	Charge Mass	Standoff (mm)	Delta R (m)	Delta L (m)	FML Thickness (mm)
Uniform Loading					
PPW01	15	200	0.098	0.105	4.59
PPW03	30	200	0.162	0.176	4.5
PPW04	10	200	0.068	0.066	4.53
PPW05	20	200	0.114	0.11	4.48
PPW07	25	200	0.143	0.137	4.51
PPW10	30	200	0.148	0.155	4.58
PPW12					4.51
WLW01	15	200	0.095	0.105	5.08
WLW02	30	200	0.164	0.169	4.91
WLW06	35	200	0.174	0.186	5.01
WLW07					5.05
WLW10	20	200	0.11	0.111	4.9
WLUD02	30	200	0.158	0.165	4.92
WLUD03	20	200	0.115	0.109	4.9
WLUD04	15	200	0.096	0.096	5.16
WLUD05	10	200	0.071	0.068	5.21
WLUD06	25	200	0.134	0.132	5.05
WLUD09	35	200	0.166	0.174	5.06
WLUD10	40	200	0.185	0.2	5.11
WLUD12					5.01
Localised Loading					
PPW02	3	20	0.018	0.015	4.45
PPW06	3	20	0.015	0.014	4.55
PPW08	10	40	0.069	0.072	4.46
PPW09	7	40	0.034	0.036	4.53
WLW05	10	20	0.05	0.046	4.98
WLW03	5	20	0.026	0.028	4.96
WLW04	3	20	0.017	0.014	5.14
WLW08	10	40	0.07	0.071	5.08
WLUD07	10	40	0.075	0.078	4.99
Failed Charges					
PPW11	15	40			4.49
WLW09	25	200			4.91
WLW11	20	200			5.23
WLW12	10	200			5.2
WLW13	10	200			4.9
WLW14	35	200			5.06
WLUD01	30	200			4.94
WLUD08	10	40			4.99
WLUD11	3	20			4.94

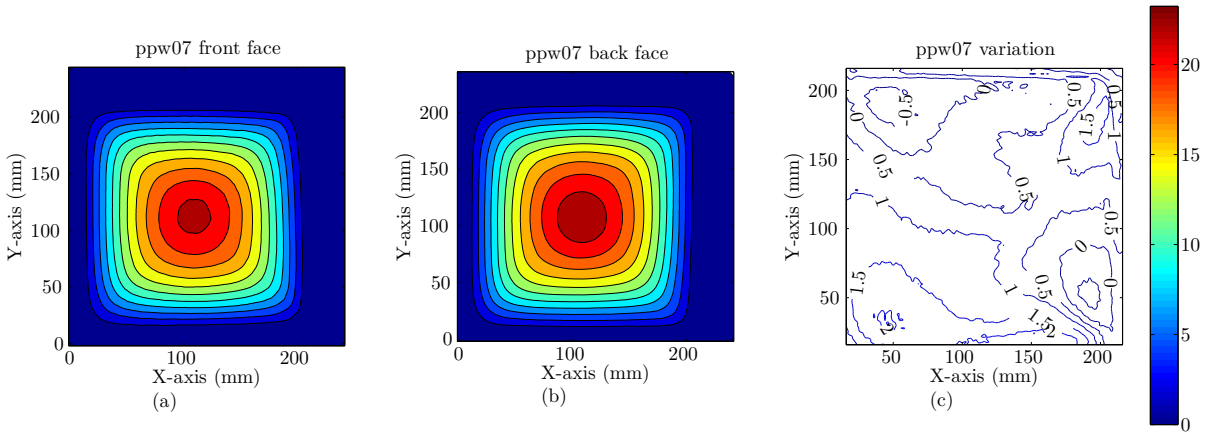

Figure D.2: Contour plots of (a) front face displacements, (b) back face displacements and (c) variation of section thickness of a PPW panel subjected to 25 g at 200 mm standoff distance.

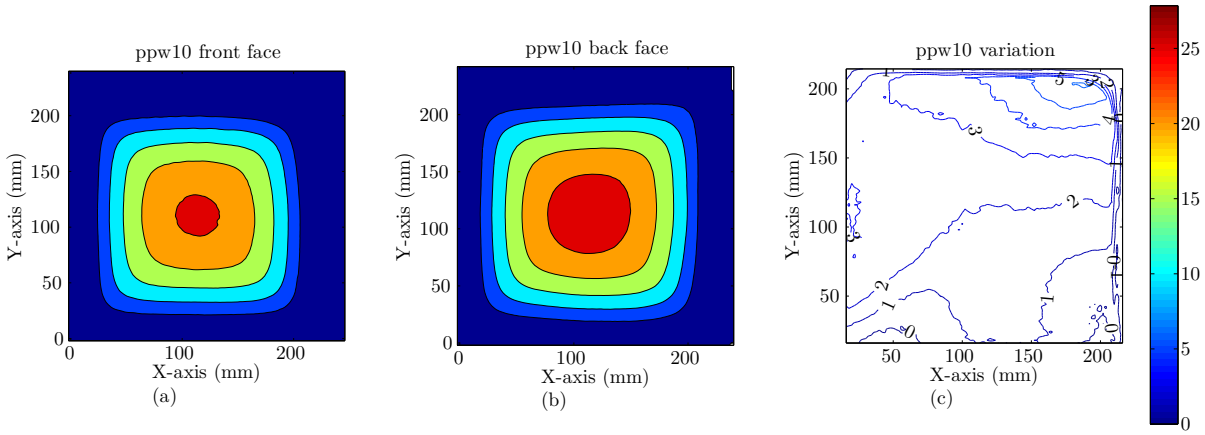

Figure D.3: Contour plots of (a) front face displacements, (b) back face displacements and (c) variation of section thickness of a PPW panel subjected to 30 g at 200 mm standoff distance.

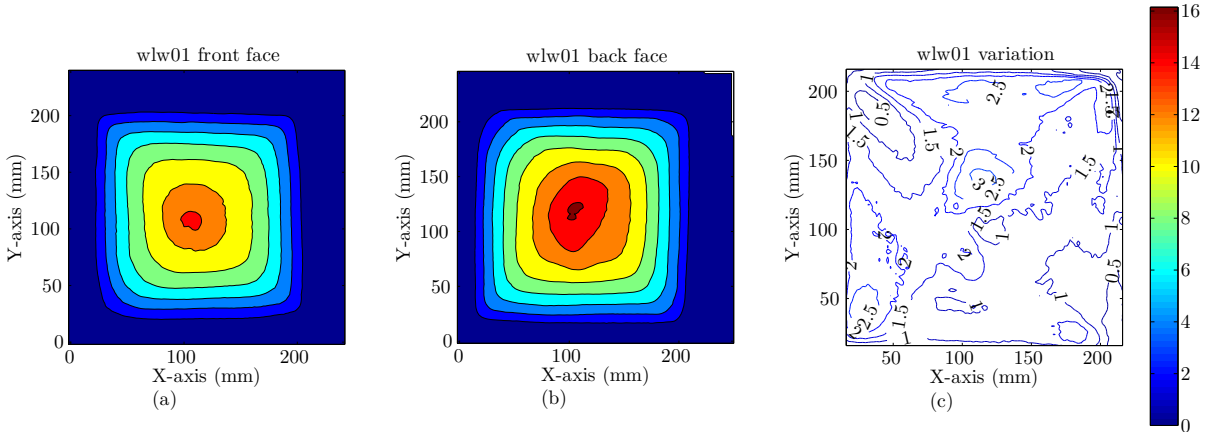

Figure D.4: Contour plots of (a) front face displacements, (b) back face displacements and (c) variation of section thickness of a WLW panel subjected to 15 g at 200 mm standoff distance.

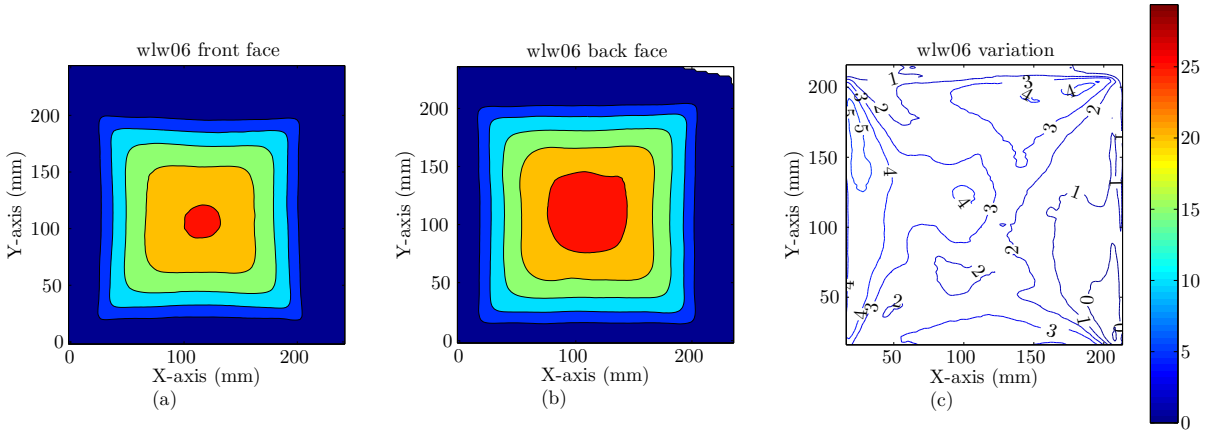

Figure D.5: Contour plots of (a) front face displacements, (b) back face displacements and (c) variation of section thickness of a WLW panel subjected to 35 g at 200 mm standoff distance.

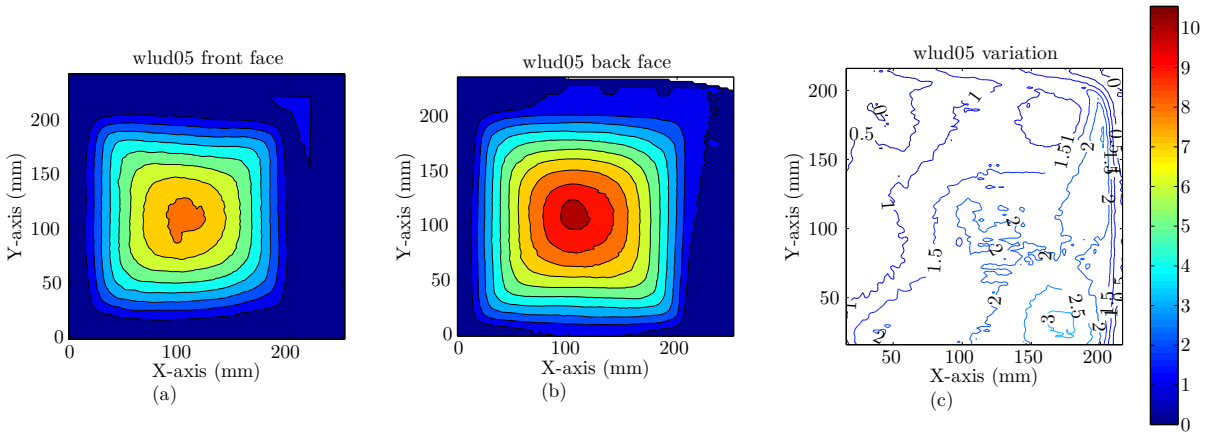

Figure D.6: Contour plots of (a) front face displacements, (b) back face displacements and (c) variation of section thickness of a WLUD panel subjected to 10 g at 200 mm standoff distance.

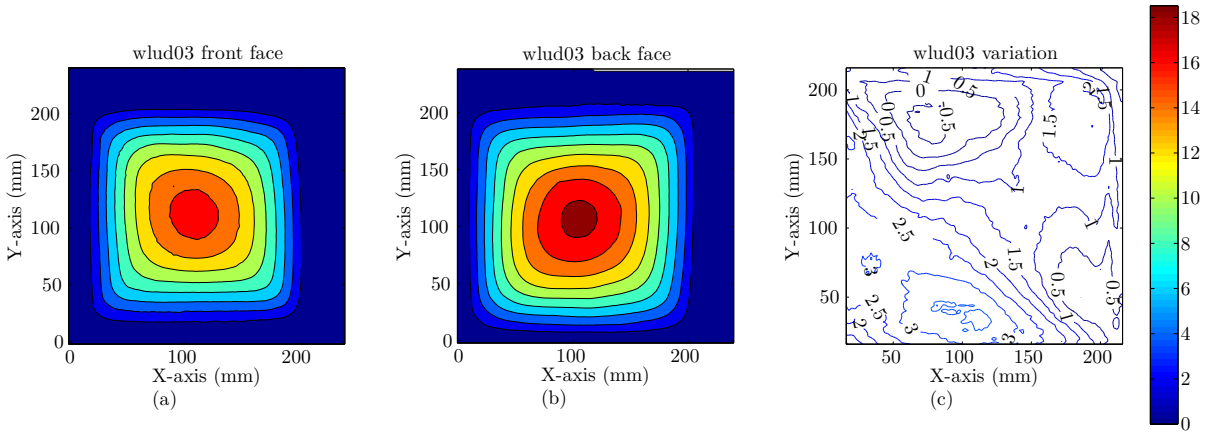

Figure D.7: Contour plots of (a) front face displacements, (b) back face displacements and (c) variation of section thickness of a WLUD panel subjected to 20 g at 200 mm standoff distance.

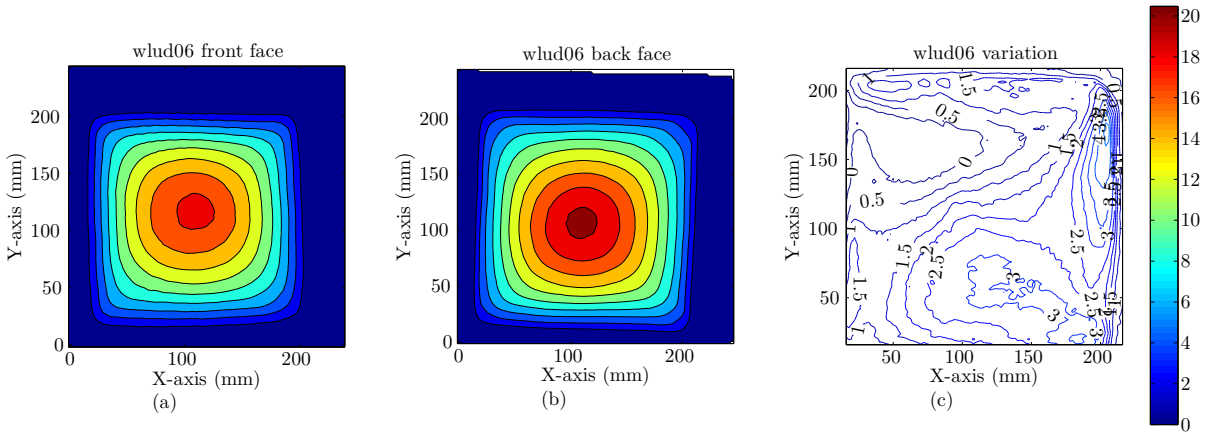

Figure D.8: Contour plots of (a) front face displacements, (b) back face displacements and (c) variation of section thickness of a WLUD panel subjected to 25 g at 200 mm standoff distance.

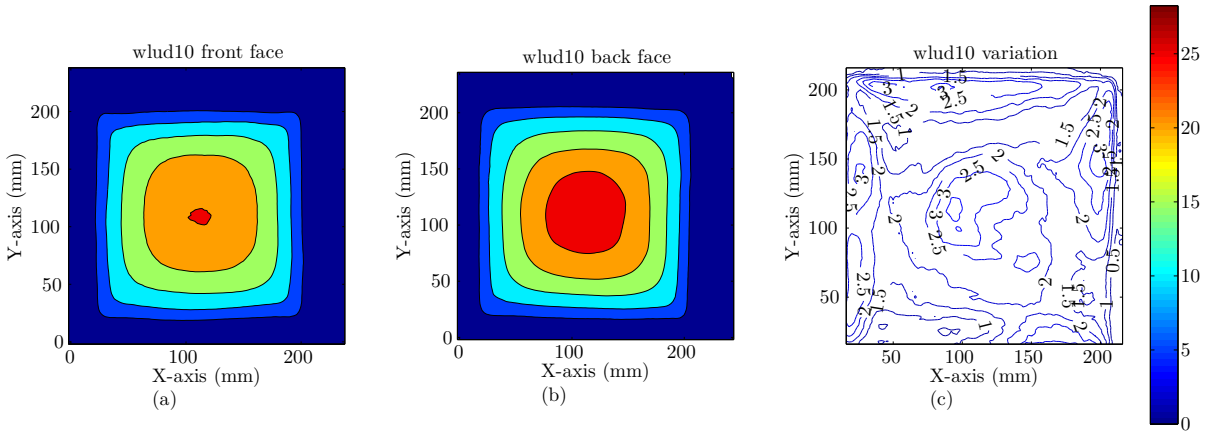

Figure D.9: Contour plots of (a) front face displacements, (b) back face displacements and (c) variation of section thickness of a WLUD panel subjected to 40 g at 200 mm standoff distance.